FERMILAB-THESIS-2012-68

Università degli Studi di Siena

Facoltà di Scienze Matematiche Fisiche e Naturali

Tesi di Dottorato in Fisica Sperimentale
PhD Thesis in Experimental Physics

XXIII Ciclo

First Observation of Charmed Resonances in the $\Lambda_b^0 \to \Lambda_c^+ \pi^- \pi^+ \pi^-$ Inclusive Decays and Measurement of their Relative Branching Ratios at CDF

Candidate
Patrizia Barria

Advisor
Dott. Maria Agnese Ciocci

Contents

Contents

Contents

To my mother,
my father ,
and my brothers

Abstract

We present the observation of the Λ_b^0 decay into a $\Lambda_c^+\pi^-\pi^+\pi^-$ final state, in $p\bar{p}$ collisions at $\sqrt{s} = 1.96$ TeV. The data analyzed were collected by the CDF II detector at the Fermilab Tevatron collider, and correspond to $2.4\,\text{fb}^{-1}$ of integrated luminosity. We fit the invariant mass distribution of the reconstructed candidates to extract a signal yield of 848 ± 93 Λ_b^0 into $\Lambda_c^+\pi^-\pi^+\pi^-$. We also present, in the same final state, the observation of the charmed resonant decays $\Lambda_b^0 \to \Sigma_c(2455)^{++}\pi^-\pi^-$, $\Lambda_b^0 \to \Sigma_c(2455)^0\pi^+\pi^-$, $\Lambda_b^0 \to \Lambda_c(2595)^+\pi^-$ and $\Lambda_b^0 \to \Lambda_c(2625)^+\pi^-$, contributing to the inclusive $\Lambda_b^0 \to \Lambda_c^+\pi^-\pi^+\pi^-$ signal, and measure the following relative branching ratios:

$$\frac{\mathcal{B}(\Lambda_b^0 \to \Lambda_c(2595)^+\pi^- \to \Lambda_c^+\pi^-\pi^+\pi^-)}{\mathcal{B}(\Lambda_b^0 \to \Lambda_c^+\pi^-\pi^+\pi^-(all))} = (2.5 \pm 0.6 \pm 0.5) \times 10^{-2}$$

$$\frac{\mathcal{B}(\Lambda_b^0 \to \Lambda_c(2625)^+\pi^- \to \Lambda_c^+\pi^-\pi^+\pi^-)}{\mathcal{B}(\Lambda_b^0 \to \Lambda_c^+\pi^-\pi^+\pi^-(all))} = (6.2 \pm 1.0^{+1.0}_{-0.9}) \times 10^{-2}$$

$$\frac{\mathcal{B}(\Lambda_b^0 \to \Sigma_c(2455)^{++}\pi^-\pi^- \to \Lambda_c^+\pi^-\pi^+\pi^-)}{\mathcal{B}(\Lambda_b^0 \to \Lambda_c^+\pi^-\pi^+\pi^-(all))} = (5.2 \pm 1.1 \pm 0.8) \times 10^{-2}$$

$$\frac{\mathcal{B}(\Lambda_b^0 \to \Sigma_c(2455)^0\pi^+\pi^- \to \Lambda_c^+\pi^-\pi^+\pi^-)}{\mathcal{B}(\Lambda_b^0 \to \Lambda_c^+\pi^-\pi^+\pi^-(all))} = (8.9 \pm 2.1^{+1.2}_{-1.0}) \times 10^{-2}$$

$$\frac{\mathcal{B}(\Lambda_b^0 \to \Lambda_c^+\rho^0\pi^- + \Lambda_c^+\pi^-\pi^+\pi^-(other) \to \Lambda_c^+\pi^-\pi^+\pi^-)}{\mathcal{B}(\Lambda_b^0 \to \Lambda_c^+\pi^-\pi^+\pi^-(all))} = (77.3 \pm 3.1^{+3.0}_{-3.3}) \times 10^{-2}$$

$$\frac{\mathcal{B}(\Lambda_b^0 \to \Lambda_c(2595)^+\pi^- \to \Lambda_c^+\pi^-\pi^+\pi^-)}{\mathcal{B}(\Lambda_b^0 \to \Lambda_c(2625)^+\pi^- \to \Lambda_c^+\pi^-\pi^+\pi^-)} = (40.3 \pm 9.8^{+2.3}_{-1.8}) \times 10^{-2}$$

$$\frac{\mathcal{B}(\Lambda_b^0 \to \Sigma_c(2455)^{++}\pi^-\pi^- \to \Lambda_c^+\pi^-\pi^+\pi^-)}{\mathcal{B}(\Lambda_b^0 \to \Sigma_c(2455)^0\pi^+\pi^- \to \Lambda_c^+\pi^-\pi^+\pi^-)} = (58.1 \pm 16.9^{+6.3}_{-9.1}) \times 10^{-2}$$

$$\frac{\mathcal{B}(\Lambda_b^0 \to \Lambda_c(2625)^+\pi^- \to \Lambda_c^+\pi^-\pi^+\pi^-)}{\mathcal{B}(\Lambda_b^0 \to \Sigma_c(2455)^{++}\pi^-\pi^- \to \Lambda_c^+\pi^-\pi^+\pi^-)} = (119.7 \pm 26.0^{+4.7}_{-9.1}) \times 10^{-2}$$

Abstract

In these measurements the first uncertainty is statistical and the second one is systematic, $\Lambda_b^0 \to \Lambda_c^+\pi^-\pi^+\pi^-(all)$ indicates the Λ_b^0 inclusive decay and $\Lambda_b^0 \to \Lambda_c^+\pi^-\pi^+\pi^-(other)$ includes the $\Lambda_c^+\pi^-\pi^+\pi^-(nr)$, with the three pions system not resonant (nr), when assuming a null contribution from the $\Lambda_b^0 \to \Lambda_c^+ a_1(1260)^- \to \Lambda_c^+\rho^0\pi^- \to \Lambda_c^+\pi^-\pi^+\pi^-$ and equal contribution from $\Lambda_b^0 \to \Lambda_c^+\rho^0\pi^- \to \Lambda_c^+\pi^-\pi^+\pi^-$ and $\Lambda_b^0 \to \Lambda_c^+\pi^-\pi^+\pi^-(nr)$, or, a $\Lambda_b^0 \to \Lambda_c^+ a_1(1260)^- \to \Lambda_c^+\rho^0\pi^- \to \Lambda_c^+\pi^-\pi^+\pi^-$ when assuming null the contribution from the $\Lambda_b^0 \to \Lambda_c^+\pi^-\pi^+\pi^-(nr)$ and equal contribution from $\Lambda_b^0 \to \Lambda_c^+\rho^0\pi^-$ and $\Lambda_b^0 \to \Lambda_c^+ a_1(1260)^- \to \Lambda_c^+\rho^0\pi^- \to \Lambda_c^+\pi^-\pi^+\pi^-$.

Introduction

The Tevatron and Large Hadron Collider (LHC) experiments, unlike the *B-Factories*, have the unique opportunity to study the production and the decays of b-hadrons with c and s quarks, and among them especially the b-baryons which are the less known to date [1]. The Collider Detector at Fermilab (CDF) experiment pioneered this field of research, as shown in Tab. 1. Moreover, it currently has the world's largest data sample of bottom baryons. This is mainly due to the combination of the large accumulated integrated luminosity delivered by the Tevatron, and the use of the displaced track trigger, a sophisticated piece of hardware, which is capable to select online events with secondary vertices, a typical feature of heavy hadrons decays, thus rejecting most part of the background from light quarks.

For the CDF B group of physics, this creates new opportunities to study heavy baryons, to expand our knowledge of the structure of baryonic matter and also gives the chance to search for new b-baryon decays, and, among these, new Λ_b^0 decays, the main challenge of this work of Thesis.

The work presented in this Thesis is part of the CDF research program on Λ_b^0 decays. The weak decays of the Λ_b^0 baryon are a good laboratory for testing some approximations in Quantum Chromo Dynamics (QCD) calculations due to the high b-quark mass, as for example Heavy Quark Effective Theory (HQET) [2], [3]. Alternatively, when using such calculations, the Λ_b^0 may provide a means to determine Cabibbo-Kobayashi-Maskawa (CKM) matrix elements with different systematic uncertainties than the determinations from the decays of B-mesons [4]. The Λ_b^0 baryon is poorly known. At the time of writing of this Thesis, only nine Λ_b^0 decay modes have been observed, with the sum of their measured Branching Ratios (BRs) of the order of only 0.1 with large uncertainties on the measurements [1], and the $\Lambda_b^0 \to \Lambda_c^+ \pi^- \pi^+ \pi^-$ decay mode was unobserved. While theoreti-

cal predictions are available for the $\Lambda_b^0 \to \Lambda_c^+\pi^-$ branching fraction [5], [6], and are in agreement with the experimental measurement [1], no prediction is available for the $\Lambda_b^0 \to \Lambda_c^+\pi^-\pi^+\pi^-$ decay.
The CDF observation of resonance structures in the Λ_b^0 semileptonic decays $\Lambda_b^0 \to \Lambda_c^+\pi^+\pi^-\ell\overline{\nu}_\ell$ [7], (the pink highlighted decays of Tab. 1), leads us to speculate that similar resonance structures may exist in the corresponding hadronic decay mode $\Lambda_b^0 \to \Lambda_c^+\pi^-\pi^+\pi^-$, where the $\ell\overline{\nu}_\ell$ pair is replaced by a $\overline{u}d$ quark pair.

Process	Measurement	Ldt(fb^{-1})	# Events	Reference
$\Lambda_b^0 \to J/\Psi\Lambda$	Mass	0.22	89	*PRL 96, 202001 (2006)* [8]
	Lifetime	1.00	538	*PRL 98, 122001 (2007)* [9]
$\Lambda_b^0 \to \Lambda_c^+\pi^-$	$\mathcal{B}$	0.11	214	*PRL 98, 122002 (2007)* [10]
$\Lambda_b^0 \to \Lambda_c^+\ell\overline{\nu}_\ell$ anything	b-quark frag.	0.36	1760	*PR D77, 072003 (2008)* [11]
$\Lambda_b^0 \to \Lambda_c^+\ell\overline{\nu}_\ell$	$\mathcal{B}$	0.17	980	*PR D79, 032001 (2009)* [7]
$\Lambda_b^0 \to \Lambda_c(2595)^+\ell\overline{\nu}_\ell$	$\mathcal{B}$/discovery	0.17	31	*PR D79, 032001 (2009)* [7]
$\Lambda_b^0 \to \Lambda_c(2625)^+\ell\overline{\nu}_\ell$	$\mathcal{B}$/discovery	0.17	53	*PR D79, 032001 (2009)* [7]
$\Lambda_b^0 \to \Sigma_c(2455)^0\ell\overline{\nu}_\ell$	$\mathcal{B}$/discovery	0.17	16	*PR D79, 032001 (2009)* [7]
$\Lambda_b^0 \to \Sigma_c(2455)^{++}\ell\overline{\nu}_\ell$	$\mathcal{B}$/discovery	0.17	26	*PR D79, 032001 (2009)* [7]
$\Sigma_b^+ \to \Lambda_b^0\pi^+$	mass/discovery	1.10	32	*PRL 99, 191806 (2007)* [12]
$\Sigma_b^{*+} \to \Lambda_b^0\pi^+$	mass/discovery	1.10	77	*PRL 99, 191806 (2007)* [12]
$\Sigma_b^- \to \Lambda_b^0\pi^+$	mass/discovery	1.10	59	*PRL 99, 191806 (2007)* [12]
$\Sigma_b^{*-} \to \Lambda_b^0\pi^+$	mass/discovery	1.10	69	*PRL 99, 191806 (2007)* [12]
$\Xi_b^- \to J/\Psi\Xi^-$	mass/observation	1.90	18	*PRL 99, 052002 (2007)* [13]
$\Lambda_b^0 \to p\pi^-$	$\mathcal{B}$/discovery	1.00	110	*PRL 103, 031801 (2009)* [14]
$\Lambda_b^0 \to pK^-$	$\mathcal{B}$/discovery	1.00	156	*PRL 103, 031801 (2009)* [14]

Table 1: *CDF b-Baryon measurements (Run II).*

This Thesis describes the search and the first observation of the $\Lambda_b^0 \to \Lambda_c^+\pi^-\pi^+\pi^-$[1] as well as the search and the first observation of the resonant decays $\Lambda_b^0 \to \Lambda_c(2595)^+\pi^-$, $\Lambda_b^0 \to \Lambda_c(2625)^+\pi^-$, $\Lambda_b^0 \to \Sigma_c(2455)^{++}\pi^-\pi^-$, $\Lambda_b^0 \to \Sigma_c(2455)^0\pi^-\pi^+$, contributing to the inclusive $\Lambda_b^0 \to \Lambda_c^+\pi^-\pi^+\pi^-$ signal observed, and the measurement of their relative BRs. The data sample used in this work corresponds to 2.4 fb^{-1} of $p\overline{p}$ collisions collected by CDF II between February 2002 and May 2007.
This thesis is organized as follows.

Chapter 1 summarizes the theoretical and experimental framework which motivate this work of Thesis.

Chapter 2 describes the Tevatron Collider, the CDF Detector and Trigger system.

Chapter 3 depicts the topology of the $\Lambda_b^0 \to \Lambda_c^+\pi^-\pi^+\pi^-$ and $\Lambda_b^0 \to \Lambda_c^+\pi^-$ decay modes, with the $\Lambda_c^+ \to pK^-\pi^+$ final state, and how, through the specialized

[1] Throughout this thesis, references to a specific charge state imply the charge-conjugate as well, unless otherwise specified.

online trigger selection for b-hadronic decays, we reconstruct the candidates, and finally focusing on the analysis cut optimization applied to obtain clear signals of these two Λ_b^0 decays on the data.

Chapter 4 explains the motivations and the MC tools for a search of charmed resonances in the Λ_b^0 final state $\Lambda_c^+\pi^-\pi^+\pi^-$. This Chapter, in particular, describes the production of fully simulated samples of the decays expected to contribute to the experimental $\Lambda_c^+\pi^-\pi^+\pi^-$ signal observed, and how the features of these samples are exploited to determine an offline selection that will be applied on real data to extract, with high efficiency, the contribution of each of the charmed resonant decay mode. The MC procedure adopted, for the production of these MC samples, is validated using the reconstructed clean signal of $\Lambda_b^0 \to \Lambda_c^+\pi^-$, since it has a larger statistics and a larger signal to background ratio than the $\Lambda_b^0 \to \Lambda_c^+\pi^-\pi^+\pi^-$. The validation is done through a detailed comparison between real data and MC for several kinematic quantities and is described in Appendix A.

Chapter 5 reports the fitting procedure applied to the mass distribution, used to extract the total yield of $\Lambda_b^0 \to \Lambda_c^+\pi^-\pi^+\pi^-$, then, after applying the requirements to separate the different resonant charmed decay modes, decribes the fitting procedure, applied to the obtained the mass distributions, to extract the yields of the decay modes contributing to the $\Lambda_c^+\pi^-\pi^+\pi^-$ final state. The data modeling used by the fits of the mass distributions, is here described. It includes the signal, the combinatorial background, and the physical background. The modeling of the signal and of the physical background (described also in Appendix B and Appendix C) makes use of full simulated samples of these contributions.

Chapter 6 describes the raw measurements of the relative BRs. These make use of the yields of the decay modes contributing to the inclusive $\Lambda_b^0 \to \Lambda_c^+\pi^-\pi^+\pi^-$ decay, of their efficiencies, and of the yield of the inclusive decay mode itself. The efficiency of each decay mode is determined using the corresponding MC simulated sample.

Chapter 7 gives an overview of the two main sources of systematic uncertainty in the measurement of the relative branching fractions, those related to the fitting procedure and affecting the yields, and those related to the estimate of the relative efficiencies, then a summary of the results of this Thesis work is presented.

The measurements reported in this Thesis are the first mandatory step towards the measurement of the absolute BRs of these new Λ_b^0 decay modes. Such measurement may be compared with the theoretical predictions (still unavailable for

these decay modes), making use of CKM matrix elements and of dynamic factors determined, in the case of b–hadrons decays, with the HQET.
The CDF collaboration recently first updated the relative BRs measured in this Thesis [15], with minor changes in the analysis, using the same amount of data (2.4 fb^{-1}), then measured the relative BR $\mathcal{B}(\Lambda_b^0 \to \Lambda_c^+\pi^-\pi^+\pi^-(all))/\mathcal{B}(\Lambda_b^0 \to \Lambda_c^+\pi^-)$ and finally derived the absolute branching fractions of the decay modes contributing to $\Lambda_b^0 \to \Lambda_c^+\pi^-\pi^+\pi^-$ [16].
Also LHCb collaboration at LHC recently did the same measurements [17].
A comparison of the results obtained by CDF and LHCb is done in the Conclusion.
The measurements subject of this Thesis, has been approved by the CDF Collaboration [18] and were presented for the first time in [19].
The CDF Collaboration results, not subject of this Thesis, concerning the updated measurements of the relative branching fractions and the absolute BRs above mentioned, are meant to be submitted in Physical Review D.

Chapter 1

Theoretical Framework and Analysis Motivations

1.1 Standard Model Introduction

All experimental data from high energy experiments studied so far can be described by the Standard Model (SM) [20], [21], [22] of particles and their interactions. Data collected in the last years, mainly by the experiments at the large particle accelerators (SLAC, SPS, Tevatron, LEP, HERA), allowed to test the agreement between measurements and theoretical calculations of SM with a precision of $10^{-3} - 10^{-4}$. In this model the fundamental constituents of matter are spin $1/2$ *fermions*, the *quarks* and the *leptons*, and the interactions between them are described by the exchange of *gauge bosons*: *photons* for the electromagnetic interaction, *bosons* $W^{\pm}$ and Z for the weak interaction and finally *gluons*, which are electrically neutral but carry color (strong) charge, for the strong interaction. It should be noted that the SM is not accepted as an accurate description of how the universe operates at its most fundamental level since it does not include gravity (~ 40 order of magnitude smaller than the strong nuclear force, it is not expected to contribute significantly to physical process in high energy particle physics) but it only represents our best current knowledge. The formulation of the SM as a gauge theory guarantees its renormalizability, but forbids explicit mass terms for fermions and gauge bosons. The masses of the particles are generated in a gauge invariant way by the *Higgs Mechanism*, via a spontaneous breaking of the electroweak symmetry. This mechanism also implies the presence of a massive scalar particle in the mass spectrum of the theory, the *Higgs boson*. The experiments at the Fermilab Tevatron proton antiproton collider, and at the CERN proton proton collider LHC, are in an excellent position to give conclusive answers to many open questions of fundamental physics, as the existence of the Higgs boson (the only

fundamental particle in the SM which has still to be experimentally verified), the origin of the CP asymmetry and the existence of physics beyond SM. Extensive discussion of the SM can be found in [20], [21], [22] while in this chapter we recall some aspects of the SM pertinent to the analysis described in this Thesis and the experimental and the theoretical aspects that motivate this study.

1.1.1 The fundamental particles and their interactions

Whitin the SM all the elementary particles are divided in two families:

- *fermions* with spin $^1/_2$ that follow *Fermi-Dirac* statistics;
- *bosons* with spin 1 that follow *Bose-Einstein* statistics.

The SM includes 12 fundamental fermions and their corresponding anti-particles: 6 interact just through the electroweak interaction and are called *leptons*, the others 6 interact also through the strong interaction and are called *quarks*.
Leptons are organized in three generations as follow:

$$\begin{pmatrix} e \\ \nu_e \end{pmatrix} \qquad \begin{pmatrix} \mu \\ \nu_\mu \end{pmatrix} \qquad \begin{pmatrix} \tau \\ \nu_\tau \end{pmatrix}$$

with their properties summarized in Tab. 1.1.

Name	Mass (GeV/c^2)	Charge (e)	lifetime(τ) or lifetime/mass (τ/m)
e	511×10^{-6}	-1	$> 4.6 \times 10^{26}\ yr\ (CL = 90\%)$
ν_e	$< 2.3 \times 10^{-6}$	0	$\tau/m > 300\ s/eV\ (CL = 90\%\ reactor)$
μ	105.6×10^{-3}	-1	$2.197 \times 10^{-6}\ s$
ν_μ	$< 0.17 \times 10^{-3}$	0	$\tau/m > 15.4\ s/eV\ (CL = 90\%)$
τ	1.776	-1	$(290.6 \pm 1.0) \times 10^{-15}\ s$
ν_τ	$< 15.5 \times 10^{-3}$	0	

Table 1.1: *Observed lepton properties in the SM [1].*

The *lepton flavour number* L_e, L_μ and L_τ is equal to +1 for each lepton and to -1 for its antiparticle, and is conserved in the processes where leptons are involved.
The quarks, according to SM, are divided into three generations as:

$$\begin{pmatrix} u \\ d \end{pmatrix} \qquad \begin{pmatrix} c \\ s \end{pmatrix} \qquad \begin{pmatrix} t \\ b \end{pmatrix}$$

with basic properties in the following Tab. 1.2.
Each quark has an antiquark partner so also in this case we have 12 quarks.

Name	Mass (GeV/c^2)	Charge (e)
up (u)	$(1.7 - 3.3) \times 10^{-3}$	$+2/3$
down (d)	$(4.1 - 5.8) \times 10^{-3}$	$-1/3$
charm (c)	$1.27^{+0.07}_{-0.11}$	$+2/3$
strange (s)	$(101) \times 10^{-3}$	$-1/3$
top (t)	172.0 ± 1.6	$+2/3$
bottom (b)	$4.19^{+0.18}_{-0.06}$	$-1/3$

Table 1.2: *Observed quark properties in the SM [1].*

While we can consider u and d quarks as doublet components $\pm 1/2$ of an isospin vector of value $I{=}1/2$, the other four quarks are characterized by other quantum number as:

- *Strangeness (S)*: quantum number introduced by Murray Gell-Mann that is -1 for the strange quark;
- *Charm (C)*: number which is +1 for the charm quark;
- *Bottomness (B)*: number which is -1 for the bottom quark;
- *Topness (T)*: quantum number which is +1 for the top quark.

These are useful quantum numbers since they are conserved by both the electromagnetic and strong interactions but not by the weak interaction, where they can change by 1. The quark's mass eigenstates are not the same as its weak eigenstates and this leads to process in which generation changes occur. These are characterized by a quark flavour mixing matrix : the Cabibbo-Kobayashi-Maskawa matrix (V_{CKM}) [23]. The V_{CKM} matrix is defined through:

$$\begin{pmatrix} d' \\ s' \\ b' \end{pmatrix} = \underbrace{\begin{pmatrix} V_{ud} & V_{us} & V_{ub} \\ V_{cd} & V_{cs} & V_{cb} \\ V_{td} & V_{ts} & V_{tb} \end{pmatrix}}_{V_{CKM}} \begin{pmatrix} d \\ s \\ b \end{pmatrix} \tag{1.1}$$

where q' and q are weak and mass eigenstates respectively. In the SM the V_{CKM} matrix is represented by a 3×3 unitary matrix, completely described by three real parameters and one complex phase. Technically, it specifies the mismatch of quantum states of quarks when they propagate freely and when they take part in the weak interactions. The SM sustained many test of the accuracy of its predictions. The processes examined in this Thesis involve the so-called *heavy-flavor* sector. Its experimental investigation is mostly based on the study of decays

of hadrons containing heavy-quarks (c or b-quarks) into lighter states. The t quark does not form bound states, due to its very short lifetime, and makes a separate subject by itself. The flavor changing interactions in the SM are due to the weak interactions between quarks, mediated by the charged weak current and V_{CKM} matrix , with an Hamiltonian in the form:

$$\mathcal{H}_{ew} = \frac{g_2}{\sqrt{2}} (\bar{u}, \bar{c}, \bar{t}) V_{CKM} \begin{pmatrix} d \\ s \\ b \end{pmatrix} W^{\dagger} + \text{h.c.} \tag{1.2}$$

where g_2 is a constant that represents the coupling constant, the row-vector represents the three functions corresponding the *u-like* state (quarks with charge $+2/3$), on the left of the product, and the column vector on the right, the *d-like* (quarks with charge $-1/3$).
The V_{CKM} matrix was introduced by Kobayashi and Maskawa in 1973 [23], extending the Cabibbo mixing angle [24], proposed as the source of the different coupling between weak decays of kaon and Λ particles with respect to the β-decay of the neutron.
Leptons exist as free particles but is not the same for quarks. A phenomenon called *color confinement* results in quarks being perpetually bound to one another, forming color-neutral composite particles (*hadrons*) containing either a quark and an antiquark (*mesons*) or three quarks (*baryons*), so the color charge is confined. When highly energetic quarks or gluons are produced in a high energy physics experiment, a process called *hadronization* or *showering* takes place: after a quark-antiquark pair, or more in general a *parton*[1], is produced in an interaction, the potential between them, due to gluons exchange, tries to keep them together until the strength reaches a breaking point where further quark-antiquark pairs are created, and finally bound together with the original parton. This process involves a large number of interactions at different scales until the scale of hadrons is reached. The process is then essentially non-perturbative, and not completely theoretically calculable. The quarks could also radiate gluons that create other $q\bar{q}$ pairs. The final state in which we observe the parton generated in the interaction is a collimated *jet* of particles approximately in the direction of the original parton.

1.2 Λ_b^0 Production at Tevatron

The Λ_b^0 under study here are produced in collisions of protons and anti-protons at energies of 960 GeV each. At this energy, the fundamental interaction occurs

[1] Feynman called the constituents of the proton *partons*, so it refers to both valence quarks, sea quarks and gluons.

between the quarks and gluons contained in the colliding hadrons. The center of mass energy of the interaction depends on the fraction of energy carried by the colliding partons and, in principle, is enough to produce every known particle. This is the main difference between a hadron collider and B Factories where e^+ and e^- collide producing the Υ resonance that then decay in B^0 and $B^\pm$ mesons. At B Factories only the decay products of these mesons are present in the event. On the contrary, at hadron colliders, where all b-hadrons can be produced and among these the Λ_b^0 baryon subject of this Thesis, several low momentum interactions occur between quarks in the collision. Their final states are constituited by low momentum tracks that overlap to decay products of the interesting collision. In Tab. 1.3 we report the production rate of $b\bar{b}$ at CDF in Run II (CDF II) compared with the one at B Factories.

	BaBar	Belle	CDF	LHC
Luminosity $\mathrm{cm}^{-2}\mathrm{s}^{-1}$	4.6×10^{33}	8.3×10^{33}	1×10^{32}	1×10^{34}
$\sigma_{b\bar{b}}$	1.15 nb	1.15 nb	100 μb	500 μb†
Production rate	5 Hz	10 Hz	1000 Hz	500 KHz
$\sigma_{b\bar{b}}/\sigma_{had}$	0.25	0.25	$\approx 10^{-3}$	

† prediction [25].

Table 1.3: *This table compares the production rate of $b\bar{b}$ pairs in different environment. These numbers don't take into account experimental efficiencies for their detection.*

Between the two rates there are three order of magnitude.
However, at the Tevatron the cross section for this process is three order of magnitude smaller than the total cross section of hadron production.
Fig. 1.1 shows some examples of $b\bar{b}$ production Feynman diagrams. Several other diagrams concur to this process but we neglect them here. Starting from the top to the above they are so named:

- **direct production**: a quark with the corresponding antiquark annihilate producing a gluon and then a $b\bar{b}$;
- **gluon fusion**: two gluons from p and $\overline{p}$ interact;
- **flavor excitation**: a gluon interacts with virtual b and $\bar{b}$ extracting them from the hadron;
- **gluon splitting**: the collision occurs between two gluons and one of them produces a $b\bar{b}$ couple.

All these processes can be calculated in perturbative QCD.
The final states of the interaction have to be colorless *mesons* or *baryons*.

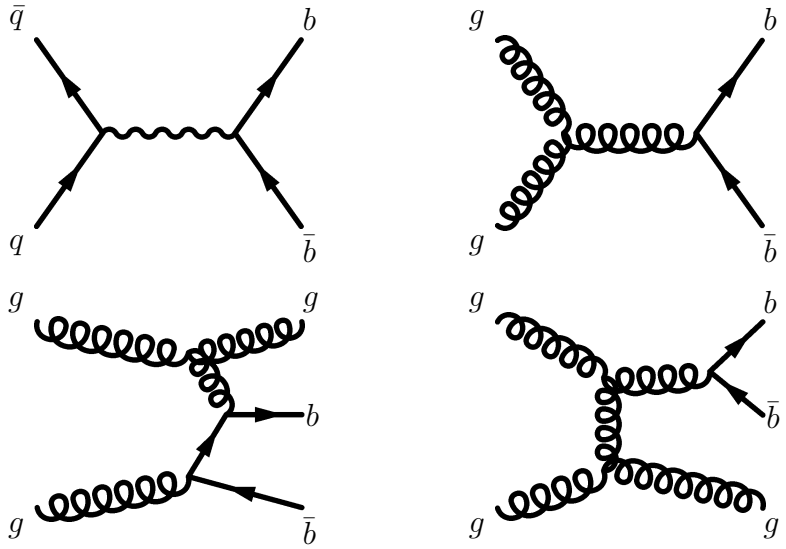

Figure 1.1: *Examples of $b\bar{b}$ production Feynman diagrams in a $p\bar{p}$ environments in a hadron collider. The reported processes are known as direct production, gluon fusion, flavor excitation and gluon splitting.*

The process that generates them, starting from a free b-quark, is called *hadronization*. Non perturbative QCD is used to compute all these processes where, in the final states, there are colorless mesons and baryons generated from a free b-quark by hadronization, a long distance process with small momentum transfer in which perturbative QCD is not applicable. Several phenomenological models have been developed to describe it [26], [27].
The hadrons, produced in the hadronization of a b-quark, are mainly $B^+(\bar{b}u)$, $B^0(\bar{b}d)$, $B_s^0(\bar{b}s)$, and $\Lambda_b^0(bud)$ and the different probabilities to hadronize into one of these particles are given by the measured fractions f_u, f_d, f_s, and f_{baryon} [1] respectively.
Experiments like LEP, where b-hadrons are produced in the Z^0 decay, and CDF extracted their mean value assuming identical hadronization in both Z^0 decay and $p\bar{p}$ collisions although, in principle, they can differ because of the different b-quark momentum distribution. All the hadronization fraction measurements have been made looking at particles produced above a certain p_T threshold, and the Fig. 1.2 shows how this threshold could affect the measurement:

- if both Λ_b^0 and B^0 have the same p_T distribution, the hadronization measurement would be independent of the p_T cut;
- if the two distributions are different, as in Fig. 1.2, the p_T threshold introduces a bias on the hadronization fractions.

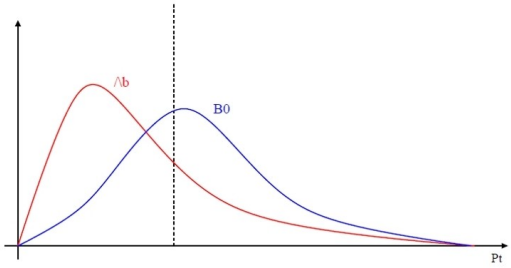

Figure 1.2: *Effect of a particle transverse momentum on the Λ_b^0 production fraction measurement: assuming the two distribution to be different, the fraction of measured Λ_b^0 depends on the p_T threshold.*

The data from the CDF experiment have shown, [28], [29], [30], that down to p_T values of the order of 4 GeV/c the p_T spectrum of Λ_b^0 is actually softer than the B^0. This means that if one measures the f_i factors down to this p_T level the fraction of Λ_b^0 would be larger (see Fig. 1.2) and we have to correct to the f_Λ measured by CDF [31].

1.3 Experimental Properties of Λ_b^0

The Λ_b^0 baryon is the lightest baryon, containing a b-quark, predicted by the SM. At CERN the UA1 collaboration in 1991 claimed the first observation of Λ_b^0 in the decay mode $\Lambda_b^0 \to J/\psi\Lambda$ with 4.7 pb^{-1} of data [32].

Quantity	Value
Λ_b^0 mass	$(5640 \pm 50 \pm 30)$MeV/c^2
$\mathcal{B}(\Lambda_b^0 \to J/\psi\Lambda)$	$(1.8 \pm 1.0) \times 10^{-2}$

Table 1.4: *UA1 measurement.*

The UA1 measurement is reported in Tab. 1.4, however the CDF and LEP experiments didn't see this decay and put an upper limit on the branching fraction smaller than UA1's results [33], [34].
A new result came from CDF in 1997 [35] using 110 pb^{-1} of data collected during the *run* 1992÷1995, contradicting the UA1 claim (see Tab. 1.5):

Quantity	Value
Λ_b^0 mass	$(5621 \pm 4 \pm 3)\text{MeV/c}^2$
$\mathcal{B}(\Lambda_b^0 \to J/\psi\Lambda)$	$(3.7 \pm 1.7) \times 10^{-4}$

Table 1.5: *CDF measurements for the process* $\Lambda_b^0 \to J/\psi\Lambda$.

While the B-mesons are well studied, less is known about the Λ_b^0 baryon. Tab. 1.6 summarizes experimental knowledge of Λ_b^0 decays and BR ($\mathcal{B}$) measurements at the time of writing this Thesis: only few decay modes of the Λ_b^0 have been observed, with a sum of their measured branching fractions of the order of only 0.1 and large uncertainties on the measurements.

Λ_b^0 **Decay Modes**	**Fraction**(Γ_i/Γ)	**Experiment**	p MeV/c	$\sqrt{s}$ TeV
$J/\psi(1S)\Lambda \times B(b \to \Lambda_b^0)$	$(4.7 \pm 2.3) \times 10^{-5}$	CDF [35]	1741	1.8
$pD^0\pi^-$			2371	
$\Lambda_c^+\pi^-$	$(8.8 \pm 3.2) \times 10^{-3}$	CDF [10]	2343	1.96
$\Lambda_c^+ a_1(1260)^-$	seen	DELPHI [34]	2153	
$\Lambda_c^+\pi^-\pi^+\pi^-$			2592	
$\Lambda K^0 2\pi^+ 2\pi^-$		FMPS [36]	2323	
$\Lambda_c^+\ell\overline{\nu}_\ell$ *anything* [a]	$(10.7 \pm 3.2) \times 10^{-2}$	ALEPH [37]	-	
$\Lambda_c^+\ell\overline{\nu}_\ell$	$(5.0^{+1.9}_{-1.4}) \times 10^{-2}$	DELPHI [38]	2345	
$\Lambda_c^+\pi^+\pi^-\ell\overline{\nu}_\ell$	$(5.6 \pm 3.1) \times 10^{-2}$	DELPHI [38]	2335	
$\Lambda_c(2595)^+\ell\overline{\nu}_\ell$	$(6.3^{+4.0}_{-3.1}) \times 10^{-2}$	CDF [7]	2211	1.96
$\Lambda_c(2625)^+\ell\overline{\nu}_\ell$	$(1.1^{+0.6}_{-0.4}) \times 10^{-2}$	CDF [7]	2196	1.96
$\Sigma_c(2455)^0\pi^+\ell\overline{\nu}_\ell$		CDF [7]	2272	1.96
$\Sigma_c(2455)^{++}\pi^-\ell\overline{\nu}_\ell$		CDF [7]	2272	1.96
ph^- [b]	$< 2.3 \times 10^{-5}$ @90% C.L.	CDF [39]	2730	1.96
$p\pi^-$	$(3.8 \pm 1.3) \times 10^{-6}$	CDF [14]	2730	1.96
pK^-	$(6.0 \pm 1.9) \times 10^{-6}$	CDF [14]	2709	1.96
$\Lambda\gamma$	$< 1.3 \times 10^{-3}$ @90% C.L.	CDF [40]	2699	1.8

[a] Not a pure measurement. See note *Production and Decay of b-flavored Hadrons* on page 877 [1].
[b] Here h^- means π^- or K^-.

Table 1.6: Λ_b^0 *information quoted from PDG [1]. The lepton is an electron or a muon.*

Fig. 1.3 reports the Λ_b^0 lifetime measurements used to evaluate the world averge Λ_b^0 lifetime [1]. Due to the precision of the latest CDF measurements one can infer

that this is not anymore an open field.

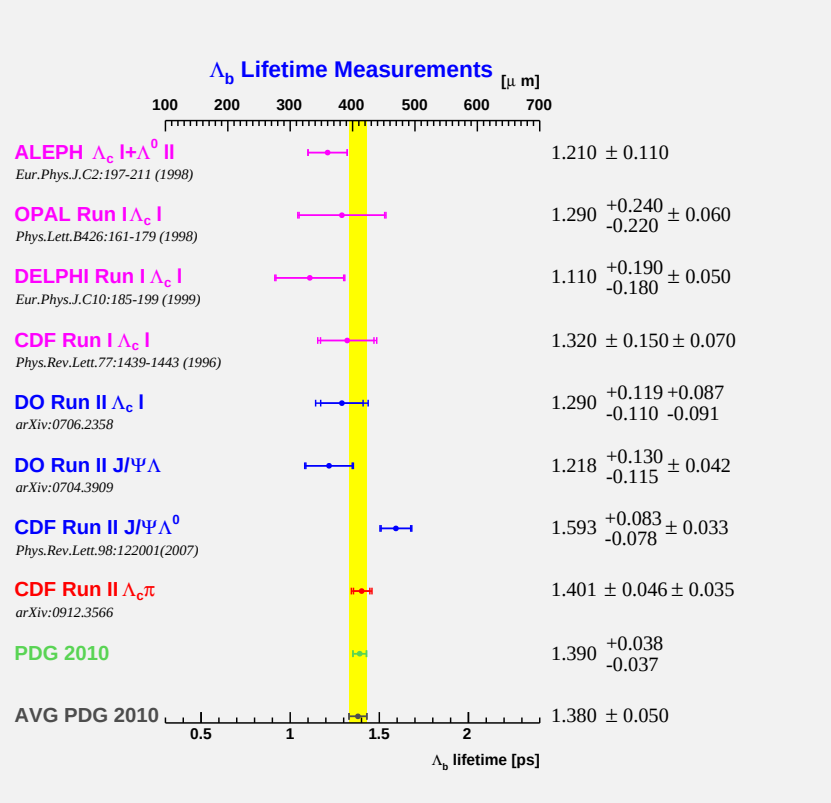

Figure 1.3: *Measurements of Λ_b^0 lifetime [1]: the lepton is an electron or a muon.*

Still looking at the Tab. 1.6, the semileptonic $\Lambda_b^0 \to \Lambda_c^+ \ell \overline{\nu}_\ell$ and the hadronic $\Lambda_b^0 \to \Lambda_c^+ \pi^-$ decay modes were observed by ALEPH and DELPHI experiments at LEP. In the first case (see Sec. 1.4) the W^- decay emits a charged lepton and an antineutrino while in the second case the $\ell \overline{\nu}_\ell$ is replaced by a $\overline{u}d$ pair. The recent CDF observation of resonance structures in the Λ_b^0 semileptonic decays $\Lambda_b^0 \to \Lambda_c^+ \pi^- \pi^+ \ell \overline{\nu}_\ell$ (see the yellow highlighted decays of Tab. 1.6), lead us to speculate that the corresponding hadronic decay $\Lambda_b^0 \to \Lambda_c^+ \pi^+ \pi^- \pi^-$, where the $\ell \overline{\nu}_\ell$ pair is replaced by an $\overline{u}d$ pair, may exists and if this happens similar resonant structures may be observed. As shown in Chap. 4, the experimental signature of such decays, i.e. the presence of two secondary vertices, the first due to the Λ_b^0 decay and the second one due to Λ_c^+ decay (since all resonances decay in less then 10^{-23} s), make them very appeling, since at CDF these two secondary vertices are well separated from the primary vertex (the Λ_b^0 production point) and a specially designed trigger is able to select online events with this typical feature of heavy hadrons decays, rejecting most part of background. The above observations, motivated the search

done in this Thesis for the Λ_b^0 into $\Lambda_c^+\pi^+\pi^-\pi^-$ inclusive decay and for the investigation of charmed resonant contibutions to this final state. First the observation, and then the measurement of the absolute BR of these new decay modes will improve our knowledge of the Λ_b^0 baryon. Moreover, the absolute measurements of these new BRs can be compared with the theoretical predictions (still unavailable for these decays) making use of CKM matrix elements [23], [24], and of dynamic factor determined in the case of b-hadrons decays with the HQET [2], [3] (see also Sec. 1.4.2).

1.4 *b* Hadron Decay

We define a hadron as heavy if it contains a *charm* or a *bottom* quark (the *top* quark decays before it hadronizes) or, in other words, if one of its constituent quarks has a large mass if compared to the scale of QCD, Λ_{QCD}, which is $200 - 300\,\text{MeV}$.
A b-quark usually decays into a c quark emitting a W^- boson (see Fig. 1.4) and afterwords the W^- decays into a $q\overline{q}$ or $\ell\overline{\nu}_\ell$ pair.

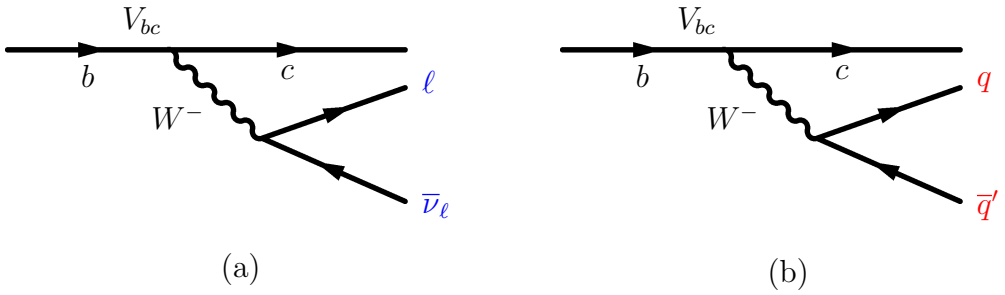

Figure 1.4: *b-quark decay:* **1.4(a)** *b semileptonic decay and* **1.4(b)** *b hadronic decay.*

The magnitude of the lifetime of b-hadrons is governed by the *quark-quark* coupling V_{bc} and by the decay dynamics.

1.4.1 *b* Decay Mode

The simplest decay model for heavy quarks, like b and c, is the *Spectator Model* (see Fig. 1.5). In this model the heavy quark in a hadron is bound to the lighter *spectator* quarks, the weak decay of heavy quark can be treated separately and all hadrons retaining a given heavy quark are expected to have the same lifetime.
Looking at the muon decays, the virtual W^- boson decays to $e^-\overline{\nu}_e$ since this is the only kinematically allowed channel, but in the bottom decays the number of possible decay product increases to nine: $e^-\overline{\nu}_e$, $\mu^-\overline{\nu}_\mu$, $\tau^-\overline{\nu}_\tau$, $\overline{u}d$, $\overline{c}s$ with three

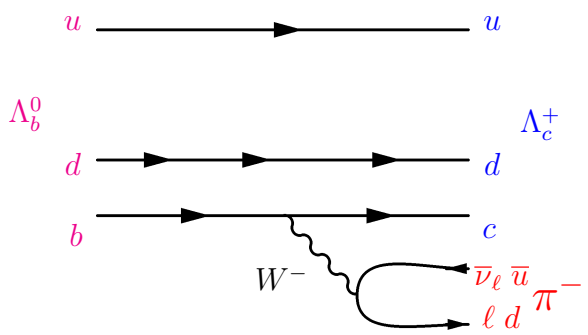

Figure 1.5: *Semileptonic* $\Lambda_b^0 \to \Lambda_c^+ \ell \overline{\nu}_\ell$ *and hadronic decay mode* $\Lambda_b^0 \to \Lambda_c^+ \pi^-$*: in the spectator model the b-quark decays weakly while the additional quark is a spectator to the* Λ_b^0 *baryon decay process.*

colour combination for the last two possibilities. Once adjusted the quark-quark coupling and the mass of the decaying particle in the muon decay formula, the lifetime of bottom hadrons is roughly estimated as:

$$\Gamma_b = \Gamma_\mu \times \frac{9 V_{cb}^2 M_b^5}{M_\mu^5} \tag{1.3}$$

In Eq. 1.3 we assume b decays entirely to c.
Considering $M_b \approx 4.2\,\mathrm{GeV/c^2}$ [1] and $V_{cb} \approx 0.04$ we have :

$$\tau_b = \frac{1}{\Gamma_b} \approx 1.3\ ps \tag{1.4}$$

In this result we have to consider the uncertainty on the quark mass and on the measurement of V_{cb}. Fig. 1.7 lists the current results for lifetime measurements of various b-hadrons: in analogy with the charmed hadron decays, the necessity for the inclusion of non-spectator diagrams is made obvious by the spread of the measured lifetimes.
So, in addiction to the spectator diagrams, there are some other diagrams for the b-hadron decays that directly involve the spectator quarks, and that contribute to the decay of heavy hadrons. In particular, for the Λ_b^0 baryon, subject of this Thesis, likewise to the spectator diagrams we have the Weak Exchange Diagrams (WE). In the Weak exchange (WE) process for baryon decay, such as the Λ_b^0 with spin=$^1/_2$ from the quark model prediction, the spin assignment causes no helicity suppression. The diagrams contributing to the $\Lambda_b^0 \to \Lambda_c^+ \pi^-$ decay modes reported respectively in Fig. 1.5 and Fig. 1.6, are just an example.

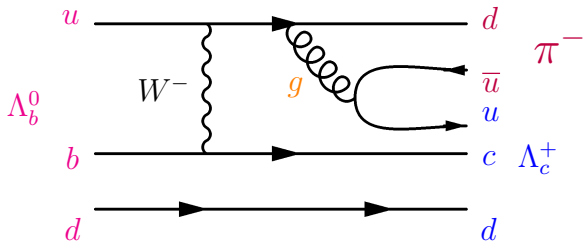

Figure 1.6: *Weak Exchange diagram for the* $\Lambda_b^0 \to \Lambda_c^+ \pi^-$ *decay mode.*

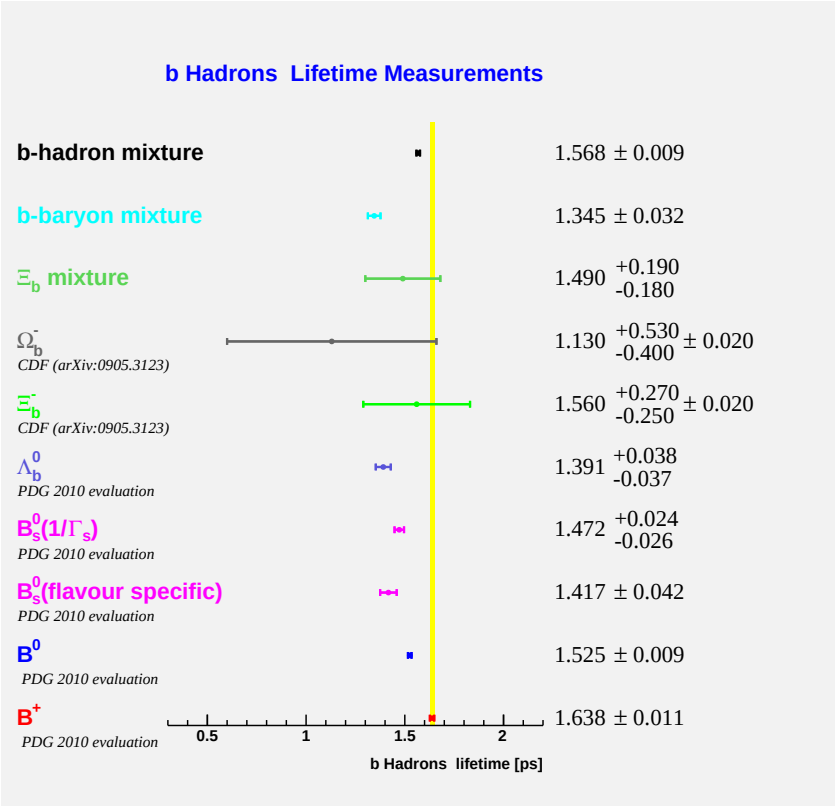

Figure 1.7: *Measurements of bottom hadron lifetimes [1].*

1.4.2 Heavy Quark Effective Theory (HQET)

This work presents a measurement of the Λ_b^0 relative decay rate. The transition amplitude ($\mathcal{M}$) that describes the decay rate of a b-hadron into some final state f, is derived by drawing all the possible Feynman diagrams at the quark level and summing up all the contributions. The underlying weak interaction is simple while the strong interaction binding the quarks into hadrons introduces several complications. When the quarks or gluons travel over a distance of $1/\Lambda_{QCD}$ or longer, the coupling constant of the strong interaction (α_s) diverges, so perturbation theory breaks down and non-perturbative effect take over. For the energy scale of our concern, Λ_{QCD} is around $200\,\mathrm{MeV/c^2}$. To better understand the separation between the perturbative and non-perturbative physics, we introduce a theoretical tool, the Operator Product Expansion (OPE) [41], so the $\mathcal{M}$ becomes:

$$\mathcal{M} = -\frac{4G_F}{\sqrt{2}} V_{CKM} \sum_j C_j \langle f| O_j |B\rangle \left[1 + \mathcal{O}\left(\frac{m_b^2}{M_W^2}\right)\right], \tag{1.5}$$

where j indicates the contribution from the j^{th} Feynman diagram, G_F is the Fermi coupling constant, and V_{CKM} is the CKM matrix element (see Eq. 1.1). The Wilson coefficients C_j [41] act as effective coupling constants, contain the physics at short distance, can be computed using perturbation theory, and are model independent. The $\langle f| O_j |B\rangle$ is usually referred to the hadronic matrix element, where O_j is a local operator. The hadronic matrix element contain the long distance physics and can only be evaluated using non-perturbative methods. Contributions from the higher order operators are suppressed by a power of m_b^2/M_W^2, where m_b and M_W indicate the masses of b-quark and the W boson.
The HQET [42], [43] significantly simplifies the form of the hadronic matrix element, stems from the SM and describes the hadrons containing a b or a c quark. The concept of *heavy* is relative. In the HQET, the masses of *heavy* c, b and t quarks are much larger than QCD energy scale, while the masses of *light* u, d and s quarks are much smaller than Λ_{QCD}. In the limit $m_{c,b,t} \gg \Lambda_{QCD}$, a new type of symmetry *spin-flavor heavy quark symmetry* arises. The momentum transfer between heavy and light quarks is $\mathcal{O}(\Lambda_{QCD})$ or, equivalently speaking, the typical size of a hadron system is of the order of Λ_{QCD}^{-1}. The change in the heavy quark velocity is then $\sim \Lambda_{QCD}/m_Q$, which vanishes when m_Q is infinitely large.
The velocity of the heavy quark is, therefore, almost unaffected by the strong interaction, i.e. the quark-quark interaction terms disappear in the Lagrangian. The only strong interaction of a static heavy quark is with gluons via the color charge. This *quark-gluon* interaction is spin-independent. Consequently, the light quark system knows nothing about the spin, mass and flavor of the *nucleus*, i.e. a b-hadron at rest is identical to a charm hadron at rest regardless of their spin orientations. The *heavy quark symmetry* implies that we can relate properties of the

beauty hadrons to those of the charm hadrons. For example, Aglietti [44] derived a formula to estimate the Λ_b mass: $M_{\Lambda_c} - 1/4(M_D + 3M_{D^*}) = M_{\Lambda_b} - 1/4(M_B + 3M_{B^*})$, which gives $M_{\Lambda_b} \sim 5630\,\mathrm{MeV/c^2}$, in good agreement with the world average, 5624 ± 9 GeV/c^2. An analogy can be found in atomic systems, where the isotopes with different nuclei have the same chemical properties. When performing a calculation of the B or charm mass, decay rate or lifetime, we could start from the limit of $m_{c,b,t} \gg \Lambda_{QCD}$. The correction terms are added in expansion of the power of $1/m_Q$, where m_Q is the mass of the heavy quark. The $1/m_Q$ corrections take into account finite mass effects and are different from quarks of different masses. A more complete description of HQET may be found in [2] , [45], and [46].
The focus of this analysis, examining the Λ_b^0 to Λ_c^+ decay, is best suited to treatment using HQET since both the initial and the final state hadrons contain a heavy quark. In addition, the light quark system in a Λ_b^0 baryon is in a spin-0 state; the sub-leading corrections have a simpler form than those for the mesons [47].
The HQET can be used to calculate the partial widths of b-hadron decays.
This analysis concerns the decays reported on Tab. 4.1 and, with the exception of $\Lambda_b^0 \to \Lambda_c^+ \pi^-$ [5], there are no HQET theoretical predictions for the partial widths of these decays.

Chapter 2

The TeVatron Collider and the CDF Detector

The measurement described in this Thesis is based on a data sample collected by the CDF II detector during Run II of the Fermilab's Tevatron Collider. This chapter provides a general description of the experimental apparatus, both collider and detector, and of the trigger, focusing on the elements more important for this analysis.

2.1 The Tevatron Collider

The Fermilab (FNAL) Tevatron Collider was until quite recently the worlds highest energy accelerator, before the LHC at CERN have turned on since 2010, colliding antiprotons with protons at a center of mass energy of $\sqrt{s} = 1.96\,\text{TeV}$. LHC started operating in March 2010 at a center of energy 7 TeV and plans to increase the center of energy to 14 TeV in 2014. The Tevatron is the last stage of a complex system accelerators (see Fig. 2.2), used in successive steps, to produce, store and accelerate the particles up to 150 GeV before to be injected in the Tevatron where they are accelerated to the final energy before the collisions take place in the center of two detectors: CDF and DØ.
Fermilab, just 35 miles west of Chicago, Illinois, has been one of the largest and most important particle physics facilities in the world. At the end of September 2011 the Tevatron terminated the operations. The first $p\bar{p}$ collisions have been produced in 1986 and the accelerator started to collect interesting events at the end of 1987, during a period called *Run 0*[1] (see Tab. 2.1).

[1]The Run is not to be confused with the run, defined in CDF as a continuous period of data-taking in approximately constant detector and beam conditions.

Since then, several extensive upgrades have been undertaken leading to major improvements of the collider performance.
Run I (see Tab. 2.1) went from 1992 to 1996 and the center of mass energy was 1.8 TeV.
A major upgrade of the Tevatron took place between September 1997 and March 2001, beginning of the so called *Run II* (see Tab. 2.1), when both the accelerator complex and the collider detectors were improved mainly in order to increase the luminosity of the accelerator and gathering data samples of $2\,\text{fb}^{-1}$ or more (notice that at the moment more than $10\,\text{fb}^{-1}$ has been acquired by the CDF detector). The upgraded machine accelerates 36 bunches of protons and antiprotons, whereas the previous version of the accelerator operated with only 6. Consequently, the time between bunch crossings has been decreased from 3.5 μs for the previous version to 396 ns for the current collider. The center of mass energy was also increased from 1.8 to 1.96 TeV.

The Tevatron is an approximately circular synchrotron of 1 km radius, employing 772 dipole, 2 half-dipole, and 204 quadrupole superconducting magnets. Each is approximately 6 m long, 4 tons in mass, and is made of NbTi alloy filaments embedded in copper, kept at 4.3 °K temperature by a large cryogenic system.

A 4400 A current flows through each magnet to produce the 4.2 T magnetic field necessary to keep the particles on their orbit, while they are accelerated by eight Radio-frequency cavities (RF) driven at approximately 53.105 MHz.

Date		$\sqrt{s}$ [TeV]	$\mathcal{L}$ $[cm^{-2}s^{-1}]$	$\int \mathcal{L}dt$ $[pb^{-1}]$
Mar 1983	End of the construction	-	-	-
Jul 1983	Proton energy: 512 GeV	-	-	-
Oct 1983	Fixed-target program	-	-	-
Feb 1984	Proton energy: 800 GeV	-	-	-
Oct 1985	First $p\bar{p}$ collisions	1.6	10^{24}	-
Oct 1986	Proton energy 900 GeV	-	-	-
Jun 1988–May 1989	*Run 0*	1.8	2×10^{30}	$\simeq 4.5$
Aug 1992–Feb 1996	*Run I*	1.8/0.63	28×10^{30}	$\simeq 180$
Aug 2000	Beam energy: 980 GeV	-	-	-
Mar 2001	*Run II* start	1.96	5×10^{30}	-
Sep 2011	Best performances	1.96	4.5×10^{32}	$\simeq 12000$

Table 2.1: *Chronological overview of the Tevatron operation and performance. The fourth column reports the peak luminosity. The fifth column reports the delivered integrated luminosity. The last row shows the best performance as of this writing.*

The particles are accelerated through the RF buckets. A bucket is one interval of the longitudinal restoring force provided by the RF cavities that results in a stable

phase space where a bunch may be captured and accelerated. While operating in collider mode, the Tevatron collides counter-rotating bunches of protons and antiprotons every 396 ns in two interaction regions along the ring: BØ which is the site of the CDF in Run II experiment (CDF II), and DØ where the DØ experiment is located. In the Tevatron the beam collisions are head-to-head.

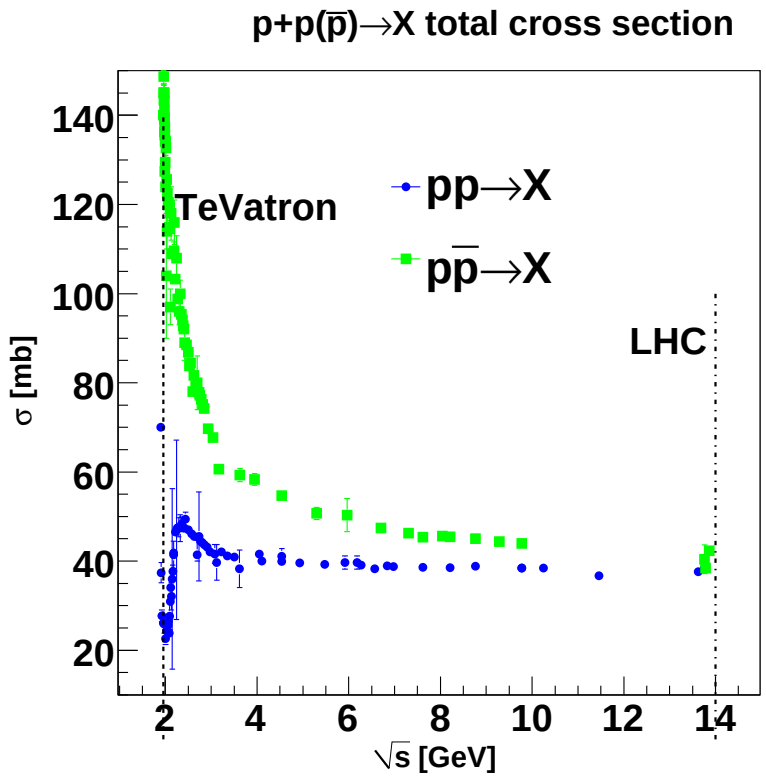

Figure 2.1: *The figure compares the total cross section as function of the* $\sqrt{s}$ *for* $pp \to X$ *and* $p\bar{p} \to X$ *[1].*

As shown in Fig. 2.1 the choice of $p\bar{p}$ beams maximizes the total cross section with respect to pp, at the Tevatron center of mass energies. At the same time the choice to have particle beams of opposite charge simplifies the design of the final stage with respect the proton-proton colliders. Fig. 2.2 shows a sketch of the accelerator system. The beams are accelerated to the final energy using different techniques, combined to have the better performance. The first acceleration stage is the production of proton and antiproton beams described in Sec. 2.1.1 and in Sec. 2.1.2.

2.1.1 Proton Production

The proton are extracted using an hot hydrogen gas in the molecular state H_2, passed through a magnetron, which extracts a $50 - 55\,\text{mA}$ current of $15 - 22\,\text{KeV}$ H^- ions, subsequently accelerated every 66 ms to 750 KeV by a three staged diode-capacitor voltage multiplier (Cockroft-Walton) accelerator [48]. The proton beam, segmented into bunches, is then injected into a two-staged 150 m long linear accelerator (Linac, see Fig. 2.2).

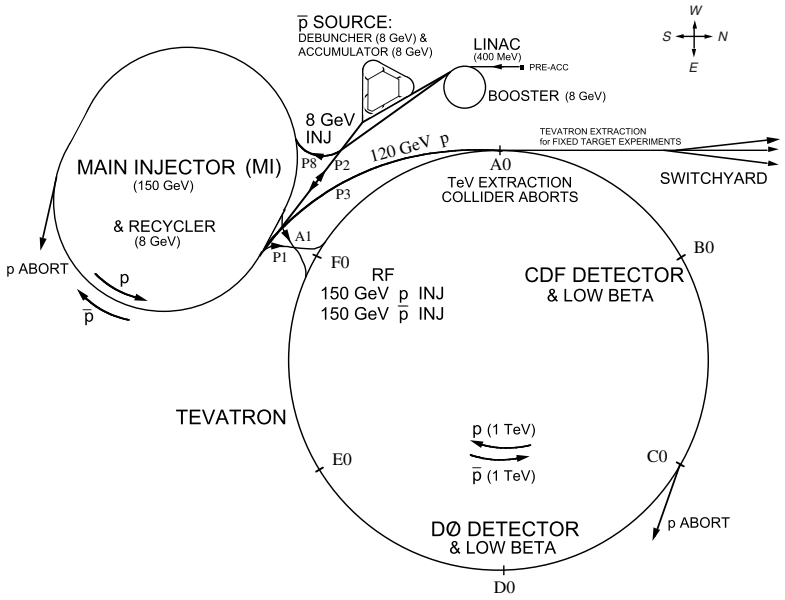

Figure 2.2: *The figure shows the accelerator system operating at FNAL.*

First, a drift tube accelerator resonating at 201.249 MHz accelerates bunches of protons up to 116 MeV; then the H^- beams are segmented in bunches and a Linac and Radio Frequency cavity, a side-coupled cavity accelerator at 804.996 MHz, increase their energy to 401.5 MeV [49] before injection into the Booster. The Booster (see Fig. 2.2) is an alternating gradient synchrotron (orbit radius of 75.5 m) that accelerates protons to 8 GeV in 33 ms, sweeping from 38 to 53.105 MHz. At injection, a thin carbon foil is used to strip the electrons from the H^- ions to obtain protons. Injecting H^- ions rather than protons into the Booster allows the injection to proceed over multiple revolutions of the beam around the Booster Ring (usually 10–12)[2]. There are two basic modes during collider operations: antiproton accumulation and injection (see Sec. 2.1.2 and Sec. 2.1.3).

[2]If protons were instead injected, the magnetic field used to inject new protons onto orbit in the Booster would also deflect the already revolving protons out of orbit.

2.1.2 Anti-Proton Production

To produce antiprotons, the proton bunches are extracted to be injected in the Main Injector, where they are accelerated up to 120 GeV. Antiprotons are produced by the following reaction:

$$p + \begin{pmatrix} n \\ p \end{pmatrix} \quad \rightarrow \quad p + p + \begin{pmatrix} n \\ p \end{pmatrix} + \overline{p} \tag{2.1}$$

The beam of the Main Injector is directed against a target made of Nickel alloys containing chromium, iron and other metals. Before colliding, the protons bunches are rotated by 90° in phase space, so that they have a large spread in energy but a small lag in arrival time at the target. A spatially broad beam of particles is produced and then focused using a cylindrical Lithium Lens[3]. This beam, which has a bunch structure similar to the incident proton beam, is passed through a pulsed dipole magnet. The magnetic field selects the negatively charged antiprotons with about 8 GeV of kinetic energy. About 20 antiprotons are produced for every 10^9 protons on target and then stored into the *Debuncher*. The Debuncher is a triangular-shaped synchrotron with mean radius of 90 m. The beam is stochastically cooled [50][4] and then transferred to the *Accumulator*, which is another triangular-shaped synchrotron with a mean radius of 75 m. The Accumulator is a storage ring for the antiprotons; they are stored at an energy of 8 GeV and cooled until needed. The antiprotons are then sent into the Main Injector, where they are accelerated to 150 GeV. Finally, the antiprotons are transferred to the Tevatron, where 36 previously injected bunches of protons are already circulating in opposite direction. Since 2004, an additional Recycler Ring has been added in the same tunnel of the Main Injector and provides additional storage and cooling of the antiprotons. Recently, relativistic electron cooling was successfully implemented in the Recycler, further enhancing the Tevatron performance [51][5]. The antiproton production rate is low mainly because the production efficiency is 20×10^{-9}, followed by other inefficiency in the transfers.

[3]Lithium is used to minimize beam loss from multiple-scattering.

[4]Stochastic cooling is a technique used to reduce the transverse and energy spread of a particle beam without any accompanying beam-loss. This is achieved by applying iteratively a feedback mechanism that senses with extreme sensitivity the beam deviation from the ideal orbit with electrostatic plates, processes and amplifies it, and transmits an adequately-sized synchronized correction pulse to another set of plates downstream [50]. Bunch rotation is an RF manipulation technique that, using adequate phasing, transforms a beam with a large time spread and a small energy spread in a beam with a large energy spread and a small time spread, or vice versa.

[5]Electron cooling is a method of damping through the interaction between the antiproton beam and an electron beam propagating together at the same average velocity.

2.1.3 Injection and Collision

The antiproton accumulation process usually takes about $10-15$ hours to collect a sufficient number of antiprotons, then the accumulation is stopped and the accelerator is prepared for a new injection. The first injection step is the extraction of a set of seven proton bunches from the Booster into the Main Injector [52], where they are accelerated up to 150 GeV. Within the Booster the protons are coalesced[6] in a single bunch of $\approx 300 \times 10^9$. This process has an efficiency of 90%. When the proton bunches are ready, they are moved into the Tevatron. This process is repeated every 12.5 s, until 36 proton bunches, separated by 396 ns, are loaded into the Tevatron central orbit. The transfer efficiency is 65%. The proton injection precedes the antiproton injection, because if proton bunch losses are large this will point to tune the orbits. If this is the case, the proton injection is aborted and restarted, at this stage the process can be quickly recovered, while a large antiproton lost needs a new accumulation. When the proton bunches are injected and stable, the antiproton bunches are extracted from the Accumulator (or from the Recycler) to the Main Injector, accelerated to 150 GeV, then coalesced into four bunches with an efficiency of $\approx 80\%$. The four bunches, separated by 396 ns, are injected into the Tevatron, where protons are counter-routing. The two beams have orbits spatially separated of $3-5$ mm, that corresponds to $3-5\sigma$ of the beam size, to avoid beam interactions outside the collision points. The antiproton process is repeated to have 36 antiproton bunches. After the end of antiprotons injection start a *store*, defined as an accelerated period of collisions. A store lasts usually about $15-20$ hours. The proton and antiproton beams share the same magnets and Radio Frequency system. After the injection the beams are accelerated up to 980 GeV in about one minute. The beams are finally brought into collision at the two instrumented interaction-points located along two straight sections of the Tevatron: DØ and BØ where the DØ and CDF II detectors, respectively, are located. Special high-power quadrupole magnets (*low-β squeezers*), installed on the beam pipe at either side of the detectors, reduce the transverse spatial spread of the beams to maximize the collision rate in the interaction regions. The resulting transverse spatial distribution of the luminous region is approximately a two-dimensional Gaussian, with $\sigma_T \approx 30\,\mu$m. The typical longitudinal dimension of a bunch is $60-70$ cm. The interaction region has a roughly Gaussian distribution along the beam direction, with width $\sigma_z \approx 28$ cm. The center of the luminous region is shifted toward the nominal interaction point by fine tuning of the squeezers. The 36 bunches of protons (antiprotons) are distributed among the 1113 buckets in three equispaced *trains* of 12 bunches each (see Fig. 2.3).

[6] Coalescing is the process of compacting into one dense bunch many smaller bunches.

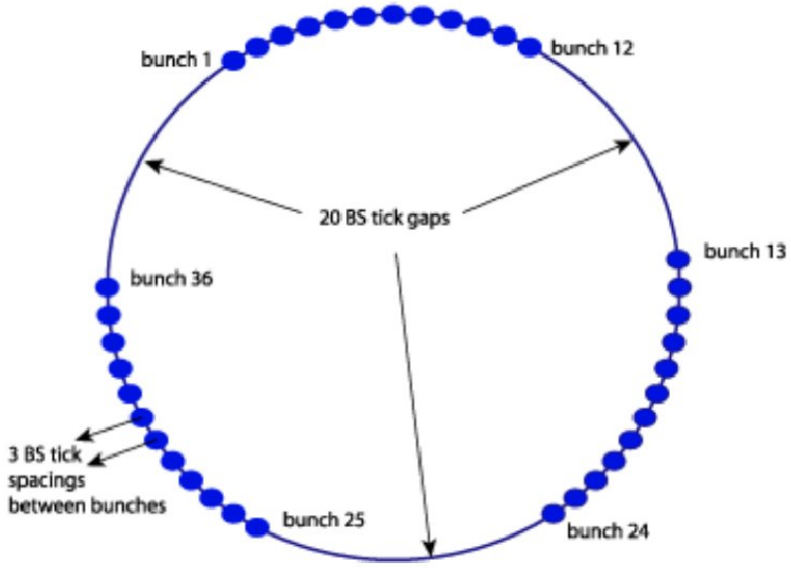

Figure 2.3: *Bunch structure of the Tevatron (BS = beam sync ticks = 132 ns).*

The inter-bunch spacing is 396 ns (21 buckets) within a train, while a 2.6 μs spacing (139 buckets, *abort gap*) is kept between trains. The need for the abort gap is two-fold: it allows antiprotons injection (in coincidence with the proton abort gap) without perturbing the already revolving protons with the injecting magnet. Furthermore, when beam abortion is needed, the abort gap allows ramping-up the deflecting magnets without interfering with the beam during the transient, possibly damaging the detectors. As a consequence of this bunch distribution, the average bunch-crossing rate is 1.7 MHz, resulting from a 2.53 MHz rate, when the proton and antiproton trains are crossing, and zero rate in correspondence of the abort gaps. The transverse profile of the beam is shaped to its optimized configuration to avoid detector damage from the tails of the $(p\overline{p})$ distributions interacting with the beam pipe: retractable collimators (iron plates) are moved perpendicularly toward the beam and trim-off the residual halo. When the beam profile is narrow enough and the conditions are safely stable, the detector is powered and the data-taking starts. The number of overlapping inelastic interactions N for each bunch crossing is a Poisson-distributed variable that depends on the instantaneous luminosity. The observed distribution of the multiplicity of interaction vertexes yields $\overline{N} \approx$ 0.2, 1.0, 2.0, and 6.0 for respectively, $\mathcal{L} \approx 1 \times 10^{31}$, 5×10^{31}, 10×10^{31}, and 30×10^{31} luminosities [53]. The luminosity decreases as a function of time during the store because of the interactions of the beam with residual molecules of gas in the beam pipe, beam-halo interactions, and $\overline{p}$ depletion due to the collisions.

During the $10 - 20\,\mathrm{h}$ of a store, the luminosity decreases by a factor of $2.5 - 5$, the majority of data being collected at $\mathcal{L} \approx \mathcal{L}_0/2$. Just after the final injection, a new antiproton accumulation cycle is started. When the antiproton stack is sufficiently large and the colliding beams are degraded, the detector high-voltages are switched-off and the store is dumped. The beam is extracted via a switch-yard and sent to an absorption zone. Beam abortion can occur also accidentally when a superconducting magnet rises its temperature above the critical value (i.e., the magnet *quenches*), destroying the orbit of the beams. The time between the end of a store and the beginning of collisions of the next one is typically $1 - 2\,\mathrm{hours}$, during which time calibrations of the sub-detectors and cosmic rays tests are usually performed.

2.1.4 Instantaneous Luminosity

The performances of the Tevatron collider are evaluated in terms of two key parameters: the available center-of-mass energy, $\sqrt{s}$, and the instantaneous luminosity, $\mathcal{L}$. The former defines the accessible phase-space for the production of resonances in the final states. The latter is defined as the interaction rate per unit cross section of the colliding beams (collisions/(cm^{2}s)). In the absence of a crossing angle or position offset, the luminosity at the CDF or DØ is given by the expression:

$$\mathcal{L} = \frac{f_{bc} N_b N_p N_{\bar{p}}}{2\pi(\sigma_p^2 + \sigma_{\bar{p}}^2)} F\left(\frac{\sigma_l}{\beta^*}\right), \tag{2.2}$$

where f_{bc} is the revolution frequency, N_b is the number of bunches, $N_{p(\bar{p})}$ is the number of protons (antiprotons) per bunch, and $\sigma_{p(\bar{p})}$ is the transverse and longitudinal rms proton (antiproton) beam size at the interaction point.

Parameter	Run II value
number of bunches (N_b)	36
revolution frequency [MHz] (f_{bc})	1.7
bunch rms [m] σ_l	0.37
bunch spacing [ns]	396
protons/bunch (N_p)	2.7×10^{11}
antiprotons/bunch ($N_{\bar{p}}$)	3.0×10^{10}
total antiprotons	1.1×10^{12}
β^* [cm]	35

Table 2.2: Accelerator nominal parameters for Run II configuration.

F is a form factor with a complicated dependence on the low beta value, β^*, and the

bunch length, σ_l[7]. Tab. 2.2 shows the design Run II accelerator parameters [52].

For physics studies the integrated luminosity defined as:

$$L = \int_0^T \mathcal{L}(t)dt$$

is the quantity of interest, since for a specific process of cross-section σ, the number of events that are generated in a specific time interval T are: $n(T) = L\sigma$ and $N = \sigma \times Ldt$. The integrated luminosity depends on the peak performances of the accelerator and the Fig. 2.4(a) and Fig. 2.4(b) show, respectively, the evolution in the integrated luminosity, and the instantaneous luminosity at the start of store delivered by Tevatron, since the machine was turned on up to September 2011. The progressive increase in the integrated luminosity and the continuous records in the instantaneous luminosity[8] prove the good performance of the accelerator.

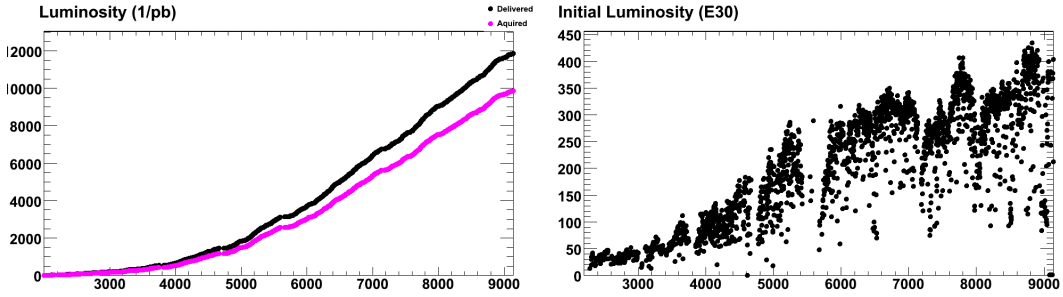

(a) (b)

Figure 2.4: **2.4(a):** *Integrated luminosity as a function of the time (or store number). The black curve is the luminosity delivered and the purple curve is luminosity written to tape.* **2.4(b):** *Initial luminosity as a function of the time (or store number).*

2.2 The CDF II Detector

The upgraded CDF detector [54] is a large multi-purpose solenoidal magnetic spectrometer designed with an approximately cylindrically symmetric layout in the azimuthal plane and in the *forward* and *backward* directions [55], [56] designed to study $p\bar{p}$ collisions at the Tevatron. Fig. 2.5 shows the CDF II detector and

[7]The β function is a measure of the beam width, along the accelerator and is proportional to the beam's x and y extent in phase space. β^* is the value of this function in the collision point.

[8]In June 2011, the record instantaneous luminosity was $4.34 \times 10^{32}\,\mathrm{cm}^{-2}\mathrm{s}^{-1}$.

the different sub-systems in a solid cutaway view, while Fig. 2.6 shows Elevation view of one half of the detector.

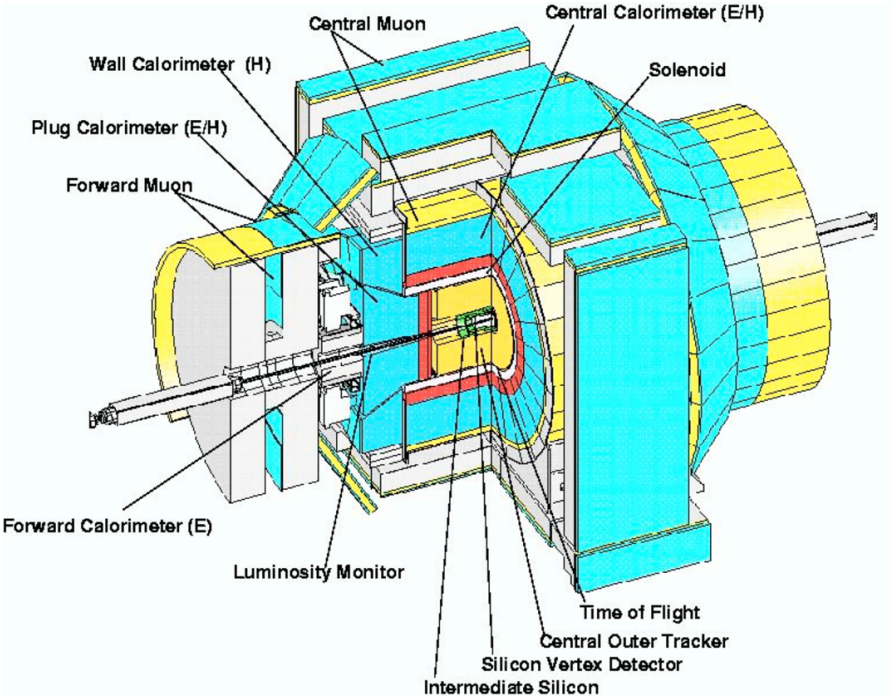

Figure 2.5: *The CDF II detector with a quadrant cut to expose the different subdetectors.*

CDF II consists of five main subdetector systems: tracking, particle identification, calorimetry, muon identification and luminosity detector. The protons and antiprotons beams travel towards each other along the horizontal axis (beam line or beam axis). Any plane perpendicular to the beam line is called a transverse plane and the intersection point between the beam line and the transverse plane is referred to as a beam spot. The innermost system is the integrated tracking system: a silicon microstrips detector and an open-cell wire drift chamber, the Central Outer Tracker (COT) that surrounds the silicon detector. The tracking system is surrounded by the Time Of Flight detector (TOF) system, designed to provide particle identification for low-momentum charged particles (momentum below to 2 GeV/c). Both the tracking and the TOF detector are placed inside the supeconducting coil, which generates a 1.4 T uniform horizontal magnetic field along the z axis inside the tracking volume. The trajectories of the charged particles inside the tracking volume are helixes. The tracking system is designed to measure the momentum and the trajectory of the charged particles. Multiple-track reconstruction allows to identify the vertices where either the $p\bar{p}$ interaction

took place (primary vertex) or the decay of a long-lived particle took place (secondary or displaced vertex). The solenoid coil is surrounded by the calorimeters, which measure the energy of particles that shower when interacting with matter. The calorimeters are surrounded by the muon detectors. Muons are "minimally ionizing particles", they only deposit small amounts of ionization energy in the material. Therefore, they are able to penetrate both the tracking and calorimeter systems. The integrated material of the tracking system, of the TOF detector, of the solenoid and of the calorimeter serves as a particle filter. Particles which penetrate through all that material are mostly muons, and they are detected by the tracks in the muon chambers, located outside the calorimeter.

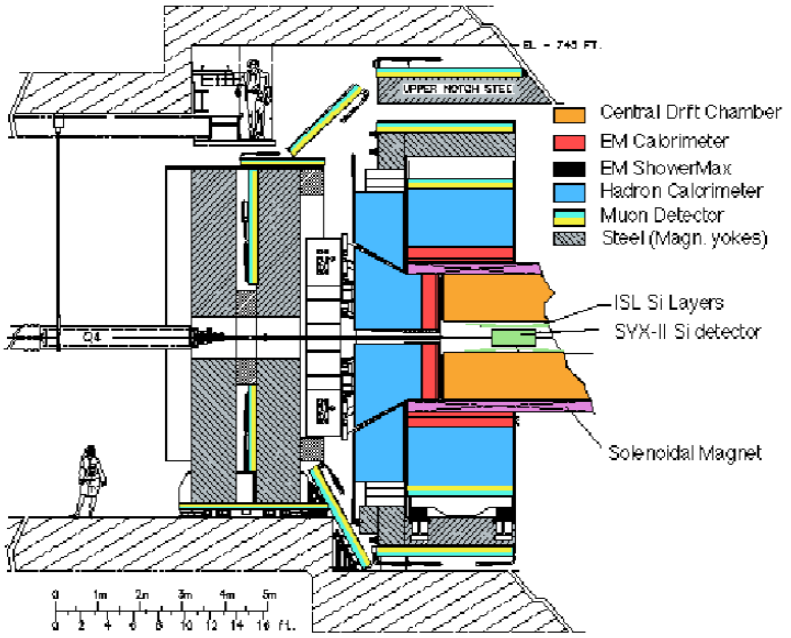

Figure 2.6: *Elevation view of one half of the CDF II detector.*

At the forward region of the CDF II detector two modules of Cherenkov Luminosity Counters (CLC) [57] are placed. They point to the center of the interaction region to record the number of $p\bar{p}$ interactions and measure the instantaneous luminosity. The most important parts of the detector for the Λ_b^0 analysis are the tracking system and the trigger, and these will be described in detail in the following sections. The description of the remaining systems will be brief. More detailed information on all these systems can be found in [58] and [59].

2.2.1 Coordinates and Standard Definitions in CDF

CDF adopts a left handed cartesian coordinate system with origin at the nominal BØ interaction point, coincident with the center of the drift chamber (see Sec. 2.3.2). The positive z-axis lies along the nominal beam-line and has the direction of the proton beam (east). The $x - y$ plane is therefore perpendicular to the beam-line, with the y-axis pointing upward and the x-axis in the horizontal plane, pointing radially outward with respect the center of the accelerator ring (see Fig. 2.7). Since the colliding beams of the Tevatron are unpolarized, the resulting physical observations are invariant under rotations around the beam line axis. Thus, a cylindrical coordinate system (r, φ , z) is particularly convenient to describe the detector geometry. The CDF detector is approximately cylindrically

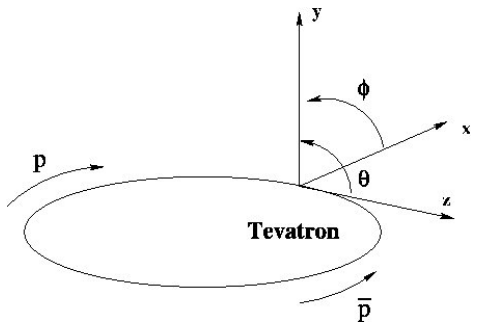

Figure 2.7: *CDF coordinate system.*

symmetric around the beam axis. Its geometry can be described in cartesian as well as in cylindrical coordinates.

The left-handed cartesian system is centered on the nominal interaction point with the z axis laying in the direction of the proton beam and the x axis on the Tevatron plane pointing radially outside.

The cylindrical coordinates are the azimuthal angle, φ, and the polar angle, θ,:

$$\varphi = \tan^{-1}\frac{y}{x} \quad \theta = \tan^{-1}\frac{\sqrt{x^2+y^2}}{z}$$

A momentum-dependent particle coordinate named *rapidity* is also commonly used. The rapidity is defined as

$$Y = \frac{1}{2}\ln\frac{E+p_z}{E-p_z},$$

where E is the energy and p_z is the z component of the momentum of the particle (p). It is used instead of the polar angle θ because it is Lorentz invariant. In the relativistic limit, or when the mass of the particle is ignored, rapidity becomes

dependent only upon the production angle of the particle with respect to the beam axis. This approximation is called *pseudo-rapidity*, η, and is defined by

$$\eta = -\ln\left(\tan\frac{\theta}{2}\right)$$

A value of $\theta = 90°$ would be perpendicular to the beam axis and corresponding to $\eta = 0$. The pseudo-rapidity is commonly used to identify different detector regions according to their position with respect to the beamline and interaction vertex position, as shown in Fig. 2.9.

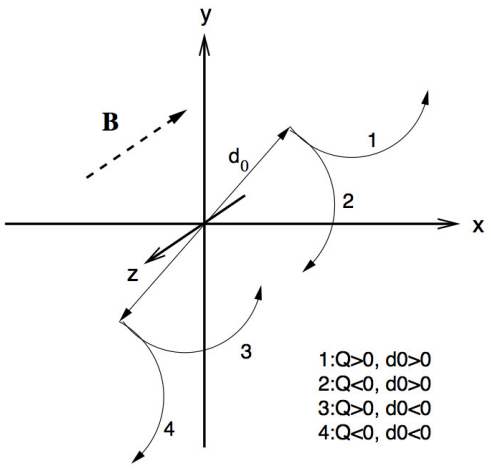

Figure 2.8: *Schematic drawing of the impact parameter d_0.*

Additional quantities are useful to define for studying $p\bar{p}$ interactions, among these the transverse momentum, the transverse energy and the five parameter of helices describing the trajectories of charged particles. The transverse momentum, p_T, of a particle is defined as $p \cdot \sin\theta$. Charged particles moving through a homogeneous solenoidal magnetic field along the z direction follow helical trajectories. Knowing that the projection of the helix on the $x - y$ plane is a circle, to uniquely parameterize a helix in three dimensions, five parameters are needed:

- $\boldsymbol{C}$ – signed helix (half)-curvature, defined as $C = q/2R$, where R is the radius of the helix and q is the charge of the track. This is directly related to the transverse momentum. When the magnetic field (B) is measured in Tesla, C in m^{-1} and p_T in GeV: $p_T = 0.15\ qB/|C|$;

- $\boldsymbol{\varphi_0}$ – φ azimuthal angle of the particle at the point of closest approach to the z-axis;

d_0 – signed impact parameter, i.e. the radial distance of closest approach to the z-axis, defined as $d_0 = q(\sqrt{x_0^2 + y_0^2} - R)$, where x_0 and y_0 are the coordinates of the center. This is schematically drawn in Fig. 2.8;

λ – helix pitch, i.e. $\cot(\theta)$, where θ is the polar angle of the particle at the point of its closest approach to the z-axis. This is directly related to the longitudinal component of the momentum: $p_z = p_T \cot\theta$;

z_0 – the z coordinate of the point of closest approach.

Another useful quantity, defined for decaying particles is the displacement L_{xy} :

$$L_{xy} = \frac{\widehat{x_V} \cdot \vec{p_T}}{|p_T|} \tag{2.3}$$

where x_V is the the decay length in the transverse plane of the decaying particle and p_T is its transverse momentum. In the following we will call L_{xy} *transverse decay length.*

2.3 The Tracking System

The tracking system is immersed in a 1.4 T solenoidal magnetic field for the measurement of charged particles momenta. We will describe this system, shown in Fig. 2.9, starting from the device closest to the beam and moving outwards.

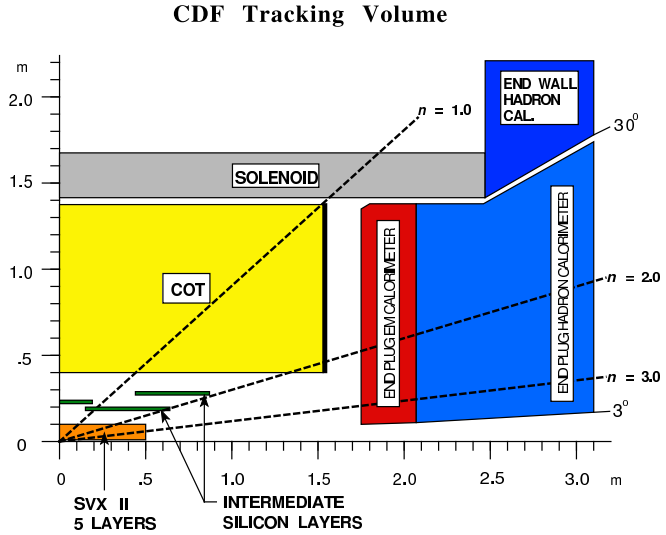

Figure 2.9: *Elevation view of one quadrant of the inner portion of the CDF II detector showing the tracking volume surrounded be the solenoid and the forward calorimeters.*

The innermost tracking device is a silicon detector, which consists of three subdetectors that cover the region $|\eta| < 2$ and 2π of azimuthal angle. The first layer of silicon sensors, called Layer ØØ (L00) [60], is installed directly onto the beryllium beam pipe, with the sensors at radii 1.35 and 1.62 cm from the beam. The beam pipe is made of beryllium because this metal has the best mechanical qualities with the lowest nuclear interaction cross section. The L00 is followed by Silicon VerteX (SVXII) [61], made of five concentric layers of silicon sensors located at radii between 2.45 and 10.6 cm. The Intermediate Silicon Layers (ISL) [62] form the outermost silicon detector, with one layer of sensors at a radius of 22 cm in the central region and two layers at radii 20 and 28 cm in the forward region. Surrounding the silicon detectors is the COT [63], a 3.1 m long cylindrical open-cell drift chamber covering the volume between 43.4 cm and 132.3 cm of radius and $|\eta| < 1$.

2.3.1 The Silicon Detectors

The silicon strip detectors [64] at CDF II provide a precise determination of the particle trajectory close to the beam line. The impact parameter resolution measured in the transverse plane is of 27 μm. A silicon detector is fundamentally a reverse-biased $p-n$ junction. When a charged particle passes through the detector material, it causes ionization. For a semiconductor, this means that electron-hole pairs are produced. Electrons drift towards the anode, and holes drift towards the cathode, where the charge is gathered. The amount of charge is, to first order, proportional to the path length traversed in the detector material by the charged particle. By segmenting the p or n side of the junction into *strips* and reading out the charge deposition separately on every strip, we obtain sensitivity to the position of the charged particle. All the CDF II silicon detectors are implemented as microstrip detectors. Charge deposition from a single particle passing through the silicon sensor can be read out on one or more strips. This charge deposition is used to determine the hit position in the direction perpendicular to the strips. There are two types of microstrip detectors: single and double-sided. In single-sided detectors only one (p) side of the junction is segmented into strips. Double-sided detectors have both sides of the junction segmented into strips. The benefit of double-sided detectors is that while one (p) side has strips parallel to the z direction, providing $r - \varphi$ position measurements, the (n) side can have strips at an angle (stereo angle) with respect to the z direction, and can provide z position information. For SVXII, made of double sided silicon sensor, four silicon sensors are assembled into a *ladder* structure which is 29 cm long. The readout electronics are mounted directly to the surface of the silicon sensor at each end of the ladder. The ladders are organized in an approximately cylindrical configuration, creating *barrels*. A SVXII barrel is segmented into 12 wedges, each covering approximately

30° in φ, and for each wedge there are five layers. Each layer provides one axial measurement on one side and a measurement at the stereo angle on the other side (see Tab. 2.3). The resolution on the single hit is 12 μm.

Property	Layer 0	Layer 1	Layer 2	Layer 3	Layer 4
number of φ strips	256	384	640	768	869
number of z strips	256	576	640	512	869
stereo angle	90°	90°	+1.2°	90°	−1.2°
φ strip pitch [μm]	60	62	60	60	65
z strip pitch [μm]	141	125.5	60	141	65
active width [mm]	15.30	23.75	38.34	46.02	58.18
active length [mm]	72.43	72.43	72.38	72.43	72.43

Table 2.3: *Relevant parameters for the layout of the sensors of the five SVXII layers.*

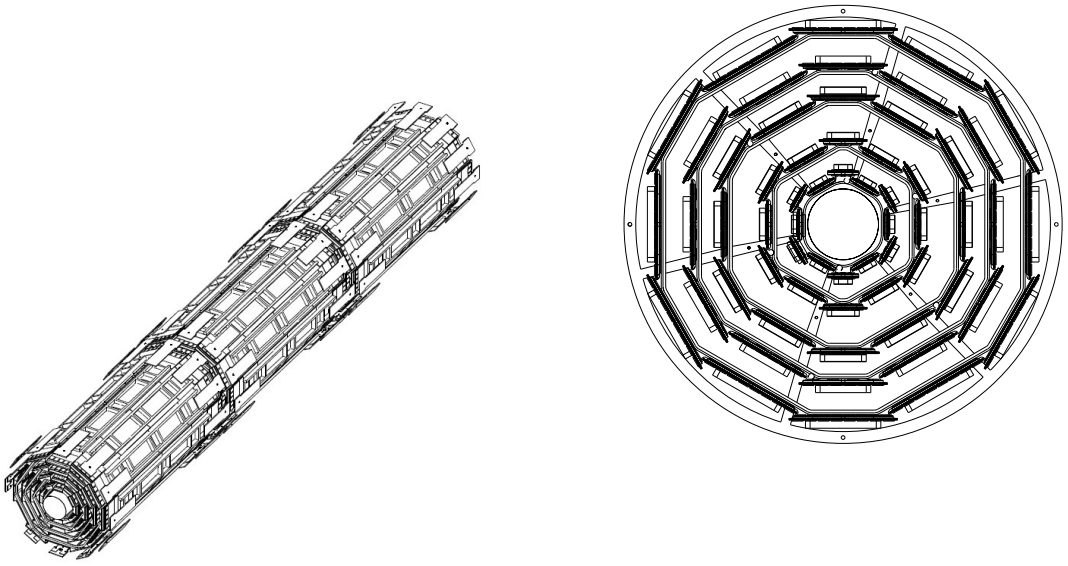

(a) (b)

Figure 2.10: *The SVXII silicon detector.* **2.10(a):** *Three-dimensional view of the detector, showing the barrel structure along the beam axes.* **2.10(b):** *The transverse plane section shows in detail the layers sequence.*

There are three SVXII barrels, mounted adjacent to each other along the z-axis, as shown in Fig. 2.10, covering the nominal interaction region at the center of the CDF II Detector. The coverage of the silicon detector subsystem is shown in Fig. 2.11. The L00, is made of single-sided silicon sensors which only provide $r - \varphi$ measurements, but also, being only at 1.5 cm from the interaction point, provides the best resolution on the transverse impact parameter. The ISL is made of double-sided silicon sensors and it provides up to two additional tracking layers depending on track pseudo-rapidity (see Fig. 2.11). In particular ISL provides a higher tracking efficiency by connecting tracks in SVX with the ones in COT and allows to extend tracking beyond the COT limit ($|\eta| < 1$), and up to $|\eta| < 2$. All the silicon detectors are used in the offline track reconstruction algorithm.

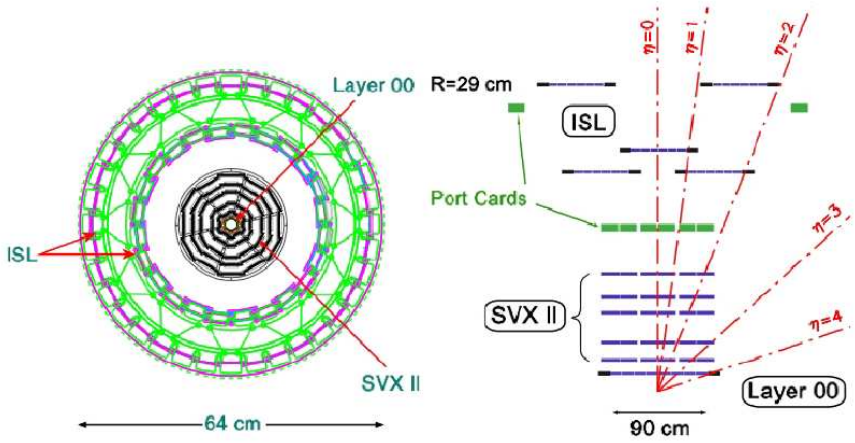

Figure 2.11: *Silicon Detectors: $x - y$ and $z - y$ plane views.*

2.3.2 The Central Outer Tracker (COT)

The COT drift chamber provides the tracking of charged particles at large radii in the pseudo-rapidity region $|\eta| < 1$, giving an accurate information in the $r - \varphi$ plane for the measurement of the transverse momentum, and substantially less accurate information in the $r - z$ plane for the measurement of the z component, p_z. The COT contains 96 sense wire layers, which are radially grouped into eight *superlayers*. This can be seen from the end plate section shown in Fig. 2.12(a). Each superlayer is divided into cells, and each cell contains 12 sense wires. The maximum drift distance is approximately the same for all superlayers. Therefore, the number of cells in a given superlayer scales approximately with the radius of the

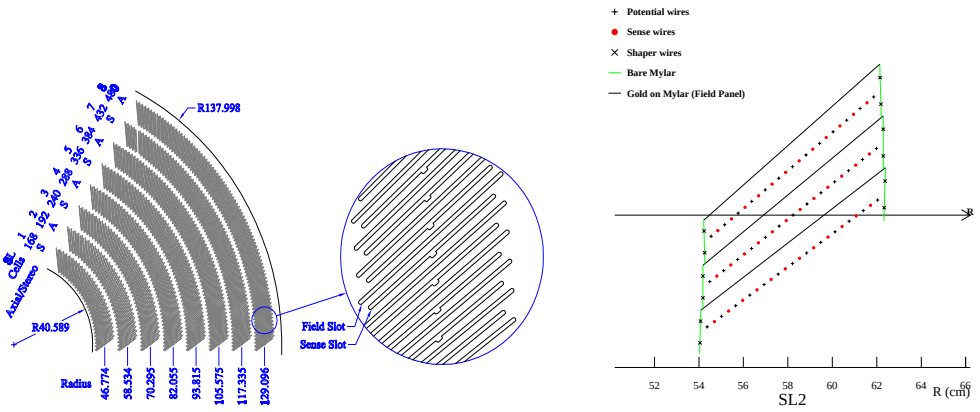

(a) COTsector (b) COT Cell

Figure 2.12: *A 1/6 section of the COT end-plate 2.12(a). For each super-layer is given the total number of cells, the wire orientation (axial or stereo), and the average radius in* cm. *The enlargement shows in details the slot where the wire planes (sense and field) are installed. Fig. 2.12 shows a sketch of an axial cross section of three cells in the superlayer 2, the arrow shows the radial direction.*

superlayer. The entire COT contains 30,240 sense wires spanning the entire length of the detector in z. Approximately half the wires run along z direction (*axial*). The other half are strung at a small angle (2°) with respect to the z direction (*stereo*). This allows to perform track reconstruction in the $r-z$ plane. The active volume of the COT begins at a radius of 43.4 cm from the beamline and extends out to a radius of 132.3 cm. The chamber is 310 cm long. Particles originating from the interaction point with $|\eta| < 1$ pass through all the 8 superlayers of the COT. The cell layout, shown in Fig. 2.12(b) for superlayer 2, consists of a wire plane containing sense and potential wires (for field shaping) and a field (or cathode) sheet on either side of the cell. Both the sense and potential wires are 40 μm diameter gold plated tungsten wires. The field sheet is 6.35 μm thick mylar with vapor-deposited gold on both sides. Each field sheet is shared with the neighboring cell. The COT is filled with an Argon-Ethane gas mixture and Isopropyl alcohol (49.5:49.5:1). The gas mixture is chosen to have a constant drift velocity across the cell width. When a charged particle passes through the detector volume, the gas is ionized. Electrons drift towards the nearest sense wire. The electric field in a cylindrical system grows exponentially with decreasing radius. As a consequence, an avalanche multiplication of charge happens inside the high electric field region, in the vicinity of the wire, due to *electron-atom*

collisions. The resulting charge reaches the wire and this so called *hit* is read out by electronics. The avalanche discharge provides a gain of ~ 104. The maximum electron drift is approximately 100 ns. Due to the magnetic field, electrons drift at a Lorentz angle of $\sim 35°$ with respect to the radius. The cell is tilted by $\sim 35°$ with respect to the radial direction to compensate for this effect. Signals on the sense wires are processed by the ASDQ (Amplifier, Shaper, Discriminator with charge encoding) chip, which provides input projection, amplification, pulse shaping, baseline restoration, discrimination, and charge measurement [65]. The pulse is sent through ~ 11 m of micro-coaxial cable, via repeater cards, to Time to Digital Converter (TDC) boards in the collision hall. The pulse leading edge gives the arrival time information and the pulse width, in nanosecond, and is related to the amount of charge collected by the wire. After calibrating the width variations due to the COT geometry, to the path length of the associated track, to the gas gain differences for the 96 wires, the Landau associated to the track is determined, using the amount of the charge collected (in nanosecond) for each hit along the track path length. From the Landau distribution the energy loss is measured and used for particle identification. A detailed description of the calibration is found in [66], [67]. The TDC boards contain also the buffer where the data are stored while waiting for the events to be accepted by the trigger. The TDC auxiliary card catch hits for the XFT track trigger processor (see Sec. 2.9.1). Hit times are later processed by pattern recognition (tracking) software to form helical tracks. The hit resolution of the COT is about 40 μm. The transverse momentum resolution has been measured using cosmic ray events to be:

$$\frac{\sigma_{p_T}}{p_T^2} = 0.0017\,[\mathrm{GeV/c}]^{-1} \tag{2.4}$$

The tracking algorithms reconstruct particle trajectories (helixes) that best correspond to the observed hits. Reconstructed trajectories are referred to as *tracks*. The tracks with available COT information are important for several reasons:

- they are fundamental for the trigger based on charged tracks and for the special Level-2 (L2) trigger optimized for B-physics (see Sec. 2.8.2) used to collect data analysed in this Thesis;
- they form the basis of the TOF reconstruction to provide particle identification information for the track parent particle;
- they are used in the silicon reconstruction to match the hits in the Silicon VerteX (SVX) detector to the COT track trajectory;
- they, themselves, contain information about particle velocity through the measurement of the energy loss.

All the tracks that we use in the Λ_b^0 analysis are required to have the COT and the SVXII information.

2.3.3 Track Reconstruction

As explained in the previous chapter, charged particles leave small charge depositions as they pass through the alternative layers of the tracking system. Using these depositions, pattern recognition algorithms reconstruct the particle original trajectory measuring the five parameters of the helix (see Sec. 2.2.1) that best match to the observed hits.

CDF employs several algorithms for track reconstruction depending on which component of the detector a particle travels through. The principal one is the Outside-In (OI) reconstruction [68]. This algorithm, exploiting the information from both the central drift chamber and the silicon detectors, is used to track the particles in the central region ($|\eta| < 1$). It first reconstructs tracks in the COT and then extrapolates them inwards toward the beam.

The first step of pattern recognition in the COT looks for circular paths[9] in the axial superlayers. Cells in the axial superlayers are searched for sets of 4 or more hits that can be fit to a straight line. These sets are called *segments*. Once segments are found, there are two approaches to track finding [69] (*segment linking* and *histogram linking* algorithms). One approach is to link together the segments which are consistent with lying tangent to a common circle. The other approach is to constrain its circular fit to the *beamline* (see Sec. 2.3.4). Once a circular path is found in the $r - \varphi$ plane, segments and hits in the stereo superlayer are added depending on their proximity to the circular fit. This results in a three-dimensional track fit. Typically, if one algorithm fails to reconstruct a track, the other algorithm will not. This arises in high track reconstruction efficiency in the COT for tracks passing through all 8 superlayers (97% for tracks with $p_T > 10\,\mathrm{GeV/c}$)[10].

Once a track is reconstructed in the COT, it is extrapolated inward to the silicon system. Based on the estimated errors on the track parameters, a three dimensional *road* is formed around the extrapolated track. Starting from the outermost layer, and working inwards, silicon hits found inside the road are added to the track. As hits get added, the road gets narrowed according to the knowledge of the updated track parameters and their covariance matrix. Reducing the width of the road reduces the chance of adding a wrong hit to the track, and also reduces the computation time. In the first pass of this algorithm, axial hits are added. In the second pass, hits with stereo information are added to the track. At the end,

[9] The helical track, when projected onto the $r - \varphi$ plane, is a circle.

[10] The track reconstruction efficiency mostly depends on how many tracks are reconstructed in the event. If there are many tracks close to each other, hits from one track can shadow hits from the other track, resulting in efficiency losses.

the track combination with the highest number of hits and lowest χ^2/ndf for the five parameters helix fit is kept.

Due to the limited COT coverage and the strict hits requirement (at least four of eight superlayers), tracking in the forward regions requires different algorithms [70], [71] that are not described here because the tracks in the forward regions are not used in this analysis.

2.3.4 Primary Vertex

In this Thesis the location of the primary $p\bar{p}$ vertex is required to calculate the decay length corresponding to the secondary vertices candidates and the impact parameter of charged tracks.

The primary vertex location, for a given event, is found by fitting high quality tracks to a common point of origin. At high luminosities, multiple collisions occur on a given bunch crossing. For a luminosity of $10^{32}\,\mathrm{cm}^{-2}\mathrm{s}^{-1}$, there are an average of 2.3 interactions per bunch crossing. Typically, since the luminous region is sufficiently long (with $\sigma_z = 29\,\mathrm{cm}$), the primary vertices associated to the collisions are well separated in z. An iterative algorithm is used to find the vertex associated to the hardest collision: the first estimate of its position (x_V, y_V, z_V) is binned in the z coordinate, then the z position of each vertex is calculated from the weighted average of the z coordinates of all tracks within 1 cm of the first iteration vertex, with a typical resolution of $100\,\mu$m; finally the vertex associated with the highest sum of the tracks p_T is defined as primary vertex of the event.

The locus of all primary vertices defines the beamline, the position of the luminous region of the beam-beam collisions through the detector. A linear fit to (x_V, y_V) vs. z_V yields the beamline for each stable running period. The beamline is used as a constraint to refine the knowledge of the primary vertex in a given event. Typically the beam transverse section is circular with width of $\approx 30\ \mu$m at $z = 0$, rising to $\approx 50 - 60\ \mu m$ at $|z| = 40\,\mathrm{cm}$. The beam is not necessarily parallel nor centered in the detector and moves as a function of time.

2.4 Time Of Flight detector (TOF)

The TOF [72] is a cylindrical array made of 216 scintillating bars and is located between the external surface of the COT and the magnet cryostat containing the superconducting solenoid. It was added in 2001 to improve the capability to distinguish different kind of long-lived particles, measuring the time elapsed between the collision time and when a particle is revealed by the detector. Bars are 280 cm long and with a $4 \times 4\,\mathrm{cm}^2$ cross section oriented along the beam axis all around the inner cryostat surface, installed in the 4.7 cm radial space between

the outer surface of COT and the cryostat of the super-conducting solenoid at an average radius of 140 cm, which corresponds to 4.7 ns flight-time for a particle roughly at the speed of light.

Both longitudinal sides of the bars collect the light produced by the charged particles in the scintillator bars into 432 fine-mesh, 19-stage photon-multipliers and measure accurately the timing of the two pulses. The time between the bunch crossing and the scintillation signal in these bars defines the β of the charged particle while the momentum is provided by the tracking system. Particle Identification (PID) information is available through the combination for a track of TOF and track energy loss (COT) measurements.

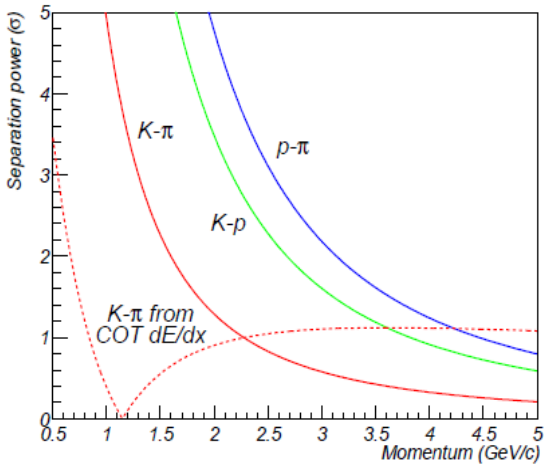

Figure 2.13: *Separation power of TOF for different particles at CDF, with dE/dx separation power for kaon and pion from COT superimposed.*

The design of the photon-multipliers permits them to maintain an adequate gain even in the 1.4 T magnetic field. The preamplified PhotoMultiplier Tube (PMT) signals follow two parallel paths: the timing signal is discriminated and digitized, while the charge signal is digitized to be eventually used at trigger level and for subsequent extraction of the offline corrections.

Using the time measurement from this detector and the measured momentum from the COT is possible to deduce the particle mass by the formula:

$$m = \frac{p}{c}\sqrt{\frac{c^2t^2}{L^2} - 1} \tag{2.5}$$

where p is the momentum measured, L is the path length of the track, and t is the difference between the arrival time of the TOF signal with respect to the

the bunch-crossing time. The expected separation power[11] for the various particle species that is achievable with TOF alone, assuming ≈ 110 ps for the time of flight resolution, as a function of momentum is shown in Fig. 2.13. For comparison, the expected K/π separation from the COT dE/dx measurement is also shown in Fig. 2.13 to illustrate the complementary power of COT with respect to the TOF particle identification. PID algorithms are not used in this thesis.

2.5 Calorimeter System

Even if not used in this analysis, the calorimeter system, together with the muon and tracking systems, is one of the main sub-detector apparatus of CDF II detector. A detailed description of this system can be found in [59]. The CDF II calorimetry system has been designed to measure energy and direction of neutral and charged particles leaving the tracking region. In particular, it is devoted to jet reconstruction and it is also used to measure the missing energy associated to neutrinos.

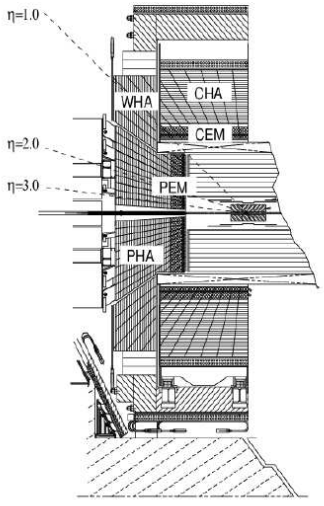

Figure 2.14: *Elevation view of the CDF detector showing the components of the CDF calorimeter: CEM, CHA, WHA, PEM and PHA.*

[11] The expected separation power is defined as $\frac{TOF_i(p)-TOF_j(p)}{\sigma_{TOF}}$ where $TOF_i(p) = \frac{L}{c}\sqrt{\frac{m_i c^2}{p^2}+1}$ is the expected time of fight of the i particle of mass m_i and momentum p. σ_{TOF} is the time of flight resolution.

Particles hitting the calorimeter can be divided in two classes, according to their main interaction with the matter: electromagnetically interacting particles, such as *electrons* and *photons*, and hadronically interacting particles, such as *mesons* or *baryons* produced in hadronization processes. To detect these two classes of particles, two different calorimetric parts have been developed: an inner electromagnetic and an outer hadronic section, providing coverage up to $|\eta| < 3.64$. In order to supply information on particle position, the calorimeter is also segmented in radial sections, called *towers*, projected toward the geometrical center of the detector. Each tower consists of alternating layers of passive material and scintillator tiles. The signal is read out via wavelength shifters (WLS) embedded in the scintillator and light from WLS is then carried by light guides to photomultiplier tubes. The central sector of the calorimeter, covering the region $|\eta| < 1.1$, was recycled from Run I, while brand new calorimeters (called plug calorimeters) were built up to cover the forward and backward regions. Fig. 2.15(b) shows the Plug calorimeter system while Fig. 2.14 shows an elevation view of the components of the CDF calorimeter: Central Electro Magnetic calorimeter (CEM), Central HAdronic calorimeter (CHA), Wall HAdronic calorimeter (WHA), Plug ElectroMagnetic calorimeter (PEM), and Plug HAdronic calorimeter (PHA).

The Central Calorimeter

Apart from upgrades on the readout electronics, needed to follow the increased collision rate, the central calorimeter is almost the same used during Run I. The CEM is segmented in $\Delta\eta \times \Delta\varphi = 0.11 \times 15^\circ$ projective towers consisting of alternate layers of lead and scintillator, while the CHA and Central Wall HAdronic calorimeters (CWA), whose geometry tower segmentation matches the CEM one, use iron layers as radiators.
A perspective view of a central electromagnetic calorimeter module (*wedge*) is shown in Fig. 2.15(a), where both the arrangement in projected towers and the light-gatering system are visible. The projective geometry has been used in order to take advantage of the momentum conservation in the transverse plane: before the $p\bar{p}$ collision, the projection in the transverse plane w.r.t. the beam direction of the beam energy is null, therefore this quantity have to be the same also after the collision took place. Thus, the for each tower the transverse energy E_T is defined as $E_T = Esin\theta$, where E is the energy detected by the tower and θ is the angle between the beam axis and the tower direction, in the CDF detector coordinates system. Two position detectors are embedded in each wedge of CEM:

- The **Central Electromagnetic Strip multi-wire proportional chambers (CES)** is a two-dimensional stripwire chamber arranged in correspondence to maximum shower development ($\sim 5.9X_0$). It measures the charge deposit

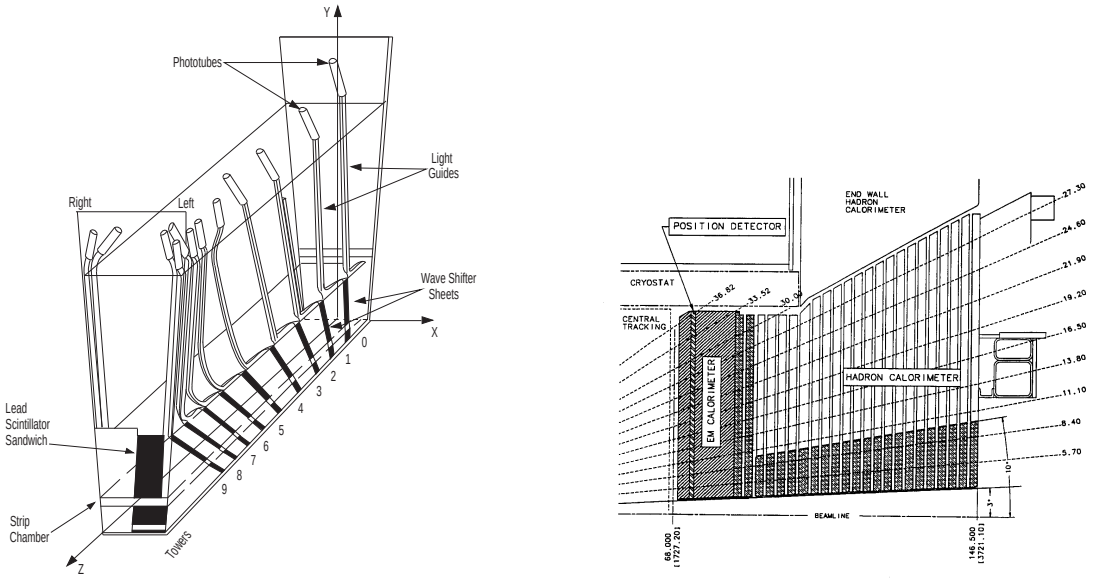

(a) CEM Wedge

(b) Plug calorimeters

Figure 2.15: *The plot show one azimuthal electromagnetic calorimeter wedge 2.15(a), the second plot shows an elevation view of one quarter of the plug calorimeter 2.15(b).*

of the electromagnetic showers, providing information on their pulse-height and position with a finer azimuthal segmentation than calorimeter towers. This results in an increased purity on electromagnetic object reconstruction.

- The **Central Pre-Radiator (CPR)** consists of two wire camber modules placed immediately in front of the calorimeter. It acts as pre-shower detector by using the tracker and the solenoid coil material as radiators, resulting to be a very useful tool in rejection of electron and photon background.

Calorimeter	CEM	CHA	WHA	PEM	PHA
Absorber	Lead	Steel	Steel	Lead	Iron
Segmentation ($\eta \times \varphi$)	0.1×15	0.1×15	0.1×15	(0.1 ÷ 0.6)×(7.5 ÷ 15)	(0.1 ÷ 0.6)×(7.5 ÷ 15)
Num. Towers ($\eta \times \varphi$)	20×24	9×24	6×24	12×24(48)	11×24(48)
Thickness	18 X_0,1 λ_{int}	4.7 λ_{int}	4.7 λ_{int}	23 X_0,1 λ_{int}	6.8 λ_{int}
Resolution (%)	$14/\sqrt{E_T} \oplus 2$	$50/\sqrt{E_T} \oplus 3$	$75/\sqrt{E_T} \oplus 4$	$16/\sqrt{E} \oplus 1$	$80/\sqrt{E} \oplus 5$

Table 2.4: *Summary of the main characteristics of the CDF II calorimeter system.*

Calorimeter response is fast enough to match the time requirements imposed by Run II. However, wire chambers associated to CES and CPR may need to be

integrated over several beam crossings; this will not be a problem since the high granularity of these devices guarantees a low detector occupancy. Tab. 2.4 summarizes the basic quantities of calorimeter detectors.

The Plug Calorimeter

The plug calorimeter (see Fig. 2.15(b)), covers the η region from 1.1 to 3.64. The new configuration, based on the same principles as the central calorimeter, allows the detector to operate in the Run II environment and makes experimental data more homogeneous. Both electromagnetic and hadronic sectors are divided in 12 concentric η regions, with $\Delta\eta$ ranging from 0.10 to 0.64, according to increasing pseudo-rapidity, each of them is segmented in 48 or 24 (for $|\eta| < 2.11$ or $|\eta| > 2.11$ respectively) projective towers. The actual size of these towers was chosen so that identification of electron in b-jets would be optimized. Projective towers consist in alternating layers of absorbing material (lead and iron for electromagnetic and hadronic sector respectively) and scintillator tiles. The first layer of the electromagnetic tile is thicker (10 mm instead of 6 mm) and made of material with higher photon yield. They act as a pre-shower detector.

2.6 Muon Detectors

The particles produced by the interaction and subsequent decays are absorbed by the system described above with a very high probability. The most common particle that escapes the calorimetric system is the muon. Muons are over 200 times more massive than electrons, so bremsstrahlung radiation, inversely proportional to the mass squared of the incident particle, is suppressed by a factor of 4×10^4 with respect to electrons. Muons do not interact via strong interaction with nuclei in matter either. Therefore, a muon with enough energy will pass through the calorimeter systems releasing only a small amount of its energy. At CDF the minimum muon energy required to reach the muon detectors, placed radially outside of the calorimeters, is 1.4 GeV. In addition to the calorimeters, steel absorbers are placed upstream of the muon systems to reduce punch-through hadrons.
The muon system is the outermost layer of the CDF II detector and consists on drift cells and scintillation counters which are used to reconstruct segment of track, *the stubs*, from minimum ionizing particles. These stubs are matched using dedicated algorithms with the COT information in order to reconstruct the full trajectory of the muons. Some additional steel shielding layers, in between the chambers and the calorimeters, reduce the probability for other particles to escape the calorimetric system. Four independent systems detect penetrating charged particles (*muons*)

in the $|\eta| \lesssim 1.5$ pseudo-rapidity range reconstructing a small segment of their path (*the stub*) sampled by the chambers, employing similar combinations of drift tubes, scintillation counters, and absorbers with differential azimuthal coverage [73], [74]. The momentum measurement is performed by pointing back the stub to the corresponding track in the COT. Scintillators serve as trigger or trigger veto for muons while the drift chambers measure the φ coordinate using the absolute difference of drift electrons arrival time between two cells, and the z coordinate by charge division. All type of muon detectors use a single wire, rectangular drift chambers, arranged in arrays with various azimuthal segmentation and coupled with scintillator counters. The chambers use a 50:50 gas admixture of Argon and Ethane, and operates in proportional regime. The four sub-detector systems are (see Fig. 2.16 for their coverage in the $\eta - \varphi$ plane):

Central MUon detector (CMU): the CMU detector is located around the central hadronic calorimeter at a radius of 347 cm from the beamline with coverage $0.03 \lesssim |\eta| \lesssim 0.63$. It is segmented into 24 wedges of 15°, but only 12.6° in φ, with a gap of 2.4°, of each wedge is active, resulting in an overall azimuthal acceptance of 84%. Each wedge is further segmented into three 4.2° modules each containing four layers of four drift cells.

Central Muon uPgrade (CMP): the CMP is a second set of muon drift chambers outside of CMU with an additional 60 cm-thick steel absorbers between

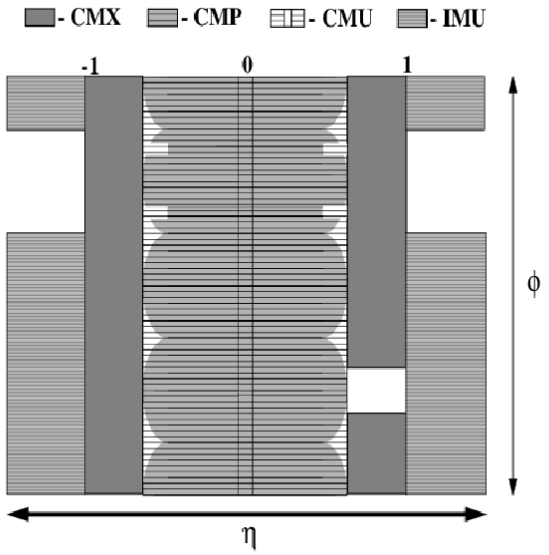

Figure 2.16: *Muon detectors coverage in the $\eta - \varphi$ plane.*

them. The material further reduces the probability of hadronic punch-through to the CMP. Muons need a transverse momentum of about 2.2 GeV to reach the CMP. The CMP system is arranged in a box shape of similar acceptance as the CMU and conventionally serves as a confirmation of CMU for higher momentum muons. A layer of scintillation counters (CSP) is mounted on the outer surfaces of the CMP. The CMP and CMU have a large overlap in coverage and are often used together. CMP helps to cover CMU φ gaps and the CMU covers the CMP η gaps. Muon candidates which have both CMU and CMP stubs are the less contaminated by fake muons.

Central Muon eXtension (CMX): the CMX consists of drift tubes and scintillation counters (CSX) assembled in conically arranged sections. The CMX extends the pseudo-rapidity coverage to $0.6 \lesssim |\eta| \lesssim 1$. There are 8 layers of drift chambers in total with a small stereo angle between layers.

Intermediate MUon system (IMU): the IMU extends the pseudo-rapidity coverage even further to $1.0 \lesssim |\eta| \lesssim 1.5$. The IMU is mounted on the toroid magnets which provide shielding and consists of Barrel MUon chambers (BMU), Barrel Scintillation counters (BSU) and Toroid Scintillation counters (TSU).

2.7 Cherenkov Luminosity Counters (CLC) and Measurement of the Luminosity

The main purpose of this detector (CLC) (see Fig. 2.17) is to measure the instantaneous luminosity ($\mathcal{L}$) in the BØ interaction point. The relation used is $\bar{N} \times f_{b.c.} = \sigma_{p\bar{p}} \times \varepsilon \times \mathcal{L}$, where $\bar{N}$ is the number of interaction for bunch-crossing (BC), $f_{b.c.}$ the BC frequency, which is on average 2.5 MHz for 36 × 36 bunch operations, $\sigma_{p\bar{p}}$ is the inelastic cross section[12], and ε is the detector efficiency. The inelastic cross section is obtained by extrapolating the combined results for the inelastic $p\bar{p}$ cross section of CDF at $\sqrt{s} = 1.8\ TeV$ and E811 measurements at $\sqrt{s} = 1.96\ TeV$ [75] at the Run II energy. The global uncertainty on the luminosity is $\approx 5.6\%$. This detector covers the $3.7 \lesssim |\eta| \lesssim 4.7$ range, with two symmetrical detector placed in the forward and in the backward regions. It is composed by long Cherenkov detectors, $100 - 108$ cm, with a conical shape, filled with Isobutane that guarantees high refraction index and good transparency for ultraviolet photons. The light emitted are collected in a PMT shielded by the solenoidal magnetic field. The luminosity measured by the CLC is used to monitor the Tevatron performance.

[12]The proton-antiproton inelastic cross section at the Tevatron is $\sigma_{p\bar{p}} = 59.3$ mb.

2.7. Cherenkov Luminosity Counters (CLC) and Measurement of the Luminosity

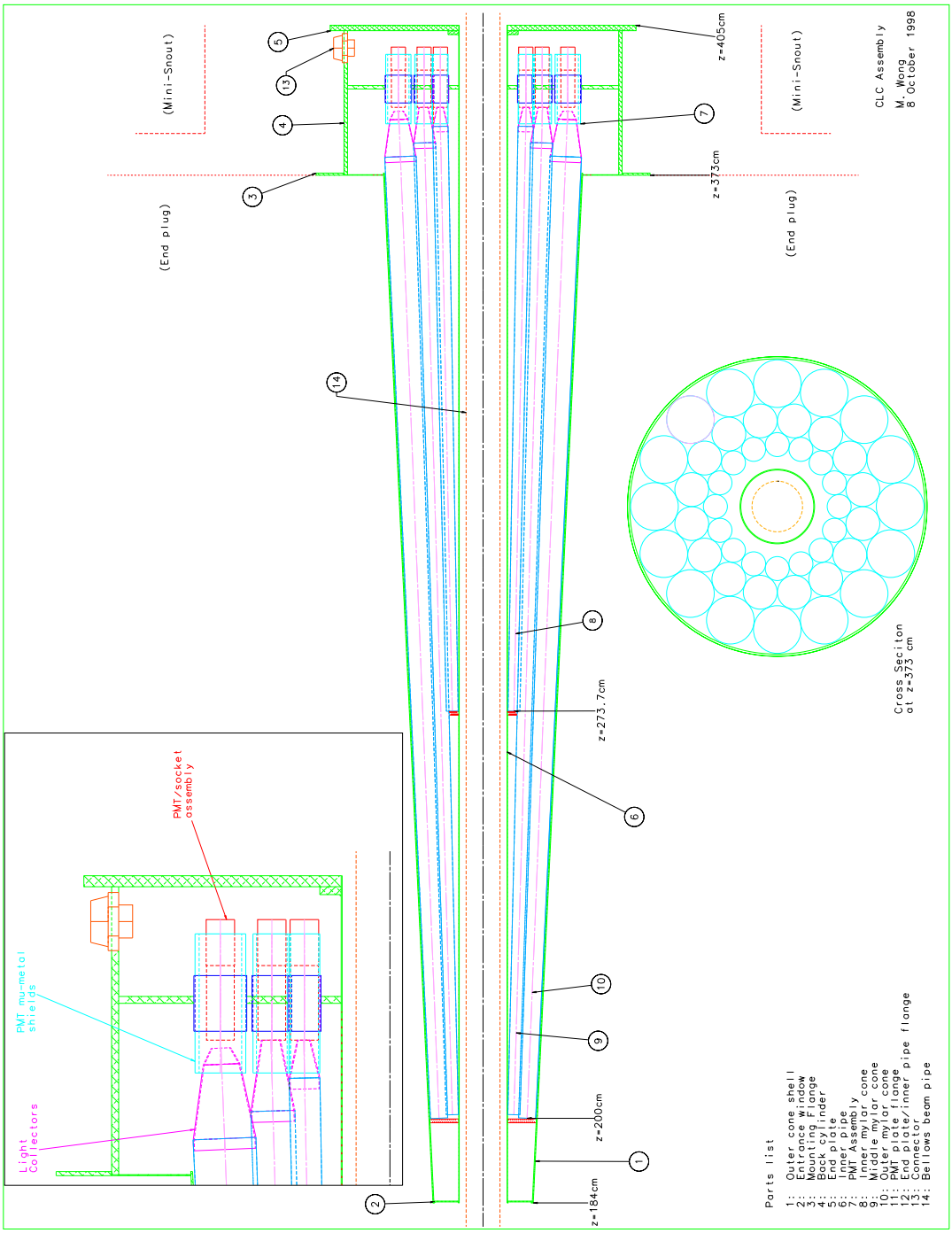

Figure 2.17: *Longitudinal section of the CLC system forward.*

2.8 Trigger and DAQ

At the typical Tevatron instantaneous luminosity $\mathcal{L} \approx 4 \times 10^{32}\,\mathrm{cm}^{-2}\mathrm{s}^{-1}$, and with an inelastic $p\bar{p}$ cross section of $\sigma_{p\bar{p}} \approx 60\,\mathrm{mb}$, approximately 2.5×10^7 inelastic collisions per second occur, corresponding to one inelastic $p\bar{p}$ interaction per bunch-crossing on average[13]. Since the read-out of the entire detector needs about 2 ms on average, after the acquisition of one event, another approximately 5,000 interactions would remain unrecorded. When an event recording is prevented because the system is busy with a different event or a different task, this is called *dead-time*.

The average size of information associated to each event is 140 Kb. Even in case of deadtime-less read-out of the detector, in order to record all events, an approximate throughput and storage rate of 350 Gb/s would be needed, largely beyond the possibility of currently available technology[14].

The read-out system has to reduce the 2.3 MHz interaction-rate to the 100 Hz storage rate attainable at CDF. The challenge for the whole system is to cut-off events that don't have the minimal requirements to be reconstructed or seem to contain well-known processes, that don't need further study, focusing the acquisition system on the interesting processes.

DAQ is segmented in three levels (see Fig. 2.18). Each level receiving the accepted event from the previous one, and, provided with detector information with increasing complexity and with more time for processing, determines if one of a set of existing criteria is verified by the event.

Prior to any trigger level, the bunched structure of the beam is exploited to reject cosmic-ray events by gating the front-end electronics of all sub-detectors in correspondence of the bunch crossing. The front-end electronics of each sub-detector, packaged in Vesa Module Eurocard (VME) modules hosted in about 120 crates, has a 42-cells deep pipeline synchronized with the Tevatron clock-cycle set to 132 ns. The Tevatron clock picks up a timing marker from the synchrotron RF and forwards this bunch-crossing signal to the trigger and to the front-end electronics. Since the inter-bunch time is 396 ns, three times the Tevatron clock-cycle, the pipeline can collect data corresponding to a maximum of 14 bunch crossings. The pipeline depth gives the amount of time that Level-1 (L1) trigger has to decide to accept or reject an event otherwise the buffer content is overwritten: $396\,\mathrm{ns} \cdot 14 = 5.5\,\mu\mathrm{s}$. An event accepted by the L1 is then passed to the Level-2 (L2) buffer, where the number of buffers in the pipeline is 4, that gives $5.5\,\mu\mathrm{s} \cdot 4 = 22\,\mu\mathrm{s}$. This means that if an event is accepted by the L1 and the L2 doesn't have a free buffer deadtime will incur. Level-3 (L3) is composed by a computer farm, the L2

[13] Abort gaps can be neglected for this estimate.

[14] The maximum current storage rate is approximately 250 Kb/s

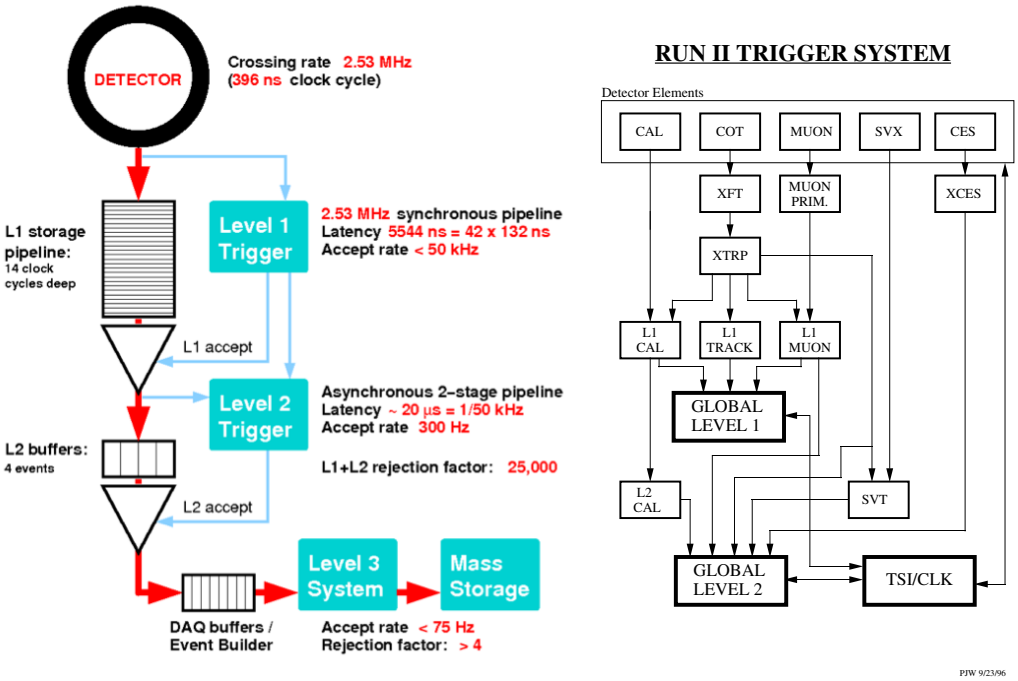

(a) (b)

Figure 2.18: *Block diagram showing the global trigger* **2.18(a)** *and the data flow for the L1 and L2 systems at CDF II* **2.18(b)**.

output rate is low enough to avoid in general deadtime problem in the connection between L2 and L3. The following description will emphasize the aspect of the CDF Trigger that are related with the selection of rare events including b-hadrons with high purity.

2.8.1 Level-1

L1 is a synchronous system of custom designed hardware which reconstructs information from three parallel streams: the calorimeter (total energy and single tower information), the COT (only 4 axial superlayers are used for two-dimensional tracks), and the muon systems (stubs in the CMU, CMP and CMX). The XFT is a custom processor used to identify two-dimensional tracks in the $r-\varphi$ plane in the COT. The XFT is capable of reconstructing tracks with $p_T \gtrsim 1.5\,\text{GeV}$ with an efficiency of about 95% and a fake rate of a few percent. The XFT has an angular segmentation of 1.25°, and an angular resolution of 0.3°. The momentum

resolution is $\sigma_{p_T}/p_T^2 \approx 0.017\,[\mathrm{GeV/c}]^{-1}$. XFT sends the track information to the extrapolation unit (XTRP) which feeds three L1 elements: L1 CAL, L1 TRACK, and L1 MUON. L1 CAL and L1 MUON use extrapolated tracks and information from the calorimetry and muon systems respectively to search for possible electron, photon, jets and muon candidates. A decision stage combines the information from these low-resolution physic objects, called *primitives*, into more sophisticated objects, e.g., track primitives are matched with muon stubs or tower primitives, to from muon, electron, or jet object, which are subject to basic selection. The accepted events are buffered for L2 analysis.

2.8.2 Level-2

The L2 is an asynchronous system of custom-designed hardware which processes events accepted by the L1 in the time-ordered fashion. Additional information from the shower-maximum strip chambers in the central calorimeter and the axial hits in the SVXII is combined with the L1 primitives to produce L2 primitives. A simplified energy-clustering is done in the calorimeters, merging the energies in adjacent towers to the energy of a seed tower above threshold. L1 track primitives matched with consistent shower-maximum clusters provided refined electron candidates whose azimuthal position is known within 2° accuracy. Information from the r, φ sides of the SVXII is combined with L1 tracks primitives to form two-dimensional tracks with resolution similar to the offline one by the silicon-based trigger system, (see Sec. 2.9.2). Silicon Vertex Trigger (SVT) uses SVX $r - \varphi$ hits to extend XFT track primitives inside the SVX volume, closer to beamline. The SVT improves the XFT φ_0 and p_T resolutions and adds the measurement of the impact parameter d_0 (original XFT track primitives are beamline constrained). Acting into the impact parameter, SVT is a very useful handle in order to select decay modes of heavy b-hadrons into charged prongs.
As shown in Fig. 2.19, the impact parameter of decay products is strongly related to the decay length of the mother b-hadron, therefore a selection based on the tracks impact parameter turns directly in to a proper time requirement. This innovative system is the core of all the trigger systems for B physics, and will be described in further details in Sec. 2.9. Finally, an array of programmable processors makes the trigger decision, while the L2 objects relative to the following event accepted at L1 are already being reconstructed. The L2 output rate is around 900 Hz.
Fig. 2.18(b) shows the block diagram of the CDF II trigger system with the L1 and L2 subsystems along with their interconnections.

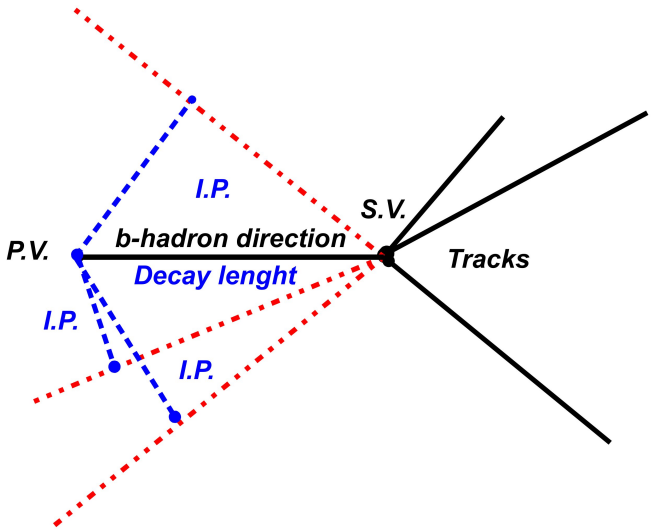

Figure 2.19: *Schematic chart showing the correlation between the tracks impact parameter (I.P.) and the decay length, in the transverse plane, of a hypothetical b-hadron decay.*

2.8.3 Level-3

After an event is accepted at L2, it has to be read out completely. The digitized output relative to the L2-accepted event arrives fragmented from all sub-detectors via optical fibers. It is collected by a custom hardware switch that arranges it in the proper order and transfers it to 300 commercial Central Processing Unit (CPU)s, organized in a modular and paralleled structure of 16 sub-systems [76]. The ordered fragments are assembled in the *event record*, a block of data that uniquely identifies a bunch crossing, and is ready for the analysis of the L3 software. This operation involves collecting data from over a couple of hundreds of VME Readout Buffers (VRBs). The Event Builder assembles the event from pieces of data from the L2 system into complete events. It is divided into 16 sub-farms, each consisting of 12 to 16 processor nodes. Once the event is built, it is sent to one node in the L3 farm. The L3 trigger reconstructs the event following given algorithms. These algorithms take advantage of the full detector information and improved resolution not available to the lower rigger levels. This includes a full three-dimensional track reconstruction and tight matching of tracks to calorimeter and muon-system information. Events that satisfy the L3 trigger requirements are then transfered onward to the Consumer Server/Data Logger (CSL) system for storage first on disk and later on tape. The average processing time per event in

L3 is on the order of a few seconds. The L3 leads to a further reduction in the output rate, roughly 75 Hz.

A set of requirements that an event has to fulfill at L1, L2 and L3 constitutes a trigger path. The CDF II trigger system implements about 200 trigger paths. An event will be accepted if it passes the requirements of any one of these paths and, depending of the trigger path, it will be stored in a trigger dataset. A complete description of the different datasets at CDF II Run II can be found in [77].

Another important feature of the trigger system of CDF is that L1 and L2 accepts can be pre-scaled. This means that only a fraction of the events that fulfill the trigger requirements are actually accepted. Even if this implies loosing potentially useful events, it becomes necessary at high luminosity. Given the continuous improving performance of the Tevatron, pre-scaling trigger has become common practice in the last years. Moreover, the trigger system allows for dynamic pre-scaling of trigger accepts, meaning that the scaling factor varies with the instantaneous luminosity, so the output bandwidth is maximally utilized. If an event satisfies the L3 requirements, the corresponding event record is transferred to mass storage at a maximum rate of 20 Mbyte/s.

The L3 decision is made after the full reconstruction of the event is completed and the integrity of its data is checked, a process that takes a few milliseconds. A fraction of the output is monitored in real time to search for detector malfunctions, to derive calibrations constants and to graphically display events.

2.9 The Track Trigger

The goal of a trigger that wants to collect a large number of rare b-hadron decays at a hadron collider is to implement the most sophisticated selection, in order to have a reasonable amount of bandwidth used by these triggers. The important quantities taken into account to have the optimal selection are: signal efficiency, the background rejection, and the final rate of the trigger.

In the CDF experiment the implementation of the strategies that have a good rejection on the background, with a reasonable efficiency on the interesting signal, had great advantage from the use of custom hardware devoted to the reconstruction of the track parameters in real-time. In the next sub-sections will be described the two processor that are doing this task at L1 and L2: XFT (see Sec. 2.9.1) and SVT (Sec. 2.9.2).

2.9.1 The COT track-processor: XFT

The COT is connected to a custom processor that identifies two-dimensional tracks, in the $r - \varphi$ plane, in time with the L1 decision. This processor is called

XFT [78], and uses pattern matching to first identify short segments of tracks, within each super-layer, and then links them into full-length tracks. The CDF II XFT is the trigger processor which reconstructs charged particle tracks in the transverse plane of the central tracking chamber. The XFT tracks are also extrapolated to the electromagnetic calorimeter and muon chambers to generate trigger electron and muon candidates. The role of the XFT in the trigger is to reduce the raw collision rate (1.7 MHz) to a maximum of about 30 KHz of interesting physics events which can be processed by the L2 trigger. The XFT uses hit data from the 4 axial superlayers of the chamber, arranged in cells of 12 wires each. A charged particle passing through an axial layer generates a characteristic pattern of 12 hits, one per wire, with a characteristic timing. Track identification is performed in two steps by the Finder boards, which search for track segments in each of the 4 axial layers of the chamber, and by the Linker boards, which search for 4/4 matches among segments in the 4 layers, consistent with a track exiting from the interaction point. If a coincidence between segments crossing four super-layers is found, two-dimensional XFT-tracks are reconstructed by linking the segments. The segments are compared with a set of about 2,400 predetermined patterns corresponding to all possible tracks with $p_T \geq 1.5\,\mathrm{GeV/c}$ originating from the beam line. The comparison proceeds in parallel each of the 288 azimuthal 1.25° sectors in which XFT logically divides the chamber. If no track is found using all four super-layers, then the best track found in the innermost three super-layers is output. The track-finding efficiency and the fake rate with respect to the offline tracks depends of the instantaneous luminosity, and were measured to be $\varepsilon \approx 96\%$, and 3% respectively, for tracks with $p_T \geq 1.5 GeV/c$ at $\mathcal{L} \simeq 10^{31}\,\mathrm{cm^{-2}s^{-1}}$. The observed momentum resolution is $\sigma_{p_T}/p_T^2 = 0.017[GeV/c]^{-1}$, and the azimuthal resolution is $\sigma_{\varphi_6} = 0.3°$, where φ_6 is the azimuthal position at the sixth COT super-layer, located at 106 cm radius from the beam line. The reconstructed tracks are reported to the eXTRaPolator unit (XTRP) and a copy of them is preserved to be used in the L2. The fake rate needs a particular treatment when the instantaneous luminosity exceeds $10^{32}\,\mathrm{cm^{-2}s^{-1}}$. In [79] is shown as in this range the presence of multiple interactions increases the XFT fake rate, with a correlated increase of the L1 rate occupied by the so called Two Track Trigger (TTT), the data used in this analysis are collected by this trigger (see Sec. 2.9).

2.9.2 The Online Silicon Vertex Tracker (SVT)

The Online Silicon Vertex Tracker (SVT) (see Fig. 2.20) is part of the L2 trigger.
It receives the list of the COT tracks reconstructed by the XFT processor (for each track the curvature C and the azimuthal angle φ are measured) and the

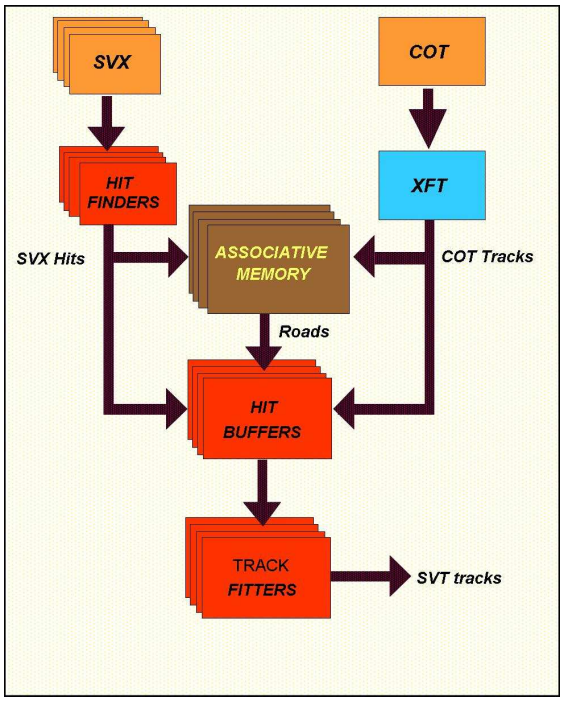

Figure 2.20: *SVT architecture.*

digitized pulse heights on the silicon layers (10^5 channels). The SVT links the XFT tracks to the silicon hits and reconstructs tracks in the transverse plane with offline-like quality. The resolution of the SVT is $\delta\varphi \simeq 1.0\,\text{mrad}$, $\delta p_T \simeq 0.003 \cdot p_T^2$ GeV/c and $\delta d_0 \simeq 35\ \mu m$, where d_0 is the track impact parameter, the radial distance of closest approach of the particle trajectory helix to the z-axis of the CDF reference system. The SVT efficiency is higher than 85%. This efficiency is defined as the ratio between the number of tracks reconstructed by SVT and all XFT-matched offline silicon tracks that are of physics analysis quality. By providing a precise measurement of the impact parameter of charged particle tracks, SVT allows triggering on events containing long lived particles. Hadrons with b quark in particular have a decay length of the order of $500\,\mu$m and tracks which come out of the b-hadrons decay vertices have an impact parameter on average grater than $100\,\mu$m.

The SVT has a widely parallelized design: it is made of 12 identical slices (*wedges*) working in parallel. Each wedge receives and processes data only from tracks in the plane perpendicular to the beamline (stereo info from SVXII is dropped) and only with p_T above $2\,\text{GeV/c}^2$. The tracking process is performed in two steps:

- **Pattern recognition**: candidate tracks are searched among a list of precal-

culated low resolution patterns (*roads*);

- **Track fitting**: a full resolution fit of the hit coordinates found within each road is performed using a linearized algorithm.

The pattern recognition step is performed in a completely parallel way by the Associative Memory (AM) system which uses full custom Very Large-Scale Integration (VLSI) chips (AMchips [80]). The AM system compares all the silicon clusters and XFT tracks with the set of precalculated patterns. Each SVT wedge uses 32,000 patterns which cover more than 95% of the phase space for $p_T \geq 2$ GeV/c.

The track fitting method is based on linear approximations and principal components analysis [81].

Fig. 2.21 shows the SVT track impact parameter resolution for tracks with $p_T > 2$ GeV/c. The width of the Gaussian fit for the distribution in Fig. 2.21 is 55 μm. This is a combination of the intrinsic SVT impact parameter resolution, and the transverse size of the beam line: $\sigma_{fit} = \sigma_{SVT} \oplus \sigma_{beam}$, where σ_{beam} is about 30 μm. Therefore, the intrinsic SVT resolution is about 35 μm. SVT allows, for the first time at a hadron collider, to trigger directly on hadronic b decays with charged prongs.

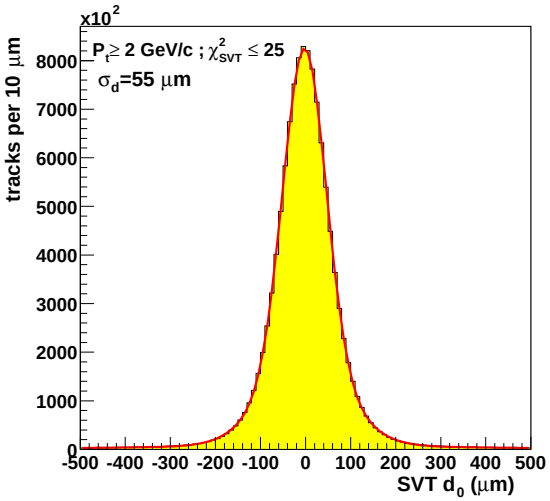

Figure 2.21: *The plot shows the distribution of the impact parameter measured by SVT processor.*

2.10 CDF MC simulation of Detector and Trigger

In a modern high energy physics experiment is important to have a precise simulation of the detector response and ability to reconstruct energy and momentum of the particle. The geometry of a detector is quite complex, so in order to reduce the uncertainties over the detector capabilities, the use of detailed MC is mandatory. Some examples of this kind of information are: the efficiency in reconstruction a decay channel, geometrical acceptances, and other similar tasks. In the standard CDF simulation, the detector geometry and material are modeled using the version 3 of the GEANT package [82] tuned using data from test-beams and from actual collisions. GEANT receives as input the positions, the four-momenta, and the identities of all particles produced by the simulated collisions that have long enough lifetimes to exit the beam pipe. It simulates their passage in the detector, modeling their interactions (*bremmstrhalung*, multiple scattering, nuclear interactions, photon conversions, etc.) and the consequent generation of signals on a channel by channel basis.

Specific packages replace GEANT for some sub-detectors: the calorimeter response is simulated with GFLASH, a faster parametric shower-simulator [83] tuned from single-particle response and shower-shape using test-beam data ($8 - 230\,\mathrm{GeV/c}$ electrons and charged pions) and collision data ($0.5 - 40\,\mathrm{GeV/c}$ single isolated tracks); the drift-time within the COT is simulated using GARFIELD standard package [84], [85] further tuned on data; the charge-deposition model in the silicon uses a parametric model, tuned on data, which accounts for restricted Landau distribution, production of δ-rays, capacitive charge-sharing between neighboring strips, and noise. Furthermore, the actual trigger logic is simulated for all digital parts of the trigger. The output of the simulated data has the same format of the collision data, allowing their analysis with the same reconstruction programs used.

The detector and trigger configuration underwent several changes during data-taking. Minor variations may occur between runs, while larger variations occur, for instance, after major hardware improvements, or Tevatron shut-down periods. For a more detailed simulation of the actual experimental conditions, the simulation has been interfaced with the offline database that reports, on a run-by-run basis, all known changes in configuration (position and slope of the beam line, relative mis-alignments between sub-detectors, trigger-table used, set of SVT parameters) and local or temporary inefficiencies of the silicon tracker (active coverage, noisy channels, etc.). This allows simulating the detailed configuration of any set of real runs, to match the distribution of real data in any given sample to very high precision.

Chapter 3

Data Sample and Reconstruction of Λ_b^0 Decay Signals

After a description of the data sample used in the analysis and of the corresponding trigger requirements, in this chapter we describe the offline procedure to reconstruct and select the $\Lambda_b^0 \to \Lambda_c^+\pi^-$ and the $\Lambda_b^0 \to \Lambda_c^+\pi^-\pi^+\pi^-$ candidates (with $\Lambda_c^+ \to pK^-\pi^+$) in order to obtain clear signals of both decays.

3.1 Overview

We are searching for $\Lambda_b^0 \to \Lambda_c^+\pi^-$ and $\Lambda_b^0 \to \Lambda_c^+\pi^-\pi^+\pi^-$, where the inclusive decay of the Λ_c^+ is $\Lambda_c^+ \to pK^-\pi^+$[1]. The event topology of the decays[2] we want to study is schematically shown in Fig. 3.1. We know that b-hadrons decay, by weak interaction, with a decay length $c\tau \sim 370\ \mu m$ [1]. At CDF their decay length, $\gamma\beta c\tau$[3], typically has a mean value of 500 μm and, due to the fact that its resolution is $\sim 50\,\mu$m, the secondary decay vertex is clearly distinguished from the interaction vertex of $p\overline{p}$ collisions. The Λ_c^+, produced in the secondary vertex, decays into three charged particles, p, K^- and π^+, after less than 100 μm.
In Fig. 3.1 there are the four (see Fig. 3.1(a)) or six (see Fig. 3.1(b)) final particle decays, for which three of them produced in the tertiary vertex (corresponding to the Λ_c^+ decay vertex) and one, or three, directly produced in the secondary vertex. Due to the solenoidal magnetic field, an helicoidal trajectory is associated to each

[1] In Tab. 4.2 are reported the Λ_c^+ exclusive decays contributing to this final state.

[2] It's worth to remember that every time we consider a Λ_b^0 decay mode also the conjugated channel $\overline{\Lambda}_b^0$ are included even if not explicity mentioned.

[3] Given $|p|$ and E as the energy of a particle we can define: $\beta = \frac{|p|c}{E}$ and $\gamma = \frac{1}{\sqrt{1-\beta^2}}$.

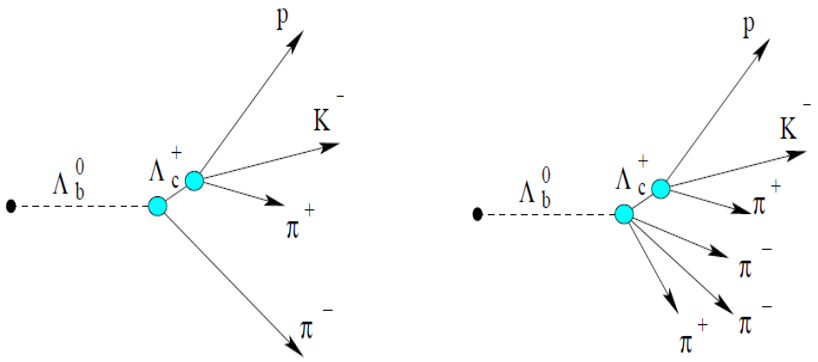

(a) (b)

Figure 3.1: $\Lambda_b^0 \to \Lambda_c^+ \pi^-$ **3.1(a)** *and* $\Lambda_b^0 \to \Lambda_c^+ \pi^- \pi^+ \pi^-$ **3.1(b)** *event topology.*

of four or six tracks (see Fig. 3.1) . Therefore, a minimum requirement on the distance between the beamline (*primary vertex*, see Sec. 2.3.4) and the secondary vertex reconstructed in the transverse plane (L_{xy}), reduces the contamination due to short lived charmed hadrons. Moreover, the particles produced in the b decays also have a larger impact parameter in the transverse plane (d_0) than the tracks produced in the primary vertex, but smaller than the decay products particles of K_s^0 and Λ. Consequentely, a minimum and a maximum cut on the track d_0 rejects the background from the primary tracks, K_s and Λ, or secondary tracks generated by the particle interaction with the material. The reconstruction of the two decay modes in Fig. 3.1 corresponds to identify and parametrize the p K^- π^+ tracks, decay products of Λ_c^+, and the π^- (see Fig. 3.1(a)) or π^- π^+ π^- (see Fig. 3.1(b)) tracks, decay products of Λ_b^0.
All the data used in this Thesis are selected by three special trigger paths[4] of the TTT described in Sec. 3.2.1. The term TTT is used within CDF to indicate triggers that require at least two charged tracks in the event with some further requirements able to extract fully hadronic decays of b-hadrons from a large background of tracks, just using the tracks reconstructed by SVT. Then, the data selected by these trigger paths are processed by a CDF standard package (`Production`) to extract data with more quality. The `Production` package uses the most recent and reliable information on the detector calibration that are not accessible during

[4]We call the combination of various trigger requests as path.

the online selection. In this way the reconstructed events are divided into different datasets according to the trigger requests. After the `Production` the total size of the datasets corresponds to about 42.8 TB and we apply a procedure of *skimming* to obtain smaller tertiary datasets. Sec. 3.3.1 describes the skimming procedure. Finally we optimize the analysis cuts using the tertiary datasets in Sec. 3.4.

3.2 Data Sample

This analysis uses 2.4 fb^{-1} of data collected by CDF II detector between February, 4^{th} 2002 and May, 13^{th} 2007. The datasets used have been selected by three different trigger paths of the TTT triggers designed for the the selection of multibody b-hadronic decays, `B_CHARM_LOWPT`, `B_CHARM_L1` and the `B_CHARM_HIGHPT` (see following Section and Tab. 3.2) and spans Run[5] numbers from 138425 to 241664. Only *good runs*, where all components of the detector relevant for this analysis are reliably working, are included. The information about the data quality is stored in the run database for each subsystem of the detector and for each run [86]. The set of these requirements is essential to guarantee that the data from various pieces of the detector are present, passed the minimun quality check, and actually can be used for the B Physics analysis. We used events collected in runs where the following systems were declared good by the CDF Data Quality Monitoring Group: SVX, COT, CLC and all the trigger levels. We excluded the runs when SVX was off and when there were high voltage problems in the COT. Moreover, requirements on the online and offline data quality were applied. Each dataset is organized in more secondary datasets, corresponding to different data periods during which the detector was operated under a stable configuration (since trigger settings, average instantaneous luminosity, system calibrations, etc. can change over time).

3.2.1 Trigger Requirements

To select multibody hadronic b-decays CDF uses three different TTT paths:

- `B_CHARM_LOWPT`;
- `B_CHARM_L1` (or `SCENARIO A`);
- `B_CHARM_HIGHPT` (`SCENARIO C`).

[5] A run is a period of continuous operation of the CDF II Data Acquisition. Many different cases can require the DAQ to be stopped and restarted including the need to enable or disable a sub-detector, a change in the trigger Table, a problem in the trigger/DAQ chain etc.

The requirements of each trigger path are summarized in Tab. 3.1, while the variables are described in the following.

Level-1 (L1) selection: requires a pair of XFT tracks, each with a minimum transverse momentum, p_T, above a given threshold; also the scalar sum of their transverse momentum $\sum p_T$ has to be greater then a given threshold. In addition, the azimuthal opening angle between them, as measured at the radial distance of the COT super-layer 6 $(\Delta\varphi_6)$[6], has to satisfy the requirements of Tab. 3.1.

Level-2 (L2) selection: using the two SVT reconstructed tracks (p_T, φ_0, d_0 in Tab. 3.1 and p_{T1}, p_{T2}, d_1, d_2, φ_1 and φ_2 in the following), computes the transverse decay length (L_{xy}) and the transverse impact parameter (d_{CV}) of the b candidate vertex with the following equations:

$$p_x = p_{T1}cos\varphi_1 + p_{T2}cos\varphi_2 \qquad p_y = p_{T1}sin\varphi_1 + p_{T2}sin\varphi_2 \tag{3.1}$$

so, the flight direction of the b candidate vertex is given by:

$$cos\varphi_V = \frac{p_x}{p_T} \qquad sin\varphi_V = \frac{p_y}{p_T} \tag{3.2}$$

where

$$p_T = \sqrt{p_x^2 + p_y^2} \tag{3.3}$$

and the coordinates of the b candidate vertex, with respect to the origin coordinates (0,0) in the $x-y$ plane, are:

$$x_V = \frac{d_1 cos\varphi_2 - d_2 cos\varphi_1}{cos\varphi_1 sin\varphi_2 - cos\varphi_2 sin\varphi_1} \qquad y_V = \frac{d_1 sin\varphi_2 - d_2 sin\varphi_1}{cos\varphi_1 sin\varphi_2 - cos\varphi_2 sin\varphi_1} \tag{3.4}$$

therefore

$$L_{xy} = \frac{x_V \cdot p_x + y_V \cdot p_y}{p_T} \qquad d_{CV} = x_V sin\varphi_V - y_V cos\varphi_V \tag{3.5}$$

Then, using the SVT reconstructed quantities at L2, the selection of Tab. 3.1 is applied.

Level-3 selection (L3): this trigger level performs the selection on tracks that are reconstructed using the offline algorithm (see Sec. 2.3.3) and with an associated track reconstruted by SVT. The matching is done in φ and curvature. The tolerances are respectively 15 mrad and $1.5 \times 10^{-4} cm^{-1}$.

[6] φ_6 is the azimuthal angle of the tracks measured at the COT superlayer 6. It is related to φ_0 by the relation: $\varphi_6 = \varphi_0 + sin^{-1}(r \cdot C)$, where $r = 105.575$ cm and C is the track's curvature.

The same cuts, as at L2, are performed on hybrid tracks. The cut on the impact parameter requires the knowledge of the exact beam position.
Within CDF the most accurate online measurement of the beam position, in each barrel, is provided by the SVT tracks. The L3, using the COT and SVX reconstructed tracks, calculates the impact parameter and the L_{xy}, using the reconstructed primary vertex position (see Sec. 2.3.4) in the transverse plane. L3 applies a fiducial geometric cut on the tracks pseudorapidity: $|\eta_{1,2}| \leq 1.2$.

	Level-1	**Level-2**	**Level-3**
	XFT tracks	SVT tracks	COT+SVXII tracks
B_CHARM_HIGHPT	opposite charge $p_T > 2.5\ GeV/c$ $\Delta\varphi_6 < 135°$ $\sum p_T > 6.5\ GeV/c$ $\chi^2_{SVT} < 25$	opposite charge $p_T > 2.5\ GeV/c$ $2° < \Delta\varphi_0 < 90°$ [a] $\sum p_T > 6.5\ GeV/c$ $120\ \mu m < \lvert d_0\rvert < 1\ mm$ $L_{xy} > 200\ \mu m$ $\chi^2_{SVT} < 25$	opposite charge $p_T > 2.5\ GeV/c$ $2° < \Delta\varphi_0 < 90°$ $\sum p_T > 6.5\ GeV/c$ $80\ \mu m < \lvert d_0\rvert < 1\ mm$ $L_{xy} > 200\ \mu m$ $\lvert\Delta z_0\rvert < 5\ cm$ $\lvert\eta\rvert < 1.2$ $\chi^2_{SVT} < 25$
B_CHARM_SCENA	opposite charge $p_T > 2.0\ GeV/c$ $\Delta\varphi_6 < 135°$ $\sum p_T > 5.5\ GeV/c$ $\chi^2_{SVT} < 25$	opposite charge $p_T > 2.0\ GeV/c$ $2° < \Delta\varphi_0 < 90°$ $\sum p_T > 5.5\ GeV/c$ $120\ \mu m < \lvert d_0\rvert < 1\ mm$ $L_{xy} > 200\ \mu m$ $\chi^2_{SVT} < 25$	opposite charge $p_T > 2.0\ GeV/c$ $2° < \Delta\varphi_0 < 90°$ $\sum p_T > 5.5\ GeV/c$ $120\ \mu m < \lvert d_0\rvert < 1\ mm$ $L_{xy} > 200\ \mu m$ $\lvert\Delta z_0\rvert < 5\ cm$ $\lvert\eta\rvert < 1.2$ $\chi^2_{SVT} < 25$
B_CHARM_LOWPT	$p_T > 2.0\ GeV/c$ $\Delta\varphi_6 < 90°$ $\sum p_T > 4\ GeV/c$ $\chi^2_{SVT} < 25$	$p_T > 2.0\ GeV/c$ $\Delta\varphi_0 < 90°$ $\sum p_T > 4\ GeV/c$ $120\ \mu m < \lvert d_0\rvert < 1\ mm$ $L_{xy} > 200\ \mu m$ $\chi^2_{SVT} < 25$	$p_T > 2.0\ GeV/c$ $2° < \Delta\varphi_0 < 90°$ $\sum p_T > 4\ GeV/c$ $120\ \mu m < \lvert d_0\rvert < 1\ mm$ $L_{xy} > 200\ \mu m$ $\lvert\Delta z_0\rvert < 5\ cm$ $\lvert\eta\rvert < 1.2$ $\chi^2_{SVT} < 25$

Table 3.1: *B_CHARM_LOWPT, B_CHARM_HIGHPT, B_CHARM_SCENA trigger paths requirements.*

[a] This cut in $\Delta\varphi$ is used to select b-hadron decays into more than two bodies. For decays into two bodies, the condition $\Delta\varphi > 20°$ is imposed because the opening angle of the tracks cannot be very narrow, due to the kinematics and the relatively high mass of the b-hadron. In the presence of more than two bodies instead, the $\Delta\varphi$ cut cannot exclude small angular separations between tracks.

3.2.2 Trigger Prescale

In addition to various physics requirements, the CDF Trigger system is able to randomly discard events at L1. This feature of the trigger is called *prescaling*. During a Tevatron store the luminosity decreases. In order to fully use the available bandwidth, the trigger criteria have to vary accordingly to the luminosity. Higher trigger rates at high luminosity arise from both an increase in the real physics rate as well as an increase in fake triggers due to multiple interactions.
As the luminosity decreases, the trigger bandwidth becomes under-utilized and lower purity triggers are thus enabled through a system that is used to automatically increase their prescale level and to prioritize the various triggers paths.
The basic idea is that events are randomly discarded at high luminosity in order to control high accept rate. For example, a trigger prescaled with a factor N only passes every N^{th} event which satisfies that physics trigger's requirements. Originally, a *dynamic prescale* system was used which modified the prescale value depending on the current luminosity. The *dynamic prescale* system was replaced with a *floating prescale* system, where the value N is taken out of every 256 events that would pass the appropriate trigger. Currently CDF uses a sophisticated prescale scheme which allows to fully populate the trigger bandwidth at any given time. It sends an event passed L1 whenever empty L2 buffers are avaliable (there are four L2 buffers total). Only a *dynamic* and *floating prescale* schemes apply to the dataset used in this analysis. The three trigger path used for the selection of hadronic multibody b-decays are designed to exploit at the best the available bandwidth.

`B_CHARM_LOWPT`: this sequence was designed to maintain a high rate of selected events when the store has a low luminosity. The trigger path is variously prescaled during the store and activated only below a certain luminosity threshold (this is called a lumienable trigger-path).

`B_CHARM_L1` or `SCENARIO A`: this is the trigger-path which collected more data due to the trigger selection cuts which allow us to acquire a significant rate of events at low instantaneous luminosity while maintaining trigger rates at a sustainable level at moderate high values of the luminosity.

`B_CHARM_HIGHPT` or `SCENARIO C`: initially, this trigger was conceived as a not prescaled trigger with tighter condition on the selections rules in order to allow the acquisition of B Physics data at high luminosity. Currently, the rate conditions at high luminosity are very severe and `B_CHARM_HIGHPT` has a dynamic prescale as well. This trigger-path is mainly characterized by more selective requirements on p_T and $\sum p_T$.

3.3 Offline Selection

The events accepted by the trigger described and stored to tape are not optimal for physics analysis because the up-to-date calibrations of the detectors are usually not available for online event reconstruction. CDF uses a standard software package called `Production` for final quality reconstruction of the data. The `Production` gives the highest precision measurement of physical quantities (based on the best available detector calibrations, beam-line position measurements and so on) and separates the data into different datasets corresponding to different data taking periods (see Tab. 3.3). The total size of the datasets collected the three TTT path is 42.8 TB, which is too big to be analized quickly multiple times. We apply loose selection cuts to reduce them to two smaller tertiary datasets. Sec. 3.3.1 discusses the data skimming while Sec. 3.3.2 describe the offline events selection and recontruction applied by the skimming procedure. Then we optimize the analysis cuts using the tertiary datasets in Sec. 3.4.

3.3.1 Data Skimming

The skimming procedure produces smaller datasets applying loose selection cuts, aiming to futher reject the background events and to select the physical events we will use in this analisys ($\Lambda_b^0 \to \Lambda_c^+\pi^-\pi^+\pi^-$ and $\Lambda_b^0 \to \Lambda_c^+\pi^-$).
In this work of Thesis is used the `xbhd` production dataset (see Tab. 3.2 [87]) collected by the TTT, and designed for the selection of multibody hadronic decays of b-hadrons. The above period, amounts to 42.8 TB and includes $\approx 950 \times 10^6$ events in 74287 files[7].

SAM Dataset	Run Range	Data Taking Period	$\int \mathcal{L}dt\ [pb^{-1}]$	Size (TB)
`xbhd0d`	138425 – 186598	02/04/2002 – 08/22/2004	550	13
`xbhd0h`	190697 – 203799	12/07/2004 – 09/04/2005	445	9
`xbhd0i`	203819 – 233111	09/05/2005 – 01/31/2007	965	13
`xbhd0j`	233133 – 241664	01/31/2007 – 05/13/2007	450	3
		Total	2,410	38

Table 3.2: *Production output datasets used as input for skimming.*

The procedure work with the CDF Data Handling Model and the Λ_b^0 candidates reconstruction by skimming is described in the next Section. The output of the skimming is directed into two streams, one for each decay sequence and the result

[7]According to Data Volume Summary http://cdfsam-prd.fnal.gov/sam/datavolume/summary.html.

of processing is saved in SAM datasets `lblc3p` (for the $\Lambda_b^0 \to \Lambda_c^+\pi^-\pi^+\pi^-$) and `lblc1p` (for the $\Lambda_b^0 \to \Lambda_c^+\pi^-$) reducing the overall output data from 42.8 TB to 370 GB, a reduction factor of more than 100 (see Tab. 3.3).

Decay	SAM Dataset	Size (GB)	File Count	Number of Events
$\Lambda_b^0 \to \Lambda_c^+\pi^-$	`lblc1p`	66.65	56	1,216,375
$\Lambda_b^0 \to \Lambda_c^+\pi^-\pi^+\pi^-$	`lblc3p`	301.57	229	5,694,537

Table 3.3: *Output datasets from skimming and their relative sizes.*

3.3.2 Events Selection and Reconstruction

The skimming program uses a set of offline reconstructed tracks which satisfy the quality requirements (see Tab. 3.4) on the number of COT hits in the axial and stereo layers, the number of SVX $r-\varphi$ hits, the impact parameter, and the p_T. In the offline track reconstruction the used detectors are SVXII, ISL, and COT. The L00 was not used because the tracking resolution enhancement, for the used quantity, was negligible, while its use introduces some complications in the analysis, since it was not correctly simulated by the CDF MC. Each track is also required to go through all COT superlayers, exiting the COT volume at a radius, R_{COT}, of at least 140 cm. As it is shown in the flow diagram of Fig. 3.2, four (see Fig. 3.1(a)) or six (see Fig. 3.1(b)) nested tracks, satisfying the requirements of Tab. 3.4, are used in a loop to reconstruct the $\Lambda_b^0 \to \Lambda_c^+\pi^-$ or $\Lambda_b^0 \to \Lambda_c^+\pi^-\pi^+\pi^-$ candidates.

COT stereo hits ≥ 20
COT axial hits ≥ 20
SVX $r-\varphi$ hits in different layers ≥ 3
$\mid d_0 \mid < 0.2$ cm
$p_T > 400$ MeV/c
$R_{COT} \geq 140$ cm (COT exit radius)

Table 3.4: *Tracks selection criteria.*

Once each event is tested for the presence of both decays, the selected events are written to one of two output streams (one output stream per decay channel) and if the same event satisfies both selection criteria the event can be saved twice, once in each stream. The procedure used to reconstruct the $\Lambda_b^0 \to \Lambda_c^+\pi^-\pi^+\pi^-$ ($\Lambda_b^0 \to \Lambda_c^+\pi^-$) candidates, with $\Lambda_c^+ \to pK^-\pi^+$ is described in the following as well as in [87], and can be summarized in two steps:

- in the first step we reconstruct the $\Lambda_c^+ \to pK^-\pi^+$;
- in the second step we reconstruct the Λ_b^0 vertex by adding to the Λ_c^+ candidate one or three tracks, depending on the final state, which are assigned the pion mass.

To reject the background further requirements, described in the next two sections, are applied on the Λ_c^+ and Λ_b^0 candidates.

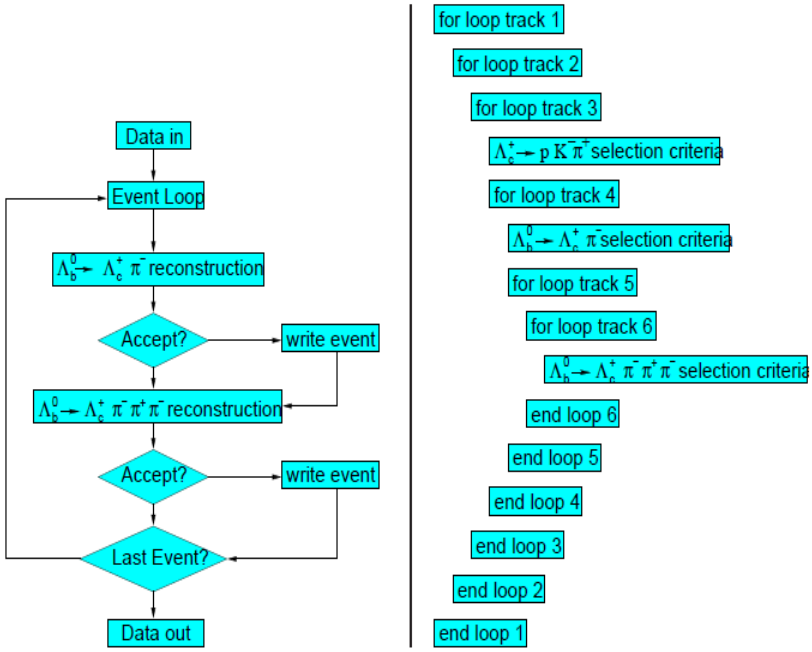

Figure 3.2: *Block diagram of the skimming code (left) and a schematic of the Λ_b^0 reconstruction (right).*

Λ_c^+ Reconstruction

The selection module loops over three tracks, assumed to be kaon, proton and pion to build Λ_c^+ candidates. The sum of the three charges has to be either -1 or 1. We require at least one of three tracks to have a matching SVT track[8]. We assign the proton and pion masses to the same-sign charged tracks and the kaon mass to the other track. The proton mass is assigned to the track with higher p_T. We also

[8] An offline track is matched with an SVT track if the difference in φ_6 (measured at superlayer 6) is less than 0.015 radians and the difference in $1/p_T$ is less than 0.08.

require the difference between the z_0 (see Sec. 2.2.1) [88] of each combination of track pairs, Δz_0, to be less than a given threshold. Thus selected, the three tracks were fit for the common vertex (tertiary vertex of Fig. 3.1) using the standard CDF Vertex Fit [88].
The fit determines the decay vertex by varying the track parameters of the decay products within their uncertainties, so that a χ^2 between the original track trajectories parameters and these determined by the fit is minimized. If the fit was successful, additional requirements on the invariant mass ($m_{pK^-\pi^+}$), vertex fit probability, decay length (L_{xy}) and p_T of the Λ_c^+ candidate were applied. Details of the Λ_b^0 candidates selection requirements are given in Tab. 3.5.

Λ_c^+ cuts	
$q_1 + q_2 + q_3$	$+1$
Δz_0	< 5 cm
$p_T(p)$	$> p_T(\pi^+)$
SVT match	1 (p or K^- or π^+)
$m(pK\pi)$	2.240-2.330 GeV/c^2
$p_T(\Lambda_c^+)$	> 4.0 GeV/c
$L_{xy}(\Lambda_c^+)$	$> 200\ \mu m$
$Prob(\chi^2(\Lambda_c^+))$	> 0.0001
L_{xy}	$> 200\ \mu m$
Λ_b^0 cuts	
$p_T(\Lambda_b^0)$	> 6.0 GeV/c
$L_{xy}(\Lambda_b^0)$	$> 200\ \mu m$
$L_{xy}(\Lambda_c^+ from \Lambda_b^0)$	$> -200\ \mu m$
$Prob(\chi^2(\Lambda_b^0))$	> 0.0001

Table 3.5: *$\Lambda_c^+ \to pK^-\pi^+$ and $\Lambda_b^0 \to \Lambda_c^+\pi^-\pi^+\pi^-$ candidates selection criteria.*

Λ_b^0 Reconstruction

If the above criteria are satisfied, the program enters a forth track loop and the flow is different for the two decay channels:

- for the $\Lambda_b^0 \to \Lambda_c^+\pi^-$ decay mode we proceed to a secondary vertex fit (Λ_b^0 decay vertex of Fig. 3.1(a));
- for the $\Lambda_b^0 \to \Lambda_c^+\pi^-\pi^+\pi^-$ channel we add two more tracks, one of each charge sign and then we proceed to the secondary vertex fit (Λ_b^0 decay vertex of Fig. 3.1(b)).

The additional track, or one of the three additional tracks, is required to have a matching SVT track. Then we expect that two SVT associated tracks, one originating from the Λ_b^0 vertex and the other originating from the Λ_c^+ vertex, satisfy the `B_CHARM_LOWPT` trigger described in Sec. 3.2.1 and Sec. 3.2.2. We call this requirement the offline trigger selection confirmation for the skimming. The other two trigger path used to select the data sample, have in fact more stringent requirements then this one, but the triggers with less stringent requirements can be prescaled. Offline we expect that events triggered by anyone of these three trigger path, satisfy offline the `B_CHARM_LOWPT` trigger requirements. Finally, a kinematic fit is performed for four (six) tracks: we constrain the tertiary vertex to point to the pion track from the $\Lambda_b^0 \to \Lambda_c^+\pi^-$ decay or to the three-pion vertex from the $\Lambda_b^0 \to \Lambda_c^+\pi^-\pi^+\pi^-$ decay[9]. We require the fit to converge and cut on the p_T and on L_{xy} of the Λ_c^+ with respect to the Λ_b^0 vertex in the $x-y$ plane and also on the χ^2 probability of the Λ_b^0 reconstructed vertex.
The requirements on the Λ_b^0 candidate are summarized in Tab. 3.5.

The invariant mass of the reconstructed candidates $\Lambda_c^+\pi^-\pi^+\pi^-$ and $\Lambda_c^+\pi^-$, after the skimming procedure is reported respectively in Fig. 3.3(a) and Fig. 3.3(b). As we can notice, looking at Fig. 3.3(a), the $\Lambda_b^0 \to \Lambda_c^+\pi^-\pi^+\pi^-$ decay mode is not visible, due to the huge combinatorial background, while the signal of $\Lambda_b^0 \to \Lambda_c^+\pi^-$ is clearly visible (see Fig. 3.3(b)). To demonstrate a signal in the $\Lambda_c^+\pi^-\pi^+\pi^-$ invariant mass spectrum, we make additional requirements on the candidates to reduce the large amount of background. We require the Λ_b^0 p_T greater than 8 GeV/c, a significance of the Λ_b^0 transverse decay length[10], defined as $L_{xy}(\Lambda_b^0)/\sigma(L_{xy}(\Lambda_b^0))$, greather than 16 and, for the case of six tracks, that the three-pions from the Λ_b^0 vertex fall in a cone of $\Delta R = \sqrt{\Delta\eta^2 + \Delta\varphi^2} < 1$[11]. The resulting invariant mass distribution is shown in Fig. 3.3(c) and Fig. 3.3(d) respectively for $\Lambda_b^0 \to \Lambda_c^+\pi^-\pi^+\pi^-$ and $\Lambda_b^0 \to \Lambda_c^+\pi^-$ candidates.

3.4 Optimization of the $\Lambda_b^0 \to \Lambda_c^+\pi^-\pi^+\pi^-$selection

To optimize the selection used to demostrate the signal in the $\Lambda_c^+\pi^-\pi^+\pi^-$ spectrum, we maximized the significance $S/\sqrt{S+B}$ of the signal on the data events (S is the estimated number of Λ_b^0 signal events and B is the estimated number of background events in the signal region) by varying the cuts on the most

[9]The skimming code required the final π^+ to have a track index greater than the π^+ forming the Λ_c^+ so, because tracks are ordered in p_T; the skimming code effectively requires the p_T of the π^+ from the Λ_b^0 candidate to be less than the p_T of the Λ_c^+ candidate.

[10]This variable allows us to understand how significant the Λ_b^0 decay length is with respect to the detector resolution.

[11]High momentum of the Λ_b^0 translate in a narrower cone of the decay products.

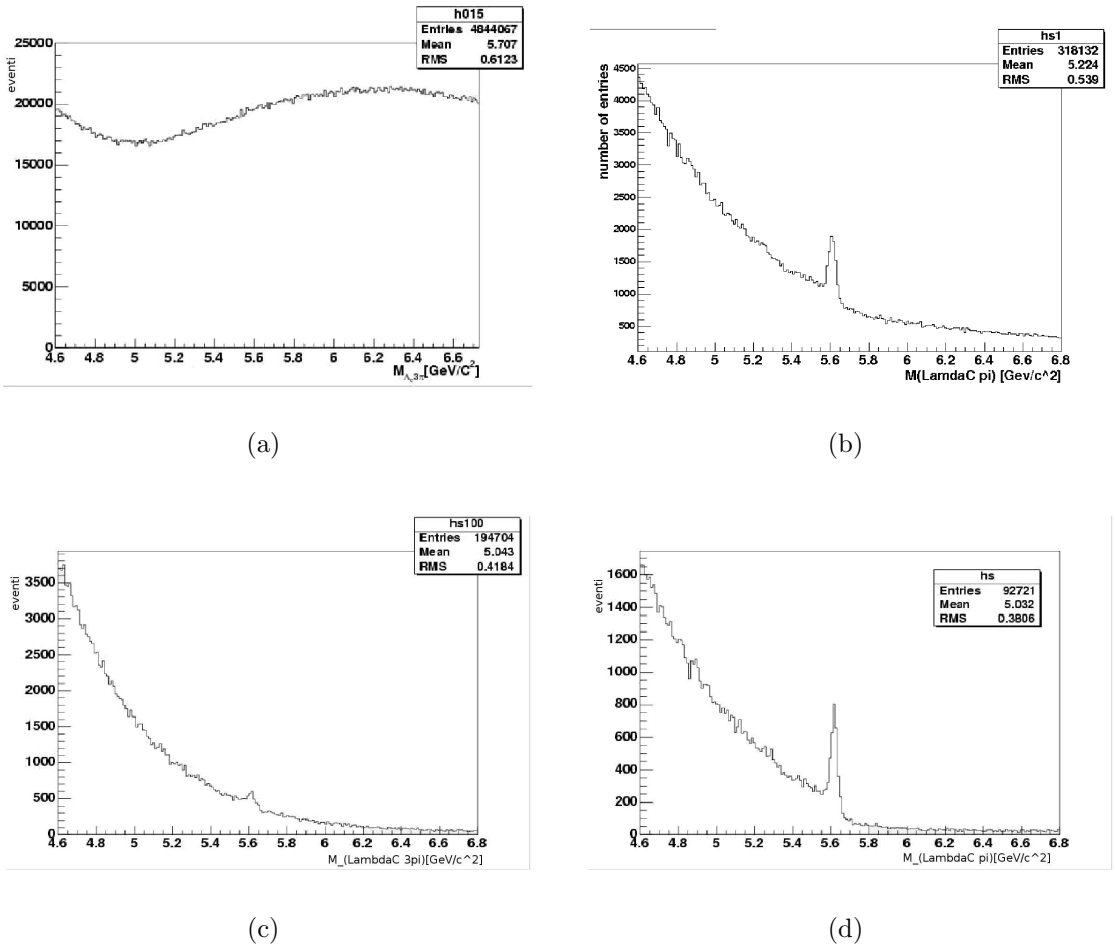

(a) (b)

(c) (d)

Figure 3.3: $\Lambda_c^+\pi^-\pi^+\pi^-$ **3.3(a)** *and* $\Lambda_c^+\pi^-$ **3.3(b)** *candidates invariant mass after the skimming.* $\Lambda_c^+\pi^-\pi^+\pi^-$ **3.3(c)** *and* $\Lambda_c^+\pi^-$ **3.3(d)** *candidates invariant mass after the skimming and the optimized cuts.*

significant kinematic quantities and looking for the cut configuration providing the maximum value of $S/\sqrt{S+B}$. A scan of the following variables has been done to perform the cuts optimization:

- Λ_b^0 transverse momentum: $p_T(\Lambda_b^0) >$ 7, 8, 9, 10 GeV/c;
- Λ_b^0 transverse decay length: $L_{xy}(\Lambda_b^0) >$ 200, 300, 400, 500 μm;
- Significance of the Λ_b^0 transverse decay length: $L_{xy}(\Lambda_b^0)/\sigma(L_{xy}(\Lambda_b^0)) > 10, 13, 15, 16, 18, 20$;
- Λ_b^0 impact parameter: $\mid d_0(\Lambda_b^0) \mid <$ 90, 80, 70, 60 μm;

- Maximum distance (ΔR) among the three pions produced in association to the Λ_c^+, in the $\eta - \varphi$ space: $\Delta R < 1.8, 1.6, 1.4, 1.2, 0.8$.

For each point of this five-dimensional space, corresponding to each possible choice of the cuts on the five variables, we determined the signal yield S and the background yield B, by performing a fit of the $\Lambda_c^+\pi^-\pi^+\pi^-$ candidate mass distribution using a Gaussian distribution to model the signal, and an exponential for the background. Using the Gaussian mean and sigma (σ) as determined by the fit, the signal and background are respectively given by the integral of the Gaussian and the exponential within $\pm 3\sigma$ from the Λ_b^0 mass (the mean of the Gaussian).

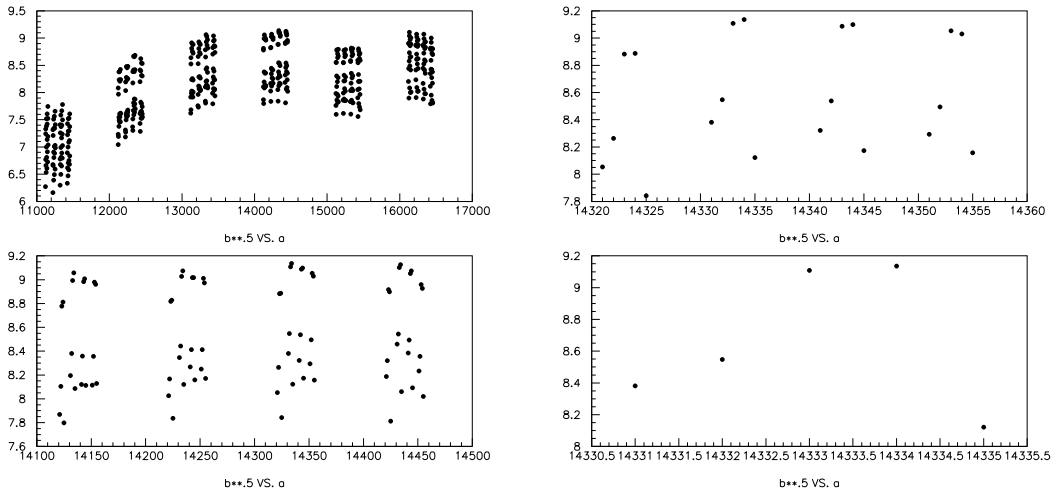

Figure 3.4: *Significance ($S/\sqrt{S+B}$) achieved in all the cut configurations scanned by the cut optimisation procedure.* **Top left plot:** *we have fixed $L_{xy}(\Lambda_b^0) > 200$ μm, the six big structures correspond to the six thresholds on the $L_{xy}(\Lambda_b^0)$ significance (10, 13, 15, 16, 18, 20);* **Bottom left plot:** *we have fixed $L_{xy}(\Lambda_b^0) > 200$ μm and $L_{xy}(\Lambda_b^0)/\sigma(L_{xy}(\Lambda_b^0)) > 16$ the four big structures correspond to four cuts on $p_T(\Lambda_b^0)$ (7 GeV/c, 8 GeV/c, 9 GeV/c, 10 GeV/c);* **Top right plot:** *we have fixed $L_{xy}(\Lambda_b^0) >$ 200 μm, $L_{xy}(\Lambda_b^0)/\sigma(L_{xy}(\Lambda_b^0)) > 16$ and $p_T(\Lambda_b^0) > 9$ GeV/c, the four structures correspond to four cuts on $\mid d(\Lambda_b^0) \mid$ (60 μm, 70 μm, 80 μm, 90 μm);* **Bottom right plot:** *we have fixed $L_{xy}(\Lambda_b^0) > 200$ μm, $L_{xy}(\Lambda_b^0)/\sigma(L_{xy}(\Lambda_b^0)) > 16$, $p_T(\Lambda_b^0) > 9$ GeV/c and $\mid d(\Lambda_b^0) \mid < 70$ μm, the five points correspond to different cuts on $\Delta R(3\pi)$ (1.8, 1.6, 1.4, 1.2, 0.8).*

In Fig. 3.4 is reported the Significance ($S/\sqrt{S+B}$) achieved scanning all the cut configurations.
The list of the optmised cuts is reported in Tab. 3.6, while in Fig. 3.5 is reported the mass difference distribution, ΔM^{--+}, defined as the difference between the

$p_t(\Lambda_b^0)$	> 9.0 GeV/c
$L_{xy}(\Lambda_b^0)/\sigma(L_{xy}(\Lambda_b^0))$	> 16
$L_{xy}(\Lambda_b^0)$	$> 200\ \mu m$
$\mid d_0(\Lambda_b^0) \mid$	$< 70\ \mu m$
$\Delta R(3\pi)$	< 1.2

Table 3.6: *Optimised cuts used to select the* $\Lambda_b^0 \to \Lambda_c^+\pi^-\pi^+\pi^-$ *decay mode.*

invariant mass of the reconstructed Λ_b^0 and Λ_c^+ from Λ_b^0 candidates: $\Delta M^{--+} = M(\Lambda_c^+\pi^-\pi^-\pi^+) - M(\Lambda_c^+)$. The use of this variable against the $\Lambda_c^+\pi^-\pi^-\pi^+$ candidate invariant mass will be explained in Chap. 5.

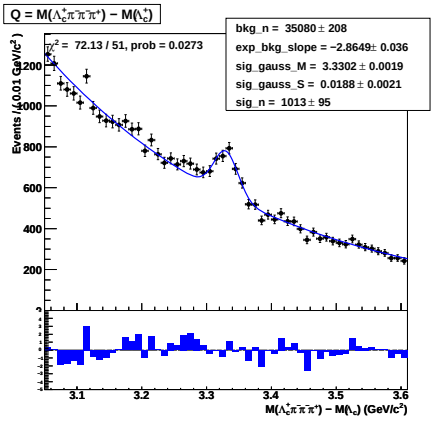

Figure 3.5: ΔM^{--+} *distribution after apply the offline selection and the optimized cuts. The distribution is modeled using as PDF the sum of an exponential (background) and a Gaussian (signal) functions.The best fit (blue curve) is overlaid to the experimental data (black points).*

Chapter 4

MC Samples of Λ_b^0 Decays with charmed resonances in $\Lambda_c^+\pi^-\pi^+\pi^-$ final states

In this Chapter motivations and tools for search charmed resonances in Λ_b^0 decays in $\Lambda_c^+\pi^-\pi^+\pi^-$ final states, with $\Lambda_c^+ \to pK^-\pi^+$, are given. MC samples of these and of others decays, expected to contribute to the experimental $\Lambda_c^+\pi^-\pi^+\pi^-$ observed signal, are described and then used to determine an offline selection that will be applied on real data to extract, with high efficiency, the contributes of each of the charmed resonant decay mode.

4.1 Introduction

Previous analysis of the backgrounds for the decay $\Lambda_b^0 \to \Lambda_c^+\ell\overline{\nu}_\ell$ found charmed resonances [7] in the final state $\Lambda_b^0 \to \Lambda_c^+\pi^+\pi^-\ell\overline{\nu}_\ell$. These decay modes were reconstructed as:

$$\begin{aligned}
\Lambda_b^0 &\to \Lambda_c^*(2595)^+\ell\overline{\nu}_\ell \\
&\hookrightarrow \Lambda_c^+\pi^+\pi^- \\
\Lambda_b^0 &\to \Lambda_c^*(2625)^+\ell\overline{\nu}_\ell \\
&\hookrightarrow \Lambda_c^+\pi^+\pi^- \\
\Lambda_b^0 &\to \Sigma_c^{++}\pi^-\ell\overline{\nu}_\ell \\
&\hookrightarrow \Lambda_c^+\pi^+ \\
\Lambda_b^0 &\to \Sigma_c^0\pi^+\ell^-\overline{\nu_\ell} \\
&\hookrightarrow \Lambda_c^+\pi^-
\end{aligned}$$

where the Λ_c^+ decays in $pK^-\pi^+$ and the lepton ℓ is a muon. This observation lead us to speculate that similar decay modes might be observed in the hadronic $\Lambda_b^0 \to \Lambda_c^+\pi^+\pi^-\pi^-$ final state, contributing to the observed signal peak of Fig. 3.5.

Chapter 4. MC Samples of Λ_b^0 Decays with charmed resonances in $\Lambda_c^+\pi^-\pi^+\pi^-$ final states

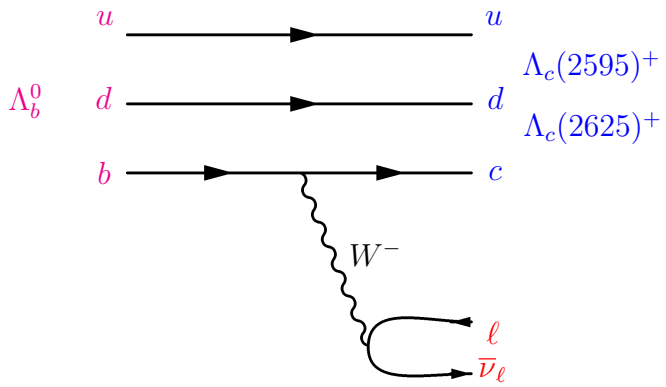

Figure 4.1: *First order Feynman diagrams of the semileptonic decays* $\Lambda_b^0 \to \Lambda_c^+(2595)^+\ell\overline{\nu}_\ell$ *and* $\Lambda_b^0 \to \Lambda_c^+(2625)^+\ell\overline{\nu}_\ell$. *For these semileptonic decays, at the first order, only the spectator model diagram is allowed.*

The semileptonic decays $\Lambda_b^0 \to \Lambda_c(2595)^+\ell\overline{\nu}_\ell$ and $\Lambda_b^0 \to \Lambda_c(2625)^+\ell\overline{\nu}_\ell$ at first order are described by the Feynman diagram in Fig. 4.1 while for the hadronic decays $\Lambda_b^0 \to \Lambda_c(2595)^+\pi^-$ and $\Lambda_b^0 \to \Lambda_c(2625)^+\pi^-$ at the first order two diagrams contribute and are reported respectively in Fig. 4.2**(a)** (the W *exchange* model diagram), and in Fig. 4.2**(b)** (the *spectator exchange* model).

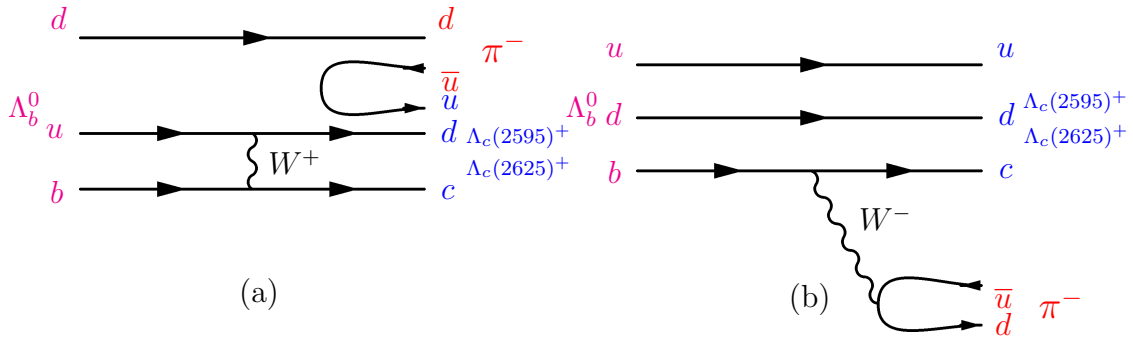

Figure 4.2: *First order Feynman diagrams contributing to the hadronic decays* $\Lambda_b^0 \to \Lambda_c(2595)^+\pi^-$ *and* $\Lambda_b^0 \to \Lambda_c(2625)^+\pi^-$. *In the* **4.2(a)** *we have a Weak Exchange Feynman diagrams while in the* **4.2(b)** *the Spectator Model.*

In the latter the $\ell\overline{\nu}_\ell$, emitted in the W^- decay (see Fig. 4.1), is replaced by a $\overline{u}d$ pair. So, if the leptonic decay of Fig. 4.1 exists and it is observable also

the corresponding hadronic decay might, in principle, exists and be observable, if the interference between the two diagrams of Fig. 4.2 is not destructive. Having observed a signal of Λ_b^0 into $\Lambda_c^+\pi^+\pi^-\pi^-$ final state, with Λ_c^+ into $pK^-\pi^+$, we want investigate the Λ_b^0 decay modes reported in Tab. 4.1, since, in principle, each of them might contribute to the signal observed. The properties of these decays are studied using simulated samples, that are then processed like real data. The MC samples are described in Sec. 4.2. These samples are then used to establish offline requirements able to separate and determine the individual contributions, of the charmed resonant decay modes and of the others, to the observed signal of Λ_b^0 in $\Lambda_c^+\pi^+\pi^-\pi^-$ final state.

4.2 MC Simulated Samples

MC simulations are an essential tool for data analysis and represent a fast and tuned interface between the predicted model and the collected data, allowing a better understanding of the data.
To generate a particle decay sample in the CDF MC there are three different steps: the first step is the particle generation, then the particle is forced to decay in a particular final state, and finally the decay products are propagated within the CDF detector.
The particle generation was simulated using `BGenerator` [89] algorithm, a MC program based on Next-to-Leading Order (NLO) calculations. In this step the algorithm uses, as input information, the joint distribution of the transverse momentum and of the pseudo-rapidity (η) for the different b-hadrons. Single Λ_b^0 are generated using a p_T vs η spectrum modified to match the p_T spectrum observed in fully reconstructed $\Lambda_b^0 \to \Lambda_c^+\pi^-$ decays [90]. Since we use a particle spectrum rather than the quark spectrum as input to `BGenerator`, fragmentation is turned off. A p_T threshold of 7 GeV/c and $|\ \eta\ | < 1.3$ are used at generation, and this assumption is standard in the CDF simulation and is valid for the detector range covered by the tracking system. The meson decays rely on `EvtGen` [91], a decayer tool extensively tuned by the *B Factory* experiments. Then the geometry and the behavior of active volumes of the CDF II detector are simulated using a dedicated software based on the third version of GEANT [82] package.
GEANT is a wide spread program able to simulate the response of High Energy Physics detectors at hit level. Finally, the trigger effects are simulated by `TRGSim++`, a software that implements the details of the trigger logic used by CDF II. The `TRGSim++` appends to each simulated event trigger banks and trigger bits as for data.
A particular trigger path is selected by requiring the corresponding trigger bit. MC samples are used through this Thesis in several applications; in this chapter

are used to study the kinematic features of the decay modes contributing to the observed signal, that can be exploited to separate them. MC reconstruction of Λ_b^0 decays is performed in the same way as for real data.

$$
\begin{aligned}
\Lambda_b^0 &\to \Lambda_c^+\pi^+\pi^-\pi^- \\
&\to \Lambda_c^*(2595)^+\pi^- \\
&\quad \hookrightarrow \Lambda_c^+\pi^+\pi^- \\
&\to \Lambda_c^*(2625)^+\pi^- \\
&\quad \hookrightarrow \Lambda_c^+\pi^+\pi^- \\
&\to \Sigma_c^{++}\pi^-\pi^- \\
&\quad \hookrightarrow \Lambda_c^+\pi^+ \\
&\to \Sigma_c^0\pi^-\pi^+ \\
&\quad \hookrightarrow \Lambda_c^+\pi^- \\
&\to \Lambda_c^+\rho^0\pi^- \\
&\quad \hookrightarrow \pi^+\pi^- \\
&\to \Lambda_c^+\pi^+\pi^-\pi^-(nr)
\end{aligned}
$$

Table 4.1: *Decay modes of Λ_b^0 into $\Lambda_c^+\pi^-\pi^+\pi^-$ final state, with Λ_c^+ into $pK^-\pi^+$.*

We performed a MC simulation of the six Λ_b^0 decay modes of Tab. 4.1 all reconstructed in the $\Lambda_c^+\pi^-\pi^+\pi^-$ final state, generating for each decay mode the same number of events ($\approx 7.5 \times 10^6$ events).
We forced each generated Λ_b^0 to decay through a single and specified decay chain using the `EvtGen` decay package, and a user defined decay table, and in particular Λ_c^+ are forced to decay to the $pK^-\pi^+$ final state including the resonance structure as measured by Aitala, et al. [92].

Decay Mode	Branching Ratio %
$\Lambda_c^+ \to p\overline{K}^*(892)^0$	1.6 ± 0.5
$\Lambda_c^+ \to \Delta(1232)^{++}K^-$	0.86 ± 0.3
$\Lambda_c^+ \to \Lambda(1520)\pi^+$	1.8 ± 0.6
$\Lambda_c^+ \to pK^-\pi^+$ (non resonant)	2.8 ± 0.8

Table 4.2: *List of $\Lambda_c^+ \to pK^-\pi^+$ resonant and direct decay modes and measured BRs in percent [1]. The total branching ratio of $\Lambda_c^+ \to pK^-\pi^+$ is $(5.0 \pm 1.3)\%$.*

The decay modes contributing to Λ_c^+ into $pK^-\pi^+$ final state and their measured BRs are reported in Tab. 4.2 [1]. In the simulation the central values of these measurements are assumed. In Tab. 4.3 is reported the list of decay modes and

BRs of the $\Lambda_c(2595)^+$, $\Lambda_c(2625)^+$, $\Sigma_c(2455)^{++}$ and $\Sigma_c(2455)^0$ assumed in the simulation and corresponding to their central values in the PDG [1]. Most of the decays in this Table have a decay with a Λ_c^+ in the final state, the $\Sigma_c(2455)^{++}$ and $\Sigma_c(2455)^0$ decay respectively to $\Lambda_c^+\pi^+$ and to $\Lambda_c^+\pi^-$ with a BR of 100%, while the $\Lambda_c(2595)^+$ and $\Lambda_c(2625)^+$ decay (directly or indirectly) to $\Lambda_c^+\pi^+\pi^-$ with a BR of 66%. Also a phase space model is used for all baryon decays. CDF software version 6.1.4mc was used to generate the Λ_b^0 decays and to perform full detector and trigger emulation.
There is a known difference between the p_T spectrum of the B-mesons ($p_T(B^0)$) and of the Λ_b^0 ($p_T(\Lambda_b^0)$) produced at a hadron collider (see Fig. 1.2).
To generate our MC sample we followed the prescription based on $360\,\mathrm{pb}^{-1}$ of data [90] and performed a detailed comparison between real data and MC for several kinematic quantities to check that the $p_T(\Lambda_b^0)$ distribution determined in [90] was still valid using a data sample of $2.4\,\mathrm{fb}^{-1}$. For this study we used our second skimmed dataset [87], the reconstructed $\Lambda_b^0 \to \Lambda_c^+\pi^-$ candidates, since it has a larger statistics and a larger signal to background ratio than the one of the $\Lambda_b^0 \to \Lambda_c^+\pi^-\pi^+\pi^-$. The details of this study are reported in Appendix A.

Decay modes	Branching Ratio %
$\Lambda_c(2595)^+$	
$\Lambda_c(2595)^+ \to \Sigma_c(2455)^{++}\pi^-$	24 %
$\Lambda_c(2595)^+ \to \Sigma_c(2455)^0\pi^+$	24 %
$\Lambda_c(2595)^+ \to \Sigma_c(2455)^+\pi^0$	24 %
$\Lambda_c(2595)^+ \to \Lambda_c^+\pi^+\pi^-$	18 %
$\Lambda_c(2595)^+ \to \Lambda_c^+\pi^0\pi^0$	9 %
$\Lambda_c(2595)^+ \to \Lambda_c^+\gamma$	1 %
$\Lambda_c(2625)^+$	
$\Lambda_c(2625)^+ \to \Lambda_c^+\pi^+\pi^-$	66 %
$\Lambda_c(2625)^+ \to \Lambda_c^+\pi^0\pi^0$	33 %
$\Lambda_c(2625)^+ \to \Lambda_c^+\gamma$	1 %
$\Sigma_c(2455)^{++}$	
$\Sigma_c(2455)^{++} \to \Lambda_c^+\pi^+$	100 %
$\Sigma_c(2455)^0$	
$\Sigma_c(2455)^0 \to \Lambda_c^+\pi^-$	100 %

Table 4.3: *Decay modes of the $\Lambda_c(2595)^+$, $\Lambda_c(2625)^+$, $\Sigma_c(2455)^{++}$, $\Sigma_c(2455)^0$ and the BRs assumed in the simulation corresponding to their central value in the PDG [1].*

4.3 Identification of Charmed Resonant Decay Modes in $\Lambda_c^+\pi^-\pi^+\pi^-$ final state

The decays of Tab. 4.1 and the others decays are expected to contribute to the experimental $\Lambda_c^+\pi^-\pi^+\pi^-$ signal observed in Chap. 3. Kinematic properties of simulated samples of these decays can be exploited to determine an offline selection that will be applied on real data to identify, with high efficiency, the contributes of each charmed resonant decay mode. To this aim, the MC samples of Tab. 4.1 are used. Then, the charmed resonances candidates are reconstructed: the $\Lambda_c^+\pi^-\pi^+$ from Λ_b^0 candidates are used to form Λ_c^+ resonance candidates ($\Lambda_c(2595)^+$ and $\Lambda_c(2625)^+$), while for $\Sigma_c(2455)^{++}$ ($\Sigma_c(2455)^0$) is used $\Lambda_c^+\pi^+$ ($\Lambda_c^+\pi^-$). In this study the two SVT associated tracks, one SVT track originating from the Λ_b^0 vertex and the other originating from the Λ_c^+ vertex, have to satisfy `B_CHARM_LOWPT` trigger requirements (see Sec. 3.2.1) the offline requirements (see Sec. 3.3) as well the optimized cuts (see Sec. 3.4). In the reconstructed $\Lambda_b^0 \to \Lambda_c^+\pi^-\pi^+\pi^-$ sample we searched for the following charmed resonant decay modes: $\Lambda_b^0 \to \Lambda_c(2595)^+\pi^-$, $\Lambda_b^0 \to \Lambda_c(2625)^+\pi^-$, $\Lambda_b^0 \to \Sigma_c(2455)^{++}\pi^-\pi^-$, and $\Lambda_b^0 \to \Sigma_c(2455)^0\pi^+\pi^-$. The available energy transferred to the decay products in the charmed baryons decays ($\Lambda_c(2595)^+$, $\Lambda_c(2625)^+$, $\Sigma_c(2455)^{++}$, and $\Sigma_c(2455)^0$) into Λ_c^+ is small. Therefore the mass differences $M(\Lambda_c^+\pi^+\pi^-) - M(\Lambda_c^+)$, $M(\Lambda_c^+\pi^+) - M(\Lambda_c^+)$, and $M(\Lambda_c^+\pi^-) - M(\Lambda_c^+)$ are determined with better resolution than the masses of the charmed baryons, since the mass resolution of the Λ_c^+ signal and most of the mass systematic uncertainties cancel in the mass difference spectrum. For this reason the variables chosen to discriminate the resonant charmed decay modes of Λ_b^0 are the difference between the reconstructed mass of the candidate hypothesis ($M(\Lambda_c^+\pi^+\pi^-)$ for Λ_c^+ resonances, $M(\Lambda_c^+\pi^+)$ for Σ_c^{++} and $M(\Lambda_c^+\pi^-)$ for the Σ_c^0 resonances) and the mass of the Λ_c^+ candidate, ($M(\Lambda_c^+)$).

Variable	Quantity	Decay
ΔM^{+-}	$M(\Lambda_c^+\pi^+\pi^-) - M(\Lambda_c^+)$	$\Lambda_b^0 \to \Lambda_c(2595)^+\pi^-$ and $\Lambda_b^0 \to \Lambda_c(2625)^+\pi^-$
ΔM^{+}	$M(\Lambda_c^+\pi^+) - M(\Lambda_c^+)$	$\Lambda_b^0 \to \Sigma_c^{++}\pi^-\pi^-$
ΔM^{-}	$M(\Lambda_c^+\pi^-) - M(\Lambda_c^+)$	$\Lambda_b^0 \to \Sigma_c^0\pi^-\pi^+$
ΔM^{--+}	$M(\Lambda_c^+\pi^-\pi^-\pi^+) - M(\Lambda_c^+)$	others

Table 4.4: *Variables used to identify resonant charmed baryons in the decays of Λ_b^0 candidates and to separate them from the other Λ_b^0 decay modes.*

In Tab. 4.4 we report the name chosen for these variables, ΔM^{+-}, ΔM^{+} and ΔM^{-}, the quantity stored in these variable and the reconstructed charmed resonant candidate associated to this variable. For the sum of two decay modes, $\Lambda_b^0 \to \Lambda_c^+\rho^0\pi^-$ and the $\Lambda_b^0 \to \Lambda_c^+\pi^-\pi^+\pi^-(nr)$, since we do not separate their contribution, we use

the variable ΔM^{--+}, defined as the difference between the reconstructed mass of the Λ_b^0 candidate and the mass of the reconstructed Λ_c^+ in the Λ_b^0 decay. These variables are used in the next section to distinguish and select, with high efficiency and low contamination, each resonant charmed Λ_b^0 decay mode from the other Λ_b^0 decays in $\Lambda_c^+\pi^-\pi^+\pi^-$ final state.

4.3.1 ΔM^{+-} distribution for $\Lambda_b^0 \to \Lambda_c(2595)^+\pi^-$ and $\Lambda_b^0 \to \Lambda_c(2625)^+\pi^-$

In the following we show that using the variable ΔM^{+-} (see Tab. 4.4) we are able to separate the $\Lambda_b^0 \to \Lambda_c(2595)^+\pi^-$ and $\Lambda_b^0 \to \Lambda_c(2625)^+\pi^-$ signals from the other Λ_b^0 decay modes.
Fig. 4.3 shows the ΔM^{+-} distribution of the six MC signals when all the optimized cuts are applied: in the chosen ΔM^{+-} histogram mass range only the $\Lambda_b^0 \to \Lambda_c(2595)^+\pi^-$ and $\Lambda_b^0 \to \Lambda_c(2625)^+\pi^-$ decay modes contribute significantly and are clearly separated by the others.

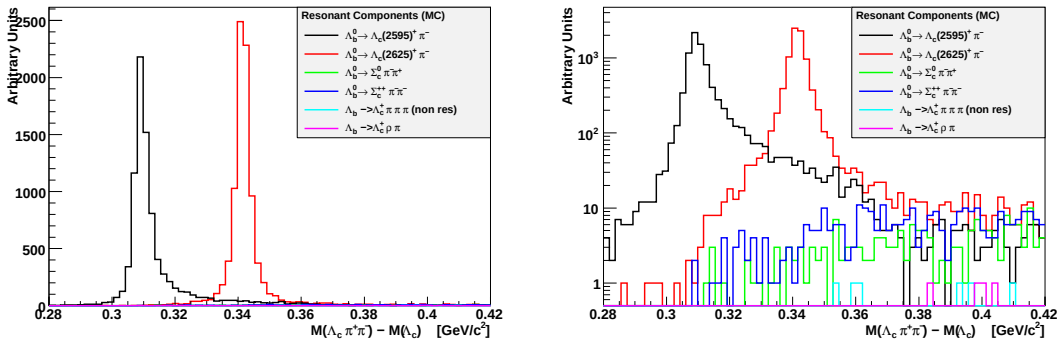

(a) (b)

Figure 4.3: *MC ΔM^{+-} distribution of all the $\Lambda_b^0 \to \Lambda_c^+\pi^-\pi^+\pi^-$ decay modes. The main contribution is due to $\Lambda_b^0 \to \Lambda_c(2595)^+\pi^-$ and $\Lambda_b^0 \to \Lambda_c(2625)^+\pi^-$ decay modes* **4.3(a)** *with respect to the others and in* **4.3(b)** *the logarithmic scale shows the limited contribution due to the others decay modes.*

Each $\Lambda_b^0 \to \Lambda_c^+\pi^-\pi^+\pi^-$ event produces two ΔM^{+-} candidates, since there are two possible $\Lambda_c^+\pi^-\pi^+$ combinations, due to the two π^- in the final state, but in the window $0.280\,\mathrm{GeV/c^2} < \Delta M^{+-} < 0.420\,\mathrm{GeV/c^2}$ (see Fig. 4.3(a)) only the combination with the lower transverse momentum π^- contributes.
By applying the cut $\Delta M^{+-} < 0.380\,\mathrm{GeV/c^2}$ we have a high efficiency on $\Lambda_b^0 \to$

$\Lambda_c(2595)^+\pi^-$ and $\Lambda_b^0 \to \Lambda_c(2625)^+\pi^-$ and a negligible one on the remaining four decay modes as summarized in Tab. 4.5.

Λ_b^0 Decay Mode	Efficiency %
$\Lambda_b^0 \to \Lambda_c(2595)^+\pi^-$	99.4
$\Lambda_b^0 \to \Lambda_c(2625)^+\pi^-$	98.7
$\Lambda_b^0 \to \Sigma_c(2455)^{++}\pi^-\pi^-$	1.2
$\Lambda_b^0 \to \Sigma_c(2455)^0\pi^+\pi^-$	0.8
$\Lambda_b^0 \to \Lambda_c^+\rho^0\pi^-$	0.1
$\Lambda_b^0 \to \Lambda_c^+\pi^-\pi^+\pi^-(\mathrm{nr})$	0.1

Table 4.5: *Decay modes efficiency in percent after the cut* $\Delta M^{+-} < 0.380\,\mathrm{GeV/c^2}$.

4.3.2 ΔM^+ distribution for $\Lambda_b^0 \to \Sigma_c(2455)^{++}\pi^-\pi^-$

The variable used to separate the $\Lambda_b^0 \to \Sigma_c(2455)^{++}\pi^-\pi^-$ signal from the others is ΔM^+. First of all we vetoed the $\Lambda_b^0 \to \Lambda_c(2595)^+\pi^-$ and $\Lambda_b^0 \to \Lambda_c(2625)^+\pi^-$ decay modes requiring $\Delta M^{+-} > 0.380\,\mathrm{GeV/c^2}$.
The relevance of this veto is due to the $\Lambda_c(2595)^+$ decay into $\Sigma_c(2455)^{++}\pi^-$ with a branching fraction of 24 % (see Tab. 4.3 and [1]), and also to the $\Lambda_c(2625)^+$ decay; without this veto, both decays can in principle contaminate the ΔM^+ distribution in the ΔM^+ region where the $\Sigma_c(2455)^{++}$ signal is located. Tab. 4.6 summarizes the MC efficiencies, after the veto is applied, on both $\Lambda_c(2595)^+$ and $\Lambda_c(2625)^+$.

Λ_b^0 Decay Mode	Efficiency
$\Lambda_b^0 \to \Lambda_c(2595)^+\pi^-$	0.6%
$\Lambda_b^0 \to \Lambda_c(2625)^+\pi^-$	1.3%

Table 4.6: *Efficiency on* Λ_c^+ *resonances after the veto on* $\Delta M^{+-} > 0.380\,\mathrm{GeV/c^2}$.

Fig. 4.4 shows the ΔM^+ distribution of the six decay modes reported in Tab. 4.1 with the cut $\Delta M^{+-} > 0.380\,\mathrm{GeV/c^2}$. The $\Lambda_b^0 \to \Sigma_c(2455)^{++}\pi^-\pi^-$ signal peaks and is entirely confined into the region $\Delta M^+ < 0.190\,\mathrm{GeV/c^2}$ (see Fig. 4.4(a)), where the contribution of the other decay modes is negligible, as shown in Tab. 4.7.

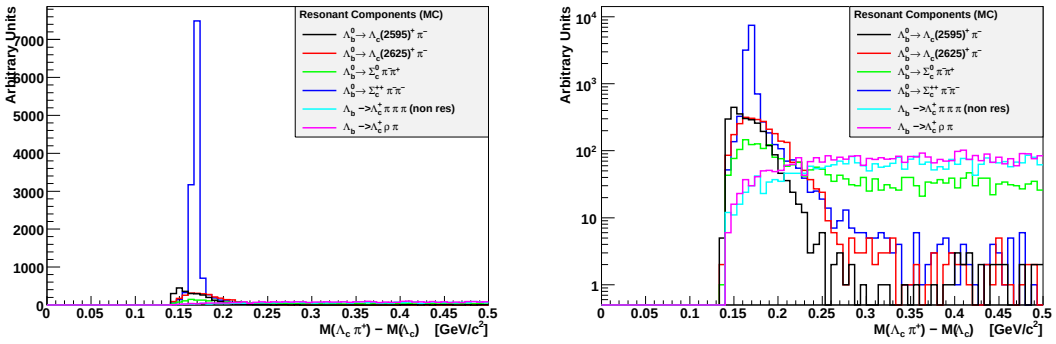

(a) (b)

Figure 4.4: *MC* ΔM^+ *distribution of all the* $\Lambda_b^0 \to \Lambda_c^+\pi^-\pi^+\pi^-$ *decay modes after we vetoed* $\Lambda_b^0 \to \Lambda_c(2595)^+\pi^-$ *and* $\Lambda_b^0 \to \Lambda_c(2625)^+\pi^-$ *with the cut* $\Delta M^{+-} > 0.380\,\mathrm{GeV/c^2}$. *The main contribution is due to the* $\Lambda_b^0 \to \Sigma_c(2455)^{++}\pi^-\pi^-$ *signal in the region* $\Delta M^+ < 0.190\,\mathrm{GeV/c^2}$ **4.4(a)**. *The logarithmic scale shows the limited contribution due to the others decay modes* **4.4(b)**.

Λ_b^0 Decay Mode	Efficiency %
$\Lambda_b^0 \to \Sigma_c(2455)^{++}\pi^-\pi^-$	99.4
$\Lambda_b^0 \to \Lambda_c(2595)^+\pi^-$	negligible
$\Lambda_b^0 \to \Lambda_c(2625)^+\pi^-$	negligible
$\Lambda_b^0 \to \Sigma_c(2455)^0\pi^+\pi^-$	4.8
$\Lambda_b^0 \to \Lambda_c^+\rho^0\pi^-$	2.4
$\Lambda_b^0 \to \Lambda_c^+\pi^-\pi^+\pi^-$(nr)	1.6

Table 4.7: *Decay modes efficiency in percent after the veto on* Λ_c^+ *resonances and requiring* $\Delta M^+ < 0.190\,\mathrm{GeV/c^2}$.

4.3.3 ΔM^- distribution for $\Lambda_b^0 \to \Sigma_c(2455)^0\pi^-\pi^+$

To extract the $\Lambda_b^0 \to \Sigma_c(2455)^0\pi^+\pi^-$ we adopted the same procedure vetoing the $\Lambda_b^0 \to \Lambda_c(2595)^+\pi^-$ and $\Lambda_b^0 \to \Lambda_c(2625)^+\pi^-$ requiring $\Delta M^{+-} > 0.380\,\mathrm{GeV/c^2}$. The reasons that lead us to apply this cut are the same as reported in Sec. 4.3.2 with the exception that, in this case, the variable used is ΔM^-.

Fig. 4.5 shows the ΔM^- distribution of the six decay modes reported in Tab. 4.1 when the $\Lambda_b^0 \to \Lambda_c(2595)^+\pi^-$ and the $\Lambda_b^0 \to \Lambda_c(2625)^+\pi^-$ are vetoed with the cut $\Delta M^{+-} > 0.380\,\mathrm{GeV/c^2}$.
The $\Lambda_b^0 \to \Sigma_c(2455)^0\pi^+\pi^-$ signal peaks and is entirely confined to the region $\Delta M^- < 0.190\,\mathrm{GeV/c^2}$, where the contribution of the other decay modes is negli-

gible as shown in Tab. 4.8.

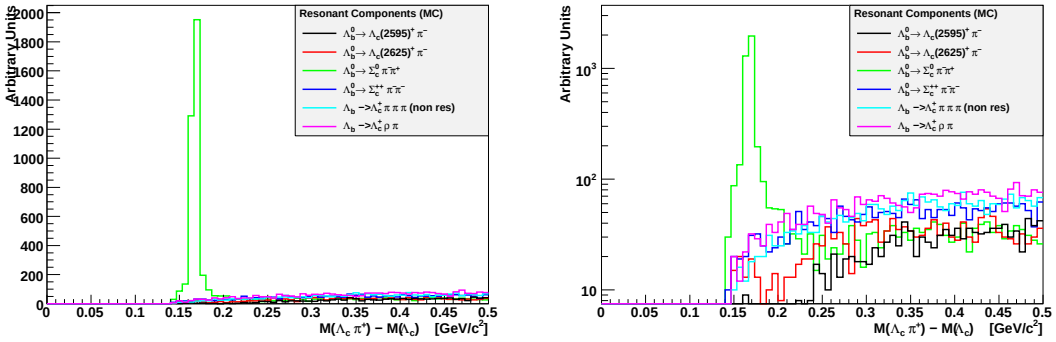

(a) (b)

Figure 4.5: *MC ΔM^- distribution of all the $\Lambda_b^0 \to \Lambda_c^+\pi^-\pi^+\pi^-$ decay modes after we vetoed $\Lambda_b^0 \to \Lambda_c(2595)^+\pi^-$ and $\Lambda_b^0 \to \Lambda_c(2625)^+\pi^-$ with the cut $\Delta M^{+-} > 0.380\,\mathrm{GeV/c^2}$.* **4.5(a):** *The $\Lambda_b^0 \to \Sigma_c(2455)^0\pi^+\pi^-$ is the main contribution the region $\Delta M^- < 0.190\,\mathrm{GeV/c^2}$, where the contribution of the other decay modes is negligible.* **4.5(b):** *The logarithmic scale enhances the limited contribution due to the other decay modes.*

Also in this case there are two $\Lambda_c^+\pi^-$ candidates per event but only the combination with the lowest transverse momentum π^- contributes to the chosen ΔM^- histogram mass window.

Λ_b^0 Decay Mode	Efficiency %
$\Lambda_b^0 \to \Sigma_c(2455)^0\pi^+\pi^-$	98.5
$\Lambda_b^0 \to \Lambda_c(2595)^+\pi^-$	negligible
$\Lambda_b^0 \to \Lambda_c(2625)^+\pi^-$	negligible
$\Lambda_b^0 \to \Sigma_c(2455)^{++}\pi^-\pi^-$	0.8
$\Lambda_b^0 \to \Lambda_c^+\rho^0\pi^-$	< 1.3
$\Lambda_b^0 \to \Lambda_c^+\pi^-\pi^+\pi^-(\mathrm{nr})$	1.3

Table 4.8: *Decay modes efficiency in percent after the veto on Λ_c^+ resonances and requiring $\Delta M^- < 0.190\,\mathrm{GeV/c^2}$.*

4.3.4 ΔM^{--+} distribution for $\Lambda_b^0 \to \Lambda_c^+\rho^0\pi^-$ and $\Lambda_b^0 \to \Lambda_c^+\pi^-\pi^+\pi^-(nr)$

To extract the $\Lambda_b^0 \to \Lambda_c^+\rho^0\pi^-$ and the $\Lambda_b^0 \to \Lambda_c^+\pi^-\pi^+\pi^-(nr)$ decay modes on the real data we need to veto all the previous decay modes requiring $\Delta M^{+-} > 0.380\,\mathrm{GeV/c^2}$, $\Delta M^{+} > 0.190\,\mathrm{GeV/c^2}$, and $\Delta M^{-} > 0.190\,\mathrm{GeV/c^2}$.
The fraction of events passing these cuts is reported in Tab. 4.9.

Λ_b^0 Decay Mode	Efficiency %
$\Lambda_b^0 \to \Lambda_c^+\rho^0\pi^-$	98.6
$\Lambda_b^0 \to \Lambda_c^+\pi^-\pi^+\pi^-$	98.6
$\Lambda_b^0 \to \Lambda_c(2595)^+\pi^-$	0.6
$\Lambda_b^0 \to \Lambda_c(2625)^+\pi^-$	1.2
$\Lambda_b^0 \to \Sigma_c(2455)^{++}\pi^-\pi^-$	1.8
$\Lambda_b^0 \to \Sigma_c(2455)^0\pi^+\pi^-$	4.4

Table 4.9: *Decay modes efficiency in percent after the veto on Λ_c^+ resonances and requiring $\Delta M^{+-} > 0.380\,\mathrm{GeV/c^2}$, $\Delta M^{+} > 0.190\,\mathrm{GeV/c^2}$, and $\Delta M^{-} > 0.190\,\mathrm{GeV/c^2}$.*

The ΔM^{+-}. ΔM^{+} and ΔM^{-} cuts chosen to separate the charmed resonant $\Lambda_b^0 \to \Lambda_c^+\pi^-\pi^+\pi^-$ decay modes on real data are summarized in Tab. 4.10.

Λ_b^0 Decay Mode	ΔM^{+-} [GeV/c^2]	ΔM^{+} [GeV/c^2]	ΔM^{-} [GeV/c^2]
$\Lambda_b^0 \to \Lambda_c(2595)^+\pi^-$	< 0.380	-	-
$\Lambda_b^0 \to \Lambda_c(2625)^+\pi^-$	< 0.380	-	-
$\Lambda_b^0 \to \Sigma_c(2455)^{++}\pi^-\pi^-$	> 0.380	< 0.190	-
$\Lambda_b^0 \to \Sigma_c(2455)^0\pi^+\pi^-$	> 0.380	-	< 0.190
$\Lambda_b^0 \to \Lambda_c^+\rho^0\pi^- + \Lambda_b^0 \to \Lambda_c^+\pi^-\pi^+\pi^-$(nr)	> 0.380	> 0.190	> 0.190

Table 4.10: *ΔM^{+-}, ΔM^{+} and ΔM^{-} cuts used to select the $\Lambda_b^0 \to \Lambda_c^+\pi^-\pi^+\pi^-$ decay modes.*

Chapter 4. MC Samples of Λ_b^0 Decays with charmed resonances in $\Lambda_c^+\pi^-\pi^+\pi^-$ final states

Chapter 5

Yieds of $\Lambda_b^0 \to \Lambda_c^+ \pi^- \pi^+ \pi^-$ Decay Modes

In this Chapter we extract the yields of the $\Lambda_b^0 \to \Lambda_c^+ \pi^- \pi^+ \pi^-$ decay modes fitting the ΔM^{+-}, ΔM^{+}, ΔM^{-} and ΔM^{--+} mass distributions in the experimental data. To this aim, we use the Λ_b^0 candidates reconstructed in the skimmed data sample after applying the offline trigger confirmation and the optimized selection described in Chap. 3. The different decay modes are then separated using the requirements determined in the previous chapter. The data modeling, used by the fit of the distributions, includes the signal, the combinatorial background, and the physical background.

5.1 Total yield $\Lambda_b^0 \to \Lambda_c^+ \pi^- \pi^+ \pi^-$

To extract this yield, after applying the offline trigger confirmation and the optimized selection (see Chap. 3) on the skimmed data sample, we performed an extended likelihood fit to the inclusive ΔM^{--+} mass distribution of the reconstructed candidates, reported in Fig. 5.1(a).
The fit uses as Probability Density Function (PDF) the sum of an exponential (to model the background) and a Gaussian (to model the signal). Fig.5.1(a) shows the ΔM^{--+} mass distribution with the best fit (blue curve) overlaid. The modeling we used for the background is not accurate since the fit pulls[1] (bottom of the same figure) show some discrepancies in the mass region $[3.24 - 3.3]$ GeV/c^2.
Since the overall background is due to the combinatorial and physical background,

[1]The pulls in each bin of the histogram are evaluated using the bin content of the histogram (Data) and the expected by the best fit (Fit) as: $\frac{(Data - Fit)}{\sqrt{Data}}$

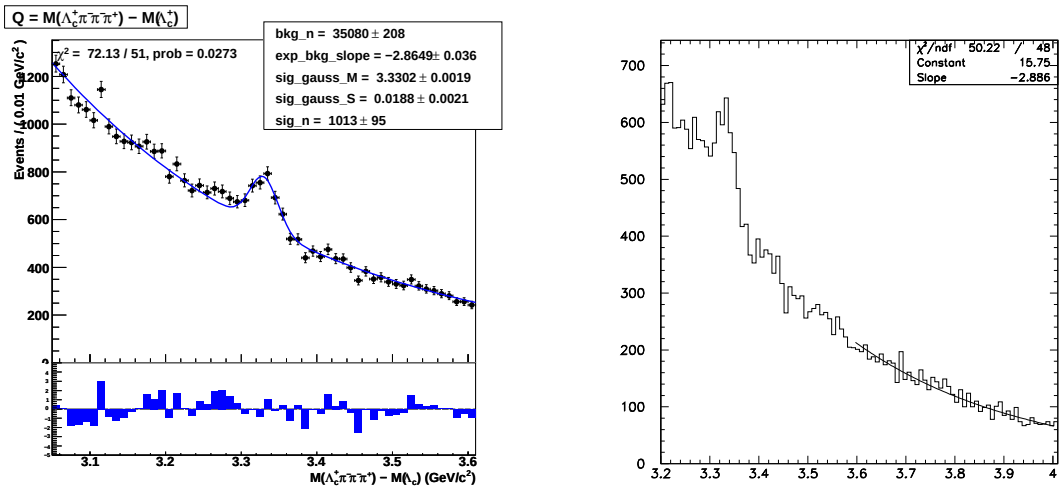

(a) (b)

Figure 5.1: *ΔM^{--+} mass distribution.* **5.1(a):** *The distribution is modeled using as PDF the sum of an exponential (background) and a Gaussian (signal) functions. Best fit (blue curve) is overlaid.* **5.1(b):** *Best fit (black curve), in the high mass region $[3.6 - 4.01]$ GeV/c^2, where only the combinatorial background contributes: the modeling in the fit uses an exponential as PDF.*

we try, in the following, to improve our modeling. While the main contribution to the physical background is expected in the lower mass region, and it is mainly due to misreconstructed and semileptonic decays of Λ_b^0 and B-mesons, in the high mass region only the combinatorial background is expected to contribute. So, in order to determine the shape of the combinatorial background, we fit the ΔM^{--+} mass distribution of Fig. 5.1(b) in the high mass region $[3.6 - 4.01]$ GeV/c^2, assuming an exponential PDF. The shape of the combinatorial background, in the modeling of the overall background, will be fixed to the value returned by this fit (`slope` parameter in the fit result legenda of Fig. 5.1(b)). In order to produce a template shape of ΔM^{--+} for the physical background, we used large MC samples of several decay modes that might contribute to this background. The background description is improved by adding to the combinatorial modeling the templates for the following B-meson decays: $\overline{B}{}^0_{(s)} \to D^{(*)+}_{(s)}\pi^-\pi^+\pi^-$[2] with inclusive $D^{(*)+}_{(s)}$ decays. Performing the fit and using as PDF for the combinatorial background the above exponential with the fixed shape, we observed a noticeable improvement in the fit

[2]With $D^{(*)+}_{(s)}$ we indicate the excited D^{*+} and D_s^{*+} mesons and the D^+ and D_s^+.

(see Fig. 5.2(a)) while adding the background due to the $B^0 \rightarrow$ Inclusive decay modes we noticed a negligible effect (see Fig. 5.2(b)). However, these fits show some disagreement with data in the mass region $[3.15 - 3.20]$ GeV/c^2, probably due to some reflections, so we decided to exclude this region from the fit.
Fig. 5.2(c) reports the fit results in the reduced mass region when the background model is given by the exponential, plus the $\overline{B}^0_{(s)} \rightarrow D^{(*)+}_{(s)}\pi^-\pi^+\pi^-$ while the Fig. 5.2(d) shows the best fit results when we included also the $B^0 \rightarrow$ Inclusive.
We use the signal Gaussian mean (3.332 GeV/c^2) and sigma ($\sigma = 0.016$ GeV/c^2), as determined by the fit of ΔM^{--+} of Fig. 5.2(d), to define a $\pm 3\sigma$ mass window centered in the mean value of the Gaussian: $\mid \Delta M^{--+} - 3.332 \mid < 0.048$ GeV/c^2. We call this interval the $\Lambda_b^0 \pm 3\sigma$ *mass window*. The yield of $\Lambda_b^0 \rightarrow \Lambda_c^+\pi^-\pi^+\pi^-$ decays estimated by the fit is 848 ± 93 events (`sig_n` in the fit results legenda of Fig. 5.2(d)). We have also tried to model other contributions to the physical background, such as the Cabibbo suppressed (CS) decay modes of our signal (see Appendix C), misreconstructed $\Lambda_b^0 \rightarrow \Lambda_c^+\pi^-\pi^+\ell\overline{\nu}_\ell$ semileptonic and $\Lambda_b^0 \rightarrow \Lambda_c^+\pi^-\pi^+\pi^-\pi^0$ decays, where in the latter a π^0 is lost. For each of these contribution a template shape was determined using large MC samples. The fit including in the model these contributions changes neither the shape nor the $\Lambda_b^0 \rightarrow \Lambda_c^+\pi^-\pi^+\pi^-$ yield estimate. We decided to not include these contribution in the modeling. The CS decay mode contributions, which affect the estimate of the yield (see Appendix C), will be considered as a systematic affecting the yield of the Cabibbo favored (CF) (see Chap. 7).

5.2 Yield Estimates of the Charmed Resonant Decay Modes

To determine the yields of the charmed resonant decay modes of Tab. 4.1 we reconstruct the mass difference distribution for the $\Lambda_c(2595)^+$, $\Lambda_c(2625)^+$, $\Sigma_c(2455)^{++}$ and $\Sigma_c(2455)^0$ (ΔM^{+-}, ΔM^+ and ΔM^-) resonance candidates in the $\Lambda_b^0 \pm 3\sigma$ mass window, applying all the requirements of Tab. 4.10 to select them, then, we performed an unbinned extended likelihood fit on each distribution, using RooFit version 3.1 [93], to extract the yield of the corresponding charmed resonant Λ_b^0 decay mode. The experimental masses and widths [1] of the resonances are summarized in Tab. 5.1.

5.2.1 $\Lambda_b^0 \rightarrow \Lambda_c(2595)^+\pi^-$ and $\Lambda_b^0 \rightarrow \Lambda_c(2625)^+\pi^-$

Fig. 5.3(a) shows the ΔM^{+-} mass distribution for candidates in the Λ_b^0 mass window $\mid \Delta M^{--+} - 3.332 \mid < 0.048$ GeV/c^2 requiring $\Delta M^{+-} < 0.380$ GeV/c^2

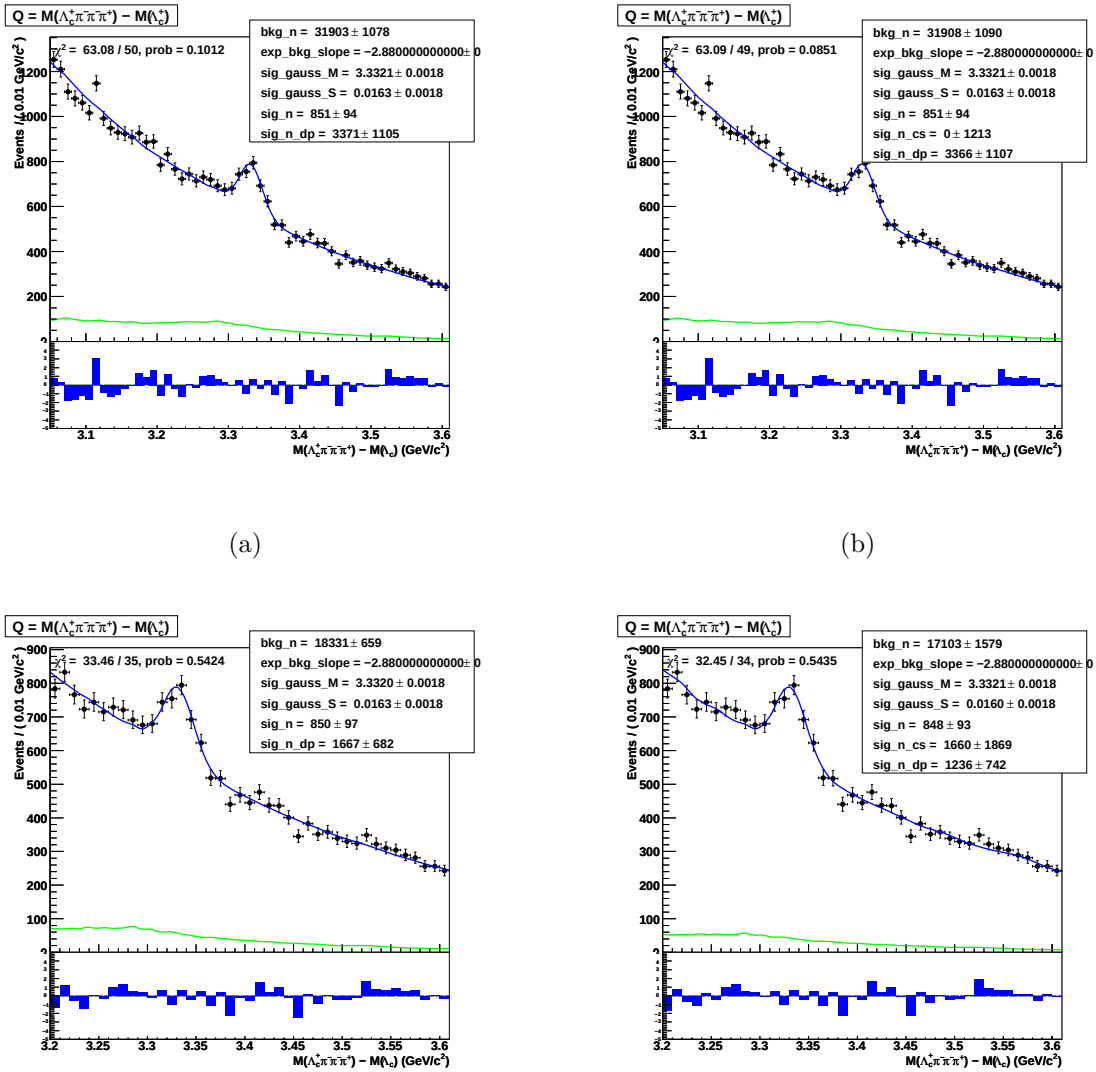

Figure 5.2: *ΔM^{--+} distribution with overlaid the best fit (blue curve). In the modeling the exponential shape is fixed to the shape determined from the fit in the high mass region:* **5.2(a):** *$\overline{B}^0 \to D^{(*)+}\pi^-\pi^+\pi^-$ and $\overline{B}^0_{(s)} \to D^{(*)+}_{(s)}\pi^-\pi^+\pi^-$ contributions (green line) are used to model the physical background. The $D^{(*)+}$ and $D^{(*)+}_{(s)}$ decay modes are inclusive.* **5.2(b):** *$\overline{B}^0 \to D^{(*)+}\pi^-\pi^+\pi^-$, $\overline{B}^0_{(s)} \to D^{(*)+}_{(s)}\pi^-\pi^+\pi^-$, and the $B^0 \to$ Inclusive contributions (green line) are used to model the background.* **5.2(c):** *same as in Fig. 5.2(a) but in $[3.2-3.6]GeV/c^2$ ΔM^{--+} range.* **5.2(d):** *same as in Fig. 5.2(b) but in $[3.2-3.6]GeV/c^2$ ΔM^{--+} range.*

Resonance	M [MeV/c^2]	$M - M(\Lambda_c^+)$ [MeV/c^2]	Width [MeV/c^2]
$\Lambda_c(2595)^+$	2595.4 $\pm$ 0.6	308.9 $\pm$ 0.6	$3.6^{+2.0}_{-1.3}$
$\Lambda_c(2625)^+$	2628.1 $\pm$ 0.6	341.7 $\pm$ 0.6	< 1.9 (90 % c.l.)
$\Sigma_c(2455)^{++}$	2454.02 $\pm$ 0.18	167.56 $\pm$ 0.11	2.23 $\pm$ 0.30
$\Sigma_c(2455)^0$	2453.76 $\pm$ 0.18	167.30 $\pm$ 0.11	2.2 $\pm$ 0.4

Table 5.1: *Experimental masses [1], mass differences with respect to Λ_c^+ mass and widths for the charmed resonances [1] described in the text.*

(see Sec. 4.3.1 and Tab. 4.10) to select $\Lambda_c(2595)^+$ and $\Lambda_c(2625)^+$. The fit model assumes two Voigtian PDF[3] to describe the two Λ_c^+ resonances (the signal) and a first degree polynomial for the background. Since the difference in ΔM value of two resonances is tiny (see Tab. 5.1), we assumed that both signals have the same detector resolution (sigma of the Gaussian resolution) hence, both Voigtian PDF have the same parameter for the Gaussian sigma. The proximity to the threshold of the $\Lambda_c(2595)^+$ resonance distorts the shape of the Breight-Wigner [94] for this signal, and its width is mass dependent. In order to account for this distortion, the Breight-Wigner width (W), describing the $\Lambda_c(2595)^+$ resonance, is parameterized as:

$$W = W_1(1 + \alpha * (\Delta M - \Delta M^{mean})) \tag{5.1}$$

where W_1 is the central value of the Breit-Wigner width of Tab. 5.1 for the $\Lambda_c(2595)^+$. Here ΔM is the experimental world average central value for $\Lambda_c(2595)^+$ (see Tab. 5.1), ΔM^{mean} is the signal Gaussian mean value of ΔM^{+-} for $\Lambda_c(2595)^+$ in our data and is a free parameter of the fit; α is a constant and it is also a parameter of the fit. The yields for $\Lambda_b^0 \to \Lambda_c(2595)^+\pi^-$ and $\Lambda_b^0 \to \Lambda_c(2625)^+\pi^-$ signals, as determined by the fit (respectively `Nsig1` and `Nsig2`, in the fit results legenda of Fig. 5.3(a)), are reported in Tab. 5.2.

As a cross-check, we estimated the number of Λ_b^0 in the region of the $\Lambda_c(2595)^+$ and $\Lambda_c(2625)^+$ resonances: Fig. 5.3(b) reports the fit of the ΔM^{--+} distribution selected by applying the $\Delta M^{-+} < 0.380\,\mathrm{GeV/c^2}$ cut. The obtained Λ_b^0 yield (`sig_n` , in the fit results legenda of Fig. 5.3(b)) is consistent with sum of yields of $\Lambda_c(2595)^+$ and $\Lambda_c(2625)^+$ signals. The Fig. 5.4(a) and Fig. 5.4(b) show the same fit separately for each resonant decay mode: still the yields of the two Λ_b^0 charmed resonances decays (`sig_n`, of Fig. 5.4(a) for the yield of $\Lambda_c(2595)^+$ and of Fig. 5.4(b) for the one of $\Lambda_c(2625)^+$) are consistent with these of Fig. 5.3(a) showing that our procedure to extract the yield is correct.

[3] *i.e.* Breit-Wigner function convoluted with a Gaussian to model the detector mass resolution.

Λ_b^0 Decay Mode	$M - M(\Lambda_c^+)$ [MeV/c^2]	Yield
$\Lambda_b^0 \to \Lambda_c(2595)^+\pi^- \to \Lambda_c^+\pi^-\pi^+\pi^-$	309.1±0.6	46.6±9.7
$\Lambda_b^0 \to \Lambda_c(2625)^+\pi^- \to \Lambda_c^+\pi^-\pi^+\pi^-$	341.6±0.2	114±13
$\Lambda_b^0 \to \Sigma_c(2455)^{++}\pi^-\pi^- \to \Lambda_c^+\pi^-\pi^+\pi^-$	168.0±0.4	81±15
$\Lambda_b^0 \to \Sigma_c(2455)^0\pi^+\pi^- \to \Lambda_c^+\pi^-\pi^+\pi^-$	168.0±0.4	41.5±9.3
$\Lambda_b^0 \to \Lambda_c^+\pi^-\pi^+\pi^-$ (with charm. res. vetoed)	3332.9±2.4	610±88

Table 5.2: *Yields estimated by fitting the ΔM^{+-}, ΔM^{+} and ΔM^{-} distribution of the resonant candidates, in the Λ_b^0 mass region. The last row reports the yield of the $\Lambda_b^0 \to \Lambda_c^+\pi^-\pi^+\pi^-$ with the charmed resonances vetoed. The dataset is given by the two trigger paths `B_CHARM_LOWPT` and `B_CHARM`; the applied cuts are the optimised cuts with trigger confirmation.*

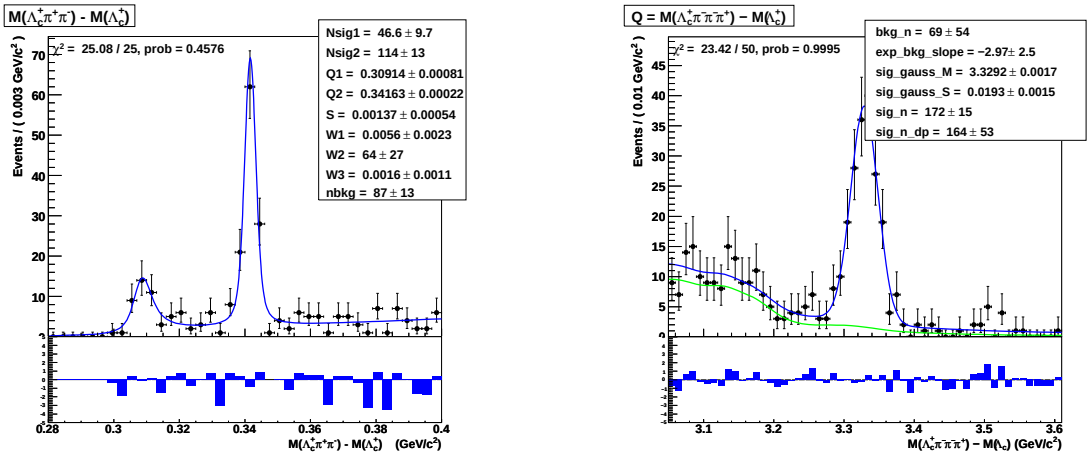

(a) (b)

Figure 5.3: *ΔM^{+-} distribution for the candidates in the Λ_b^0 $\pm 3\sigma$ mass window region with overlaid the best fit (blue curve) 5.3(a) and ΔM^{--+} distribution when $\Delta M^{+-} < 0.380$ GeV/c^2 5.3(b) with overlaid the best fit distribution (blue curve) and the background contribution (green curve).*

5.2.2 $\Lambda_b^0 \to \Sigma_c(2455)^{++}\pi^-\pi^- \to \Lambda_c^+\pi^-\pi^+\pi^-$

The $\Sigma_c(2455)^{++}$ and $\Sigma_c(2455)^0$ signals have lower yields and significantly larger and more complex background. In this case, in order to estimate the experimental resolution using a larger statistics sample, we use data from a left sideband of Λ_b^0 mass window ($2.10\,\mathrm{GeV/c^2} < \Delta M^{--+} < 3.38\,\mathrm{GeV/c^2}$) since this left sideband is

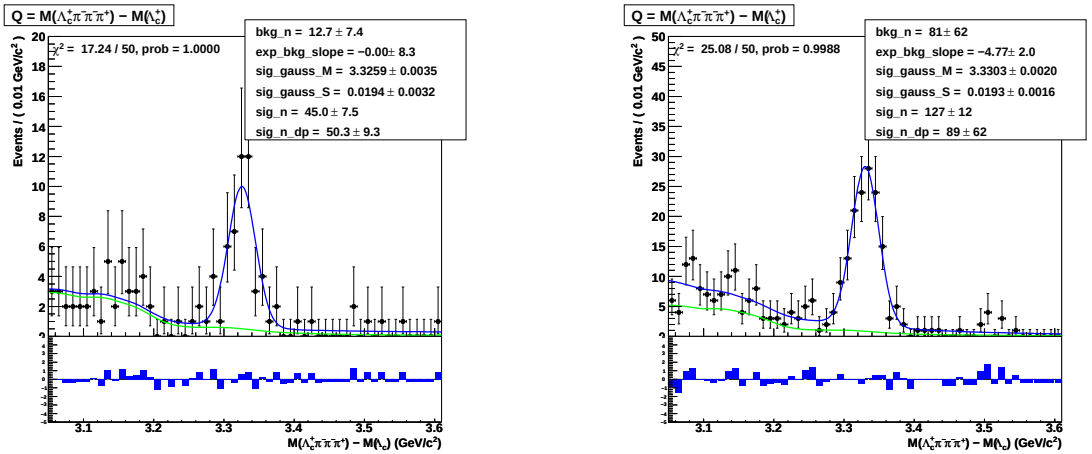

(a) (b)

Figure 5.4: **5.4(a):** *ΔM^{--+} distribution made for candidates when $\Delta M^{+-} < 0.325\,\mathrm{GeV/c^2}$ in order to select the $\Lambda_b^0 \to \Lambda_c(2595)^+\pi^-$ decay mode, with overlaid the best fit distribution (blue curve) and the contributing background (green curve).* **5.4(b):** *ΔM^{--+} distribution made for candidates in the $0.325\,\mathrm{GeV/c^2} < \Delta M^{+-} < 0.380\,\mathrm{GeV/c^2}$ window in order to select the $\Lambda_b^0 \to \Lambda_c(2625)^+\pi^-$ decay mode, with overlaid the best fit distribution (blue curve) and the contributing background (green curve).*

rich in Λ_b^0 semileptonic decays. Fig. 5.5(a) and Fig. 5.5(b) show the ΔM^+ distribution of the $\Sigma_c(2455)^{++}$ candidates in the Λ_b^0 left sideband region. The fit was performed in a narrow ΔM^+ range, where the background shape can be considered linear. The modeling assumes a first degree polynomial for the background and a Voigtian PDF for the signal.
In the fit shown in the Fig. 5.5(a) the Breit-Wigner mean and width and Gaussian sigma are free to float and are determined by the fit. We verified that the obtained values of the these two parameters (indicated as `Q_M` and `Q_W` in the fit results legenda of Fig. 5.5(a)) were consistent with those of the PDG (see Tab. 5.1).
As a test, in Fig. 5.5(b) we fixed the Breit-Wigner width to the PDG value and the best fit returns consistent results for the sigma of the Gaussian (indicated with `Q_S` in the fit results legendas of Fig. 5.5(a) and Fig. 5.5(b)). We assume as Gaussian sigma for the $\Sigma_c(2455)^{++}$ the average of these two sigmas: $(1.0 \pm 0.2)\,\mathrm{MeV/c^2}$. In the following we will show that this assumption is correct. Fig. 5.6(a) and Fig. 5.6(b) show the ΔM^+ mass distribution with the best fit overlaid, separately for particles ($\Sigma_c(2455)^{++}$) and anti-particles ($\Sigma_c(2455)^{--}$). In these fits the Breit-Wigner width is fixed to the PDG value and the Gaussian sigmas (`Q_S`, in the

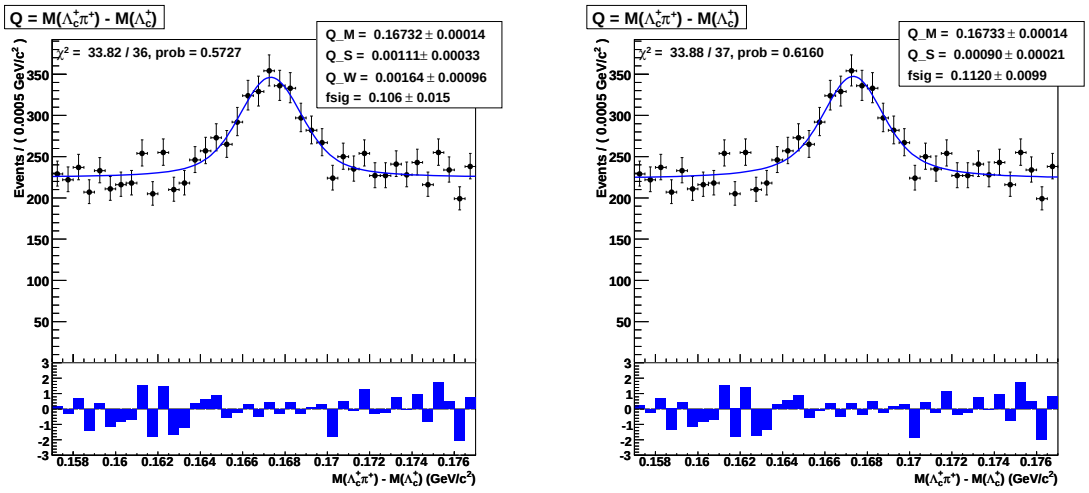

(a) (b)

Figure 5.5: *ΔM^+ distribution of the $\Sigma_c(2455)^{++}$ candidates in the Λ_b^0 left sideband region with overlaid the best fit (blue curve). In the fit in* **5.5(a)** *both Breit-Wigner width and the Gaussian resolution are floating while in* **5.5(b)** *the Breit-Wigner width is fixed to the PDG value and the Gaussian resolution is floating and determined by the fit.*

fit results legenda of Fig. 5.6(a) and Fig. 5.6(b)) agree, and are compatible with $(1.0 \pm 0.2\,\mathrm{MeV/c^2})$.

Fig. 5.7(a) shows the ΔM^+ distribution of the $\Sigma_c(2455)^{++}$ candidates, when the Λ_b^0 reconstructed candidate is in the $\Lambda_b^0 \pm 3\sigma$ mass window. Both resonances, $\Lambda_c(2595)^+$ and $\Lambda_c(2625)^+$, are vetoed requiring $\Delta M^{+-} > 0.380\,\mathrm{GeV/c^2}$ (see Sec. 4.3.2 and Tab. 4.10). The fit function used to extract the yield is composed of an Argus PDF [95] for the background and a Voigtian PDF, with the Gaussian sigma fixed to $1.0\,\mathrm{MeV/c^2}$, for the signal. A Gaussian constraint is also applied on the Breit-Wigner width. The obtained yield is 81 ± 15 events (`Nsig`, in the fit results legenda of Fig. 5.7(a)). In Fig. 5.7(b) the ΔM^{--+} distribution is reported requiring a $\Sigma_c(2455)^{++}$ $(160\,\mathrm{MeV/c^2} < \Delta M^+ < 176\,\mathrm{MeV/c^2})$ in the Λ_b^0 candidate showing the corresponding Λ_b^0 signal when the ΔM^{--+} is fitted assuming a Gaussian for the signal and an exponential for the background.

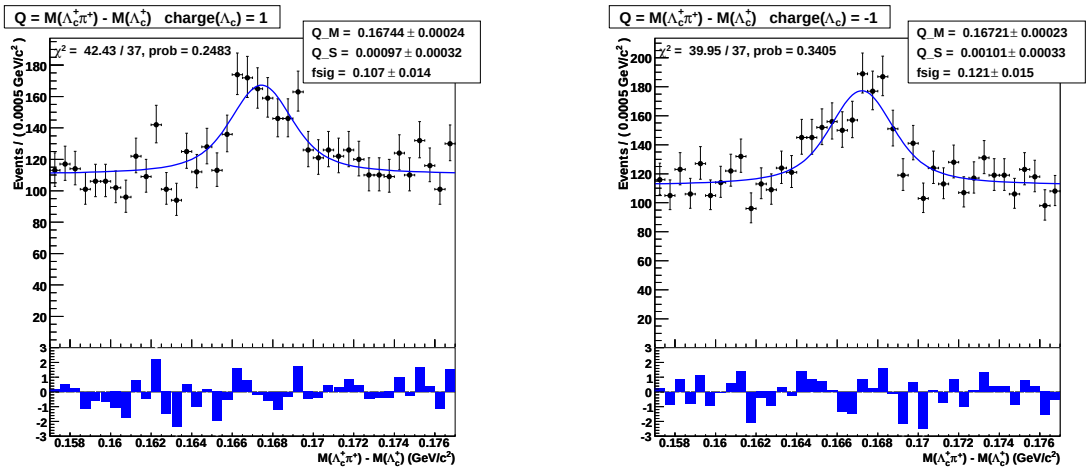

(a) (b)

Figure 5.6: **5.6(a):** *ΔM^+ distribution of the $\Sigma_c(2455)^{++}$ with overlaid the best fit (blue curve) -* ***particles*** **5.6(a)** *and $\Sigma_c(2455)^{--}$ -* ***antiparticles*** **5.6(b)** *in the left sideband region.*

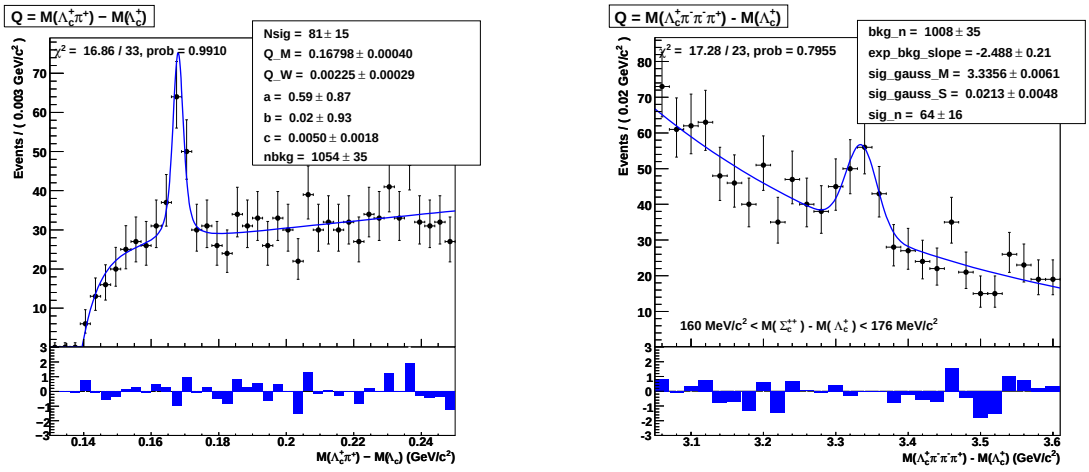

(a) (b)

Figure 5.7: **5.7(a):** *ΔM^+ distribution of the $\Sigma_c(2455)^{++}$ candidates in the $\Lambda_b^0 \pm 3\sigma$ mass window with the resonances $\Lambda_c(2595)^+$ and $\Lambda_c(2625)^+$ vetoed with the cut $\Delta M^{+-} > 0.380\,\mathrm{GeV/c^2}$. The Gaussian resolution has been fixed to $1.0\,\mathrm{MeV/c^2}$.* **5.7(b):** *ΔM^{--+} distribution in the $\Sigma_c(2455)^{++}$ signal mass window $160\,\mathrm{MeV/c^2} < \Delta M^+ < 176\,\mathrm{MeV/c^2}$.*

5.2.3 $\Lambda_b^0 \to \Sigma_c(2455)^0\pi^-\pi^+ \to \Lambda_c^+\pi^-\pi^+\pi^-$

The technique used for the $\Sigma_c(2455)^0$ signal yield is the same as above for the $\Sigma_c(2455)^{++}$. Also in this case we use data from the left sideband of Λ_b^0 mass window ($2.10\,\mathrm{GeV/c^2} < \Delta M^{--+} < 3.38\,\mathrm{GeV/c^2}$) and the fit to determine the Gaussian resolution is performed in a narrow ΔM^- range, where the background can be considered linear. The modeling assumes a first degree polynomial for the background, and a Voigtian PDF for the signal. In Fig. 5.8(a), where the distribution ΔM^- is shown, the Voigtian PDF has a Gaussian constraint on the Breit-Wigner mean (`Q_M` in the fit results legenda in Fig. 5.8(a)), while the Gaussian sigma is floating and determined by the fit (`Q_S` in the fit results legenda of the figure in Fig. 5.8(a)). In Fig. 5.8(b), we fixed the width to the PDG value (see Tab. 5.1) and the fit results are in agreement with the ones of Fig. 5.8(a). Both Gaussian sigma (`Q_S` in the fit result legenda) are compatible with $(1\pm0.2)\,\mathrm{MeV/c^2}$ and are consistent with the Gaussian sigma of the other charmed resonances.

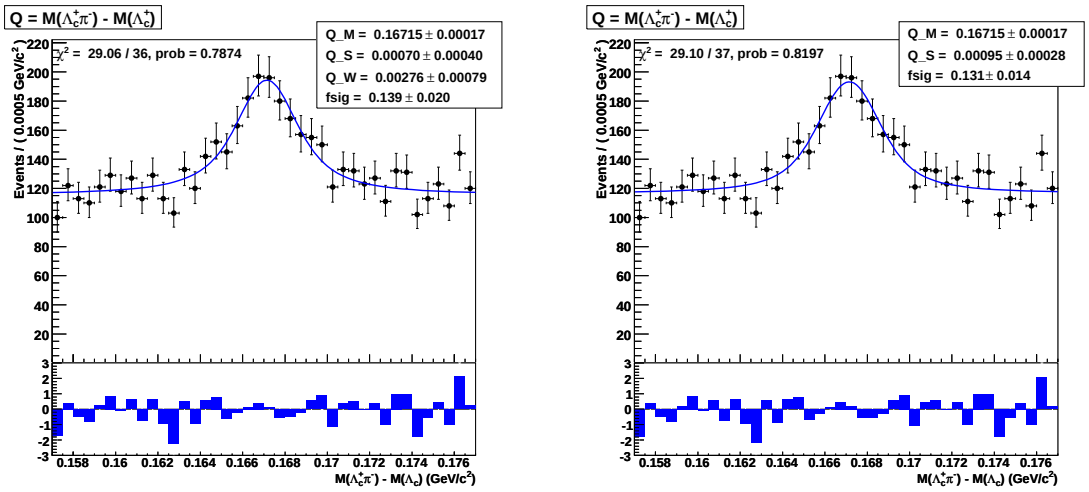

(a) (b)

Figure 5.8: *ΔM^- distribution of the $\Sigma_c(2455)^0$ candidates in the left Λ_b^0 sideband region:* **5.8(a):** *The Voigtian PDF has a Gaussian constraint on the Breit-Wigner width and a floating resolution.* **5.8(b):** *The Breit-Wigner width in Voigtian PDF is fixed to the PDG value. The Gaussian sigma (`Q_S` in the top left, fit results legenda) as returned by the fit agrees with the one determined in Fig. 5.8(a).*

The fit of the ΔM^- distribution is then performed separately for particles (see Fig. 5.9(a)) and anti-particles (see Fig. 5.9(b)). In these fits, the Breit-Wigner

width is fixed to the PDG value while the Gaussian is free to float. Also in this case the values of the Gaussian sigmas (`Q_S`, in the fit results legenda of the two figures) agree, and are compatible with $(1 \pm 0.2)\,\mathrm{MeV/c^2}$.
Fig. 5.9(c) shows the ΔM^- distribution of the $\Sigma_c(2455)^0$ candidates, when the Λ_b^0 reconstructed candidate is in the $\Lambda_b^0 \pm 3\sigma$ mass window and both the resonances, $\Lambda_c(2595)^+$ and $\Lambda_c(2625)^+$, are vetoed requiring $\Delta M^{+-} > 0.380\,\mathrm{GeV/c^2}$ (see Sec. 4.3.3 and Tab. 4.10). Since the Gaussian sigma in all the fits done is is compatible with $(1.0 \pm 0.2\,\mathrm{MeV/c^2})$, like in the case of the $\Sigma_c(2455)^{++}$, the function used in the fit to extract the yield is the composition of an Argus, for the background, and a Voigtian PDFs for the signal, with the Gaussian resolution sigma fixed to $1.0\,\mathrm{MeV/c^2}$ and a Gaussian constraint on the Breit-Wigner width. The estimated yield is 41.5 ± 9.3 events (`Nsig`, in the fit results legenda of Fig. 5.9(d)). In Fig. 5.9(d) the ΔM^{--+} distribution is reported requiring a $\Sigma_c(2455)^0$ candidate ($160\,\mathrm{MeV/c^2} < \Delta M^- < 176\,\mathrm{MeV/c^2}$) in the Λ_b^0 candidate showing the corresponding Λ_b^0 signal when the modeling assumed in the fit uses a Gaussian and an exponential function respectively for the signal and the background.

5.3 Yield of $\Lambda_b^0 \to \Lambda_c^+\pi^-\pi^+\pi^-$ Final State without Charmed Resonances

The ΔM^{--+} distribution, after removing the $\Lambda_b^0 \to \Lambda_c(2595)^+\pi^-$, $\Lambda_b^0 \to \Lambda_c(2625)^+\pi^-$, $\Lambda_b^0 \to \Sigma_c(2455)^{++}\pi^-\pi^-$ and $\Lambda_b^0 \to \Sigma_c(2455)^0\pi^-\pi^+$ resonances by applying the cuts $\Delta M^{+-} > 0.380\,\mathrm{GeV/c^2}$, $\Delta M^+ > 0.190\,\mathrm{GeV/c^2}$ and $\Delta M^- > 0.190\,\mathrm{GeV/c^2}$, is reported in Fig. 5.10(a).

For the determination of the yields, we performed a fit (see Appendix B) modeling the signal with a Gaussian shape with a floating contribution, the combinatorial background with a fixed slope and floating contribution, and the physical background with the templates of the $\overline{B}{}^0_{(s)} \to D^{(*)+}_{(s)}\pi^-\pi^+\pi^-$ (with inclusive $D^{(*)+}_{(s)}$ decay modes) and the $B^0 \to$ Inclusive decays (see Appendix B); for the physical background, the shapes of the B-mesons decays are obtained from MC and their contribution is left free to float in the fit.
However, the best fit of Fig. 5.10(a) shows some disagreement with data in the mass region $[3.15 - 3.20]\,\mathrm{GeV/c^2}$, probably due to some reflections, so we decided to exclude this region from the fit. Fig. 5.10(b) reports the best fit in the reduced mass region $[3.2{-}4.01]\,\mathrm{GeV/c^2}$. The total yield associated to the $\Lambda_b^0 \to \Lambda_c^+\pi^-\pi^+\pi^-$ final state, without charmed resonances, is $610{\pm}88$ events as shown in the fit result legenda (see `sig_n` on Fig. 5.10(b)).

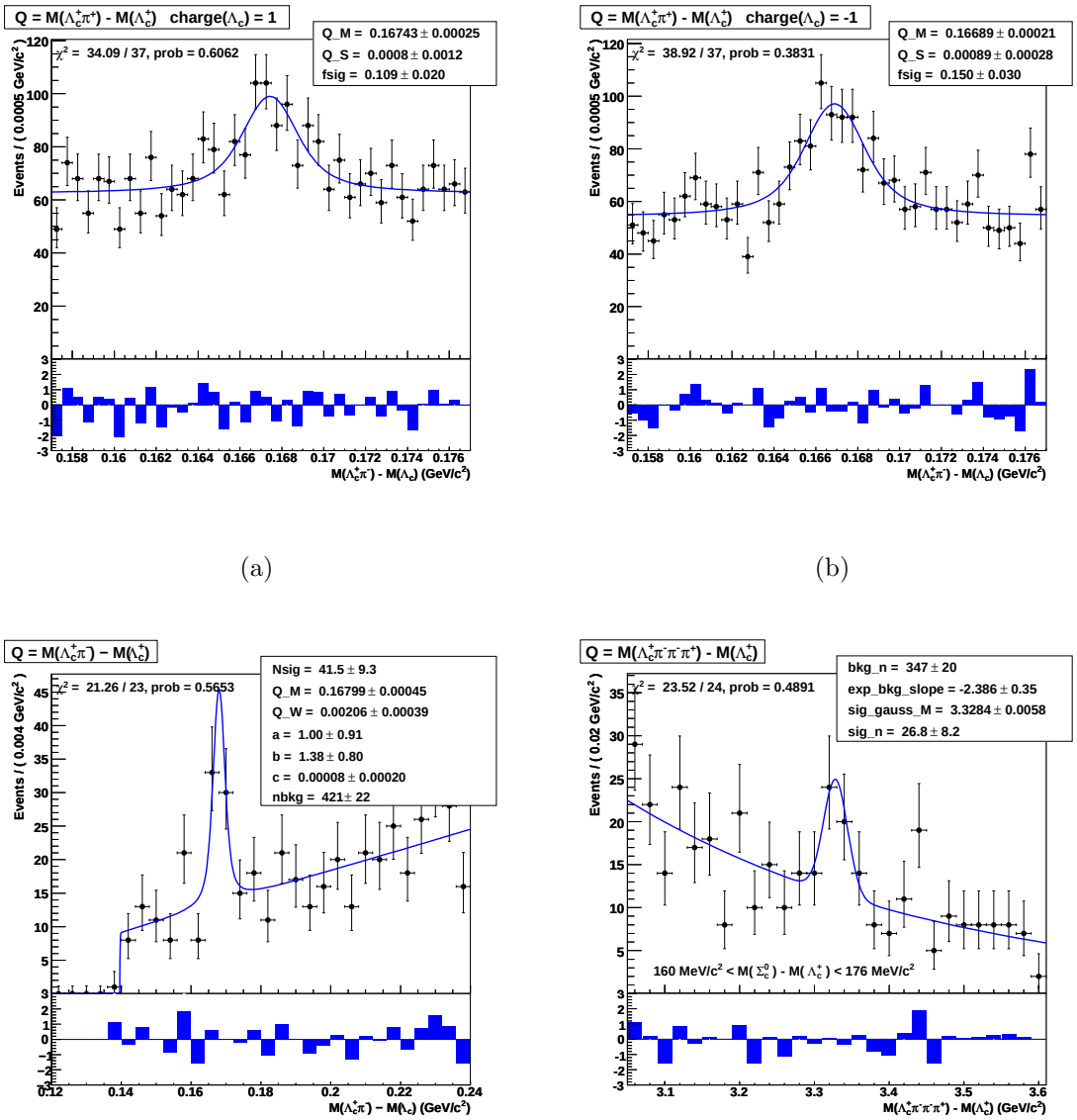

Figure 5.9: *ΔM^- distribution of the $\Sigma_c(2455)^0$ candidates in the left sideband region for **particles** 5.9(a) and **antiparticles** 5.9(b) with overlaid the best fit (blue curve). 5.9(c): ΔM^- distribution corresponding to $\Sigma_c(2455)^0$ resonance in the Λ_b^0 mass window with $\Lambda_c(2595)^+$ and $\Lambda_c(2625)^+$ vetoed, with overlaid the best fit (blue curve). 5.9(d): ΔM^{--+} distribution in the $\Sigma_c(2455)^0$ signal mass window $160\,\mathrm{MeV/c^2} < \Delta M^+ < 176\,\mathrm{MeV/c^2}$ with overlaid the best fit (blue curve).*

5.3. Yield of $\Lambda_b^0 \to \Lambda_c^+\pi^-\pi^+\pi^-$ Final State without Charmed Resonances

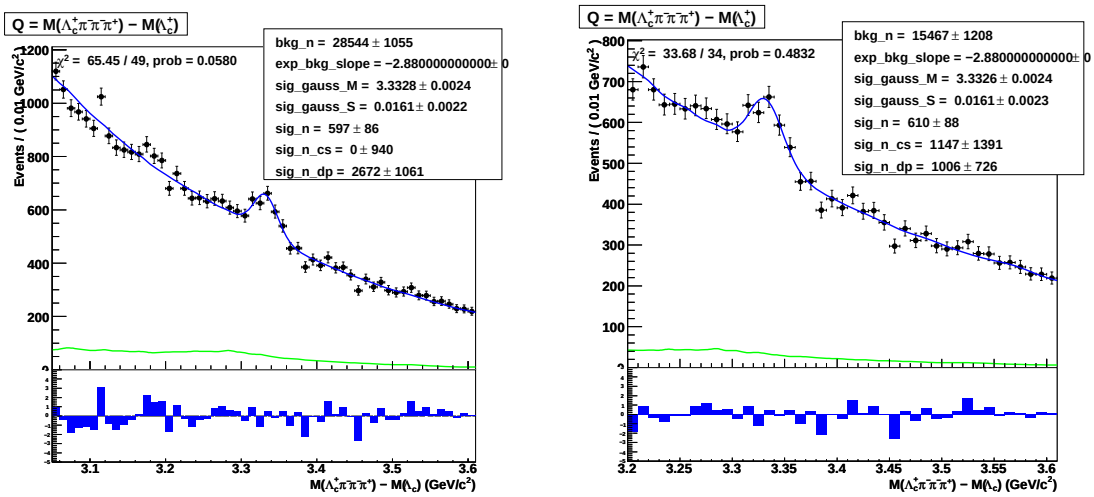

(a) (b)

Figure 5.10: *ΔM^{--+} distribution in [3.05-4.01]GeV/c^2 5.10(a) and in [3.2-4.01]GeV/c^2 5.10(b) mass range, with charmed resonant decay modes removed with the cuts $\Delta M^{+-} > 0.380\,\mathrm{GeV/c^2}$, $\Delta M^{+} > 0.190\,\mathrm{GeV/c^2}$ and $\Delta M^{-} > 0.190\,\mathrm{GeV/c^2}$ with overlaid the best fit (blue curve). The background modeling assumes an exponential with floating contribution and fixed slope plus the floating contribution of the $\overline{B}{}^0_{(s)} \to D^{(*)+}_{(s)}\pi^-\pi^+\pi^-$ (with inclusive $D^{(*)+}_{(s)}$ decays) templates and the floating contribution of the template of the $B^0 \to$ Inclusive decay; the best fit contribution is overlaid (green curve).*

Chapter 6

Measurement of Relative Branching Fractions

In this Chapter we describe the measurement of the following relative branching fractions:

$\mathcal{B}(\Lambda_b^0 \to \Lambda_c(2595)^+\pi^- \to \Lambda_c^+\pi^-\pi^+\pi^-)/\mathcal{B}(\Lambda_b^0 \to \Lambda_c^+\pi^-\pi^+\pi^-(all))$
$\mathcal{B}(\Lambda_b^0 \to \Lambda_c(2625)^+\pi^- \to \Lambda_c^+\pi^-\pi^+\pi^-)/\mathcal{B}(\Lambda_b^0 \to \Lambda_c^+\pi^-\pi^+\pi^-(all))$
$\mathcal{B}(\Lambda_b^0 \to \Sigma_c(2455)^{++}\pi^-\pi^- \to \Lambda_c^+\pi^-\pi^+\pi^-)/\mathcal{B}(\Lambda_b^0 \to \Lambda_c^+\pi^-\pi^+\pi^-(all))$
$\mathcal{B}(\Lambda_b^0 \to \Sigma_c(2455)^0\pi^+\pi^- \to \Lambda_c^+\pi^-\pi^+\pi^-)/\mathcal{B}(\Lambda_b^0 \to \Lambda_c^+\pi^-\pi^+\pi^-(all))$
$\mathcal{B}(\Lambda_b^0 \to \Lambda_c^+\rho^0\pi^- + \Lambda_b^0 \to \Lambda_c^+\pi^-\pi^+\pi^-(other) \to \Lambda_c^+\pi^-\pi^+\pi^-)/\mathcal{B}(\Lambda_b^0 \to \Lambda_c^+\pi^-\pi^+\pi^-(all))$
$\mathcal{B}(\Lambda_b^0 \to \Lambda_c(2595)^+\pi^- \to \Lambda_c^+\pi^-\pi^+\pi^-)/\mathcal{B}(\Lambda_b^0 \to \Lambda_c(2625)^+\pi^- \to \Lambda_c^+\pi^-\pi^+\pi^-)$
$\mathcal{B}(\Lambda_b^0 \to \Sigma_c(2455)^{++}\pi^-\pi^- \to \Lambda_c^+\pi^-\pi^+\pi^-)/\mathcal{B}(\Lambda_b^0 \to \Sigma_c(2455)^0\pi^+\pi^-)$
$\mathcal{B}(\Lambda_b^0 \to \Lambda_c(2625)^+\pi^- \to \Lambda_c^+\pi^-\pi^+\pi^-)/\mathcal{B}(\Lambda_b^0 \to \Sigma_c(2455)^{++}\pi^-\pi^-)$

where $\Lambda_b^0 \to \Lambda_c^+\pi^-\pi^+\pi^-(all)$ *indicates the* Λ_b^0 *inclusive decay and the* $\Lambda_b^0 \to \Lambda_c^+\pi^-\pi^+\pi^-(other)$ *includes the* $\Lambda_b^0 \to \Lambda_c^+\pi^-\pi^+\pi^-(nr)$*, with the three pions system not resonant (nr), when assuming a null contribution from the* $\Lambda_b^0 \to \Lambda_c^+ a_1(1260)^- \to \Lambda_c^+\rho^0\pi^- \to \Lambda_c^+\pi^-\pi^+\pi^-$*, or, a* $\Lambda_b^0 \to \Lambda_c^+ a_1(1260)^- \to \Lambda_c^+\rho^0\pi^- \to \Lambda_c^+\pi^-\pi^+\pi^-$ *when assuming null the contribution from the* $\Lambda_b^0 \to \Lambda_c^+\pi^-\pi^+\pi^-(nr)$*. To measure all of them, we use the yields determined in the previous Chapter and the MC efficiencies of the* Λ_b^0 *decay modes.*
The systematic uncertainty affecting these measurements will be discussed in the next Chapter.

6.1 Overview

The second goal of this Thesis is the measurement of the above relative BR. The relative BR $\mathcal{B}(\Lambda_b^0 \to \Lambda_c(2595)^+\pi^- \to \Lambda_c^+\pi^-\pi^+\pi^-)/\mathcal{B}(\Lambda_b^0 \to \Lambda_c^+\pi^-\pi^+\pi^-(all))$, indicating with the symbol A the state $\Lambda_c(2595)^+\pi^-$, can be expressed as:

$$\frac{\mathcal{B}(\Lambda_b^0 \to A \to \Lambda_c^+\pi^-\pi^+\pi^-)}{\mathcal{B}(\Lambda_b^0 \to \Lambda_c^+\pi^-\pi^+\pi^-(all))} = \frac{N(\Lambda_b^0 \to \Lambda_c(2595)^+\pi^- \to pK^-\pi^+\pi^-\pi^+\pi^-)_{prod}}{N(\Lambda_b^0 \to \Lambda_c^+\pi^-\pi^+\pi^-(all) \to pK^-\pi^+\pi^-\pi^+\pi^-)_{prod}} \tag{6.1}$$

where we indicate with $N(\Lambda_b^0 \to \Lambda_c(2595)^+\pi^- \to pK^-\pi^+\pi^-\pi^+\pi^-)_{prod}$ and $N(\Lambda_b^0 \to \Lambda_c^+\pi^-\pi^+\pi^-(all) \to pK^-\pi^+\pi^-\pi^+\pi^-)_{prod}$ the corresponding number of $\Lambda_b^0 \to \Lambda_c(2595)^+\pi^-$ and $\Lambda_b^0 \to \Lambda_c^+\pi^-\pi^+\pi^-$ produced in the $p\bar{p}$ collisions. This same ratio, can be espressed:

$$\frac{N(A)_{obs}}{(N(A)_{obs} + N(B)_{obs} \times \frac{\varepsilon_A}{\varepsilon_B} + N(C)_{obs} \times \frac{\varepsilon_A}{\varepsilon_C} + N(D)_{obs} \times \frac{\varepsilon_A}{\varepsilon_D} + N(E)_{obs} \times \frac{\varepsilon_A}{\varepsilon_E})} \tag{6.2}$$

In this formula, we indicated with the symbol B the state $\Lambda_c(2625)^+\pi^-$, with C the state $\Sigma_c(2455)^{++}\pi^-\pi^-$, with D the state $\Sigma_c(2455)^0\pi^+\pi^-$, with E we assume, for the moment, $\Lambda_c^+\rho^0\pi^-$+ $\Lambda_c^+\pi^-\pi^+\pi^-(nr)$; $N(j)_{obs}$, with $(j = A, B, C, D, E)$, is the yield of the j^{th} decay mode, as determined in Chap. 5, and $\varepsilon(j)$ is the absolute efficiency of each decay mode. For the number of events $N(j)_{obs}$ and efficiencies $\varepsilon(j)$ we have:

- $N(A) = N(\Lambda_b^0 \to \Lambda_c(2595)^+\pi^- \to \Lambda_c^+\pi^-\pi^+\pi^-)_{obs}$
- $N(B) = N(\Lambda_b^0 \to \Lambda_c(2625)^+\pi^- \to \Lambda_c^+\pi^-\pi^+\pi^-)_{obs}$
- $\dfrac{\varepsilon(A)}{\varepsilon(B)} = \dfrac{\varepsilon(\Lambda_b^0 \to \Lambda_c(2595)^+\pi^- \to \Lambda_c^+\pi^-\pi^+\pi^-)}{\varepsilon(\Lambda_b^0 \to \Lambda_c(2625)^+\pi^- \to \Lambda_c^+\pi^-\pi^+\pi^-)}$
- $N(C) = N(\Lambda_b^0 \to \Sigma_c(2455)^{++}\pi^-\pi^- \to \Lambda_c^+\pi^-\pi^+\pi^-)_{obs}$
- $\dfrac{\varepsilon(A)}{\varepsilon(C)} = \dfrac{\varepsilon(\Lambda_b^0 \to \Lambda_c(2595)^+\pi^- \to \Lambda_c^+\pi^-\pi^+\pi^-)}{\varepsilon(\Lambda_b^0 \to \Sigma_c(2455)^{++}\pi^-\pi^- \to \Lambda_c^+\pi^-\pi^+\pi^-)}$
- $N(D) = N(\Lambda_b^0 \to \Sigma_c(2455)^0\pi^+\pi^- \to \Lambda_c^+\pi^-\pi^+\pi^-)_{obs}$
- $\dfrac{\varepsilon(A)}{\varepsilon(D)} = \dfrac{\varepsilon(\Lambda_b^0 \to \Lambda_c(2595)^+\pi^- \to \Lambda_c^+\pi^-\pi^+\pi^-)}{\varepsilon(\Lambda_b^0 \to \Sigma_c(2455)^0\pi^+\pi^- \to \Lambda_c^+\pi^-\pi^+\pi^-)}$

- $N(E) = N(\Lambda_c^+\rho^0\pi^- + \Lambda_c^+\pi^-\pi^+\pi^-(nr) \rightarrow \Lambda_c^+\pi^-\pi^+\pi^-)_{obs}$
- $$\frac{\varepsilon(A)}{\varepsilon(E)} = \frac{\varepsilon(\Lambda_b^0 \rightarrow \Lambda_c(2595)^+\pi^- \rightarrow \Lambda_c^+\pi^-\pi^+\pi^-)}{\varepsilon(\Lambda_b^0 \rightarrow \Lambda_c^+\rho^0\pi^- + \Lambda_b^0 \rightarrow \Lambda_c^+\pi^-\pi^+\pi^-(nr) \rightarrow \Lambda_c^+\pi^-\pi^+\pi^-)}$$

To the mixed E state, without charmed resonances, in addition to the $\Lambda_b^0 \rightarrow \Lambda_c^+\rho^0\pi^-$ and $\Lambda_b^0 \rightarrow \Lambda_c^+\pi^-\pi^+\pi^-(nr)$ also the $\Lambda_b^0 \rightarrow \Lambda_c^+ a_1(1260)^-$ can in principle contribute (the BRs of the $a_1(1260)^-$ are not measured), since it may decay into $\rho^0\pi^-$ with the $\rho^0 \rightarrow \pi^+\pi^-$ [1]. In this case, at the production, the mixed state E is due to a combination of the Λ_b^0 decay modes $\Lambda_c^+\rho^0\pi^-$, $\Lambda_c^+\pi^-\pi^+\pi^-(nr)$ (with the three pions system not resonant) and $\Lambda_c^+ a_1(1260)^-$, in unknown proportions.
Since we do not know the proportions of the three decay modes in the mixed state E, we assumed proportions (1/2, 1/2, 0) respectively for $\Lambda_c^+\rho^0\pi^-$, $\Lambda_c^+\pi^-\pi^+\pi^-(nr)$, and $\Lambda_c^+ a_1(1260)^-$ to compute the overall selection efficiency $\varepsilon(E)$. As a consequence, the efficiency $\varepsilon(E)$ is evaluated as the average of the relative efficiencies of $\Lambda_c^+\rho^0\pi^-$ and $\Lambda_c^+\pi^-\pi^+\pi^-(nr)$ (see Sec. 6.2). This assumption is important since the selection efficiencies of these two decay modes are different and the resulting efficiency for the sum of $\Lambda_c^+\rho^0\pi^-$ and $\Lambda_c^+\pi^-\pi^+\pi^-(nr)$ depends on the value of the assumed fractions. We determined the absolute efficiency of each decay mode using the MC samples. These samples are described in Chap. 4 for all the Λ_b^0 decays above with the exception of the $\Lambda_b^0 \rightarrow \Lambda_c^+ a_1(1260)^- \rightarrow \Lambda_c^+\rho^0\pi^- \rightarrow \Lambda_c^+\pi^-\pi^+\pi^-$. Also for this decay mode a MC sample was generated, following the same procedure adopted in Chap. 4 as for the others MC samples, and we forced the $a_1(1260)^-$ to decay into $\rho^0\pi^-$ with the $\rho^0 \rightarrow \pi^+\pi^-$. In the next section we show (see Tab. 6.1) that the absolute efficiency of this latter decay mode can be assumed equal to the one of the $\Lambda_b^0 \rightarrow \Lambda_c^+\pi^-\pi^+\pi^-(nr)$, since the two efficiencies agree. This means that if we measure $\mathcal{B}(\Lambda_b^0 \rightarrow \Lambda_c^+\rho^0\pi^- + \Lambda_c^+\pi^-\pi^+\pi^-(nr) \rightarrow \Lambda_c^+\pi^-\pi^+\pi^-)/\mathcal{B}(\Lambda_b^0 \rightarrow \Lambda_c^+\pi^-\pi^+\pi^-(all))$ assuming fractions (1/2, 1/2, 0) we obtain the same result as $\mathcal{B}(\Lambda_b^0 \rightarrow \Lambda_c^+\rho^0\pi^- + \Lambda_c^+ a_1(1260)^-) \rightarrow \Lambda_c^+\pi^-\pi^+\pi^-)/\mathcal{B}(\Lambda_b^0 \rightarrow \Lambda_c^+\pi^-\pi^+\pi^-(all))$ with fractions (1/2, 0, 1/2). For this reason the relative BR of the E state can be witten: $\mathcal{B}(\Lambda_b^0 \rightarrow \Lambda_c^+\pi^-\pi^+\pi^-(other) \rightarrow \Lambda_c^+\pi^-\pi^+\pi^-)/\mathcal{B}(\Lambda_b^0 \rightarrow \Lambda_c^+\pi^-\pi^+\pi^-(all))$ where $\Lambda_b^0 \rightarrow \Lambda_c^+\pi^-\pi^+\pi^-(other)$ includes the $\Lambda_c^+\pi^-\pi^+\pi^-(nr)$, with the three pions system not resonant (nr), when assuming a null contribution from the $\Lambda_b^0 \rightarrow \Lambda_c^+ a_1(1260)^- \rightarrow \Lambda_c^+\rho^0\pi^- \rightarrow \Lambda_c^+\pi^-\pi^+\pi^-$ and proportions (1/2, 1/2, 0) , or a $\Lambda_b^0 \rightarrow \Lambda_c^+ a_1(1260)^- \rightarrow \Lambda_c^+\rho^0\pi^- \rightarrow \Lambda_c^+\pi^-\pi^+\pi^-$ when assuming null the contribution from the $\Lambda_b^0 \rightarrow \Lambda_c^+\pi^-\pi^+\pi^-(nr)$ and proportions (1/2, 0, 1/2). This will be further discussed in the next section. The potential contribution of the $\Lambda_c^+ a_1(1260)^-$, was considered later in the analysis and we have not resolutions to separate the individual contributions of the three decay modes, as it will be shown in Appendix D. The assumption we made is a choice and the systematic due to this hypothesis is evaluated in Sec. 7.2.

The relative branching fractions of the other decay modes can be determined using the following formulas:

$$\frac{\mathcal{B}(\Lambda_b^0 \to \Lambda_c(2625)^+\pi^- \to \Lambda_c^+\pi^-\pi^+\pi^-)}{\mathcal{B}(\Lambda_b^0 \to \Lambda_c^+\pi^-\pi^+\pi^-(all))} = \frac{N(B)_{obs}}{(N(A)_{obs} \times \frac{\varepsilon_B}{\varepsilon_A} + N(B)_{obs} + N(C)_{obs} \times \frac{\varepsilon_B}{\varepsilon_C} + N(D)_{obs} \times \frac{\varepsilon_B}{\varepsilon_D} + N(E)_{obs} \times \frac{\varepsilon_B}{\varepsilon_E})} \tag{6.3}$$

$$\frac{\mathcal{B}(\Lambda_b^0 \to \Sigma_c(2455)^{++}\pi^-\pi^- \to \Lambda_c^+\pi^-\pi^+\pi^-)}{\mathcal{B}(\Lambda_b^0 \to \Lambda_c^+\pi^-\pi^+\pi^-(all))} = \frac{N(C)_{obs}}{(N(A)_{obs} \times \frac{\varepsilon_C}{\varepsilon_A} + N(B)_{obs} \times \frac{\varepsilon_C}{\varepsilon_B} + N(C)_{obs} + N(D)_{obs} \times \frac{\varepsilon_C}{\varepsilon_D} + N(E)_{obs} \times \frac{\varepsilon_C}{\varepsilon_E})} \tag{6.4}$$

$$\frac{\mathcal{B}(\Lambda_b^0 \to \Sigma_c(2455)^0\pi^+\pi^- \to \Lambda_c^+\pi^-\pi^+\pi^-)}{\mathcal{B}(\Lambda_b^0 \to \Lambda_c^+\pi^-\pi^+\pi^-(all))} = \frac{N(D)_{obs}}{(N(A)_{obs} \times \frac{\varepsilon_D}{\varepsilon_A} + N(B)_{obs} \times \frac{\varepsilon_D}{\varepsilon_B} + N(C)_{obs} \times \frac{\varepsilon_D}{\varepsilon_C} + N(D)_{obs} + N(E)_{obs} \times \frac{\varepsilon_D}{\varepsilon_E})} \tag{6.5}$$

$$\frac{\mathcal{B}(\Lambda_b^0 \to \Lambda_c^+\rho^0\pi^- + \Lambda_b^0 \to \Lambda_c^+\pi^-\pi^+\pi^-(nr)) \to \Lambda_c^+\pi^-\pi^+\pi^-)}{\mathcal{B}(\Lambda_b^0 \to \Lambda_c^+\pi^-\pi^+\pi^-(all))} = \frac{N(E)_{obs}}{(N(A)_{obs} \times \frac{\varepsilon_E}{\varepsilon_A} + N(B)_{obs} \times \frac{\varepsilon_E}{\varepsilon_B} + N(C)_{obs} \times \frac{\varepsilon_E}{\varepsilon_C} + N(D)_{obs} \times \frac{\varepsilon_E}{\varepsilon_D} + N(E)_{obs})} \tag{6.6}$$

$$\frac{\mathcal{B}(\Lambda_b^0 \to \Lambda_c(2595)^+\pi^- \to \Lambda_c^+\pi^-\pi^+\pi^-)}{\mathcal{B}(\Lambda_b^0 \to \Lambda_c(2625)^+\pi^- \to \Lambda_c^+\pi^-\pi^+\pi^-)} = \frac{N(A)_{obs}}{N(B)_{obs}}\frac{\varepsilon(B)}{\varepsilon(A)} \tag{6.7}$$

$$\frac{\mathcal{B}(\Lambda_b^0 \to \Sigma_c(2455)^{++}\pi^-\pi^- \to \Lambda_c^+\pi^-\pi^+\pi^-)}{\mathcal{B}(\Lambda_b^0 \to \Sigma_c(2455)^0\pi^+\pi^- \to \Lambda_c^+\pi^-\pi^+\pi^-)} = \frac{N(C)_{obs}}{N(D)_{obs}}\frac{\varepsilon(D)}{\varepsilon(C)} \tag{6.8}$$

$$\frac{\mathcal{B}(\Lambda_b^0 \to \Lambda_c(2625)^+\pi^- \to \Lambda_c^+\pi^-\pi^+\pi^-)}{\mathcal{B}(\Lambda_b^0 \to \Sigma_c(2455)^{++}\pi^-\pi^- \to \Lambda_c^+\pi^-\pi^+\pi^-)} = \frac{N(B)_{obs}}{N(C)_{obs}}\frac{\varepsilon(C)}{\varepsilon(B)} \tag{6.9}$$

In the following we describe the evaluation of the relative efficiencies and the extraction of the relative branching fractions. All the systematic affecting these measurements will be discussed in detail in Chap. 7.

6.2 Relative Efficiencies

The MC samples described in Chap. 4 and the MC sample of the $\Lambda_b^0 \to \Lambda_c^+ a_1(1260)^- \to \Lambda_c^+ \rho^0 \pi^- \to \Lambda_c^+ \pi^- \pi^+ \pi^-$ are used to estimate the relative efficiencies $\varepsilon_{ij}^{rel} = \varepsilon_i / \varepsilon_j$ necessary to perform the relative branching fractions measurements. Tab. 6.1 reports the absolute efficiencies for each Λ_b^0 decay mode as estimated with MC for the three TTT scenarios.

Λ_b^0 Decay Mode	#Generated	#ScLow	ε(x10^{-4})	#ScA	ε(x10^{-4})	#ScC	ε(x10^{-4})
$\Lambda_c(2595)^+\pi^-$	4943361	4903	9.92±0.14	3735	7.56±0.12	2868	5.80±0.11
$\Lambda_c(2625)^+\pi^-$	4943361	4811	9.73±0.14	3702	7.49±0.12	2770	5.60±0.11
$\Sigma_c(2455)^{++}\pi^-\pi^-$	7489941	6321	8.44±0.11	4681	6.25±0.09	3213	4.29±0.08
$\Sigma_c(2455)^0\pi^+\pi^-$	7489941	1862	2.49±0.06	1407	1.88±0.05	941	1.26±0.04
$\Lambda_c^+\rho^0\pi^-$	7489941	3724	4.97±0.08	2735	3.65±0.07	1710	2.28±0.05
$\Lambda_c^+\pi^-\pi^+\pi^-(nr)$	7489941	2816	3.76±0.07	2023	2.70±0.06	1270	1.70±0.05
$\Lambda_c^+ a_1(1260)^-$	6388979	2382	3.72±0.08	1688	2.64±0.06	1013	1.59±0.05

Table 6.1: *Absolute efficiencies for the three trigger scenarios (trigger confirmation+optimized cuts). We used "ScLow" for* `B_CHARM_LOWPT`*, "ScA" for* `B_CHARM`*, and "ScC" for* `B_CHARM_HIGHPT`*.*

In these samples, the Λ_b^0 are reconstructed with the same prescription as for real data, and online[1] and offline requirements are applied. Also, on each MC sample, the ΔM^{+-}, ΔM^+ and ΔM^- cuts necessary to select a specific Λ_b^0 decay modes are applied (see Tab. 4.10). From Tab. 6.1, the efficiency of the $\Lambda_b^0 \to \Sigma_c(2455)^0\pi^+\pi^-$ decay mode is significantly lower than the efficiency of the $\Lambda_b^0 \to \Sigma_c(2455)^{++}\pi^-\pi^-$ decay mode. This is due to the kinematical cut applied at the skimming level, requiring that the transverse momentum of the pion, produced in the Λ_c^+ decay, is larger than the transverse momentum of the same charge pion produced in the Λ_b^0 decay. This request has a large efficiency on $\Lambda_b^0 \to \Sigma_c(2455)^{++}\pi^-\pi^-$ since in this case the π^+ from Λ_b^0 is produced in the $\Sigma_c(2455)^{++}$ decay and it is consequently soft, while it has a lower efficiency on $\Lambda_b^0 \to \Sigma_c(2455)^0\pi^+\pi^-$ since in this case the π^+ from Λ_b^0 is not produced in the $\Sigma_c(2455)^0$ decay and it is not necessarily soft. Tab. 6.1 shows, as mentioned in the previous section, that the absolute efficiency of the $\Lambda_b^0 \to \Lambda_c^+ a_1(1260)^-$ decay mode, with $a_1(1260)^- \to \pi^-\pi^+\pi^-$ agrees with the efficiency for the $\Lambda_b^0 \to \Lambda_c^+\pi^-\pi^+\pi^-(nr)$. We assume the two efficiencies equal to the $\Lambda_b^0 \to \Lambda_c^+\pi^-\pi^+\pi^-(nr)$ (see Sec. 6.1) and all the results about efficiency or relative efficiencies for the $\Lambda_c^+\pi^-\pi^+\pi^-(nr)$ are valid also for the $\Lambda_c^+ a_1(1260)^-$.

For these three trigger scenarios we computed the relative efficiencies among all the Λ_b^0 decay modes. Tab. 6.2 reports the relative efficiencies, showing that the variation of the relative efficiencies between `B_CHARM_LOWPT` and `B_CHARM` is com-

[1] In this case explicitly the specified trigger path have to be offline confirmed.

ScLow						
	$\Lambda_c(2595)^+\pi^-$	$\Lambda_c(2625)^+\pi^-$	$\Sigma_c^{++}\pi^-\pi^-$	$\Sigma_c^0\pi^-$	$\Lambda_c^+\rho^0\pi^-$	$\Lambda_c^+\pi^-\pi^+\pi^-(nr)/\Lambda_c^+a_1(1260)^-$
$\Lambda_c(2595)^+\pi^-$	1	1.019±0.02	1.175±0.02	3.990±0.10	1.995±0.04	2.638±0.06
$\Lambda_c(2625)^+\pi^-$	0.981±0.02	1	1.153±0.02	3.915±0.10	1.957±0.04	2.589±0.06
$\Sigma_c^{++}\pi^-\pi^-$	0.851±0.01	0.867±0.01	1	3.395±0.09	1.697±0.04	2.245±0.05
$\Sigma_c^0\pi^+\pi^-$	0.251±0.01	0.255±0.01	0.295±0.01	1	0.500±0.01	0.661±0.02
$\Lambda_c^+\rho^0\pi^-$	0.501±0.01	0.511±0.01	0.589±0.01	2.000±0.06	1	1.322±0.03
$\Lambda_c^+\pi^-\pi^+\pi^-(nr)/\Lambda_c^+a_1(1260)^-$	0.379±0.01	0.386±0.01	0.445±0.01	1.513±0.05	0.756±0.02	1
ScA						
	$\Lambda_c(2595)^+\pi^-$	$\Lambda_c(2625)^+\pi^-$	$\Sigma_c^{++}\pi^-\pi^-$	$\Sigma_c^0\pi^-$	$\Lambda_c^+\rho^0\pi^-$	$\Lambda_c^+\pi^-\pi^+\pi^-(nr)/\Lambda_c^+a_1(1260)^-$
$\Lambda_c(2595)^+\pi^-$	1	1.009±0.02	1.209±0.02	4.022±0.12	2.069±0.05	2.797±0.07
$\Lambda_c(2625)^+\pi^-$	0.991±0.02	1	1.198±0.02	3.987±0.12	2.051±0.05	2.773±0.07
$\Sigma_c^{++}\pi^-\pi^-$	0.827±0.02	0.835±0.02	1	3.327±0.10	1.712±0.04	2.314±0.06
$\Sigma_c^0\pi^+\pi^-$	0.249±0.01	0.251±0.01	0.301±0.01	1	0.514±0.02	0.696±0.02
$\Lambda_c^+\rho^0\pi^-$	0.483±0.01	0.488±0.01	0.584±0.01	1.944±0.06	1	1.352±0.04
$\Lambda_c^+\pi^-\pi^+\pi^-(nr)/\Lambda_c^+a_1(1260)^-$	0.357±0.01	0.361±0.01	0.432±0.01	1.438±0.05	0.740±0.02	1
ScLow+ScA						
	$\Lambda_c(2595)^+\pi^-$	$\Lambda_c(2625)^+\pi^-$	$\Sigma_c^{++}\pi^-\pi^-$	$\Sigma_c^0\pi^-$	$\Lambda_c^+\rho^0\pi^-$	$\Lambda_c^+\pi^-\pi^+\pi^-(nr)/\Lambda_c^+a_1(1260)^-$
$\Lambda_c(2595)^+\pi^-$	1	1.014±.01±.005	1.192±.02±.017	4.006±.12±.016	2.032±.05±.037	2.718±.07±.080
$\Lambda_c(2625)^+\pi^-$	0.986±.02±.005	1	1.176±.02±.023	3.951±.12±.036	2.004±.05±.047	2.681±.07±.092
$\Sigma_c^{++}\pi^-\pi^-$	0.839±.02±.012	0.851±.02±.016	1	3.361±.10±.034	1.705±.04±.008	2.280±.06±.035
$\Sigma_c^0\pi^+\pi^-$	0.250±.01±.001	0.253±.01±.002	0.298±.01±.003	1	0.507±.02±.007	0.679±.02±.018
$\Lambda_c^+\rho^0\pi^-$	0.492±.01±.009	0500±.01±.012	0.587±.01±.003	1.972±.06±.028	1	1.337±.04±.015
$\Lambda_c^+\pi^-\pi^+\pi^-(nr)/\Lambda_c^+a_1(1260)^-$	0.368±.01±.011	0.374±.01±.013	0.439±.01±.007	1.478±.05±.038	0.748±.02±.008	1
ScC						
	$\Lambda_c(2595)^+\pi^-$	$\Lambda_c(2625)^+\pi^-$	$\Sigma_c^{++}\pi^-\pi^-$	$\Sigma_c^0\pi^-$	$\Lambda_c^+\rho^0\pi^-$	$\Lambda_c^+\pi^-\pi^+\pi^-(nr)/\Lambda_c^+a_1(1260)^-$
$\Lambda_c(2595)^+\pi^-$	1	1.035±0.03	1.352±0.02	4.617±0.11	2.541±0.05	3.422±0.08
$\Lambda_c(2625)^+\pi^-$	0.966±0.02	1	1.306±0.02	4.460±0.10	2.454±0.05	3.305±0.08
$\Sigma_c^{++}\pi^-\pi^-$	0.739±0.02	0.766±0.02	1	3.414±0.11	1.879±0.05	2.530±0.08
$\Sigma_c^0\pi^+\pi^-$	0.217±0.01	0.224±0.01	0.293±0.01	1	0.550±0.02	0.741±0.03
$\Lambda_c^+\rho^0\pi^-$	0.394±0.01	0.407±0.01	0.532±0.01	1.817±0.06	1	1.346±0.05
$\Lambda_c^+\pi^-\pi^+\pi^-(nr)/\Lambda_c^+a_1(1260)^-$	0.292±0.01	0.303±0.01	0.395±0.01	1.350±0.05	0.743±0.02	1

Table 6.2: *Relative efficiencies for B_CHARM_LOWPT (*ScLow*), B_CHARM (*ScA*) and B_CHARM_HIGHPT (*ScC*) triggers scenarios, computed using simply the absolute efficiencies reported in Tab. 6.1. Quoted errors are statistical. Relative efficiencies average between B_CHARM_LOWPT and B_CHARM (*ScLow+ScC*) where the first uncertainty is statistical while the second one is the maximum difference between the average value and the single value and it is taken as the systematic uncertainty due to the average.*

patible with the MC statistical error and the systematic uncertainty[2]. The relative efficiencies computed for B_CHARM_HIGHPT are not compatible with the efficiencies of the two lower momentum scenarios from which they differ significantly.

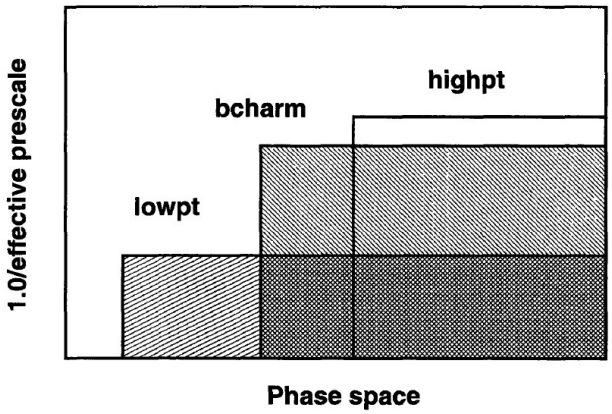

Figure 6.1: *A plot schematically representing the set of selection requirements of the trigger (phase space) versus the effective trigger prescale.*

Fig. 6.1 reports the data events selected versus the set of selection requirements (the three B_CHARM trigger scenarios) showing regions of overlapped events.
Due to their effective phase space overlap, duplicate events that passed different triggers are present, so we checked for these events in the data samples selected by the different trigger scenarios and dropped the extra one. The part of B_CHARM_LOWPT sample that is not a part of the B_CHARM_SCENA sample constitutes about 30% of the total dataset, and the part of phase space of B_CHARM_HIGHPT trigger, which is not a part of B_CHARM_SCENA trigger, is not used in this analysis for the reasons described above. The number of the events in that part is negligible because for the B_CHARM_HIGHPT trigger the selection requirements are tighter than for B_CHARM_SCENA. Thus, for the event to end up in the part of the sample with no shading (see Fig. 6.1) the corresponding B_CHARM_SCENA event has to be prescaled, otherwise the event is a part of B_CHARM_SCENA sample. For example it may happen that an event accepted by B_CHARM_HIGHPT is not accepted by B_CHARM or B_CHARM_LOWPT, even if kinematically B_CHARM_HIGHPT is a proper subsample of B_CHARM which is a proper subsample of B_CHARM_LOWPT. To properly take into account this effect it would be necessary to perform three independent analyses to the three independent samples collected by the three trigger scenarios and the knowledge of the prescale factors.

[2]See below for the evaluation of the systematic uncertainty on the relative efficiencies for each trigger path.

At the time of writing of this thesis, we did not have a method in order to determine the prescale factors[3] and we perform the following approximation: we remove the data collected only by the B_CHARM_HIGHPT trigger (i.e. events with the B_CHARM_HIGHPT trigger bit set on but the B_CHARM_LOWPT and B_CHARM trigger bits set off) from the dataset and for the analysis we use only the data collected by the B_CHARM_LOWPT or B_CHARM trigger scenarios.
For this sample we take as relative efficiencies the average of the relative efficiencies computed for the two individual trigger scenarios (see Tab. 6.2 third box). The differences between the average relative efficiencies and the individual relative efficiencies of the B_CHARM_LOWPT and B_CHARM trigger scenarios are taken as an additional source of systematic uncertainty (see Tab. 6.2 third box, where the first quoted uncertainty is the statistical uncertainty and the second one is the systematic uncertainty due to the average).
We remember that in this analysis we do not separate the contributions of the three decay modes that in principle can contribute to $\Lambda_b^0 \to \Lambda_c^+\pi^-\pi^+\pi^-$ without charmed resonances. Since we assumed, at production, proportions ($1/2$, $1/2$, 0) of $\Lambda_b^0 \to \Lambda_c^+\rho^0\pi^- \to \Lambda_c^+\pi^-\pi^+\pi^-$, $\Lambda_b^0 \to \Lambda_c^+\pi^-\pi^+\pi^-(nr)$ and $\Lambda_b^0 \to \Lambda_c^+a_1(1260)^- \to \Lambda_c^+\rho^0\pi^- \to \Lambda_c^+\pi^-\pi^+\pi^-$, we use the average of the relative efficiencies of the two contributing decay modes (reported in last two raws of Tab. 6.2 third box) to evaluate the relative efficiencies of the mixed E state in the above hypothesis. These relative efficiencies are the same when we assume at production proportions ($1/2$, 0, $1/2$) of $\Lambda_b^0 \to \Lambda_c^+\rho^0\pi^- \to \Lambda_c^+\pi^-\pi^+\pi^-$, $\Lambda_b^0 \to \Lambda_c^+\pi^-\pi^+\pi^-(nr)$ and $\Lambda_b^0 \to \Lambda_c^+a_1(1260)^- \to \Lambda_c^+\rho^0\pi^- \to \Lambda_c^+\pi^-\pi^+\pi^-$, since the absolute efficiency of $\Lambda_b^0 \to \Lambda_c^+a_1(1260)^- \to \Lambda_c^+\rho^0\pi^- \to \Lambda_c^+\pi^-\pi^+\pi^-$ was assumed equal to the $\Lambda_b^0 \to \Lambda_c^+\pi^-\pi^+\pi^-(nr)$.

The systematic on the measurements of the relative branching fractions due to these assumptions on the proportions is evaluated in Sec. 7.2.

6.3 Relative Branching Fractions

The relative branching fractions are extracted using the yields ($N(j), j = A, B, C, D, E$) determined in Chap. 5 (see Tab. 5.2) and the relative efficiencies (Tab. 6.2, third box) in the the equations from Eq. 6.2 to Eq. 6.9. The resulting relative branching fractions are reported in Tables from Tab. 6.4 to Tab. 6.8. The systematics affecting these measurements (and shown in Tables from Tab. 6.4 to Tab. 6.8, where for each measured quantity is reported the statistical and the systematic uncertainty) are discussed in next chapter. The results on the relative branching fractions are summarized in Tab. 6.3.

[3] In the updated analysis the prescale factors are determined using the method described in [96].

	Relative Branching Fractions (%)
$\frac{\mathcal{B}(\Lambda_b^0 \to \Lambda_c(2595)^+\pi^- \to \Lambda_c^+\pi^-\pi^+\pi^-)}{\mathcal{B}(\Lambda_b^0 \to \Lambda_c^+\pi^-\pi^+\pi^-(all))}$	$(2.5 \pm 0.6 \pm 0.5)$
$\frac{\mathcal{B}(\Lambda_b^0 \to \Lambda_c(2625)^+\pi^- \to \Lambda_c^+\pi^-\pi^+\pi^-)}{\mathcal{B}(\Lambda_b^0 \to \Lambda_c^+\pi^-\pi^+\pi^-(all))}$	$(6.2 \pm 1.0^{+1.0}_{-0.9})$
$\frac{\mathcal{B}(\Lambda_b^0 \to \Sigma_c(2455)^{++}\pi^-\pi^- \to \Lambda_c^+\pi^-\pi^+\pi^-)}{\mathcal{B}(\Lambda_b^0 \to \Lambda_c^+\pi^-\pi^+\pi^-(all))}$	$(5.2 \pm 1.1 \pm 0.8)$
$\frac{\mathcal{B}(\Lambda_b^0 \to \Sigma_c(2455)^0\pi^+\pi^- \to \Lambda_c^+\pi^-\pi^+\pi^-)}{\mathcal{B}(\Lambda_b^0 \to \Lambda_c^+\pi^-\pi^+\pi^-(all))}$	$(8.9 \pm 2.1^{+1.2}_{-1.0})$
$\frac{\mathcal{B}(\Lambda_b^0 \to \Lambda_c^+\rho^0\pi^- + \Lambda_b^0 \to \Lambda_c^+\pi^-\pi^+\pi^-(other) \to \Lambda_c^+\pi^-\pi^+\pi^-)}{\mathcal{B}(\Lambda_b^0 \to \Lambda_c^+\pi^-\pi^+\pi^-(all))}$	$(77.3 \pm 3.1^{+3.0}_{-3.3})$
$\frac{\mathcal{B}(\Lambda_b^0 \to \Lambda_c(2595)^+\pi^- \to \Lambda_c^+\pi^-\pi^+\pi^-)}{\mathcal{B}(\Lambda_b^0 \to \Lambda_c(2625)^+\pi^- \to \Lambda_c^+\pi^-\pi^+\pi^-)}$	$(40.3 \pm 9.8^{+2.3}_{-1.8})$
$\frac{\mathcal{B}(\Lambda_b^0 \to \Sigma_c(2455)^{++}\pi^-\pi^- \to \Lambda_c^+\pi^-\pi^+\pi^-)}{\mathcal{B}(\Lambda_b^0 \to \Sigma_c(2455)^0\pi^+\pi^- \to \Lambda_c^+\pi^-\pi^+\pi^-)}$	$(58.1 \pm 16.9^{+6.3}_{-9.1})$
$\frac{\mathcal{B}(\Lambda_b^0 \to \Lambda_c(2625)^+\pi^- \to \Lambda_c^+\pi^-\pi^+\pi^-)}{\mathcal{B}(\Lambda_b^0 \to \Sigma_c(2455)^{++}\pi^-\pi^- \to \Lambda_c^+\pi^-\pi^+\pi^-)}$	$(119.7 \pm 26.0^{+4.7}_{-9.1})$

Table 6.3: *Relative Branching Fractions in % measured in this work of Thesis. In these measurements the first uncertainty is statistical and the second one is systematic.*

	$\frac{\mathcal{B}(\Lambda_b^0 \to \Lambda_c(2595)^+\pi^- \to \Lambda_c^+\pi^-\pi^+\pi^-)}{\mathcal{B}(\Lambda_b^0 \to \Lambda_c^+\pi^-\pi^+\pi^-(all))}$	$\frac{\mathcal{B}(\Lambda_b^0 \to \Lambda_c(2625)^+\pi^- \to \Lambda_c^+\pi^-\pi^+\pi^-)}{\mathcal{B}(\Lambda_b^0 \to \Lambda_c^+\pi^-\pi^+\pi^-(all))}$	$\frac{\mathcal{B}(\Lambda_b^0 \to \Sigma_c^{++}\pi^-\pi^- \to \Lambda_c^+\pi^-\pi^+\pi^-)}{\mathcal{B}(\Lambda_b^0 \to \Lambda_c^+\pi^-\pi^+\pi^-(all))}$	$\frac{\mathcal{B}(\Lambda_b^0 \to \Sigma_c^0\pi^+\pi^- \to \Lambda_c^+\pi^-\pi^+\pi^-)}{\mathcal{B}(\Lambda_b^0 \to \Lambda_c^+\pi^-\pi^+\pi^-(all))}$
N(A)	46.6±9.7	46.6±9.7	46.6±9.7	46.6±9.7
N(B)	- 114±13 $\frac{\varepsilon_A}{\varepsilon_B}$ = 1.014	$\frac{\varepsilon_B}{\varepsilon_A}$ = 0.986 114±13	$\frac{\varepsilon_C}{\varepsilon_A}$ = 0.839 114±13	$\frac{\varepsilon_D}{\varepsilon_A}$ = 0.250 114±13
N(C)	81±15 $\frac{\varepsilon_A}{\varepsilon_C}$ = 1.192	- 81±15 $\frac{\varepsilon_B}{\varepsilon_C}$ = 1.176	$\frac{\varepsilon_C}{\varepsilon_B}$ = 0.851 81±15	$\frac{\varepsilon_D}{\varepsilon_B}$ = 0.253 81±15
N(D)	41.5±9.3 $\frac{\varepsilon_A}{\varepsilon_D}$ = 4.006	41.5±9.3 $\frac{\varepsilon_B}{\varepsilon_D}$ = 3.951	- 41.5±9.3 $\frac{\varepsilon_C}{\varepsilon_D}$ = 3.361	$\frac{\varepsilon_D}{\varepsilon_C}$ = 0.298 41.5±9.3 -
N(E)	610±88 $\frac{\varepsilon_A}{\varepsilon_E}$ = 2.375	610±88 $\frac{\varepsilon_B}{\varepsilon_E}$ = 2.343	610±88 $\frac{\varepsilon_C}{\varepsilon_E}$ = 1.993	610±88 $\frac{\varepsilon_D}{\varepsilon_E}$ = 0.593
Rel $\mathcal{B}$	2.487±0.58 %	6.168±0.96 %	5.152±1.08 %	8.870±2.07 %
Systematics				
Fit Errors				
Σ_c^{++}, Σ_c^0 Gauss Res	±0.01	±0.02	±0.11	+0.12-0.11
Comb. Exponential	±0.04	+0.09-0.10	+0.07-0.08	+0.11-0.13
Σ_c^{++} bck shape	+0.001-0.002	+0.001-0.006	+0.090-0.031	+0.003-0.008
Σ_c^0 bck shape	+0.000-0.001	+0.000-0.002	+0.000-0.002	+0.000-0.019
Cab Supp	+0.02	+0.11	+0.15	+0.25
Rel. Eff. Err				
MC Stat	±0.05	±0.12	±0.12	±0.2
Av. Trig Scen	±0.05	+0.16-0.15	±0.03	±0.12
Λ_b^0, Λ_c^+ Polar	+0.33-0.36	+0.56-0.59	+0.42-0.54	+0.24-0.19
Λ_c^+ res st	+0.06-0.05	±0.05	±0.05	+0.06-0.05
$\Lambda_c(2595)^+$ res st	+0.08-0.07	+0.005-0.006	±0.005	±0.006
$\Lambda_c(2625)^+$ res st	+0.0006	+0.0006	+0.002	+0.001
Av $\Lambda_c^+\rho^0\pi^-$ $\Lambda_c^+3\pi$	+0.32-0.25	+0.79-0.63	+0.66-0.52	+1.14-0.91
$p_T(\Lambda_b^0)$	-0.05	-0.04	-0.04	+0.0
$\tau(\Lambda_b^0)$	±0.01	+0.04-0.09	+0.05-0.00	+0.06-0.00
$\tau(\Lambda_c^+)$	±0.01	±0.04	+0.02-0.01	±0.01
Tot syst err	+0.48 % -0.46 %	+1.00 % -0.90 %	+0.83 % -0.78 %	+1.23 % -0.98 %

Table 6.4: *Relative branching fractions of the charmed resonant decay modes assuming no separation between $\Lambda_c^+\rho^0\pi^-$ and non resonant $\Lambda_c^+\pi^-\pi^+\pi^-(nr)$ or $\Lambda_c^+a_1(1260)^-$ decay modes.*

	$\frac{\mathcal{B}(\Lambda_b^0 \to \Lambda_c^+ \rho^0 \pi^- + \Lambda_b^0 \to \Lambda_c^+ \pi^- \pi^+ \pi^- (other) \to \Lambda_c^+ \pi^- \pi^+ \pi^-)}{\mathcal{B}(\Lambda_b^0 \to \Lambda_c^+ \pi^- \pi^+ \pi^- (all))}$
N(A)	46.6±9.7
	$\frac{\epsilon_E}{\epsilon_A} = 0.421$
N(B)	114±13
	$\frac{\epsilon_E}{\epsilon_B} = 0.427$
N(C)	81±15
	$\frac{\epsilon_E}{\epsilon_C} = 0.502$
N(D)	41.5±9.3
	$\frac{\epsilon_E}{\epsilon_D} = 1.686$
N(E)	610±88
	-
Rel $\mathcal{B}$	77.320±3.124 %
Systematics	
Fit Errors	
Σ_c^{++}, Σ_c^0 Gauss Res	+0.198-0.213
Comb. Exponential	+0.368-0.320
Σ_c^{++} bck shape	+0.025-0.074
Σ_c^0 bck shape	+0.000-0.016
Cab Supp	-0.543
Rel. Eff. Err	
MC Stat	+0.513-0.497
Av. Trig Scen	+0.361-0.383
Λ_b^0, Λ_c^+ Polar	+1.846-1.296
Λ_c^+ res st	+0.251-0.258
$\Lambda_c(2595)^+$ res st	+0.006-0.007
$\Lambda_c(2625)^+$ res st	+0.02
Av $\Lambda_c^+ \rho^0 \pi^-$ $\Lambda_c^+ 3\pi$	+2.279-2.858
$p_T(\Lambda_b^0)$	+0.178
$\tau(\Lambda_b^0)$	+0.155-0.038
$\tau(\Lambda_c^+)$	+0.049-0.147
Tot syst err	+3.049 % -3.283 %

Table 6.5: *Estimate of the relative branching fraction* $\mathcal{B}(\Lambda_b^0 \to \Lambda_c^+ \rho^0 \pi^- + \Lambda_b^0 \to \Lambda_c^+ \pi^- \pi^+ \pi^- (other) \to \Lambda_c^+ \pi^- \pi^+ \pi^-)/\mathcal{B}(\Lambda_b^0 \to \Lambda_c^+ \pi^- \pi^+ \pi^- (all))$ *assuming no separation between* $\Lambda_c^+ \rho^0 \pi^-$ *and non resonant* $\Lambda_c^+ \pi^- \pi^+ \pi^- (nr)$ *or* $\Lambda_c^+ a_1(1260)^-$ *decay modes.*

	$\frac{\mathcal{B}(\Lambda_b^0 \to \Lambda_c(2595)^+\pi^- \to \Lambda_c^+\pi^-\pi^+\pi^-)}{\mathcal{B}(\Lambda_b^0 \to \Lambda_c(2625)^+\pi^- \to \Lambda_c^+\pi^-\pi^+\pi^-)}$
$N(\Lambda_c(2595)^+\pi^-)$	46.6±9.7
	$\frac{\epsilon(\Lambda_c(2625)^+\pi^-)}{\epsilon(\Lambda_c(2595)^+\pi^-)} = 0.986$
$N(\Lambda_c(2625)^+\pi^-)$	114±13
Relative $\mathcal{B}$	40.313 % ± 9.787 %
Systematics	
Cab Supp	-0.455
MC Stat	+0.401-0.394
Av. Trig Scen	+0.200-0.198
Λ_b^0, Λ_c^+ Polar	+1.492-0.618
Λ_c^+ res st	+0.361-0.355
$\Lambda_c(2595)^+$ res st	+1.655-1.530
$\Lambda_c(2625)^+$ res st	+0.160
$p_T(\Lambda_b^0)$	-0.000
$\tau(\Lambda_b^0)$	+0.000-0.119
$\tau(\Lambda_c^+)$	+0.040-0.040
Tot syst err	+2.307 % -1.807 %

Table 6.6: *Measurement of the relative branching fraction* $\mathcal{B}(\Lambda_b^0 \to \Lambda_c(2595)^+\pi^- \to \Lambda_c^+\pi^-\pi^+\pi^-)/\mathcal{B}(\Lambda_b^0 \to \Lambda_c(2625)^+\pi^- \to \Lambda_c^+\pi^-\pi^+\pi^-)$ *assuming no separation between* $\Lambda_c^+\rho^0\pi^-$ *and non resonant* $\Lambda_c^+\pi^-\pi^+\pi^-(nr)$ *or* $\Lambda_c^+ a_1(1260)^-$ *decay modes.*

	$\frac{\mathcal{B}(\Lambda_b^0 \to \Sigma_c(2455)^{++}\pi^-\pi^- \to \Lambda_c^+\pi^-\pi^+\pi^-)}{\mathcal{B}(\Lambda_b^0 \to \Sigma_c(2455)^{0}\pi^+\pi^- \to \Lambda_c^+\pi^-\pi^+\pi^-)}$
$N(\Sigma_c(2455)^{++}\pi^-\pi^-)$	81±15
	$\frac{\epsilon(\Sigma_c^0\pi^-\pi^-)}{\epsilon(\Sigma_c^{++}\pi^+\pi^-)} = 0.298$
$N(\Sigma_c(2455)^{0}\pi^+\pi^-)$	41.5±9.3
Relative $\mathcal{B}$	58.164±16.882 %
Systematics	
Σ_c^{++}, Σ_c^0 Gauss Res	+1.089-0.347
Σ_c^{++} bck shape	+0.000-0.129
Σ_c^0 bck shape	+0.708-4.871
Cab Supp	-0.028
MC Stat	+1.781-1.678
Av. Trig Scen	+0.594-0.581
Λ_b^0, Λ_c^+ Polar	+5.615-7.309
Λ_c^+ res st	+1.653-1.563
$p_T(\Lambda_b^0)$	-0.172
$\tau(\Lambda_b^0)$	+0.018-0.103
$\tau(\Lambda_c^+)$	+0.104-0.086
Tot syst err	+6.284 % -9.107 %

Table 6.7: *Measurement of the relative branching fraction* $\mathcal{B}(\Lambda_b^0 \to \Sigma_c(2455)^{++}\pi^-\pi^- \to \Lambda_c^+\pi^-\pi^+\pi^-)/\mathcal{B}(\Lambda_b^0 \to \Sigma_c(2455)^{0}\pi^+\pi^- \to \Lambda_c^+\pi^-\pi^+\pi^-)$ *assuming no separation between* $\Lambda_c^+\rho^0\pi^-$ *and non resonant* $\Lambda_c^+\pi^-\pi^+\pi^-(nr)$ *or* $\Lambda_c^+ a_1(1260)^-$ *decay modes.*

	$\frac{\mathcal{B}(\Lambda_b^0 \to \Lambda_c(2625)^+\pi^- \to \Lambda_c^+\pi^-\pi^+\pi^-)}{\mathcal{B}(\Lambda_b^0 \to \Sigma_c(2455)^{++}\pi^-\pi^- \to \Lambda_c^+\pi^-\pi^+\pi^-)}$
$N(\Lambda_c(2625)^+\pi^-)$	114±13
	$\frac{\epsilon(\Sigma_c(2455)^{++}\pi^-\pi^-)}{\epsilon(\Lambda_c(2625)^+\pi^-)} = 0.851$
$N(\Sigma_c(2455)^{++}\pi^-\pi^-)$	81±15
Relative BR	1.197±0.260
Systematics	
Σ_c^{++} Gauss Res	+0.030-0.029
Σ_c^{++} bck shape	+0.008-0.021
Cab Supp	-0.013
MC Stat	±0.020
Av. Trig Scen	+0.024-0.023
Λ_b^0, Λ_c^+ Polar	+0.011-0.067
Λ_c^+ res st	±0.011
$\Lambda_c(2625)^+$ res st	-0.004
$p_T(\Lambda_b^0)$	-0.020
$\tau(\Lambda_b^0)$	+0.005-0.032
$\tau(\Lambda_c^+)$	+0.002-0.003
Tot syst err	+0.047 -0.091

Table 6.8: *Measurement of the relative branching fraction* $\mathcal{B}(\Lambda_b^0 \to \Lambda_c(2625)^+\pi^- \to \Lambda_c^+\pi^-\pi^+\pi^-)/\mathcal{B}(\Lambda_b^0 \to \Sigma_c(2455)^{++}\pi^-\pi^- \to \Lambda_c^+\pi^-\pi^+\pi^-)$ *assuming no separation between* $\Lambda_c^+\rho^0\pi^-$ *and non resonant* $\Lambda_c^+\pi^-\pi^+\pi^-(nr)$ *or* $\Lambda_c^+ a_1(1260)^-$ *decay modes.*

Chapter 7

Systematic Uncertainties

In this Chapter, we discuss how are determined the systematic uncertainties on the raw measurement of the relatives BRs, subject of the previous Chapter. Several sources of systematic can affect these measurements and can be grouped in two main categories: the ones related to the fits performed for the extraction of the signal yields, and the ones related to the estimate of the relatives efficiencies.

7.1 Systematic

Because of this analysis relies so heavily on the fit procedure adopted to extract the signal yields, and on the simulation to extract the ratio of the absolute efficiencies, a large number of systematic uncertainties must be considered to make sure that the measurement of the relative BRs is trustworthy. There are many sources of possible uncertainty, both the yields and the relative efficiencies uncertainties, which are enumerated in the following. We consider two classes of systematics: those due to the signal extraction (i.e. the number of signal events, the yields, estimated in our data samples using the fit procedure) and the additional systematics due to the extraction of the relative efficiencies. Tables from Tab. 6.4 to Tab. 6.8 show the summary of the systematic uncertainties considered in the measurement of the corresponding relative BRs (see the Tables). In these Tables each evaluated systematic uncertainty on a given BR is added in quadrature to determine the total systematic on it. In the following we describe in detail how these systematics have been evaluated.

7.1.1 Sources of Systematic affecting the Signal Yields Extraction

We consider several sources that can affect the yields extraction. For each source, the change in the yields is determined and the corresponding change in the relative BRs is assumed as contributing to the systematic uncertainty of the measureament. The sources considered are described below, and their contribution to the systematic uncertainties on the relative BRs is summarized from Tab. 6.4 to Tab. 6.8. Since the yields in the baseline analysis are extracted by a fit procedure, this class of sources is named *Fit Errors* in these Tables.

Fixing Gaussian resolution in $\Lambda_b^0 \to \Sigma_c(2455)^{++}\pi^-\pi^-$ and $\Lambda_b^0 \to \Sigma_c(2455)^0\pi^+\pi^-$ ($\Sigma_c(2455)^{++}$, $\Sigma_c(2455)^0$ Gaus Res)

To estimate the $\Lambda_b^0 \to \Sigma_c(2455)^{++}\pi^-\pi^-$ and $\Lambda_b^0 \to \Sigma_c(2455)^0\pi^+\pi^-$ yields, we performed the fits of the ΔM^+ and ΔM^- distributions fixing the Gaussian resolution to the central value, $1.0\,\mathrm{MeV/c^2}$, of the measured one $1.0 \pm 0.2\,\mathrm{MeV/c^2}$ (see Sec. 5.2.2 and Sec. 5.2.3). In Tab. 7.1 we report the yields variation of these decay modes, as a function of different choices (from $0.8\,\mathrm{MeV/c^2}$ to $1.2\,\mathrm{MeV/c^2}$ in step of $0.1\,\mathrm{MeV/c^2}$), of the Gaussian resolution. The resulting systematics on the relative branching fraction measurements is reported in Tab. 6.4, Tab. 6.5 and Tab. 6.7, where both $\Sigma_c(2455)^{++}$ and $\Sigma_c(2455)^0$ yields contribute and in Tab. 6.8 where the contribution is only due to the $\Sigma_c(2455)^{++}$.

Decay Mode	σ=0.8	σ=0.9	σ=1.0	σ=1.1	σ=1.2
$\Lambda_b^0 \to \Sigma_c(2455)^{++}\pi^-\pi^-$	79±15	80±15	81±15	82±15	83±15
$\Lambda_b^0 \to \Sigma_c(2455)^0\pi^+\pi^-$	40.9±9.2	41.2±9.3	41.5±9.3	41.8±9.4	42.2±9.4

Table 7.1: $\Lambda_b^0 \to \Sigma_c(2455)^{++}\pi^-\pi^-$ *and* $\Lambda_b^0 \to \Sigma_c(2455)^0\pi^+\pi^-$ *yields changing the Gaussian resolution,* σ*, used in the Voigtian fitting functions of Sec. 5.2.2 and Sec. 5.2.3.*

Combinatorial background shape in $\Lambda_b^0 \to \Lambda_c^+\rho\pi^-$ + $\Lambda_b^0 \to \Lambda_c^+\pi^-\pi^+\pi^-(nr)$ (Comb. Exponential)

To describe the combinatorial background shape in the modeling of ΔM^{--+} for this decay mode, we used an exponential function with a fixed slope. The fixed slope is the central value of the one returned by the fit (-2.88 ± 0.05), in the ΔM^{--+} high mass region [$3.6\,\mathrm{GeV/c^2}$ – $4.01\,\mathrm{GeV/c^2}$] (see Sec. 5.1 and Sec. 5.3). We repeated the fit to extract the Λ_b^0 yield of this decay mode by varying the

exponential slope of +0.05 (Λ_b^0 yield 623 ± 90) and of −0.05 (Λ_b^0 yield 599 ± 93). The associated systematics is evaluated as the resulting variation of the relative branching fractions and is reported in Tab. 6.4 and Tab. 6.5, since the measurement of the relative branching fractions reported in these Tables make use of the above yield.

Background shape in $\Lambda_b^0 \to \Sigma_c(2455)^{++}\pi^-\pi^-$ and $\Lambda_b^0 \to \Sigma_c(2455)^0\pi^+\pi^-$ ($\Sigma_c(2455)^{++}$ and $\Sigma_c(2455)^0$ bck shape)

The background shape in the $\Sigma_c(2455)^{++}$ and $\Sigma_c(2455)^0$ fits to extract the yield of these decay modes (Sec. 5.2.2 and Sec. 5.2.3) is an Argus function depending on four parameters; one is the threshold, fixed to the pion mass, and the other three determine the shape of the distribution. Since the three Argus parameters relative to the shape are floating in the fit, we have not to quote a systematic uncertainty associated to these parameters. We only have to evaluate the systematic uncertainty due to the assumpion that, in the fit, the threshold is fixed to the pion mass. In order to estimate the statistical uncertainty on the choice of the threshold, we use the $\Lambda_b^0 \to \Lambda_c(2595)^+\pi^-$ and $\Lambda_b^0 \to \Lambda_c(2625)^+\pi^-$ decay mode fits. We quote this uncertainty as the difference between the mass of the $\Lambda_c(2625)^+$ estimated by the fit (see Sec. 5.2.1) and the mass quoted from the PDG ($m(\Lambda_c(2625)^+)_{Fit} - m(\Lambda_c(2625)^+)_{PDG} = 0.1\,\mathrm{MeV/c^2}$). We choose the $\Lambda_c(2625)^+$ signal to estimate this uncertainty (and not the $\Lambda_b^0 \to \Lambda_c(2595)^+\pi^-$) since it has the largest statistics and, consequently, minimal statistical fluctuations. Besides, the $\Lambda_c(2625)^+ \to \Lambda_c^+\pi^+\pi^-$ is the resonant decay mode with largest momentum and it is expected to be the case with the largest error on the mass scale. The use of $0.1\,\mathrm{MeV/c^2}$ also for the uncertainty on $\Lambda_b^0 \to \Sigma_c(2455)^{++}\pi^-\pi^-$ and $\Lambda_b^0 \to \Sigma_c(2455)^0\pi^+\pi^-$ threshold is a conservative approximation. In Tab. 7.2 we report the variation of the $\Lambda_b^0 \to \Sigma_c(2455)^{++}\pi^-\pi^-$, $\Lambda_b^0 \to \Sigma_c(2455)^0\pi^+\pi^-$, $\Lambda_b^0 \to \Lambda_c(2595)^+\pi^-$, and $\Lambda_b^0 \to \Lambda_c(2625)^+\pi^-$ yields by varying the threshold by $\pm 1\,\sigma$, where $\sigma = 0.1\,\mathrm{MeV/c^2}$.
We find no variation of the $\Lambda_b^0 \to \Lambda_c(2595)^+\pi^-$ and $\Lambda_b^0 \to \Lambda_c(2625)^+\pi^-$ yields, consequently, only the $\Sigma_c(2455)^{++}$ and $\Sigma_c(2455)^0$ background shapes will contribute to the systematic that is reported in Tab. 6.4, Tab. 6.5, Tab. 6.7, where both $\Sigma_c(2455)^{++}$ and $\Sigma_c(2455)^0$ yields are used in the measurement of the relatives branching fractions reported in these Tables, and in Tab. 6.8 where only the $\Sigma_c(2455)^{++}$ contributes.

CS decay modes (Cab Supp)

In Appendix C [97] we described a method to estimate the yields of the CS decay modes expected in the $\Lambda_b^0 \to \Lambda_c^+\pi^-\pi^+\pi^-$ mass spectrum. In Chap. 5,

Decay mode Yield	thres $= m_\pi$	thres $= m_\pi + 0.1$	thres $= m_\pi - 0.1$
$N(\Sigma_c(2455)^{++}\pi^-\pi^-)$	81	+1.5	-0.5
$N(\Sigma_c(2455)^0\pi^+\pi^-)$	41.5	+0.0	+0.1
Decay mode Yield	thres $= 2m_\pi$	thres $= 2m_\pi + 0.1$	thres $= 2m_\pi - 0.1$
$N(\Lambda_c(2595)^+\pi^-)$	46.6	-	-
$N(\Lambda_c(2625)^+\pi^-)$	114	-	-

Table 7.2: *Yields of the charmed resonant decay modes for the threshold mass central value and at* $\pm 1\sigma$.

when we extracted the yields we do not take into account in the modeling of such decays since they are expected to be very few. In order to do that, for each of the CF charmed resonant decay mode expected to contribute to the signal of the $\Lambda_b^0 \to \Lambda_c^+\pi^-\pi^+\pi^-(all)$, we generated a sample of $\sim 10^7$ events with a full simulation of the corresponding CS decay modes and processed and reconstructed offline them like the corresponding CF. Fig. 7.1 reports the ΔM^{+-}, ΔM^+, and ΔM^- MC distributions for the CF (and CS, where the π^- is replaced by a K^-) decay modes $\Lambda_b^0 \to \Lambda_c(2595)^+\pi^-(K^-)$ (see Fig. 7.1(a)), $\Lambda_b^0 \to \Lambda_c(2625)^+\pi^-(K^-)$ (see Fig. 7.1(b)), $\Lambda_b^0 \to \Sigma_c(2455)^{++}\pi^-\pi^-(K^-)$ (see Fig. 7.1(c)), and $\Lambda_b^0 \to \Sigma_c(2455)^0\pi^+\pi^-(K^-)$ (see Fig. 7.1(d)). The ΔM^{--+} distributions of the CS decay modes reported in this figure are the expected ones, and each of them is obtained multiplying the corresponding original histogram bin contents by the ratio between the BRs of the CS and of the CF, both estimated in Appendix C and [97]. These distributions show that for the CS decays the difference of mass for the charmed resonances peaks exactly in the same region as the CF ones.
Fig. 7.2 shows the ΔM^{--+} distributions of the same four CF and CS Λ_b^0 decay modes which give contribution in the signal region of the CF. In the current analysis we estimated the $\Lambda_b^0 \to \Lambda_c(2595)^+\pi^-$, $\Lambda_b^0 \to \Lambda_c(2625)^+\pi^-$, $\Lambda_b^0 \to \Sigma_c(2455)^{++}\pi^-\pi^-$ and $\Lambda_b^0 \to \Sigma_c(2455)^0\pi^+\pi^-$ yields by performing fits of the ΔM^{+-}, ΔM^+ and ΔM^- distributions, for candidates falling in the Λ_b^0 mass window $|m(\Lambda_b^0) - m(\Lambda_c^+)| < 0.048$ GeV/c^2. To estimate the contamination to the yield of each resonant decay mode due to the corresponding CS one, we estimate the fraction of the CS signal events (N_{CS}) with respect to the CF signal events (N_{CF}), N_{CS}/N_{CF} falling in the same mass window as above. Tab. 7.3 reports the fraction of the expected contribution of each CS decay mode measured with respect to the corresponding CF one and the expected yield of the CS decay mode, evaluated as the fraction times the corresponding measured yield of Tab. 5.2.
These contributions are negligible if compared to the statistical error on the estimated yields. For the $\Lambda_b^0 \to \Lambda_c^+\rho^0\pi^- + \Lambda_b^0 \to \Lambda_c^+\pi^-\pi^+\pi^-(nr)$ decay modes, we

estimate the expected CS decay modes contribution as the product between the $\Lambda_b^0 \to \Lambda_c^+ \rho^0 \pi^- + \Lambda_b^0 \to \Lambda_c^+ \pi^- \pi^+ \pi^- (nr)$ yield estimated by the fit (610±88 events) and the scaling factor (0.054 from Tab. C.5) estimated in Appendix C [97].
The systematic error on the relative branching fraction measurements is evaluated as the variation between the central value and the relative branching fractions, estimated assuming the yield of each decay mode reduced by the expected yield of the associated CS decay mode. Since each of the relative branching ratios has this source of systematic, Tables from Tab. 6.4 to Tab. 6.8 report this contribution.

Decay Mode	Fraction	Exp. Yield
$\Lambda_b^0 \to \Lambda_c(2595)^+ K^-$	0.04	1.9
$\Lambda_b^0 \to \Lambda_c(2625)^+ K^-$	0.03	3.4
$\Lambda_b^0 \to \Sigma_c(2455)^{++} K^- \pi^-$	0.02	1.6
$\Lambda_b^0 \to \Sigma_c(2455)^0 K^- \pi^+$	0.02	0.8
$\Lambda_b^0 \to \Lambda_c^+ \rho \pi^- + \Lambda_b^0 \to \Lambda_c^+ 3\pi (nr)$	0.054	33

Table 7.3: *Yields of CS decay modes expected in the Λ_b^0 mass window.*

7.2 Sources of Systematic errors affecting the relative efficiencies

Also in this case, we consider several sources that can affect the relative efficiencies. For each source, the change in the relative efficiencies is determined, and the corresponding change in the relative BRs is assumed as contributing to the systematic uncertainty of the measureament. The sources considered are described below and their contribution to the systematic uncertainties on the relative BRs is summarized in Tables from Tab. 6.4 to Tab. 6.8. This class of sources is named *Rel. Eff. Err.* in these tables, and is related to the simulation, since the relative efficiencies are evaluated using MC samples.

MC statistics (MC Stat)

In Tab. 6.1 we report the absolute efficiency while in Tab. 6.2 the relative efficiencies for each pair of decay modes. For the latters, the uncertainties are statistical and are due to the size of the generated MC samples. The box labelled *ScLow+ScA* reports the relative efficiencies averaged on the `B_CHARM_LOWPT` and `B_CHARM` trigger scenarios; the first is the statistical uncertainty and the second is

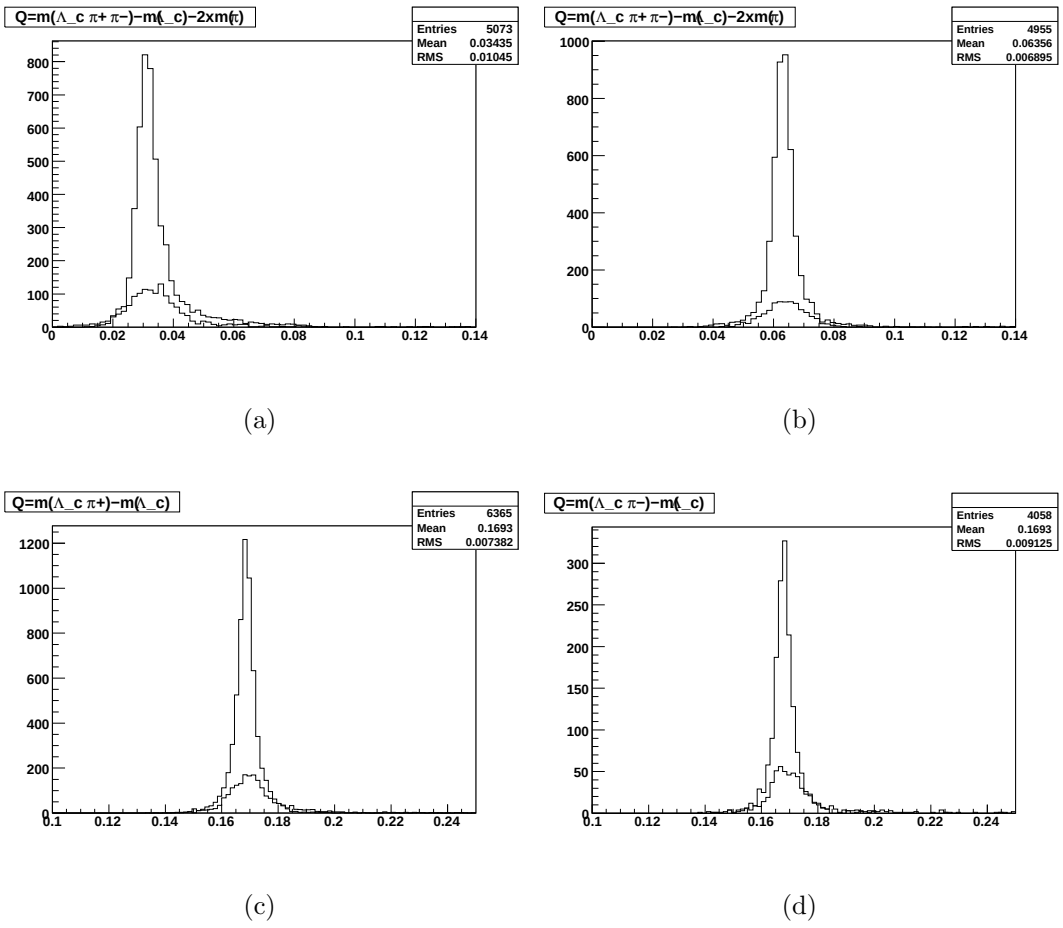

Figure 7.1: **7.1(a):** *ΔM^{+-} distribution of the CF $\Lambda_b^0 \to \Lambda_c(2595)^+\pi^-$ and CS $\Lambda_b^0 \to \Lambda_c(2595)^+K^-$;* **7.1(b):** *$\Delta M^{+-}$ distribution of the CF $\Lambda_b^0 \to \Lambda_c(2625)^+\pi^-$ and CS $\Lambda_b^0 \to \Lambda_c(2625)^+K^-$;* **7.1(c):** *$\Delta M^{+}$ distribution of the CF $\Lambda_b^0 \to \Sigma_c(2455)^{++}\pi^-\pi^-$ and CS $\Lambda_b^0 \to \Sigma_c(2455)^{++}\pi^-K^-$;* **7.1(d):** *$\Delta M^{-}$ distribution of the CF $\Lambda_b^0 \to \Sigma_c(2455)^0\pi^+K^-$ and CS $\Lambda_b^0 \to \Sigma_c(2455)^0\pi^+K^-$;*

the systematic one due to the average between the two trigger scenarios. The systematic uncertainties on the relative branching fraction measurements, due to the statistical uncertainties on the estimate of the relative efficiencies, are computed by simply propagating the statistical uncertainty on each relative efficiency to the relative branching fraction measurements. The systematic uncertainties, due to the average of the relative efficiencies of the two trigger scenarios, are computed as the differences between the measurements obtained using the average relative efficiencies and the relative efficiencies computed separately for each trigger scenario. This systematic is present for all the relative BRs measured (Tables from

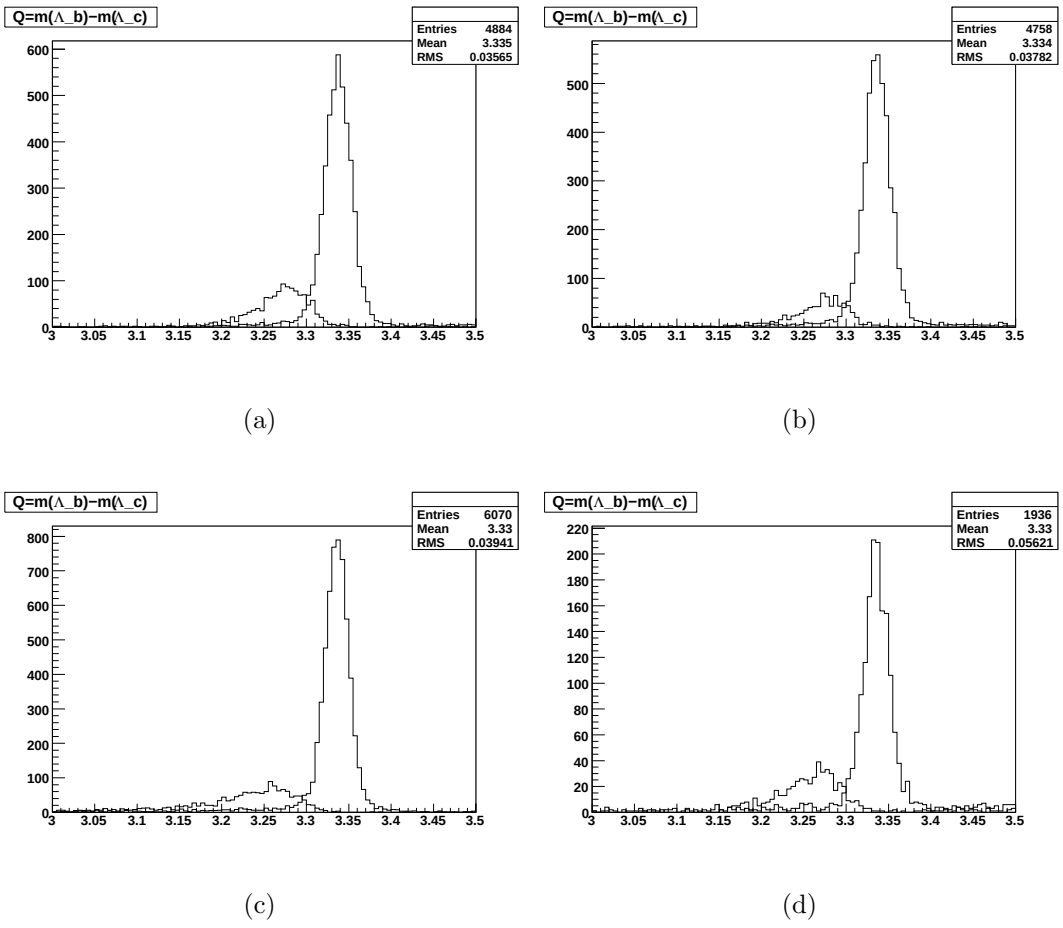

Figure 7.2: **7.2(a):** ΔM^{--+} *distribution of the CF* $\Lambda_b^0 \to \Lambda_c(2595)^+\pi^-$ *and CS* $\Lambda_b^0 \to \Lambda_c(2595)^+K^-$*;* **7.2(b):** ΔM^{--+} *distribution of the CF* $\Lambda_b^0 \to \Lambda_c(2625)^+\pi^-$ *and CS* $\Lambda_b^0 \to \Lambda_c(2625)^+K^-$*;* **7.2(c):** ΔM^{--+} *distribution of the CF* $\Lambda_b^0 \to \Sigma_c(2455)^{++}\pi^-\pi^-$ *and CS* $\Lambda_b^0 \to \Sigma_c(2455)^{++}\pi^-K^-$*;* **7.2(d):** ΔM^{--+} *distribution of the CF* $\Lambda_b^0 \to \Sigma_c(2455)^0\pi^+K^-$ *and CS* $\Lambda_b^0 \to \Sigma_c(2455)^0\pi^+K^-$*;*

Tab. 6.4 to Tab. 6.8).

Λ_c^+ resonance structure (Λ_c^+ res st)

The branching fractions of the $\Lambda_c^+ \to pK^-\pi^+$, proceeding through decay modes shown in Tab. 4.2, are measured with significant errors. In the MC generation of the Λ_c^+ into $pK^-\pi^+$ final states samples, these branching fractions are fixed to theirs PDG central values. We estimate the systematic error on the relative efficiencies, due to the uncertainty on the branching fractions of the Λ_c^+ decay

modes, by determining the absolute efficiencies of each individual decay mode i ($\varepsilon(i)_A$) and propagating the errors on the relative branching fractions in the formula of the relative efficiencies:

$$\frac{\varepsilon(A)}{\varepsilon(B)} = \frac{\sum \mathcal{B}(i) \cdot \varepsilon(i)_A}{\sum \mathcal{B}(j) \cdot \varepsilon(j)_B} \tag{7.1}$$

where each state i represents one of the following Λ_c^+ decay modes $\Lambda_c^+ \to pK^*(892)$, $\Lambda_c^+ \to \Delta(1232)^{++}K^-$, $\Lambda_c^+ \to \Lambda(1520)\pi^+$ and non-resonant $\Lambda_c^+ \to pK^-\pi^+$; A and B indicates two Λ_b^0 different decay modes into $\Lambda_c^+\pi^+\pi^-\pi^-$ final state. The error on $\varepsilon(A)/\varepsilon(B)$ is obtained by propagating the errors on the BR $\mathcal{B}(i)$. For each decay mode the values of the absolute efficiencies $\varepsilon(i)_A$ and $\varepsilon(i)_B$ are obtained from MC. We report the resulting systematic error on the relative branching fraction measurements in Tables from Tab. 6.4 to Tab. 6.8 since the Λ_c^+ is in all the decay modes considered.

$\Lambda_c(2595)^+ \to \Lambda_c^+\pi^+\pi^-$ resonance structure ($\Lambda_c(2595)^+$ res st)

$\Sigma_c(2455)^{++}$ and $\Sigma_c(2455)^0$ decay modes considered do not have resonant structures while the $\Lambda_c(2595)^+ \to \Lambda_c^+\pi^+\pi^-$ decay mode has a resonant structure with significant uncertainty on the measurement of the branching fractions [1], $\mathcal{B}(\Lambda_c(2595)^+ \to \Sigma_c(2455)^{++}\pi^-) = 24 \pm 7\%$, $\mathcal{B}(\Lambda_c(2595)^+ \to \Sigma_c(2455)^0\pi^+) = 24 \pm 7\%$, and $\mathcal{B}(\Lambda_c(2595)^+ \to \Lambda_c^+\pi^+\pi^-(3-body)) = 18 \pm 10\%$. The systematic uncertainties on the relative efficiencies involving the $\Lambda_b^0 \to \Lambda_c(2595)^+\pi^-$ decay mode are similarly estimated, as in the previous subsection, since also in this case the BRs of the $\Lambda_c(2595)^+$ are fixed in the MC to their central values. Tab. 7.4 reports the absolute efficiencies for $\Lambda_c(2595)^+$ decay channels into $\Sigma_c(2455)^{++}\pi^-$, $\Sigma_c(2455)^0\pi^+$ and $\Lambda_c^+\pi^+\pi^-$ while Tab. 7.5 reports the relative efficiencies to the other Λ_b^0 decay modes. The central value, ε, for a given trigger path is computed using the average of the efficiencies (ε_1, ε_2 and ε_3 of a given trigger path) reported in the last column of Tab. 7.4, while the error is computed as the maximum value of the difference between ε and the ε_i, relative to each $\Lambda_c(2595)^+$ decay mode for a given trigger path. The systematic uncertainties on the relative branching fractions are computed as the largest difference between the branching fractions, computed with the average relative efficiency, and the maximum and minimum relative efficiency. Tables from Tab. 6.4 to Tab. 6.6 report the corresponding systematic on the relative BR measurements, since this source contributes only in the decay modes with a $\Lambda_c(2595)^+$.

B_CHARM_LOWPT							
Λ_b^0 Decay	$\Sigma_c(2455)^{++}\pi^-$	ε_1	$\Sigma_c(2455)^0\pi^+$	ε_2	$\Lambda_c^+\pi^+\pi^-$	ε_3	ε
$\Lambda_c(2595)^+\pi^-$	1843	10.25	1751	9.74	1309	9.71	9.92
B_CHARM							
Λ_b^0 Decay	$\Sigma_c(2455)^{++}\pi^-$	ε_1	$\Sigma_c(2455)^0\pi^+$	ε_2	$\Lambda_c^+\pi^+\pi^-$	ε_3	ε
$\Lambda_c(2595)^+\pi^-$	1402	7.80	1346	7.49	987	7.32	7.56

Table 7.4: *Numbers of* $\Lambda_c(2595)^+ \to \Lambda_c^+\pi^+\pi^-$ *MC events passing all the optimised selection cuts, including trigger confirmation and absolute efficiencies (in units of* $\times 10^{-4}$*).*

B_CHARM_LOWPT					
Λ_b^0 Decay Mode	$\Lambda_c(2625)^+\pi^-$	$\Sigma_c^{++}\pi^-\pi^-$	$\Sigma_c^0\pi^-$	$\Lambda_c^+\rho^0\pi^-$	$\Lambda_c^+\pi^-\pi^+\pi^-$(nr)
$\Lambda_c(2595)^+\pi^-$	1.019±0.0.04	1.175±0.04	3.990±0.13	1.995±0.07	2.638±0.09
B_CHARM					
Λ_b^0 Decay Mode	$\Lambda_c(2625)^+\pi^-$	$\Sigma_c^{++}\pi^-\pi^-$	$\Sigma_c^0\pi^-$	$\Lambda_c^+\rho^0\pi^-$	$\Lambda_c^+\pi^-\pi^+\pi^-$(nr)
$\Lambda_c(2595)^+\pi^-$	1.009±0.03	1.209±0.04	4.022±0.13	2.069±0.07	2.797±0.09
Average B_CHARM					
B_CHARM_LOWPT					
Λ_b^0 Decay Mode	$\Lambda_c(2625)^+\pi^-$	$\Sigma_c^{++}\pi^-\pi^-$	$\Sigma_c^0\pi^-$	$\Lambda_c^+\rho^0\pi^-$	$\Lambda_c^+\pi^-\pi^+\pi^-$(nr)
$\Lambda_c(2595)^+\pi^-$	1.014±0.04	1.192±0.04	4.006±0.13	2.032±0.07	2.718±0.09

Table 7.5: *Relative efficiencies for B_CHARM_LOWPT, B_CHARM and for the average between B_CHARM_LOWPT and B_CHARM triggers scenarios, computed using the absolute efficiencies reported in Tab. 7.4. The quoted errors are the systematic uncertainties due to* $\Lambda_c(2595)^+$ *resonant structure.*

$\Lambda_c(2625)^+ \to \Lambda_c^+\pi^+\pi^-$ resonance structure ($\Lambda_c(2625)^+$ res st)

The PDG does not quote measured branching fractions for the intermediate resonant decay modes, it only assumes [1] $\mathcal{B}(\Lambda_c(2625)^+ \to \Lambda_c^+\pi^+\pi^-) = 67\%$ (due to the isospin conservation), $\mathcal{B}(\Lambda_c(2625)^+ \to \Sigma_c(2455)^{++}\pi^-) < 5\%$ and $\mathcal{B}(\Lambda_c(2625)^+ \to \Sigma_c(2455)^0\pi^+) < 5\%$ both at 90% of Confidence Level (CL). The central values of the measured relative branching fractions are computed assuming in the MC generation the $\mathcal{B}(\Lambda_c(2625)^+ \to \Sigma_c(2455)^{++}\pi^-) = 0$ and the $\mathcal{B}(\Lambda_c(2625)^+ \to \Sigma_c(2455)^0\pi^+) = 0$ and for the other decay modes the BR is reported in Tab. 4.3. We compute the systematic error associated to the uncertainty on the $\Lambda_c(2625)^+ \to \Lambda_c^+\pi^+\pi^-$ resonance structure as the variation of the measured relative branching fractions using in the MC generation $\mathcal{B}(\Lambda_c(2625)^+ \to \Sigma_c(2455)^{++}\pi^-) = 0.05$ and $\mathcal{B}(\Lambda_c(2625)^+ \to \Sigma_c(2455)^0\pi^+) = 0.05$ and $\mathcal{B}(\Lambda_c(2625)^+ \to \Lambda_c^+\pi^+\pi^-) = 0.9$. Tab. 7.6 and Tab. 7.7 report the absolute and rel-

ative efficiencies corresponding to these BRs. Tables from Tab. 6.4 to Tab. 6.6 and Tab. 6.8 report the corresponding systematic on the relative BR measurements, since this source contribute only to the decay modes with a $\Lambda_c(2625)^+$.

B_CHARM_LOWPT				
Λ_b^0 Decay	$\varepsilon(\Sigma_c(2455)^{++}\pi^-)$	$\varepsilon(\Sigma_c(2455)^0\pi^+)$	$\varepsilon(\Lambda_c^+\pi^+\pi^-)$	$\varepsilon(0.05;0.05;0.90)$
$\Lambda_c(2625)^+\pi^-$	10.27×10^{-4}	9.76×10^{-4}	9.73×10^{-4}	9.76×10^{-4}
B_CHARM				
Λ_b^0 Decay	$\varepsilon(\Sigma_c(2455)^{++}\pi^-)$	$\varepsilon(\Sigma_c(2455)^0\pi^+)$	$\varepsilon(\Lambda_c^+\pi^+\pi^-)$	$\varepsilon(0.05;0.05;0.90)$
$\Lambda_c(2625)^+\pi^-$	7.98×10^{-4}	7.66×10^{-4}	7.49×10^{-4}	7.52×10^{-4}

Table 7.6: *Absolute efficiency of the* $\Lambda_c(2625)^+ \to \Lambda_c^+\pi^+\pi^-$ *decay mode when we assume* $\mathcal{B}(\Lambda_c(2625)^+ \to \Sigma_c(2455)^{++}\pi^-) = 0.05$, $\mathcal{B}(\Lambda_c(2625)^+ \to \Sigma_c(2455)^0\pi^+) = 0.05$ *and* $\mathcal{B}(\Lambda_c(2625)^+ \to \Lambda_c^+\pi^+\pi^-) = 0.9$.

B_CHARM_LOWPT					
Λ_b^0 Decay Mode	$\Lambda_c(2595)^+\pi^-$	$\Sigma_c^{++}\pi^-\pi^-$	$\Sigma_c^0\pi^-$	$\Lambda_c^+\rho^0\pi^-$	$\Lambda_c^+3\pi$(nr)
$\Lambda_c(2625)^+\pi^-$	0.984	1.156	3.920	1.964	2.596
B_CHARM					
Λ_b^0 Decay Mode	$\Lambda_c(2595)^+\pi^-$	$\Sigma_c^{++}\pi^-\pi^-$	$\Sigma_c^0\pi^-$	$\Lambda_c^+\rho^0\pi^-$	$\Lambda_c^+3\pi$(nr)
$\Lambda_c(2625)^+\pi^-$	0.995	1.203	4.000	2.060	2.785
Average B_CHARM	B_CHARM_LOWPT				
Λ_b^0 Decay Mode	$\Lambda_c(2595)^+\pi^-$	$\Sigma_c^{++}\pi^-\pi^-$	$\Sigma_c^0\pi^-$	$\Lambda_c^+\rho^0\pi^-$	$\Lambda_c^+3\pi$(nr)
$\Lambda_c(2625)^+\pi^-$	0.990	1.180	3.960	2.012	2.691

Table 7.7: *Relative efficiencies of the* $\Lambda_c(2625)^+ \to \Lambda_c^+\pi^+\pi^-$ *decay mode when we assume* $\mathcal{B}(\Lambda_c(2625)^+ \to \Sigma_c(2455)^{++}\pi^-) = 0.05$ *and* $\mathcal{B}(\Lambda_c(2625)^+ \to \Sigma_c(2455)^0\pi^+) = 0.05$ *and* $\mathcal{B}(\Lambda_c(2625)^+ \to \Lambda_c^+\pi^+\pi^-) = 0.9$.

Averaging of $\Lambda_b^0 \to \Lambda_c^+\rho^0\pi^-$ and $\Lambda_b^0 \to \Lambda_c^+\pi^-\pi^+\pi^-(nr)$ or $\Lambda_b^0 \to \Lambda_c^+a_1(1260)^-$ relative efficiency (Av $\Lambda_c^+\rho^0\pi^-$, $\Lambda_c^+3\pi$)

In this analysis the contributions of the three decay modes $\Lambda_b^0 \to \Lambda_c^+\rho^0\pi^-$ and $\Lambda_b^0 \to \Lambda_c^+\pi^-\pi^+\pi^-(nr)$, or $\Lambda_b^0 \to \Lambda_c^+a_1(1260)^-$ are not separated. Instead, we use the average relative efficiencies of the $\Lambda_b^0 \to \Lambda_c^+\rho^0\pi^-$ and $\Lambda_b^0 \to \Lambda_c^+\pi^-\pi^+\pi^-(nr)$ (equal to relative the average of $\Lambda_b^0 \to \Lambda_c^+\rho^0\pi^-$ and $\Lambda_b^0 \to \Lambda_c^+a_1(1260)^-$) decay modes to measure the central value of the relative branching fractions.
We also assumed that each decay mode, at production, contributes with a fraction

(1/2, 1/2, 0) when considering the mixed E state composed by $\Lambda_b^0 \to \Lambda_c^+\rho^0\pi^-$ and $\Lambda_b^0 \to \Lambda_c^+\pi^-\pi^+\pi^-(nr)$, while we assumed the fractions (1/2, 0, 1/2) when the E state is composed by $\Lambda_b^0 \to \Lambda_c^+\rho^0\pi^-$ and $\Lambda_b^0 \to \Lambda_c^+a_1(1260)^-$ (see Sec. 6.1). The resulting systematic errors, reported in Tab. 6.4, are quoted as the largest difference between the central value of the relative branching fractions and the relative branching fractions, computed using the relative efficiencies for each of the two individual decay modes, as systematic error. This means to assume the two contributing fractions above respectively (1,0,0) and (0,1,0), or (1,0,0) and (0,0,1) for the mixed E state. Since we verified that for the $\Lambda_b^0 \to \Lambda_c^+a_1(1260)^-$ decay mode, with $a_1(1260)^- \to \rho^0\pi^-$ and $\rho^0 \to \pi^+\pi^-$, the efficiency is very similar to the efficiency for the $\Lambda_b^0 \to \Lambda_c^+\pi^-\pi^+\pi^-(nr)$ (see Tab. 7.8), we assumed the efficiency of the $\Lambda_c^+a_1(1260)^-$ equal to the $\Lambda_c^+\pi^-\pi^+\pi^-(nr)$ one, and we do not consider this as a possible source of systematic error. Tab. 6.4 and Tab. 6.5 report the corresponding systematic on the relative BRs measurements, since this source contributes only in the decay modes with yields from $\Lambda_c^+\rho^0\pi^-$ and $\Lambda_c^+\pi^-\pi^+\pi^-(other)$.

Λ_b^0 Decay	ScLow$\times10^{-4}$	ScA$\times10^{-4}$	ScC$\times10^{-4}$
$\Lambda_c^+\rho^0\pi^-$	4.97±0.08	3.65±0.07	2.28±0.05
$\Lambda_c^+3\pi(nr)$	3.76±0.07	2.70±0.06	1.70±0.05
$\Lambda_c^+a_1(1260)$	3.72±0.08	2.64±0.06	1.59±0.05

Table 7.8: *Absolute efficiencies of the $\Lambda_b^0 \to \Lambda_c^+\rho^0\pi^-$, $\Lambda_b^0 \to \Lambda_c^+\pi^-\pi^+\pi^-(nr)$, and $\Lambda_b^0 \to \Lambda_c^+a_1(1260)^-$ decay modes. "ScLow" is for B_CHARM_LOWPT, "ScA" is B_CHARM, and "ScC" is B_CHARM_HIGHPT. We use the only the ScLoW and ScA trigger paths*

Λ_b^0 transverse momentum spectrum (p_T (Λ_b^0))

The Λ_b^0 transverse momentum spectrum $p_T(\Lambda_b^0)$ has been measured using a sample of $\Lambda_b^0 \to \Lambda_c^+\pi^-$ decays fully reconstructed in the first 360 pb^{-1} of CDF data [90]. This spectrum is used by `Bgenerator` to generate the simulated events, and in Appendix A we have verified the consistency of our MC with the larger $\Lambda_b^0 \to \Lambda_c^+\pi^-$ sample. The uncertainty on the measured $p_T(\Lambda_b^0)$ is a source of systematic for the absolute efficiencies of each Λ_b^0 decay mode. To estimate the size of this effect, we determined the variation of the relative efficiencies when the simulated data are generated using the measured $p_T(\Lambda_b^0)$ and the measured spectrum of the B mesons $p_T(B^0)$. In order to do that, we generated samples of events $\Lambda_b^0 \to \Sigma_c(2455)^{++}\pi^-\pi^-$, $\Lambda_b^0 \to \Sigma_c(2455)^0\pi^+\pi^-$, $\Lambda_b^0 \to \Lambda_c^+\rho^0\pi^-$, $\Lambda_b^0 \to \Lambda_c^+\pi^-\pi^+\pi^-(nr)$, $\Lambda_b^0 \to \Lambda_c(2595)^+\pi^-$ and $\Lambda_b^0 \to \Lambda_c(2625)^+\pi^-$ decay modes, with the $p_T(\Lambda_b^0)$ [90], and the $p_T(B^0)$ distributions as inputs for the `Bgenerator`.
The absolute and relative efficiencies, using these two distributions, are reported

in Tab. 7.9, Tab. 7.10, and Tab. 7.11. This source of systematic is present for all the relative BRs measured and the corresponding uncertainty is reported for each of them respectively in Tables from Tab. 6.4 to Tab. 6.8.

Λ_b^0 Decay Mode	#Generated	#ScLow	ε(x10^{-4})	#ScA	ε(x10^{-4})	#ScC	ε(x10^{-4})
$p_T(\Lambda_b^0)$							
$\tau(\Lambda_b^0)$, $\tau(\Lambda_c^+)$							
$\Lambda_c(2595)^+\pi^-$	1407045	1155	8.21±0.24	881	5.76±0.21	670	4.76±0.18
$\Lambda_c(2625)^+\pi^-$	1407045	1071	7.61±0.23	818	5.82±0.20	608	4.32±0.18
$\Sigma_c(2455)^{++}\pi^-\pi^-$	2131887	1413	6.63±0.18	1045	4.90±0.15	734	3.44±0.13
$\Sigma_c(2455)^0\pi^+\pi^-$	2131887	433	2.03±0.10	336	1.58±0.09	226	1.06±0.02
$\Lambda_c^+\rho^0\pi^-$	2131887	888	4.17±0.14	651	3.05±0.12	401	1.88±0.10
$\Lambda_c^+3\pi$(nr)	2131887	669	3.14±0.12	478	2.24±0.10	310	1.45±0.08
$p_T(B^0)$							
$\tau(\Lambda_b^0)$, $\tau(\Lambda_c^+)$							
$\Lambda_c(2595)^+\pi^-$	1407045	1675	11.91±0.29	1322	9.39±0.26	1065	7.56±0.23
$\Lambda_c(2625)^+\pi^-$	1407045	1573	11.18±0.29	1214	8.62±0.24	958	6.80±0.23
$\Sigma_c(2455)^{++}\pi^-\pi^-$	2131887	2051	9.62±0.21	1544	7.24±0.18	1178	5.53±0.16
$\Sigma_c(2455)^0\pi^+\pi^-$	2131887	628	2.95±0.12	491	2.30±0.10	375	1.76±0.09
$\Lambda_c^+\rho^0\pi^-$	2131887	1187	5.53±0.16	900	4.22±0.14	624	2.93±0.12
$\Lambda_c^+3\pi$(nr)	2131887	993	4.66±0.15	741	3.48±0.13	486	2.28±0.10

Table 7.9: *Absolute efficiencies for the three trigger scenarios (trigger confirmation+optimised cuts). Λ_b^0 lifetime is PDG lifetime. "ScLow" is for B_CHARM_LOWPT, "ScA" is B_CHARM, and "ScC" is B_CHARM_HIGHPT. The MC sample, used to estimate the efficiencies, has been generated using $p_T(\Lambda_b^0)$, $\tau(\Lambda_b^0)$ and $\tau(\Lambda_c^+)$ for the top box, and $p_T(B^0)$, $\tau(\Lambda_b^0)$ and $\tau(\Lambda_c^+)$ for the bottom one.*

Λ_b^0 and Λ_c^+ lifetime uncertainty ($\tau(\Lambda_b^0)$ and $\tau(\Lambda_c^+)$)

The lifetime of Λ_b^0 and of Λ_c^+ are known with a precision of 3% and 6% respectively. A smaller Λ_b^0 (Λ_c^+) lifetime gives a smaller efficiency for reconstructing Λ_b^0 (Λ_c^+) decays (and viceversa). To take into account this effect, we repeated the analysis on the same MC samples in which we fluctuated the lifetimes of the generated Λ_b^0 (Λ_c^+) by one standard deviation in either side of the central values. We have determined the new efficiencies and the new relative efficiencies, and the variations of the relative efficiencies are propagated to the relative branching fractions to determine the associated systematic uncertainty. This source of systematic is present for all the relative BRs measured, and the corresponding uncertainty is reported for each of them respectively in Tables from Tab. 6.4 to Tab. 6.8.

B_CHARM_LOWPT						
Λ_b^0 Decay Mode	$\Lambda_c(2595)^+\pi^-$	$\Lambda_c(2625)^+\pi^-$	$\Sigma_c^{++}\pi^-\pi^-$	$\Sigma_c^0\pi^-$	$\Lambda_c^+\rho^0\pi^-$	$\Lambda_c^+\pi^-\pi^+\pi^-$(nr)
$\Lambda_c(2595)^+\pi^-$	1	1.08	1.24	4.04	1.97	2.61
$\Lambda_c(2625)^+\pi^-$	0.93	1	1.15	3.75	1.82	2.42
$\Sigma_c(2455)^{++}\pi^-\pi^-$	0.81	0.87	1	3.26	1.59	2.11
$\Sigma_c(2455)^0\pi^+\pi^-$	0.25	0.27	0.31	1	0.49	0.65
$\Lambda_c^+\rho^0\pi^-$	0.51	0.55	0.63	2.04	1	1.33
$\Lambda_c^+\pi^-\pi^+\pi^-$(nr)	0.38	0.41	0.47	1.54	0.75	1
B_CHARM						
Λ_b^0 Decay Mode	$\Lambda_c(2595)^+\pi^-$	$\Lambda_c(2625)^+\pi^-$	$\Sigma_c^{++}\pi^-\pi^-$	$\Sigma_c^0\pi^-$	$\Lambda_c^+\rho^0\pi^-$	$\Lambda_c^+\pi^-\pi^+\pi^-$(nr)
$\Lambda_c(2595)^+\pi^-$	1	1.08	1.23	4.04	2.05	2.55
$\Lambda_c(2625)^+\pi^-$	0.93	1	1.18	3.68	2.05	2.59
$\Sigma_c(2455)^{++}\pi^-\pi^-$	0.81	0.85	1	3.11	1.61	2.19
$\Sigma_c(2455)^0\pi^+\pi^-$	0.25	0.27	0.31	1	0.52	0.70
$\Lambda_c^+\rho^0\pi^-$	0.49	0.49	0.62	1.92	1	1.36
$\Lambda_c^+\pi^-\pi^+\pi^-$(nr)	0.39	0.39	0.46	1.43	0.74	1
Average B_CHARM						
B_CHARM_LOWPT						
Λ_b^0 Decay Mode	$\Lambda_c(2595)^+\pi^-$	$\Lambda_c(2625)^+\pi^-$	$\Sigma_c^{++}\pi^-\pi^-$	$\Sigma_c^0\pi^-$	$\Lambda_c^+\rho^0\pi^-$	$\Lambda_c^+\pi^-\pi^+\pi^-$(nr)
$\Lambda_c(2595)^+\pi^-$	1	1.08	1.23	4.04	2.01	2.58
$\Lambda_c(2625)^+\pi^-$	0.93	1	1.16	3.72	1.93	2.51
$\Sigma_c(2455)^{++}\pi^-\pi^-$	0.81	0.86	1	3.19	1.60	2.15
$\Sigma_c(2455)^0\pi^+\pi^-$	0.25	0.27	0.31	1	0.50	0.68
$\Lambda_c^+\rho^0\pi^-$	0.50	0.52	0.63	2.00	1	1.34
$\Lambda_c^+\pi^-\pi^+\pi^-$(nr)	0.38	0.40	0.47	1.47	0.75	1

Table 7.10: *Relative efficiencies for B_CHARM_LOWPT, B_CHARM and B_CHARM_HIGHPT triggers scenarios, computed using simply the absolute efficiencies reported in Tab. 7.9. The third box reports the average values between B_CHARM_LOWPT and B_CHARM ($p_T(\Lambda_b^0)$, Λ_b^0 and Λ_c^+ lifetime is PDG lifetime).*

Λ_b^0 and Λ_c^+ polarization uncertainty (Λ_b^0, Λ_c^+ Polar)

The SM predicts that the Λ_b^0 is produced polarized, but there is no measurement of the Λ_b^0 polarization, and MC simulation assumes both Λ_b^0 and Λ_c^+ unpolarized. In this analysis we have several Λ_b^0 decay modes to a baryon of spin $1/2$ ($\Lambda_b^0 \to \Lambda_c(2595)^+\pi^-$, $\Lambda_b^0 \to \Sigma_c(2455)^{++}\pi^-\pi^-$, $\Lambda_b^0 \to \Sigma_c(2455)^0\pi^+\pi^-$, $\Lambda_b^0 \to \Lambda_c^+\rho^0\pi^-$, and $\Lambda_b^0 \to \Lambda_c^+\pi^-\pi^+\pi^-(nr)$) and one decay to a baryon of spin $3/2$ ($\Lambda_b^0 \to \Lambda_c(2625)^+\pi^-$). For all these Λ_b^0 decay modes the angular distribution of the Λ_b^0 decay products is

$$\frac{dN}{d\cos(\theta)} \propto 1 + P_b \cdot \cos(\theta) \tag{7.2}$$

where P_b is the product of such polarization and the asymmetry parameter of the weak decay. The angle θ is defined as the angle between the momentum of the

B_CHARM_LOWPT						
Λ_b^0 Decay Mode	$\Lambda_c(2595)^+\pi^-$	$\Lambda_c(2625)^+\pi^-$	$\Sigma_c^{++}\pi^-\pi^-$	$\Sigma_c^0\pi^-$	$\Lambda_c^+\rho^0\pi^-$	$\Lambda_c^+\pi^-\pi^+\pi^-$(nr)
$\Lambda_c(2595)^+\pi^-$	1	1.06	1.24	4.05	2.14	2.56
$\Lambda_c(2625)^+\pi^-$	0.94	1	1.17	3.79	2.02	2.39
$\Sigma_c(2455)^{++}\pi^-\pi^-$	0.81	0.85	1	3.27	1.73	2.07
$\Sigma_c(2455)^0\pi^+\pi^-$	0.25	0.26	0.31	1	0.53	0.63
$\Lambda_c^+\rho^0\pi^-$	0.47	0.50	0.58	1.89	1	1.20
$\Lambda_c^+\pi^-\pi^+\pi^-$(nr)	0.39	0.42	0.48	1.59	0.83	1
B_CHARM						
Λ_b^0 Decay Mode	$\Lambda_c(2592)^+\pi^-$	$\Lambda_c(2625)^+\pi^-$	$\Sigma_c^{++}\pi^-\pi^-$	$\Sigma_c^0\pi^-$	$\Lambda_c^+\rho^0\pi^-$	$\Lambda_c^+\pi^-\pi^+\pi^-$(nr)
$\Lambda_c(2595)^+\pi^-$	1	1.09	1.30	4.08	2.23	2.70
$\Lambda_c(2625)^+\pi^-$	0.92	1	1.20	3.74	2.05	2.48
$\Sigma_c(2455)^{++}\pi^-\pi^-$	0.77	0.83	1	3.14	1.72	2.08
$\Sigma_c(2455)^0\pi^+\pi^-$	0.25	0.27	0.32	1	0.55	0.66
$\Lambda_c^+\rho^0\pi^-$	0.45	0.49	0.58	1.82	1	1.21
$\Lambda_c^+\pi^-\pi^+\pi^-$(nr)	0.37	0.40	0.48	1.52	0.83	1
Average B_CHARM						
B_CHARM_LOWPT						
Λ_b^0 Decay Mode	$\Lambda_c(2595)^+\pi^-$	$\Lambda_c(2625)^+\pi^-$	$\Sigma_c^{++}\pi^-\pi^-$	$\Sigma_c^0\pi^-$	$\Lambda_c^+\rho^0\pi^-$	$\Lambda_c^+\pi^-\pi^+\pi^-$(nr)
$\Lambda_c(2595)^+\pi^-$	1	1.08	1.27	4.07	2.18	2.63
$\Lambda_c(2625)^+\pi^-$	0.93	1	1.18	3.77	2.04	2.44
$\Sigma_c(2455)^{++}\pi^-\pi^-$	0.79	0.84	1	3.20	1.72	2.08
$\Sigma_c(2455)^0\pi^+\pi^-$	0.25	0.26	0.31	1	0.54	0.64
$\Lambda_c^+\rho^0\pi^-$	0.46	0.50	0.58	1.85	1	1.20
$\Lambda_c^+\pi^-\pi^+\pi^-$	0.38	0.41	0.48	1.56	0.83	1

Table 7.11: *Relative efficiencies for B_CHARM_LOWPT, B_CHARM and B_CHARM_HIGHPT triggers scenarios, computed using simply the absolute efficiencies reported in Tab. 7.9. The third box is the average between B_CHARM_LOWPT and B_CHARM (Λ_b^0 lifetime is PDG lifetime, $p_T(\Lambda_b^0)$ is taken as $p_T(B^0)$, Λ_b^0 and Λ_c^+ lifetime is PDG lifetime).*

charmed baryon, produced in the Λ_b^0 decay in the Λ_b^0 rest frame and the axis normal to the beam proton-Λ_b^0 production plane [30]. The strong decays of the spin $^1/_2$ intermediate baryonic resonances to a spin $^1/_2$ baryon $\Lambda_c(2595)^+ \to \Lambda_c^+\pi^+\pi^-$, $\Sigma_c(2455)^{++} \to \Lambda_c^+\pi^+$, $\Sigma_c(2455)^0 \to \Lambda_c^+\pi^-$ are isotropic in the intermediate baryonic resonance rest frame. This is assumed also for the strong decay of the spin $^3/_2$ intermediate baryonic resonance $\Lambda_c(2595)^+ \to \Lambda_c^+\pi^+\pi^-$. The Λ_c^+ could also be produced polarized but there are no measurements of this polarization. The angular distribution of the Λ_c^+ decay products is parameterised as

$$\frac{dN}{d\cos(\varphi)} \propto 1 + P_c \cdot \cos(\varphi) \tag{7.3}$$

where φ is the angle between the proton momentum measured in the Λ_c^+ rest frame and the Λ_b^0 momentum in the laboratory frame. The MC does not include polarization (both P_b and P_c are null) and we reweight the MC to estimate a systematic uncertainty of the relative efficiencies due to the unknown values of the Λ_b^0 and Λ_c^0 polarizations. The reweighting function is $\frac{dN}{d\cos(\theta)} \times \frac{dN}{d\cos(\varphi)}$ and we use the four combinations of $P_b = \pm 1$ and $P_c = \pm 1$ as limiting cases.
Tab. 7.12 reports the multiplicative factor (scaling factor) of the absolute efficiencies for all the decay modes and trigger scenarios, to obtain the new corresponding absolute efficiencies and the corresponding new relative efficiencies. The maximum variation of each relative branching fraction is taken as the associated systematic error (see Tab. 6.4). This source of systematic is present for all the relative BRs measured and the corresponding uncertainty is reported for each of them respectively in Tables from Tab. 6.4 to Tab. 6.8.

Λ_b^0 Decay	Scenario	+ +	- +	+ -	- -
$\Lambda_c(2595)^+\pi^-$	ScenLow	0.895	0.871	1.145	1.089
$\Lambda_c(2595)^+\pi^-$	ScenA	0.918	0.881	1.139	1.062
$\Lambda_c(2625)^+\pi^-$	ScenLow	0.966	0.873	1.130	1.119
$\Lambda_c(2625)^+\pi^-$	ScenA	0.887	0.883	1.119	1.111
$\Sigma_c(2455)^{++}\pi^-\pi^-$	ScenLow	0.856	0.871	1.131	1.143
$\Sigma_c(2455)^{++}\pi^-\pi^-$	ScenA	0.893	0.897	1.101	1.108
$\Sigma_c(2455)^0\pi^+\pi^-$	ScenLow	0.779	0.774	1.226	1.221
$\Sigma_c(2455)^0\pi^+\pi^-$	ScenA	0.782	0.774	1.231	213
$\Lambda_c^+\rho^0\pi^-$	ScenLow	0.776	0.776	1.219	1.228
$\Lambda_c^+\rho^0\pi^-$	ScenA	0.797	0.808	1.198	1.197
$\Lambda_c^+3\pi$(nr)	ScenLow	0.735	0.768	1.234	1.264
$\Lambda_c^+3\pi$(nr)	ScenA	0.760	0.785	1.206	1.248

Table 7.12: *Scaling factor of the absolute efficiencies for the different combination of the polarizations and trigger scenarios.*

B_CHARM_LOWPT					
Λ_b^0 Decay Mode	$\Lambda_c(2625)^+\pi^-$	$\Sigma_c^{++}\pi^-\pi^-$	$\Sigma_c^0\pi^-$	$\Lambda_c^+\rho^0\pi^-$	$\Lambda_c^+3\pi$(nr)
$\Lambda_c(2595)^+\pi^-$	0.944	1.229	4.584	2.401	3.212
$\Lambda_c(2625)^+\pi^-$		1.301	4.855	2.436	3.403
$\Sigma_c(2455)^{++}\pi^-\pi^-$			3.731	1.872	2.615
$\Sigma_c(2455)^0\pi^+\pi^-$				0.502	0.701
$\Lambda_c^+\rho^0\pi^-$					1.396
B_CHARM					
Λ_b^0 Decay Mode	$\Lambda_c(2625)^+\pi^-$	$\Sigma_c^{++}\pi^-\pi^-$	$\Sigma_c^0\pi^-$	$\Lambda_c^+\rho^0\pi^-$	$\Lambda_c^+3\pi$(nr)
$\Lambda_c(2595)^+\pi^-$	1.044	1.243	4.721	2.383	3.378
$\Lambda_c(2625)^+\pi^-$		1.190	4.522	2.283	3.236
$\Sigma_c(2455)^{++}\pi^-\pi^-$			3.799	1.918	2.719
$\Sigma_c(2455)^0\pi^+\pi^-$				0.504	0.716
$\Lambda_c^+\rho^0\pi^-$					1.418
Aver. B_CHARM					
B_CHARM_LOWPT					
Λ_b^0 Decay Mode	$\Lambda_c(2625)^+\pi^-$	$\Sigma_c^{++}\pi^-\pi^-$	$\Sigma_c^0\pi^-$	$\Lambda_c^+\rho^0\pi^-$	$\Lambda_c^+3\pi$(nr)
$\Lambda_c(2595)^+\pi^-$	0.994	1.236	4.652	2.392	3.295
$\Lambda_c(2625)^+\pi^-$		1.246	4.688	2.360	3.319
$\Sigma_c(2455)^{++}\pi^-\pi^-$			3.765	1.895	2.667
$\Sigma_c(2455)^0\pi^+\pi^-$				0.503	0.709
$\Lambda_c^+\rho^0\pi^-$					1.407

Table 7.13: *Relative efficiencies computed assuming the "+ +" polarization combination.*

B_CHARM_LOWPT					
Λ_b^0 Decay Mode	$\Lambda_c(2625)^+\pi^-$	$\Sigma_c^{++}\pi^-\pi^-$	$\Sigma_c^0\pi^-$	$\Lambda_c^+\rho^0\pi^-$	$\Lambda_c^+3\pi$(nr)
$\Lambda_c(2595)^+\pi^-$	1.017	1.175	4.490	2.239	2.992
$\Lambda_c(2625)^+\pi^-$		1.156	4.416	2.202	2.943
$\Sigma_c(2455)^{++}\pi^-\pi^-$			3.820	1.905	2.546
$\Sigma_c(2455)^0\pi^+\pi^-$				0.499	0.666
$\Lambda_c^+\rho^0\pi^-$					1.336
B_CHARM					
Λ_b^0 Decay Mode	$\Lambda_c(2625)^+\pi^-$	$\Sigma_c^{++}\pi^-\pi^-$	$\Sigma_c^0\pi^-$	$\Lambda_c^+\rho^0\pi^-$	$\Lambda_c^+3\pi$(nr)
$\Lambda_c(2595)^+\pi^-$	1.007	1.187	4.578	2.256	3.139
$\Lambda_c(2625)^+\pi^-$		1.179	4.548	2.241	3.112
$\Sigma_c(2455)^{++}\pi^-\pi^-$			3.856	1.901	2.644
$\Sigma_c(2455)^0\pi^+\pi^-$				0.492	0.686
$\Lambda_c^+\rho^0\pi^-$					1.392
Aver. B_CHARM					
B_CHARM_LOWPT					
Λ_b^0 Decay Mode	$\Lambda_c(2625)^+\pi^-$	$\Sigma_c^{++}\pi^-\pi^-$	$\Sigma_c^0\pi^-$	$\Lambda_c^+\rho^0\pi^-$	$\Lambda_c^+3\pi$(nr)
$\Lambda_c(2595)^+\pi^-$	1.012	1.181	4.534	2.248	3.066
$\Lambda_c(2625)^+\pi^-$		1.168	4.482	2.222	3.028
$\Sigma_c(2455)^{++}\pi^-\pi^-$			3.838	1.903	2.595
$\Sigma_c(2455)^0\pi^+\pi^-$				0.496	0.676
$\Lambda_c^+\rho^0\pi^-$					1.379

Table 7.14: *Relative efficiencies computed assuming the "- +" polarization combination.*

B_CHARM_LOWPT					
Λ_b^0 Decay Mode	$\Lambda_c(2625)^+\pi^-$	$\Sigma_c^{++}\pi^-\pi^-$	$\Sigma_c^0\pi^-$	$\Lambda_c^+\rho^0\pi^-$	$\Lambda_c^+3\pi$(nr)
$\Lambda_c(2595)^+\pi^-$	1.033	1.190	3.726	1.874	2.448
$\Lambda_c(2625)^+\pi^-$		1.152	3.608	1.814	2.287
$\Sigma_c(2455)^{++}\pi^-\pi^-$			3.132	1.574	2.058
$\Sigma_c(2455)^0\pi^+\pi^-$				0.503	0.657
$\Lambda_c^+\rho^0\pi^-$					1.306
B_CHARM					
Λ_b^0 Decay Mode	$\Lambda_c(2625)^+\pi^-$	$\Sigma_c^{++}\pi^-\pi^-$	$\Sigma_c^0\pi^-$	$\Lambda_c^+\rho^0\pi^-$	$\Lambda_c^+3\pi$(nr)
$\Lambda_c(2595)^+\pi^-$	1.027	1.251	3.721	1.967	2.642
$\Lambda_c(2625)^+\pi^-$		1.218	3.624	1.916	2.682
$\Sigma_c(2455)^{++}\pi^-\pi^-$			2.976	1.573	2.113
$\Sigma_c(2455)^0\pi^+\pi^-$				0.528	0.710
$\Lambda_c^+\rho^0\pi^-$					1.343
Aver. B_CHARM					
B_CHARM_LOWPT					
Λ_b^0 Decay Mode	$\Lambda_c(2625)^+\pi^-$	$\Sigma_c^{++}\pi^-\pi^-$	$\Sigma_c^0\pi^-$	$\Lambda_c^+\rho^0\pi^-$	$\Lambda_c^+3\pi$(nr)
$\Lambda_c(2595)^+\pi^-$	1.030	1.220	3.724	1.921	2.545
$\Lambda_c(2625)^+\pi^-$		1.185	3.616	1.865	2.485
$\Sigma_c(2455)^{++}\pi^-\pi^-$			3.054	1.574	2.085
$\Sigma_c(2455)^0\pi^+\pi^-$				0.516	0.684
$\Lambda_c^+\rho^0\pi^-$					1.325

Table 7.15: *Relative efficiencies computed assuming the "+ -" polarization combination.*

B_CHARM_LOWPT					
Λ_b^0 Decay Mode	$\Lambda_c(2625)^+\pi^-$	$\Sigma_c^{++}\pi^-\pi^-$	$\Sigma_c^0\pi^-$	$\Lambda_c^+\rho^0\pi^-$	$\Lambda_c^+3\pi$(nr)
$\Lambda_c(2595)^+\pi^-$	0.992	1.119	3.559	1.769	2.272
$\Lambda_c(2625)^+\pi^-$		1.129	3.573	1.783	2.292
$\Sigma_c(2455)^{++}\pi^-\pi^-$			3.178	1.579	2.003
$\Sigma_c(2455)^0\pi^+\pi^-$				0.497	0.639
$\Lambda_c^+\rho^0\pi^-$					1.284
B_CHARM					
Λ_b^0 Decay Mode	$\Lambda_c(2625)^+\pi^-$	$\Sigma_c^{++}\pi^-\pi^-$	$\Sigma_c^0\pi^-$	$\Lambda_c^+\rho^0\pi^-$	$\Lambda_c^+3\pi$(nr)
$\Lambda_c(2595)^+\pi^-$	0.964	1.159	3.521	1.836	2.380
$\Lambda_c(2625)^+\pi^-$		1.201	3.652	1.904	2.469
$\Sigma_c(2455)^{++}\pi^-\pi^-$			3.039	1.612	2.055
$\Sigma_c(2455)^0\pi^+\pi^-$				0.521	0.676
$\Lambda_c^+\rho^0\pi^-$					1.297
Aver. B_CHARM					
B_CHARM_LOWPT					
Λ_b^0 Decay Mode	$\Lambda_c(2625)^+\pi^-$	$\Sigma_c^{++}\pi^-\pi^-$	$\Sigma_c^0\pi^-$	$\Lambda_c^+\rho^0\pi^-$	$\Lambda_c^+3\pi$(nr)
$\Lambda_c(2595)^+\pi^-$	0.978	1.139	3.540	1.803	2.326
$\Lambda_c(2625)^+\pi^-$		1.165	3.613	1.844	2.380
$\Sigma_c(2455)^{++}\pi^-\pi^-$			3.109	1.595	2.029
$\Sigma_c(2455)^0\pi^+\pi^-$				0.509	0.658
$\Lambda_c^+\rho^0\pi^-$					1.291

Table 7.16: *Relative efficiencies computed assuming the "- -" polarization combination.*

Conclusions

In this Thesis we presented the observation of the $\Lambda_b^0 \to \Lambda_c^+\pi^-\pi^+\pi^-$ decay mode and its charmed resonant contributions, specifically the decay modes: $\Lambda_b^0 \to \Lambda_c(2595)^+\pi^-$, $\Lambda_b^0 \to \Lambda_c(2625)^+\pi^-$, $\Lambda_b^0 \to \Sigma_c(2455)^{++}\pi^-\pi^-$ and $\Lambda_b^0 \to \Sigma_c(2455)^0\pi^-\pi^+$ on a data sample corresponding to $2.4\,\text{fb}^{-1}$ of integrated luminosity.
We have also measured the relative branching fractions of the decay modes contributing to the $\Lambda_b^0 \to \Lambda_c^+\pi^-\pi^+\pi^-$ decay and reported in Tab. 7.17.

	Relative Branching Fraction (%)
$\frac{\mathcal{B}(\Lambda_b^0\to\Lambda_c(2595)^+\pi^-\to\Lambda_c^+\pi^-\pi^+\pi^-)}{\mathcal{B}(\Lambda_b^0\to\Lambda_c^+\pi^-\pi^+\pi^-(all))}$	$(2.5 \pm 0.6 \pm 0.5)$
$\frac{\mathcal{B}(\Lambda_b^0\to\Lambda_c(2625)^+\pi^-\to\Lambda_c^+\pi^-\pi^+\pi^-)}{\mathcal{B}(\Lambda_b^0\to\Lambda_c^+\pi^-\pi^+\pi^-(all))}$	$(6.2 \pm 1.0^{+1.0}_{-0.9})$
$\frac{\mathcal{B}(\Lambda_b^0\to\Sigma_c(2455)^{++}\pi^-\pi^-\to\Lambda_c^+\pi^-\pi^+\pi^-)}{\mathcal{B}(\Lambda_b^0\to\Lambda_c^+\pi^-\pi^+\pi^-(all))}$	$(5.2 \pm 1.1 \pm 0.8)$
$\frac{\mathcal{B}(\Lambda_b^0\to\Sigma_c(2455)^0\pi^+\pi^-\to\Lambda_c^+\pi^-\pi^+\pi^-)}{\mathcal{B}(\Lambda_b^0\to\Lambda_c^+\pi^-\pi^+\pi^-(all))}$	$(8.9 \pm 2.1^{+1.2}_{-1.0})$
$\frac{\mathcal{B}(\Lambda_b^0\to\Lambda_c^+\rho^0\pi^-+\Lambda_c^+\pi^-\pi^+\pi^-(other)\to\Lambda_c^+\pi^-\pi^+\pi^-)}{\mathcal{B}(\Lambda_b^0\to\Lambda_c^+\pi^-\pi^+\pi^-(all))}$	$(77.3 \pm 3.1^{+3.0}_{-3.3})$

Table 7.17: *Relative Branching Fractions in % measured in this work of Thesis. In these measurements the first uncertainty is statistical and the second one is systematic.*

Conclusions

The work described in this Thesis confirmed the capability of CDF to extract signals of b-baryons over large backgrounds thanks to the especially designed CDF trigger for the multibody hadronic b-decays. The observation of the new Λ_b^0 charmed resonant decay modes was the main challenge of this analysis and it is the first mandatory step towards the measurement of their absolute BRs. From the results shown in this Thesis, we were not able to separate the signals contributing to $\Lambda_b^0 \to \Lambda_c^+\pi^-\pi^+\pi^-$ final state without charmed resonant decay modes, but we know, from the study reported in Appendix D, that the decay $\Lambda_b^0 \to \Lambda_c^+ a_1(1260)^- \to \Lambda_c^+\rho^0\pi^- \to \Lambda_c^+\pi^-\pi^+\pi^-$ contributes to the $\Lambda_b^0 \to \Lambda_c^+\pi^-\pi^+\pi^-(all)$ decay.
We recently updated the relative BRs measured in this Thesis [15], assuming equal proportions, ($1/3$, $1/3$,$1/3$), of the three decay modes, $\Lambda_b^0 \to \Lambda_c^+\rho^0\pi^-$, $\Lambda_b^0 \to \Lambda_c^+\pi^-\pi^+\pi^-(nr)$ and $\Lambda_b^0 \to \Lambda_c^+ a_1(1260)^-$, with minor changes in the analysis and using the same amount of data ($2.4\,\text{fb}^{-1}$ of integrated luminosity). The updated results are reported in Tab. 7.18.

	Relative Branching Fraction (%)
$\frac{\mathcal{B}(\Lambda_b^0\to\Lambda_c(2595)^+\pi^-\to\Lambda_c^+\pi^-\pi^+\pi^-)}{\mathcal{B}(\Lambda_b^0\to\Lambda_c^+\pi^-\pi^+\pi^-(all))}$	$(2.33 \pm 0.48^{+0.43}_{-0.44})$
$\frac{\mathcal{B}(\Lambda_b^0\to\Lambda_c(2625)^+\pi^-\to\Lambda_c^+\pi^-\pi^+\pi^-)}{\mathcal{B}(\Lambda_b^0\to\Lambda_c^+\pi^-\pi^+\pi^-(all))}$	$(6.8 \pm 1.0 \pm 1.3)$
$\frac{\mathcal{B}(\Lambda_b^0\to\Sigma_c(2455)^{++}\pi^-\pi^-\to\Lambda_c^+\pi^-\pi^+\pi^-)}{\mathcal{B}(\Lambda_b^0\to\Lambda_c^+\pi^-\pi^+\pi^-(all))}$	$(6.2 \pm 1.2 \pm 1.3)$
$\frac{\mathcal{B}(\Lambda_b^0\to\Sigma_c(2455)^0\pi^+\pi^-\to\Lambda_c^+\pi^-\pi^+\pi^-)}{\mathcal{B}(\Lambda_b^0\to\Lambda_c^+\pi^-\pi^+\pi^-(all))}$	$(7.1 \pm 2.1^{+1.5}_{-1.3})$
$\frac{\mathcal{B}(\Lambda_b^0\to\Lambda_c^+\rho^0\pi^-+\Lambda_c^+\pi^-\pi^+\pi^-(other)\to\Lambda_c^+\pi^-\pi^+\pi^-)}{\mathcal{B}(\Lambda_b^0\to\Lambda_c^+\pi^-\pi^+\pi^-(all))}$	$(77.6 \pm 3.0^{+4.0}_{-4.1})$

Table 7.18: *Relative Branching Fractions in % measured after the update [15]. In these measurements the first uncertainty is statistical and the second one is systematic. Here other indicates the sum of the* $\Lambda_b^0 \to \Lambda_c^+\pi^-\pi^+\pi^-(nr)$ *and of the* $\Lambda_b^0 \to \Lambda_c^+ a_1(1260)^- \to \Lambda_c^+\rho^0\pi^- \to \Lambda_c^+\pi^-\pi^+\pi^-$.

The relative branching fractions measured in this work of Thesis are in agreement with the updated ones.
Then, using the sample of the reconstructed candidates $\Lambda_b^0 \to \Lambda_c^+\pi^-$, described in the Thesis, we measure the $\mathcal{B}(\Lambda_b^0 \to \Lambda_c^+\pi^-\pi^+\pi^-(all))/\mathcal{B}(\Lambda_b^0 \to \Lambda_c^+\pi^-)$ relative branching fraction as well as those of the intermediate states contributing to $\Lambda_b^0 \to \Lambda_c^+\pi^-\pi^+\pi^-(all)$ with respect to $\Lambda_b^0 \to \Lambda_c^+\pi^-$.
Using the known value of $\mathcal{B}(\Lambda_b^0 \to \Lambda_c^+\pi^-)$ [1] we measure the absolute BRs reported in Tab. 7.19.
Our measurement $\mathcal{B}(\Lambda_b^0 \to \Lambda_c^+\pi^-\pi^+\pi^-(all))/\mathcal{B}(\Lambda_b^0 \to \Lambda_c^+\pi^-) = 3.04 \pm 0.33^{+0.70}_{-0.50}$, where the first is the statistical uncertainty and the second is the systemayic one,

	Absolute Branching Fraction (10^{-3})
$\mathcal{B}(\Lambda_b^0 \to \Lambda_c(2595)^+\pi^- \to \Lambda_c^+\pi^-\pi^+\pi^-)$	$(0.62 \pm 0.11 \pm 0.05)$
$\mathcal{B}(\Lambda_b^0 \to \Lambda_c(2625)^+\pi^- \to \Lambda_c^+\pi^-\pi^+\pi^-)$	$(1.81 \pm 0.21^{+0.12}_{-0.13})$
$\mathcal{B}(\Lambda_b^0 \to \Sigma_c(2455)^{++}\pi^-\pi^- \to \Lambda_c^+\pi^-\pi^+\pi^-)$	$(1.67 \pm 0.29 \pm 0.10)$
$\mathcal{B}(\Lambda_b^0 \to \Sigma_c(2455)^0\pi^+\pi^- \to \Lambda_c^+\pi^-\pi^+\pi^-)$	$(1.89 \pm 0.57^{+0.40}_{-0.26})$
$\mathcal{B}(\Lambda_b^0 \to \Lambda_c^+\rho^0\pi^- + \Lambda_c^+\pi^-\pi^+\pi^-(other) \to \Lambda_c^+\pi^-\pi^+\pi^-)$	$(20.8 \pm 2.8^{+6.0}_{-4.7})$
$\mathcal{B}(\Lambda_b^0 \to \Lambda_c^+\pi^-\pi^+\pi^-(all))$	$(26.8 \pm 2.9^{+6.2}_{-4.8})$

Table 7.19: *Absolute branching fractions are derived by normalizing to the known value* $\mathcal{B}(\Lambda_b^0 \to \Lambda_c^+\pi^-) = (8.8 \pm 3.2) \times 10^{-3}$ *[1]. The first quoted uncertainty is statistical, the second is systematic, and the third is due to the uncertainty on the* $\Lambda_b^0 \to \Lambda_c^+\pi^-$ *branching fractions. Here other indicates the sum of the* $\Lambda_c^+\pi^-\pi^+\pi^-(nr)$ *and of the* $\Lambda_b^0 \to \Lambda_c^+ a_1(1260)^- \to \Lambda_c^+\rho^0\pi^- \to \Lambda_c^+\pi^-\pi^+\pi^-$

differs from the recent result from LHCb [17] $(1.43 \pm 0.16(stat) \pm 0.13(syst))$ by 2.4σ.
The relative statistical uncertainty of the two measurements is comparable but our systematic uncertainties are larger, because we include the effect of the unknown baryon polarizations and the admixture composition ($1/3$, $1/3$,$1/3$) (LHCb assumes a mixture ($1/3$, 0, $2/3$) of respectively $\Lambda_b^0 \to \Lambda_c^+\rho^0\pi^-$, $\Lambda_b^0 \to \Lambda_c^+\pi^-\pi^+\pi^-(nr)$ and $\Lambda_b^0 \to \Lambda_c^+ a_1(1260)^-$.
We must remember that LHCb used $35\,\text{pb}^{-1}$ of data collected at $\sqrt{s} = 7\,\text{TeV}$ and, moreover, is different the amount of background as well as the type.

Conclusions

Appendices

Appendices

Appendix A

Monte Carlo Validation

We have generated MC samples of Λ_b^0 using the prescription and the $p_T(\Lambda_b^0)$ and $y(\Lambda_b^0)$ reweighted spectra as described in [90]. To make sure of the distributions determined in [90] are still valid we used the $\Lambda_b^0 \to \Lambda_c^+\pi^-$ signal events, reconstructed in the data (see Fig. A.1) and in the MC sample, then we have performed a detailed comparison between real data and MC for all the Λ_b^0, the Λ_c^+ kinematical quantities and the parameters of the four tracks produced in the decay (see Figures from Fig. A.2 to Fig. A.11). To take into account the presence of background, when determining each kinematic distribution of the Λ_b^0 and Λ_c^+ reconstructed in data, we proceeded in the following way. We have not made a sideband subtraction, since it would be difficult to model the physics background due to the partially reconstructed decays present in the left mass region.
We determined the number of real Λ_b^0 in each bin by performing a fit of the mass distribution (see Fig. A.1) of the Λ_b^0 candidates belonging to that bin. The distributions for collision data and MC are normalized to the same total number of entries. These plots do not contain the cut $p_T(\Lambda_b^0) > 8$ GeV/c, which we expect to use in the optimized $\Lambda_b^0 \to \Lambda_c^+\pi^-\pi^+\pi^-$ selection (and for consistency to extend to the selection of the $\Lambda_b^0 \to \Lambda_c^+\pi^-$), so part of the current (limited) disagreement at low transverse momenta and low transverse decay lengths could be reduced.

We compared the $p_T(\Lambda_b^0)$ distribution between data and MC separately for the samples collected by the three different trigger scenarios `B_CHARM_LOWPT`, `B_CHARM` and `B_CHARM_HIGHPT` (events common to the different trigger scenarios are double or triple counted, but we expect this is not a problem). The comparison is reported in Fig. A.12, and it shows that the MC reproduces well the transverse momentun distribution for all the three trigger scenarios.

In Figures from Fig. A.2 to Fig. A.11 the upper plots show physical quantity in

Appendix A. Monte Carlo Validation

data and MC, normalized to the same number as data, while in the bottom plots is reported the ratio of the two distributions.

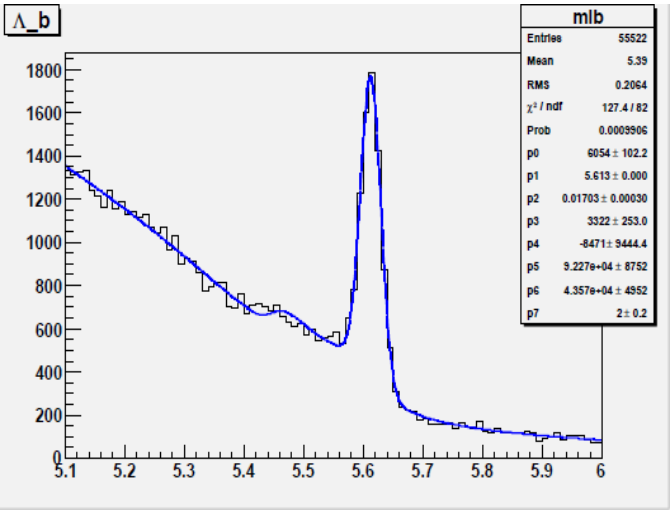

Figure A.1: $\Lambda_b^0 \to \Lambda_c^+ \pi^-$ *reconstructed candidates in the data, and used for MC validation, with overlaid the best fit curve.*

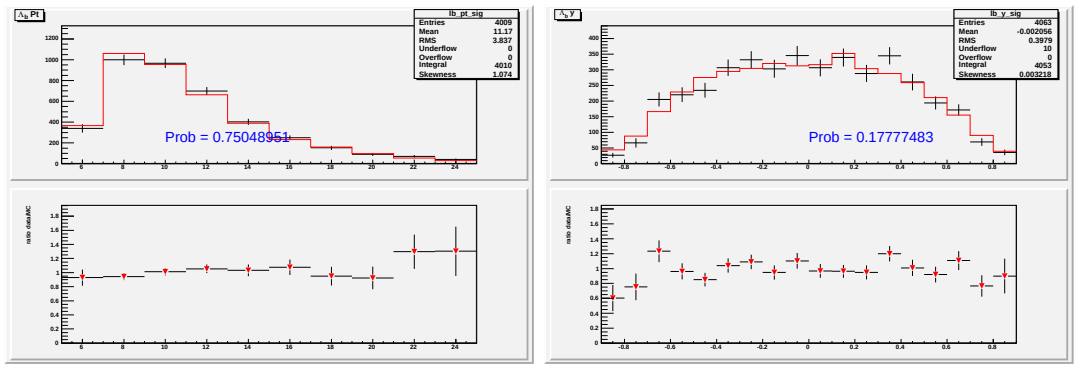

(a) (b)

Figure A.2: $p_T(\Lambda_b^0)$ **A.2(a)** *and* $y(\Lambda_b^0)$ **A.2(b)** *distributions for data (black) and MC (red). Bottom plots are the ratio data/MC.*

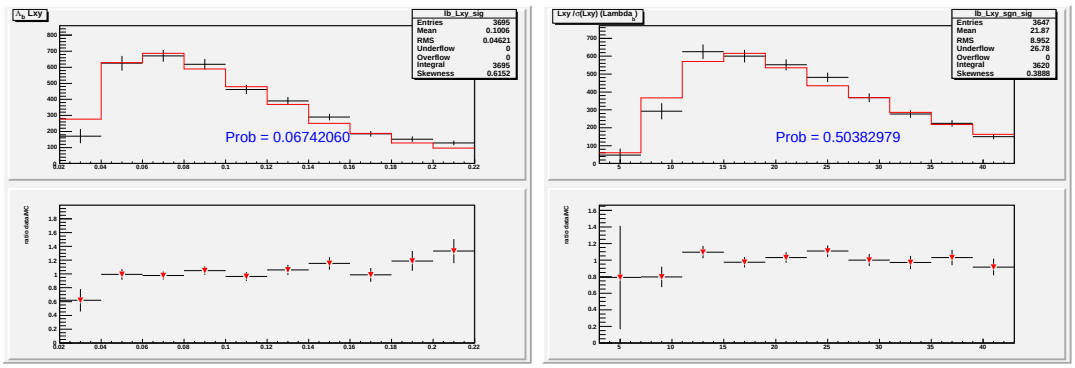

(a) (b)

Figure A.3: *$L_{xy}(\Lambda_b^0)$* **A.3(a)** *and $L_{xy}(\Lambda_b^0)/\sigma L_{xy}(\Lambda_b^0)$* **A.3(b)** *distributions for data (black) and MC (red).*

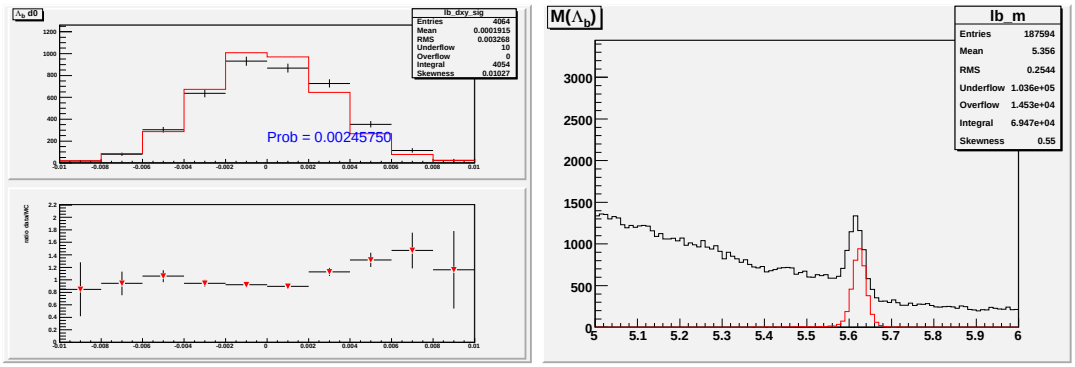

(a) (b)

Figure A.4: *$d_0(\Lambda_b^0)$* **A.4(a)** *and $m(\Lambda_b^0)$* **A.4(b)** *distributions for data (black) and MC (red).*

Appendix A. Monte Carlo Validation

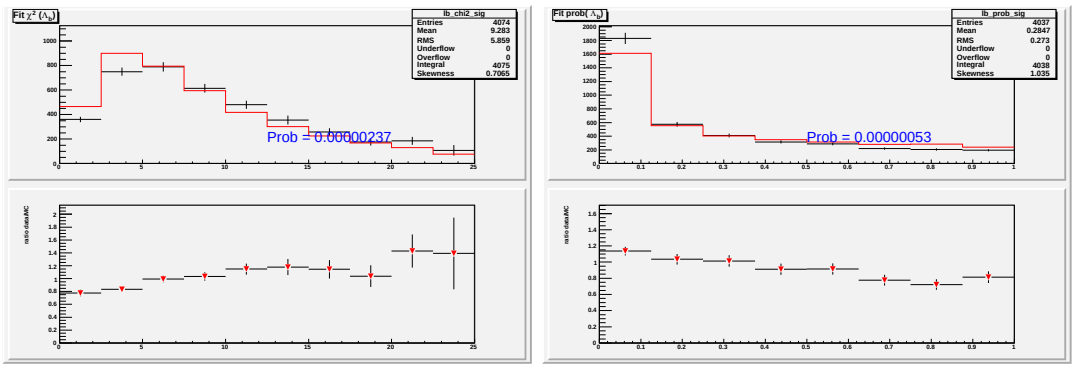

(a) (b)

Figure A.5: $\chi^2(\Lambda_b^0)$ **A.5(a)** *and* $Prob(\chi^2(\Lambda_b^0))$ **A.5(b)** *distributions of the reconstructed* Λ_b^0 *decay vertex for data (black) and MC (red).*

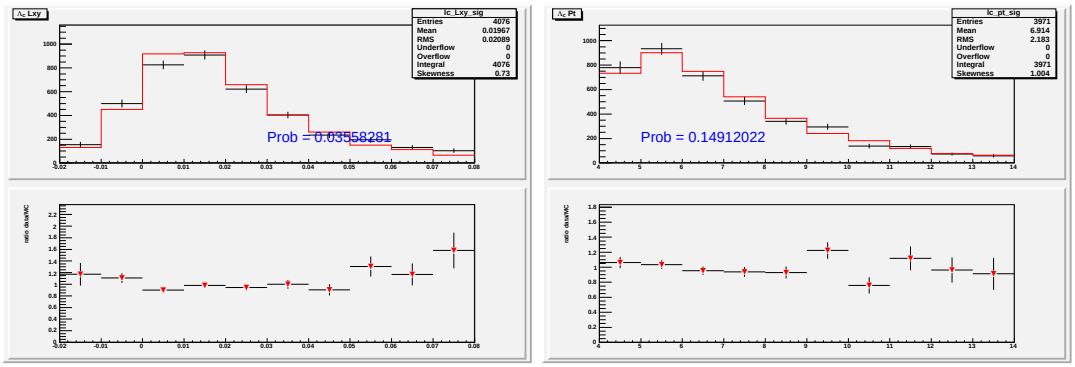

(a) (b)

Figure A.6: $L_{xy}(\Lambda_c^+)$ **A.6(a)** *and* $p_T(\Lambda_c^+)$ **A.6(b)** *distributions for data (black) and MC (red).*

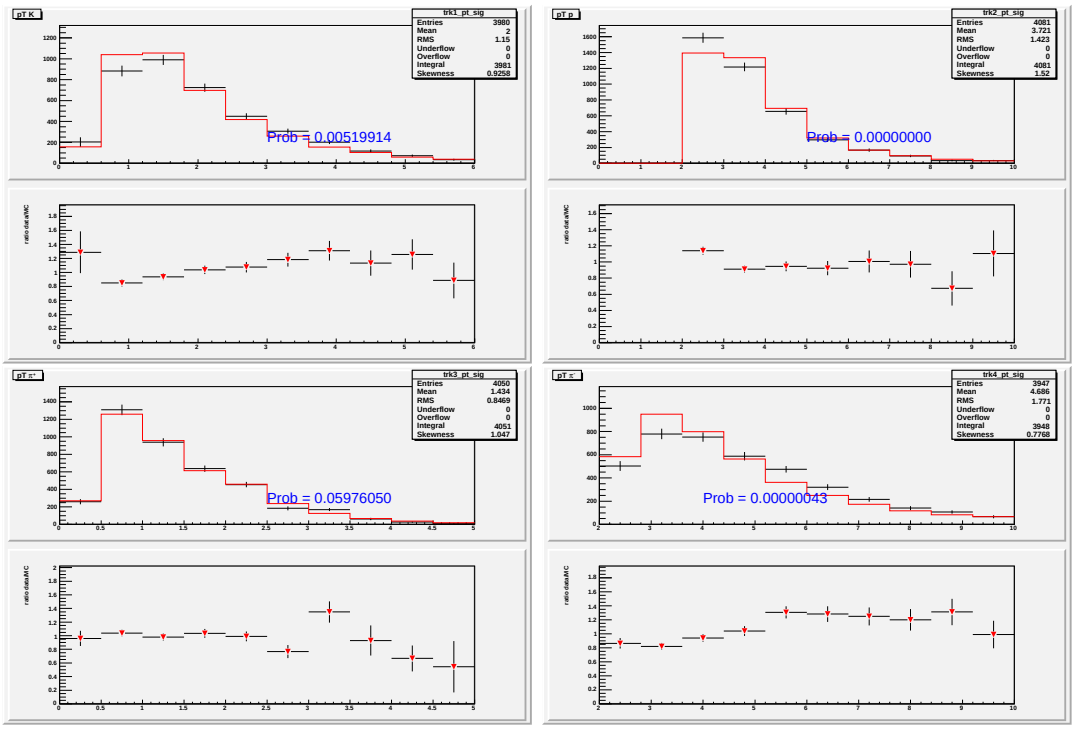

Figure A.7: *p_T distributions of the four tracks produced in the $\Lambda_b^0 \to \Lambda_c^+ \pi^-$ decay for data (black) and MC (red).*

Appendix A. Monte Carlo Validation

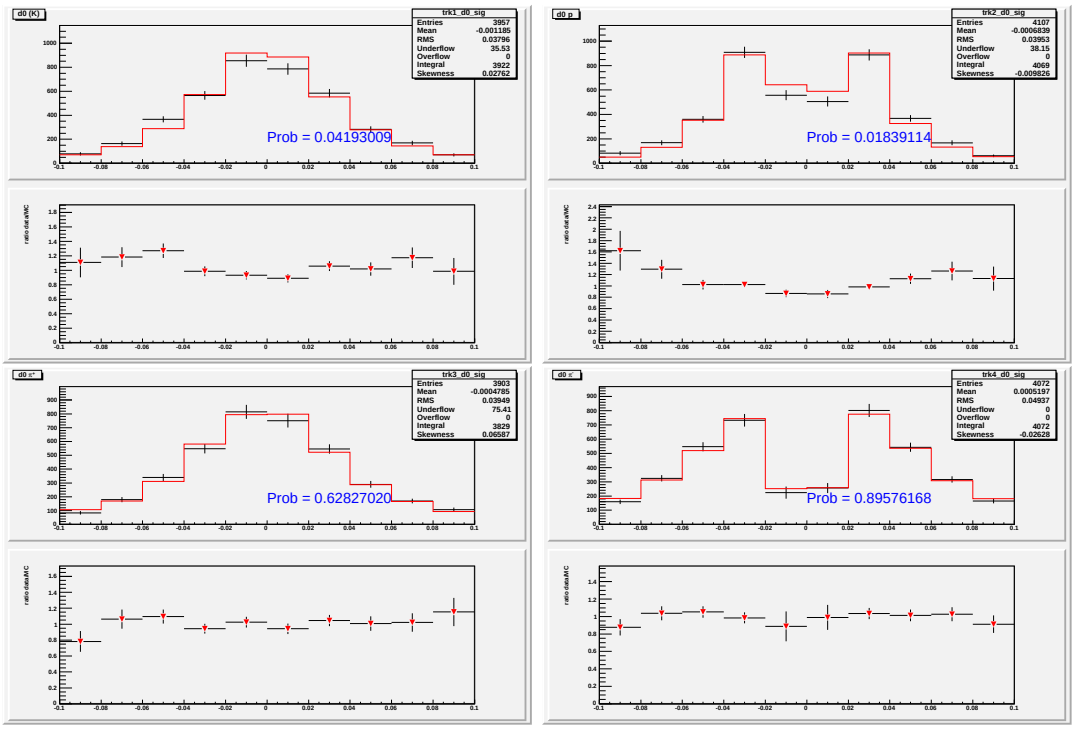

Figure A.8: *d_0 distributions of the four tracks produced in the $\Lambda_b^0 \to \Lambda_c^+ \pi^-$ decay for data (black) and MC (red).*

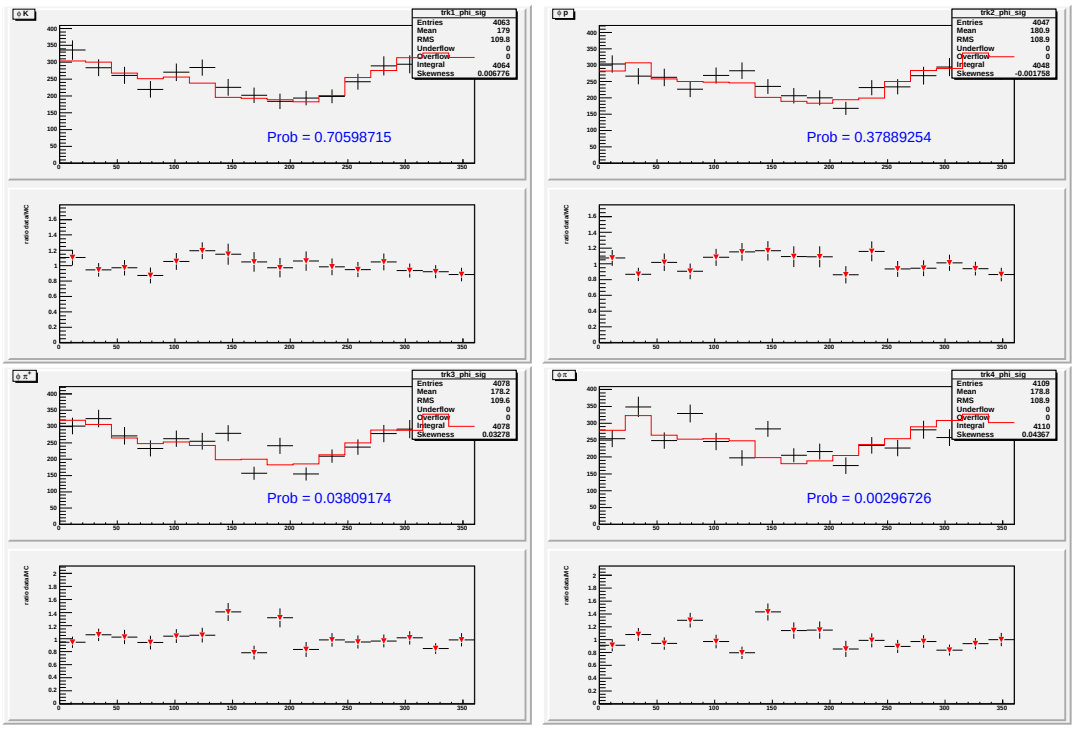

Figure A.9: *φ_0 distributions of the four tracks produced in the $\Lambda_b^0 \to \Lambda_c^+ \pi^-$ decay for data (black) and MC (red).*

Appendix A. Monte Carlo Validation

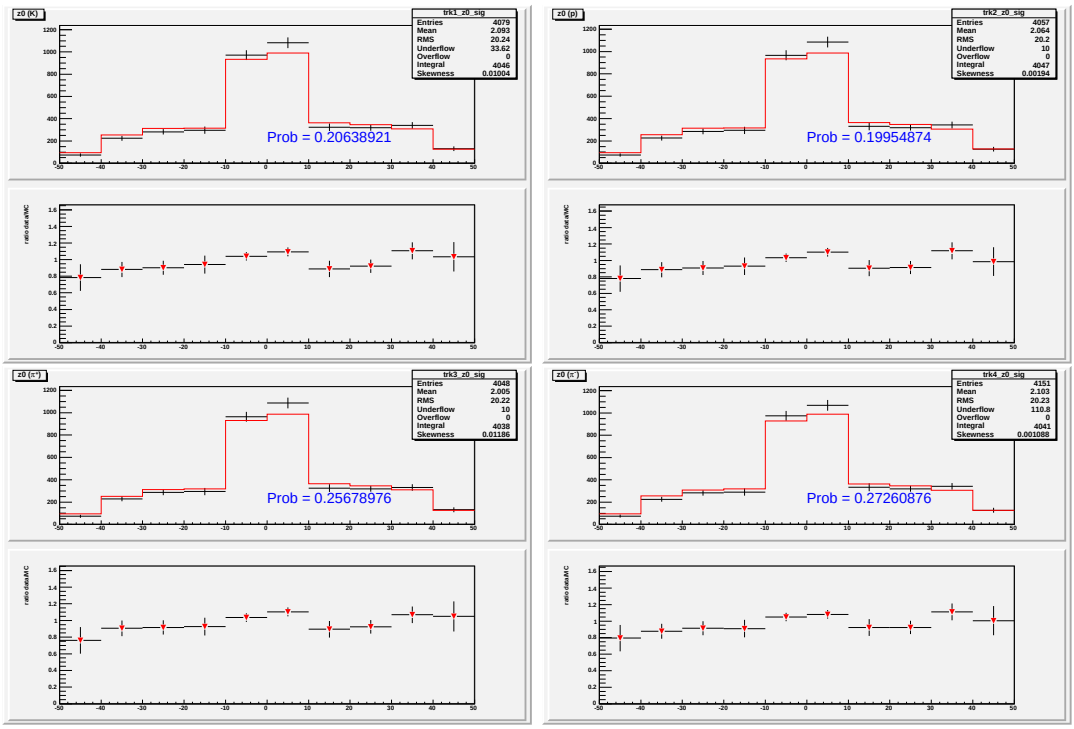

Figure A.10: *z_0 distributions of the four tracks produced in the $\Lambda_b^0 \to \Lambda_c^+ \pi^-$ decay for data (black) and MC (red).*

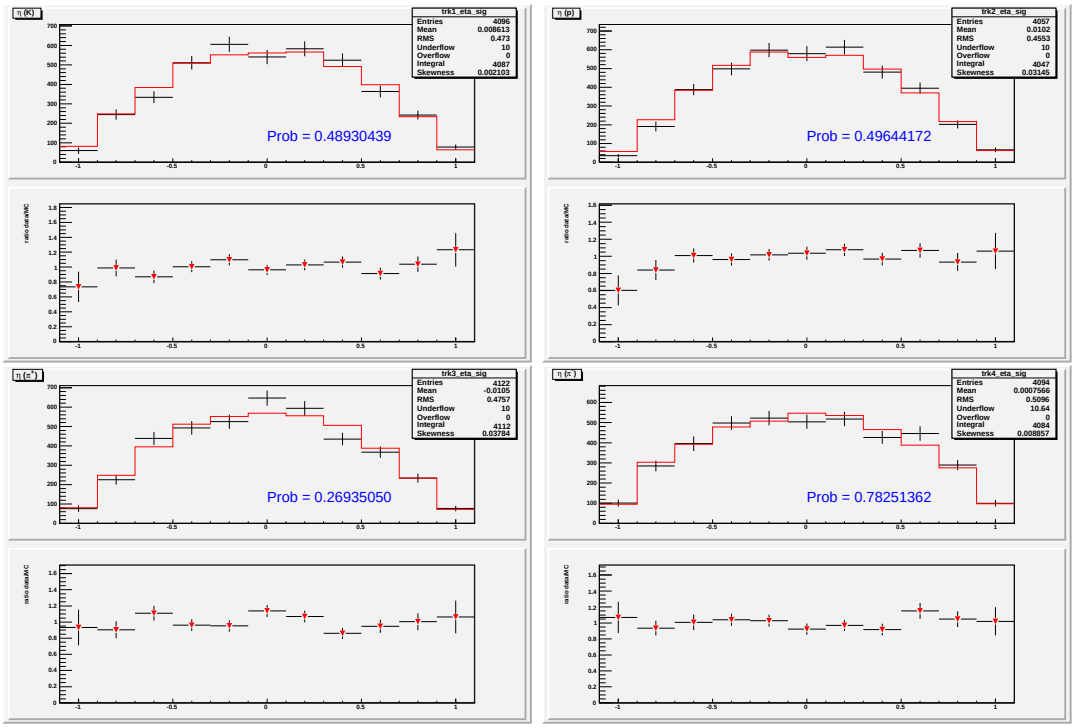

Figure A.11: *η distributions of the four tracks produced in the $\Lambda_b^0 \to \Lambda_c^+ \pi^-$ decay for data (black) and MC (red).*

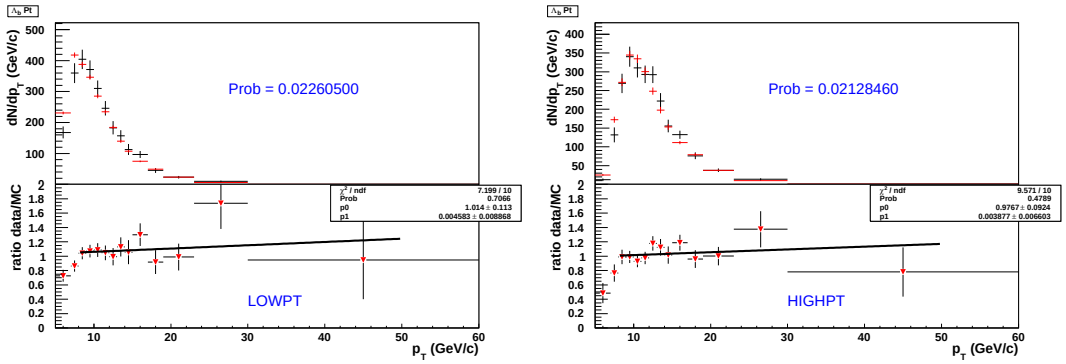

(a) (b)

Figure A.12: *$p_T(\Lambda_b^0)$ comparison between data and MC for events collected by the B_CHARM_LOWPT trigger* **A.12(a)** *and B_CHARM_HIGHPT trigger* **A.12(b)**.

Appendix A. Monte Carlo Validation

Appendix B

Physics Background Study

In Chap. 5 we extracted the signal yields of the $\Lambda_b^0 \to \Lambda_c^+\pi^-\pi^+\pi^-$ after the veto on the charmed resonant Λ_b^0 decay modes, with Λ_c^+ into a $pK^-\pi^+$ final state. A not biased extraction of these yields required an accurate modeling of the background shape and in particular of the physical background contributing into the Λ_b^0 mass window.

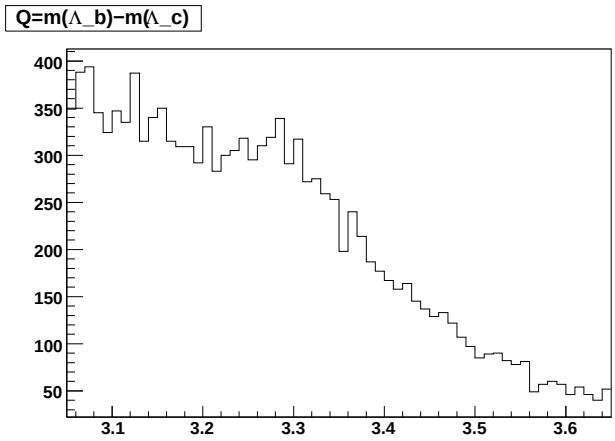

Figure B.1: *ΔM^{--+} MC distribution of $\overline{B}{}^0_{(s)} \to D^{(*)+}_{(s)}\pi^-\pi^+\pi^-$ (with inclusive $D^{(*)+}_{(s)}$ decay modes).*

Considering the inclusive $\Lambda_b^0 \to \Lambda_c^+\pi^-\pi^+\pi^-$ candidates (see Fig. 5.2(a) and Fig. 5.2(b)) and also when the distribution is done for the $\Lambda_b^0 \to \Lambda_c^+\pi^-\pi^+\pi^-$, by vetoing the $\Lambda_c(2595)^+$, $\Lambda_c(2625)^+$, $\Sigma_c(2455)^{++}$ and $\Sigma_c(2455)^0$ resonances (see Fig. 5.10(a) and

Appendix B. Physics Background Study

Fig. 5.10(b)), the $\overline{B}^0_{(s)} \to D^{(*)+}_{(s)}\pi^-\pi^+\pi^-$[1], with inclusive $D^{(*)+}_{(s)}$ decays modes, can be assumed as the main sources of the physical background to the $\Lambda^0_b \to \Lambda^+_c\pi^-\pi^+\pi^-$ signal. This kind of background occurs, for example, in the $D^+ \to K^-\pi^+\pi^+$ decay mode when one of the two π^+ produced in the D^+ decay is assigned the proton mass, and the combination of the three particles form an invariant mass compatible with the Λ^+_c so that the combination of the six tracks falls in the Λ^0_b mass region as well for a generic decay with an efficiency dependent on the $D^{(*)+}$ decay mode.
Just as an example, we present here the study done to determine the modeling of the background for the $\Lambda^0_b \to \Lambda^+_c\pi^-\pi^+\pi^-$ without charmed resonant decay modes (after applying the veto on the charmed resonances). MC distribution are obtained applying the same requirements as for data. Fig. B.1 shows the ΔM^{--+} mass distribution (template) of a MC sample of $\overline{B}^0 \to D^{(*)+}\pi^-\pi^+\pi^-$ and $\overline{B}^0_s \to D^{(*)+}_s\pi^-\pi^+\pi^-$ mixed in the proportions expected from the measured f_s/f_d ratio [1] (see Sec. 1.2) and the measured branching fractions [1], when reconstructed as a $\Lambda^0_b \to \Lambda^+_c\pi^-\pi^+\pi^-$ without charmed resonances candidate.
The distribution peaks in the region around $3.3\,\mathrm{GeV/c^2}$ and this is due to the subsample where the D^+ or D^+_s decay exactly into three charged tracks, as shown repectively in Fig. B.2(a) and Fig. B.2(b) where their ΔM^{--+} distribution is reported.

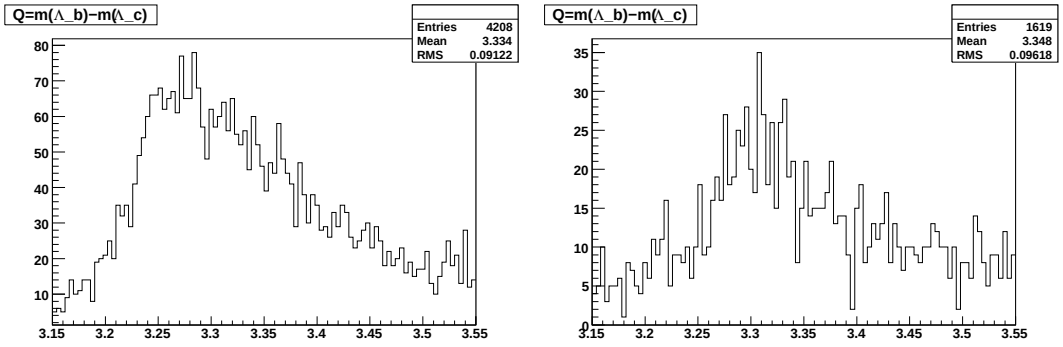

(a) (b)

Figure B.2: *ΔM^{--+} MC distribution of $\overline{B}^0 \to D^+\pi^-\pi^+\pi^-$* **B.2(a)** *and $\overline{B}^0_s \to D^+_s\pi^-\pi^+\pi^-$* **B.2(b)** *with D^+ and the D^+_s decays in three charged tracks.*

Fig. B.3(a) shows the ΔM^{--+} distribution for these candidates when the mode-

[1] In the following we indicate with $\overline{B}^0_{(s)} \to D^{(*)+}_{(s)}\pi^-\pi^+\pi^-$ the four decay modes $\overline{B}^0 \to D^+\pi^-\pi^+\pi^-$, $\overline{B}^0 \to D^{*+}\pi^-\pi^+\pi^-$, $\overline{B}^0_s \to D^+_s\pi^-\pi^+\pi^-$ and $\overline{B}^0_s \to D^{*+}_s\pi^-\pi^+\pi^-$.

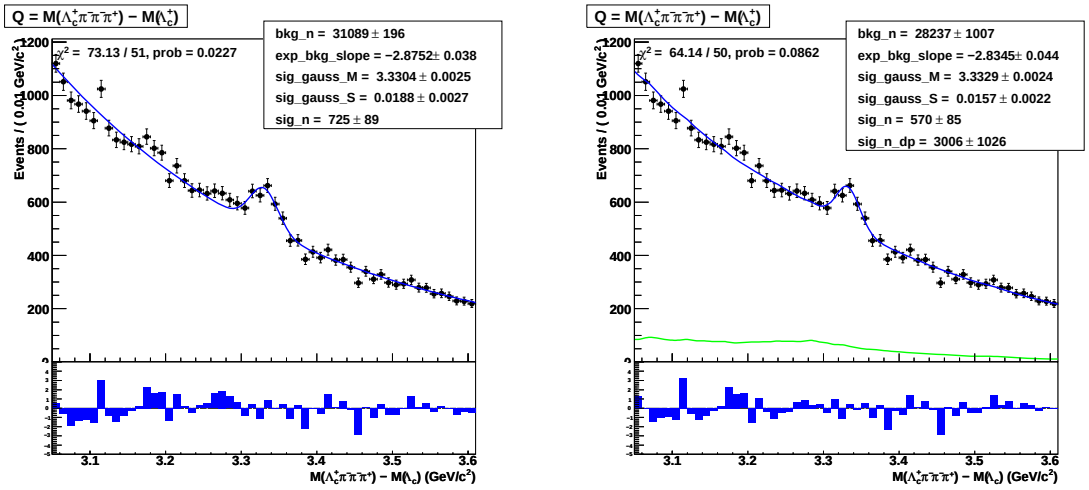

(a) (b)

Figure B.3: **B.3(a):** *Fit of all the* Λ_b^0 *candidates when the resonant decay modes have been removed with the cuts* $\Delta M^{+-} > 0.380$ GeV/c^2, $\Delta M^{+} > 0.190$ GeV/c^2 *and* $\Delta M^{-} > 0.190$ GeV/c^2, *the background is modeled using an exponential shape with slope and normalization free to float in the fit.* **B.3(b):** *Unlike the previous plots here have been also included the floating contribution due to* $\overline{B}^0 \to D^{(*)+}\pi^-\pi^+\pi^-$ *and* $\overline{B}_s^0 \to D_s^{(*)+}\pi^-\pi^+\pi^-$ *(with inclusive* $D^{(*)+}$ *and* $D_s^{(*)+}$ *decays) with a fixed shape (MC template).*

ling assumes an exponential to model the background and a gaussian to model the signal. In the fit, slope and contribution of the exponential, as well gaussian mean and sigma, are free to float. Fig. B.3(b) shows the distribution of ΔM^{--+} for the Λ_b^0 reconstructed candidates, with overlaid the best fit curve, when we add the modeling of a physical background, described by the templates made for the $\overline{B}_{(s)}^0 \to D_{(s)}^{(*)+}\pi^-\pi^+\pi^-$, to the exponential, to model the combinatorial background; the slope of the exponential and the normalization of the two background distributions are floating and determined by the fit: the green curve represents the contribution due to the physical background. By comparison of these two figures, the modeling including this physical backround is better (compare the χ^2) and the misreconstructed $\overline{B}_{(s)}^0 \to D_{(s)}^{(*)+}\pi^-\pi^+\pi^-$ decays contribute significantly to the Λ_b^0 mass window. A similar result is obtained when in the modeling we fix the slope of the exponential, using the high mass region (see Sec. 3.4), and we add, in the modeling of the physical background, also a contribute due to the B^0 inclusive decay modes.

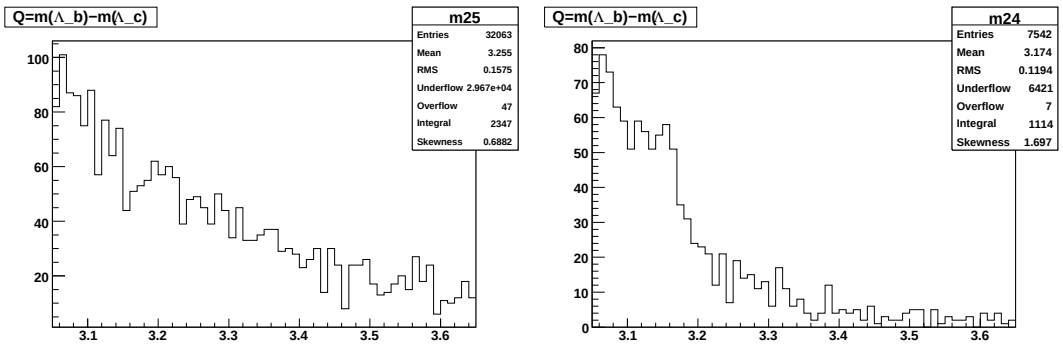

(a) (b)

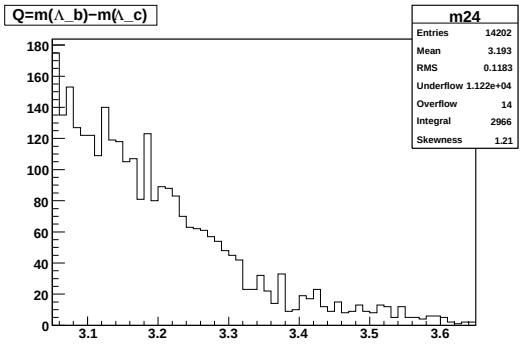

(c)

Figure B.4: *ΔM^{--+} MC distributions of $B^0 \to$ Inclusive* **B.4(a)**, *$\Lambda_b^0 \to \Lambda_c^+\pi^-\pi^+\pi^-\pi^0$* **B.4(b)** *and $\Lambda_b^0 \to \pi^-\pi^+\ell\overline{\nu}_\ell$* **B.4(c)**.

In order to do that, we used a MC sample of $B^0 \to$ Inclusive decays to obtain the corresponding ΔM^{--+} template (see Fig. B.4(a)) when these decays are reconstructed as a $\Lambda_b^0 \to \Lambda_c^+\pi^-\pi^+\pi^-$ candidate without charmed resonances. Adding this physical background contribution (fixed shape, as determined by the template and normalization free to float in the fit), the change in the signal yields is negligible. This can be inferred comparing the yield determined by the best fit of ΔM^{--+} data (value of the variable `sig_n` in the fit result legenda) of Fig. B.3(b) with the one of Fig. 5.10(a) for the $\Lambda_b^0 \to \Lambda_c^+\pi^-\pi^+\pi^-$ without charmed resonances with $\Lambda_c^+ \to pK^-\pi^+$. Added this background in the modeling, we verified that futher contribution to the physical background modeling are not significant in the Λ_b^0 mass window. ΔM^{--+} distributions for the MC samples of $\Lambda_b^0 \to \pi^-\pi^+\pi^-\pi^0$

and $\Lambda_b^0 \to \pi^-\pi^+\ell\overline{\nu}_\ell$, the templates, are shown respectively in Fig. B.4(b) and Fig. B.4(c) and show that these contributions are not significant in the Λ_b^0 mass window.

Cross Check of the Physical Background Modeling using real data

We performed further useful cross-check of the background directly on the data using the Λ_b^0 reconstructed candidates, after the veto on the charmed resonances. Fig. B.3(b) shows the ΔM^{--+} distribution for this sample. Fig. B.5(a) shows the invariant mass spectrum of the $D^+ \to K^-\pi^+\pi^+$ candidates reconstructed in these data by assigning the kaon and pion masses to the Λ_c^+ candidate decay products $K^-p\pi^+$. The fit estimates a D^+ mass of 1.868 GeV/c^2 and a signal width of 7.5 MeV/c^2. Fig. B.5(b) shows the reconstructed $\overline{B}^0 \to D^+\pi^-\pi^+\pi^-$ candidates, when we applied the same exact cuts used to reconstruct the Λ_b^0 candidates without charmed resonances.
We estimate a yield of 360±40 B^0 events ($N(B^0)$) in the ΔM^{--+} window $[3.15 - 3.55]$ GeV/c^2 used for the Λ_b^0 fit. The estimated B^0 mass is (5278 ± 1) MeV/c^2 and the width is (17.5 ± 1.6) MeV/c^2. Since the reconstruction in our data has not been a success for both the D_s^+ and $\overline{B}_s^0 \to D_s^+\pi^-\pi^+\pi^-$ signals, we decided to estimate the total contribution expected from this source relative to the estimated yield of 360±40 $\overline{B}^0 \to D^+\pi^-\pi^+\pi^-$ events. Since the MC estimates a relative efficiency $\varepsilon(B_s^0)/\varepsilon(B^0) = 1.35$, we can give a raw estimate of the expected B_s^0 yield ($N(B_s^0)$) using the following formula where for the BR of each decay we used the corresponding PDG value:

$$N(B_s^0) = N(B^0) \times \frac{f_s}{f_d} \times \frac{\mathcal{B}(\overline{B}_s^0 \to D_s^+\pi^-\pi^+\pi^-)}{\mathcal{B}(\overline{B}^0 \to D^+\pi^-\pi^+\pi^-)} \times \frac{\mathcal{B}(D_s^+ \to K^+K^-\pi^+ \; or \; \pi^-\pi^+\pi^-)}{\mathcal{B}(D^+ \to K^-\pi^+\pi^+)} \times \frac{\varepsilon(B_s^0)}{\varepsilon(B^0)} \tag{B.1}$$

$$N(B_s^0) = 360 \times \frac{0.118}{0.323} \times 1.05 \times \frac{0.066}{0.092} \times 1.35 = 133 \tag{B.2}$$

The reconstructed ΔM^{--+} distribution of the MC sample of $\overline{B}^0 \to D^+\pi^-\pi^+\pi^-$and $\overline{B}_s^0 \to D_s^+\pi^-\pi^+\pi^-$ signals, in the expected proportions, is reported in Fig. B.6(a): this background covers the entire $[3.15 - 3.55]$ GeV/c^2 window.
In the fit, this distribution is then used as template to model the physical background while an exponential is used to model the combinatorial background. The physical background normalization is given by the sum of the 360 $\overline{B}^0 \to D^+\pi^-\pi^+\pi^-$ and of the 133 $\overline{B}_s^0 \to D_s^+\pi^-\pi^+\pi^-$ which gives a total of 493 events, while the slope and the normalization of the exponential are free to float in the fit.

Appendix B. Physics Background Study

The best fit returns a Λ_b^0 yield of 596±78 signal events (value of `sig_n` in the fit results legenda of Fig. B.6(b)), which is consistent with the yield of $\Lambda_b^0 \to \Lambda_c^+\pi^-\pi^+\pi^-$ without charmed resonances signal events, when the modeling is done using the procedure described in Sec. 5.3 but in the enlarged range of mass, $[3.15 - 3.55]$ GeV/c^2 (see Fig. 5.10(a), `sig_n` value in the fit results legenda). We have also performed the same fit with floating $\overline{B}^0 \to D^+\pi^-\pi^+\pi^-$ and $\overline{B}_s^0 \to D_s^+\pi^-\pi^+\pi^-$ backgrounds (Fig. B.6(c)) and the estimate of the signal and background yields are consistent with the central result.

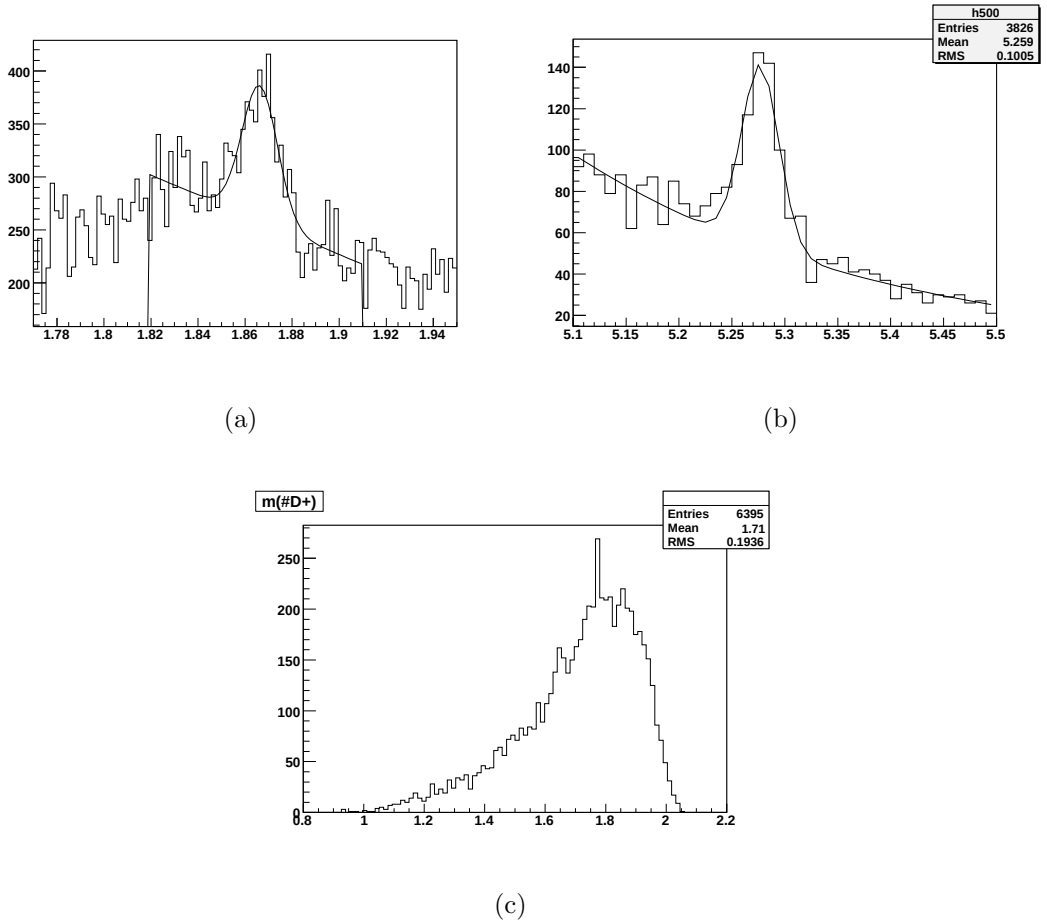

(a) (b)

(c)

Figure B.5: **B.5(a):** *D^+ signal reconstructed in data by assigning the kaon and pion masses to the Λ_c^+ decay products.* **B.5(b):** *$\overline{B}^0 \to D^+\pi^-\pi^+\pi^-$ signal reconstructed in data by using the D^+ signal (to reconstruct this signal we applied the cut $|\, m(D^+) - 1.868\,| < 0.022\,\mathrm{GeV/c^2}$).* **B.5(c):** *MC mass distribution of the Λ_c^+ (from Λ_b^0) reconstructed as D^+.*

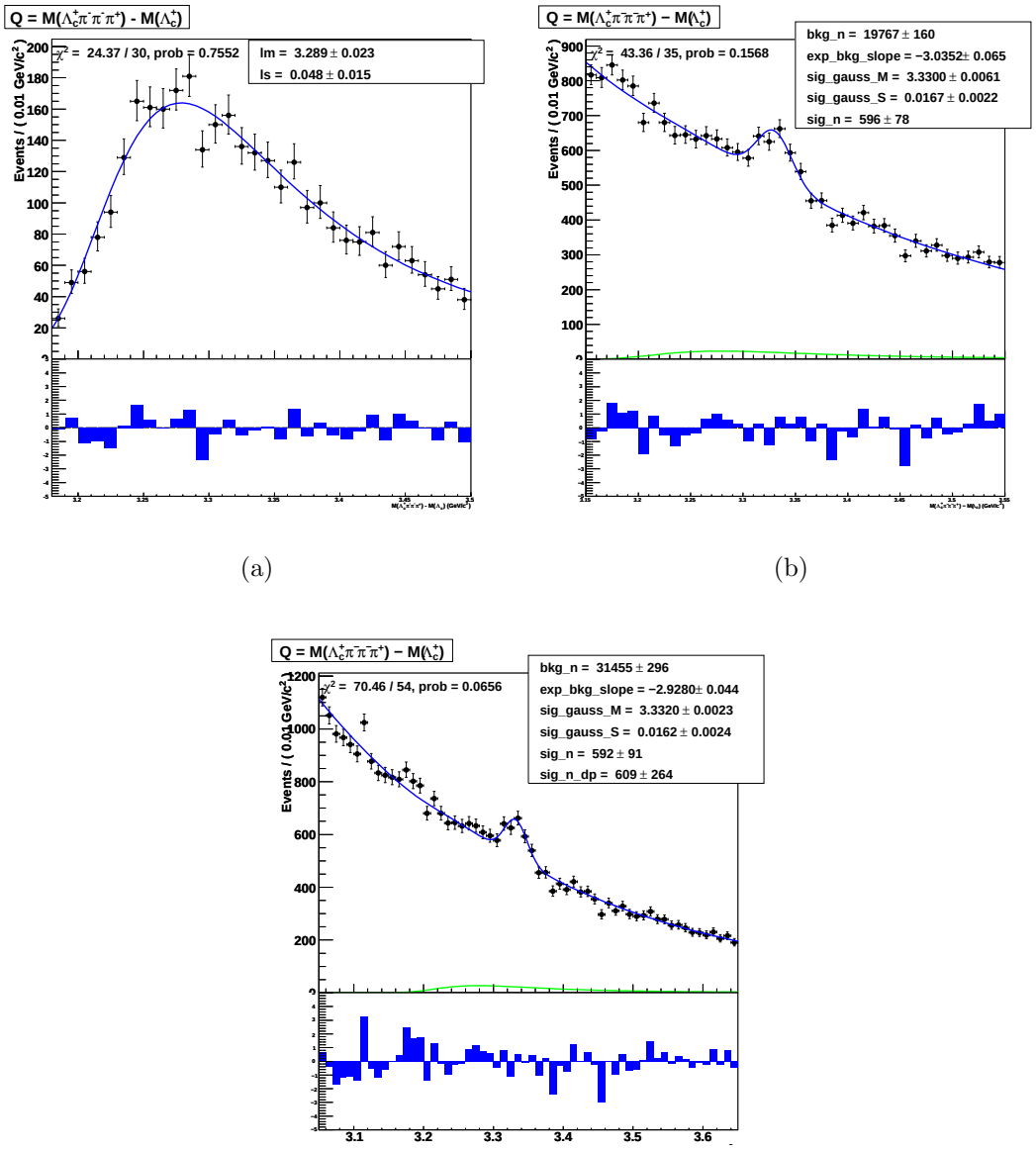

Figure B.6: **B.6(a):** *Reconstructed ΔM^{--+} distribution of the MC sample of $\overline{B}^0_{(s)} \rightarrow D^+_{(s)}\pi^-\pi^+\pi^-$ signals in the expected proportions.* **B.6(b):** *Fit of all the Λ^0_b candidates: resonant decay modes removed with the cuts $\Delta M^{+-} > 0.380\,\mathrm{GeV/c^2}$, $\Delta M^{+} > 0.190\,\mathrm{GeV/c^2}$ and $\Delta M^{-} > 0.190$ GeV/c^2 and the B^0 and B^0_s contribution fixed to 493 events.* **B.6(c):** *Fit of all the Λ^0_b candidates, including the the B^0 and B^0_s background left floating and determined by the fit.*

Appendix B. Physics Background Study

Appendix C

MC Estimate of the Cabibbo Suppressed decay modes contributions

In order to determine the yields of the Λ_b^0 in the $\Lambda_b^0 \to \Lambda_c^+\pi^-\pi^+\pi^-$ mass spectra, we need a good assessment of the backgrounds which reside under the Λ_b^0 signal peak. One such class of backgrounds are the CS decay modes, where one of the π^- is replaced by a K^-. In the following we estimate the ratios of the BRs of the CS to the CF decay modes, and estimate the fraction of CS background to the CF in all decay modes reported in Tab. C.1. We provide similar estimates for the CS background relatively to the decay $\Lambda_b^0 \to \Lambda_c^+\pi^-$. These ratios of BRs are used in Chap. 5 to estimate the expected yield of the CS background corresponding to a given yield of the CF decay mode, once the respective efficiencies are known from simulated samples. Here we give an example of how the expected contamination of a CS decay mode can be evaluated when the signal is reconstructed as the corresponding CF decay mode. We remember that the CS decay modes are not modeled in the physical background (see section Sec. 5.1), since we expect very few events, but are assumed as a systematic affecting the corresponding CF yields (see Sec. 7.1.1).

Outline

The yields of the Λ_b^0 decay modes, extracted by the fit procedure described in Chap. 5 applied to the ΔM^{--+} mass distribution, are determined assuming no contribution from the CS decay modes. The observed signals in the ΔM^{--+} mass distribution, for each decay mode, have two contributions: the CF and the CS. Denoting with N^i_{obs} the yield of the i^{th} decay mode extracted, and with N^i_{CS} and

Appendix C. MC Estimate of the Cabibbo Suppressed decay modes contributions

N^i_{CF} the corresponding contributions of the CS and of the CF we can write:

$$N^i_{obs} = N^i_{CF}(1 + N^i_{CS}/N^i_{CF}) \tag{C.1}$$

Λ_b^0 Cabibbo favored decay modes	Λ_b^0 Cabibbo suppressed decay modes
$\Lambda_b^0 \to \Lambda_c^+\pi^-$	$\Lambda_b^0 \to \Lambda_c^+K^-$
$\Lambda_b^0 \to \Lambda_c^+\pi^-\pi^-\pi^+$	$\Lambda_b^0 \to \Lambda_c^+\pi^+\pi^-K^-$
$\Lambda_b^0 \to \Lambda_c^*(2595)^+\pi^-$	$\Lambda_b^0 \to \Lambda_c^*(2595)^+K^-$
$\Lambda_b^0 \to \Lambda_c^*(2625)^+\pi^-$	$\Lambda_b^0 \to \Lambda_c^*(2625)^+K^-$
$\Lambda_b^0 \to \Sigma_c(2455)^{++}\pi^-\pi^-$	$\Lambda_b^0 \to \Sigma_c(2455)^{++}\pi^-K^-$
$\Lambda_b^0 \to \Sigma_c(2455)^0\pi^-\pi^+$	$\Lambda_b^0 \to \Sigma_c(2455)^0\pi^+K^-$
$\Lambda_b^0 \to \Lambda_c^+\rho^0\pi^-$	$\Lambda_b^0 \to \Lambda_c^+\rho^0K^-$

Table C.1: *CF and CS decay modes.*

The amount of CS background we expect, relative to the CF signals, for each decay mode i in Tab. C.1, is given by the expression:

$$\frac{N^i_{CS}}{N^i_{CF}} = \frac{\mathcal{B}(\Lambda_b^0 \to CS^i) \times \varepsilon^i_{CS}}{\mathcal{B}(\Lambda_b^0 \to CF^i) \times \varepsilon^i_{CF}} \tag{C.2}$$

where ε^i is the efficiency of reconstructed signal in mode i and $\mathcal{B}(\Lambda_b^0 \to CS^i)$ and $\mathcal{B}(\Lambda_b^0 \to CF^i)$ is the BR of the Λ_b^0 in the CS and in the corresponding CF decay modes. From Eq. C.2, in order to estimate N^i_{CS}/N^i_{CF}, we need to know the relative efficiency estimates and the relative BRs ($\mathcal{B}$) of each decay mode. In the following we describe the studies done for these estimates.

Evaluation of $\mathcal{B}(\Lambda_b^0 \to CS^i)$

The CS decay modes for which we need BR have not been observed, let alone measured. The decay amplitude, for the baryonic CF decay mode, is $\propto |V_{ud}|^2$ while is $\propto |V_{us}|^2$ for the CS one. If we consider the decay amplitude for the related mesonic decay mode, we find the same number in both cases, CF and CS decay modes. We estimate the ratio $\mathcal{B}(\Lambda_b^0 \to CS^i)/\mathcal{B}(\Lambda_b^0 \to CF^i)$ either using similar decay modes observed in B-mesons, where the measurements already exist (from the B-Factories or CDF itself), or, when these measurements are not available, simply using the ratio $|V_{ud}|^2/|V_{us}|^2$.

Just as an example, to illustrate the concepts described above, we estimate the CS $\mathcal{B}(\Lambda_b^0 \to \Sigma_c(2455)^0\pi^+K^-)$ relative to the CF decay $\Lambda_b^0 \to \Sigma_c(2455)^0\pi^+\pi^-$. The first order Feynman diagram of this decay, for the CF and for the corresponding CS, is reported in Fig. C.1.

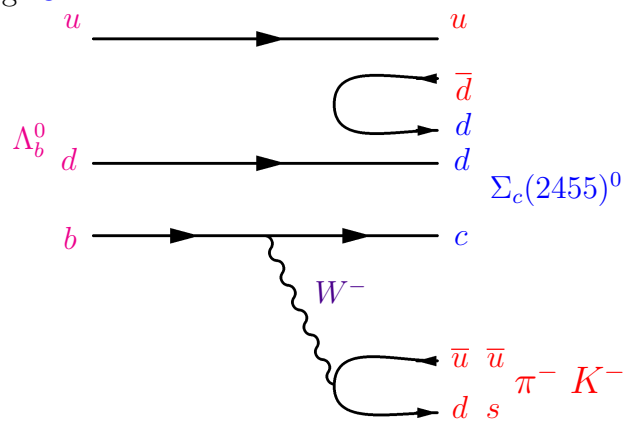

Figure C.1: *Feynman diagram illustrating the decays* $\Lambda_b^0 \to \Sigma_c(2455)^0\pi^+\pi^-$ *and* $\Lambda_b^0 \to \Sigma_c(2455)^0\pi^+K^-$.

The neutral B-meson decay modes, corresponding to the baryonic one of Fig. C.1, are reported in Fig. C.2 and Fig. C.3. The diagrams of Fig. C.2 are obtained removing the line of the Λ_b^0 u quark (one of the spectator quark) in Fig. C.1 and changing, in the same figure, the Λ_b^0 d quark in a $\overline{d}$ quark. The only difference in these two diagrams is that in one case (see Fig. C.2**(b)**) the gluon splits in a $u\overline{u}$ pair, while in the other (see Fig. C.2**(a)**) in a $d\overline{d}$ pair.

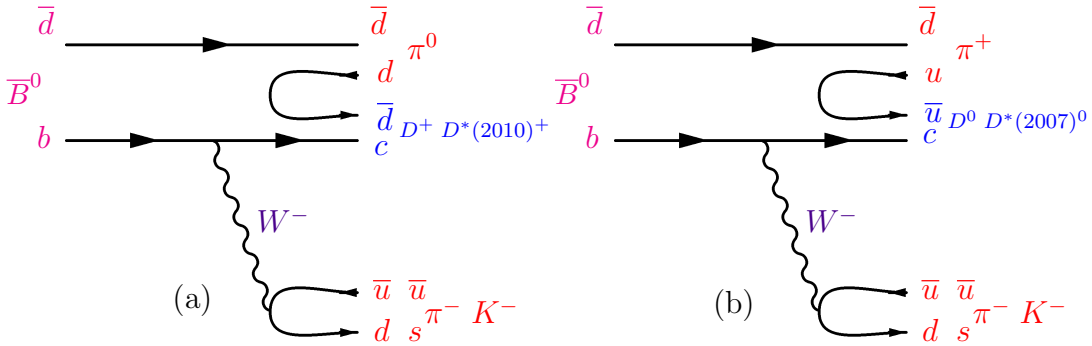

Figure C.2: *Feynman diagrams illustrating the neutral B-meson decay modes corresponding to the baryonic decay mode on Fig. C.1.*

Using the same method, the two lower order Feynman diagrams for charged B-meson decay modes are obtained removing the line of the Λ_b^0 d quark (one of the

Appendix C. MC Estimate of the Cabibbo Suppressed decay modes contributions

spectator quark) in Fig. C.1 and changing in the same figure the Λ_b^0 u quark in a $\overline{u}$ quark. As before, the only difference in these two diagrams is that in one case (see Fig. C.3**(b)**) the the gluon splits in a $u\overline{u}$ pair and in the other (see Fig. C.3**(a)**) in a $d\overline{d}$ pair. So, in principle the Feynman diagrams in Fig. C.2**(a)**, Fig. C.2**(b)**, Fig. C.3**(a)** and Fig. C.3**(b)** are equivalent and we can choose anyone of them to made our estimate.

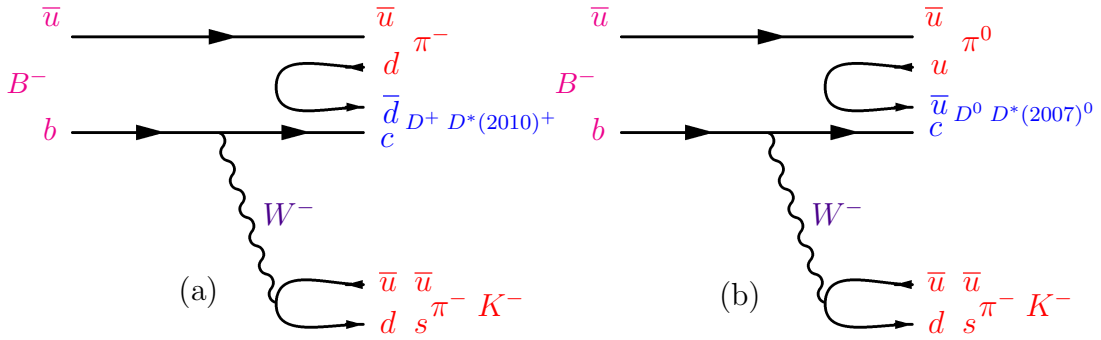

Figure C.3: *Feynman diagrams illustrating the charged B-meson decay modes corresponding to the baryonic decay mode on Fig. C.1.*

In this specific case in our calculation we used, to estimate $\mathcal{B}(\Lambda_b^0 \to \Sigma_c(2455)^0\pi^+K^-)/\mathcal{B}(\Lambda_b^0 \to \Sigma_c(2455)^0\pi^+\pi^-)$, the branching fractions of the decays $B^- \to D^+\pi^-\pi^-$ (S-wave) , $B^- \to D^*(2010)^+\pi^-\pi^-$ (P-wave) and of the corresponding CS decays, which are all measured [1]. The Feynman diagram associated to these decays is the one of Fig. C.3**(a)**. This is due to the fact that the spin 1/2 Λ_b^0 decays into a spin 1/2 Λ_c^+ and, from angular momentum conservation, we expect contributions from both S and P wave amplitudes.
The correspondence between the baryonic and mesonic decay modes here considered, is unfolded as follows:

gluon splits to a $d\overline{d}$ pair;

the decay rate for the baryonic CF decay mode is $\propto |V_{ud}|^2\,|V_{bc}|^2\,|f_1^2|$;

the decay rate for the baryonic CS decay mode is $\propto |V_{us}|^2\,|V_{bc}|^2\,|f_2^2|$;

the decay rate for the mesonic CF decay modes is $\propto |V_{ud}|^2\,|V_{bc}|^2\,|f_3^2|$;

the decay rate for the mesonic CS decay modes is $\propto |V_{us}|^2\,|V_{bc}|^2\,|f_4^2|$.

Therefore, it's easy to understand that each relative branching ratio $\mathcal{B}$ is given by:

$$\underbrace{\frac{|V_{us}|^2\,|V_{bc}|^2\,|f_2^2|}{|V_{ud}|^2\,|V_{bc}|^2\,|f_1^2|}}_{\text{baryonic decay mode}} = \underbrace{\frac{|V_{us}|^2\,|V_{bc}|^2\,|f_4^2|}{|V_{ud}|^2\,|V_{bc}|^2\,|f_3^2|}}_{\text{mesonic decay mode}} \tag{C.3}$$

where $f_3 = f_1$ and $f_4 = f_2$. Since the amplitude for the baryonic decay considered in this example includes contributions from both S-wave ($J = 0$) and P-wave ($J = 1$) transitions then, in the case of mesons, f_3 and f_4 actually have two components :

$$\begin{aligned} f_3 &= f_3(S) + f_3(P) \\ f_4 &= f_4(S) + f_4(P) \end{aligned} \tag{C.4}$$

Looking at the Eq. C.3 we have to add the two terms and then square them to get the cross terms:

$$\begin{aligned} |f_3|^2 &= |f_3(S)|^2 + |f_3(P)|^2 + \underbrace{(f_3^*(S))(f_3(P)) + (f_3(S))(f_3^*(P))}_{\text{negligible}} \\ |f_4|^2 &= |f_4(S)|^2 + |f_4(P)|^2 + \underbrace{(f_4^*(S))(f_4(P)) + (f_4(S))(f_4^*(P))}_{\text{negligible}} \end{aligned} \tag{C.5}$$

Combining Eq. C.3 and Eq. C.5 and assuming negligible the cross terms, we get:

$$\frac{\mathcal{B}^{(CS)}_{baryon}}{\mathcal{B}^{(CF)}_{baryon}} = \frac{|V_{us}|^2\ (|f_4(S)|^2 + |f_4(P)|^2)}{|V_{ud}|^2\ (|f_3(S)|^2 + |f_3(P)|^2)} = \frac{\mathcal{B}^{(CS)}_{meson\ (S)} + \mathcal{B}^{(CS)}_{meson\ (P)}}{\mathcal{B}^{(CF)}_{meson\ (S)} + \mathcal{B}^{(CF)}_{meson\ (P)}} \tag{C.6}$$

We applied this method to all studied decay modes once known the corresponding B-meson decays modes contributing.

Therefore, in the example of the $\Lambda_b^0 \to \Sigma_c(2455)^0\pi^+K^-$ and $\Lambda_b^0 \to \Sigma_c(2455)^0\pi^+\pi^-$, considering the contributions of all the corresponding B-meson decays modes Feynman diagrams we have:

$$\begin{aligned} &\frac{\mathcal{B}(\Lambda_b^0 \to \Sigma_c(2455)^0\pi^+K^-)}{\mathcal{B}(\Lambda_b^0 \to \Sigma_c(2455)^0\pi^+\pi^-)} = \frac{\mathcal{B}(B^- \to D^+\pi^-K^-) + \mathcal{B}(B^- \to D(2010)^{*+}\pi^-K^-)}{\mathcal{B}(B^- \to D^+\pi^-\pi^-) + \mathcal{B}(B^- \to D(2010)^{*+}\pi^-\pi^-)} \\ &= \frac{(0.55 \pm 0.54) \times 10^{-4} + (0.73 \pm 0.54) \times 10^{-4}}{(1.02 \pm 0.16) \times 10^{-3} + (1.35 \pm 0.22) \times 10^{-3}} \\ &= \frac{(1.28 \pm 0.76) \times 10^{-4}}{(2.37 \pm 0.27) \times 10^{-3}} \\ &= (5.40 \pm 3.26) \times 10^{-2} \end{aligned} \tag{C.7}$$

where all the used $\mathcal{B}$ are from PDG [1].

Tab. C.2 summarizes as input the B-meson decay modes contributing to the CF

Appendix C. MC Estimate of the Cabibbo Suppressed decay modes contributions

Meson Decay	$\mathcal{B}$ (PDG)	Λ_b^0 decay mode	Sum of CF/CS $\mathcal{B}$
$\overline{B}^0 \to D^*(2010)^+\pi^-$	$(2.76 \pm 0.13) \times 10^{-3}$	$\Lambda_b^0 \to \Lambda_c^*(2595)^+\pi^-$	$(2.76 \pm 0.13) \times 10^{-3}$
$\overline{B}^0 \to D^*(2010)^+K^-$	$(2.14 \pm 0.16) \times 10^{-4}$	$\Lambda_b^0 \to \Lambda_c^*(2595)^+K^-$	$(2.14 \pm 0.16) \times 10^{-4}$
$\overline{B}^0 \to D^*(2010)^+\pi^-$	$(2.76 \pm 0.16) \times 10^{-3}$	$\Lambda_b^0 \to \Lambda_c^*(2625)^+\pi^-$	—
$\overline{B}^0 \to D_2^*(2460)^+\pi^-$	*not in PDG* 2008		
$\overline{B}^0 \to D^*(2010)^+K^-$	$(2.14 \pm 0.16) \times 10^{-4}$	$\Lambda_b^0 \to \Lambda_c^*(2625)^+K^-$	—
$\overline{B}^0 \to D_2^*(2460)^+K^-$	*not in PDG* 2008		
$\overline{B}^0 \to D^0\pi^+\pi^-$	$(8.40 \pm 0.90) \times 10^{-4}$	$\Lambda_b^0 \to \Sigma_c(2455)^{++}\pi^-\pi^-$	$(14.60 \pm 2.40) \times 10^{-4}$
$\overline{B}^0 \to D^*(2007)^0\pi^+\pi^-$	$(6.20 \pm 2.20) \times 10^{-4}$		
$\overline{B}^0 \to D^0\pi^+K^-$	$(8.80 \pm 1.70) \times 10^{-5}$	$\Lambda_b^0 \to \Sigma_c(2455)^{++}\pi^-K^-$	$(12.10 \pm 5.70) \times 10^{-5}$
$\overline{B}^0 \to D^*(2007)^0\pi^+K^-$	$(3.34 \pm 5.40) \times 10^{-5}$ [a]		
$B^- \to D^+\pi^-\pi^-$	$(1.02 \pm 0.16) \times 10^{-3}$	$\Lambda_b^0 \to \Sigma_c(2455)^0\pi^+\pi^-$	$(2.37 \pm 0.27) \times 10^{-3}$
$B^- \to D^*(2010)^+\pi^-\pi^-$	$(1.35 \pm 0.22) \times 10^{-3}$		
$B^- \to D^+\pi^-K^-$	$(0.55 \pm 0.54) \times 10^{-4}$ [a]	$\Lambda_b^0 \to \Sigma_c(2455)^0\pi^+K^-$	$(1.28 \pm 0.76) \times 10^{-4}$
$B^- \to D^*(2010)^+\pi^-K^-$	$(0.73 \pm 0.54) \times 10^{-4}$ [a]		
$\overline{B}^0 \to D^+\rho^0\pi^-$	$(1.10 \pm 1.00) \times 10^{-3}$	$\Lambda_b^0 \to \Lambda_c^+\rho^0\pi^-$	$(1.10 \pm 1.00) \times 10^{-3}$
$\overline{B}^0 \to D^+\rho^0K^-$	$(0.59 \pm 0.55) \times 10^{-4}$ [a]	$\Lambda_b^0 \to \Lambda_c^+\rho^0K^-$	$(0.59 \pm 0.55) \times 10^{-4}$
$B^- \to D^0\pi^-\pi^+\pi^-$	$(5 \pm 4) \times 10^{-3}$	$\Lambda_b^0 \to \Lambda_c^+\pi^-\pi^+\pi^-$	$(15.3 \pm 4.18) \times 10^{-3}$
$B^- \to D^*(2007)^0\pi^-\pi^+\pi^-$	$(1.03 \pm 0.12) \times 10^{-2}$		
$B^- \to D^0\pi^+\pi^-K^-$	$(2.70 \pm 0.74) \times 10^{-4}$ [a]	$\Lambda_b^0 \to \Lambda_c^+\pi^-\pi^+K^-$	$(8.26 \pm 0.69) \times 10^{-4}$
$B^- \to D^*(2007)^+\pi + \pi^-K^-$	$(5.56 \pm 0.66) \times 10^{-4}$ [a]		
$\overline{B}^0 \to D^+\pi^-$	$(2.68 \pm 0.13) \times 10^{-3}$	$\Lambda_b^0 \to \Lambda_c^+\pi^-$	$(5.44 \pm 0.18) \times 10^{-3}$
$\overline{B}^0 \to D^*(2010)^+\pi^-$	$(2.76 \pm 0.13) \times 10^{-3}$		
$\overline{B}^0 \to D^+K^-$	$(2.0 \pm 0.6) \times 10^{-4}$	$\Lambda_b^0 \to \Lambda_c^+K^-$	$(4.14 \pm 0.62) \times 10^{-4}$
$\overline{B}^0 \to D^*(2010)^+K^-$	$(2.14 \pm 0.16) \times 10^{-4}$		

Table C.2: *List of CF and CS B-meson decay modes, the corresponding BR from PDG [1], baryonic Λ_b^0 decay modes and sum of BRs for the CF and CS associated B-meson decay modes.*

[a] These $\mathcal{B}$ are not in PDG [1] so that we evaluated them using Eq. C.8

and to the CS (Meson decay) , the corresponding BR ($\mathcal{B}(PDG)$), the corresponding Λ_b^0 decay mode, in which they are used (Λ_b^0 decay mode) and the sum of the BRs of the B-mesons contributing to the CF and to the CS (Sum of CF/CS $\mathcal{B}$).
The contributing mesonic decay modes were determined for the other Λ_b^0 decay modes using the same method adopted in this example. Some of the $\mathcal{B}$ for B-meson decays have not yet been measured and in this case we use the ratio in Eq. C.8:

$$\frac{\mathcal{B}(CS^i)}{\mathcal{B}(CF^i)} = \frac{|V_{us}|^2}{|V_{ud}|^2} \tag{C.8}$$

MC Evaluated Relative Efficiencies

We used MC samples to evaluate the efficiency for each decay mode of Tab. C.1. There are several components in the MC simulation:

- production and decay of the b-hadrons;

- detector simulation;
- trigger simulation;
- reconstruction.

In this example we give just an early estimate of how the efficiency can be evaluated and we use here a generator-level simulation. We generate 10^6 Λ_b^0 decays in each of the CF and CS modes of Tab. C.1 and we apply similar selections as those described in Chap. 4. Details of the simulation and efficiency calculation for this examle are given in the following sections.

Generating and Decaying b-hadrons with MC

This step is very similar to the one described in Sec. 3.2.1. We estimate the contribution of CS backgrounds to the decays previously listed in Tab. C.1 by generating MC samples containing 10^6 events of single Λ_b^0 hadrons, with a p_T threshold of 5 GeV/c and a pseudo-rapidity range $|\eta| < 1.2$ using the `BGenerator` package [89]. Single Λ_b^0's are generated using a p_T vs rapidity (y) spectrum modified to match the p_T spectrum observed in fully reconstructed $\Lambda_b^0 \to \Lambda_c^+\pi^-$ decays. Because we use a particle spectrum rather than the quark spectrum, as input to `BGenerator`, fragmentation must be explicitly turned off. We force each generated Λ_b^0 to decay through a single and specified decay chain using the `EvtGen` decay package [98] and a user defined decay Table. Also phase space model is used for all baryon decays. In addition, all Λ_c^+ are forced to decay into the $pK^-\pi^+$ final state including the resonance structures as measured by Aitala, et al. [99]. CDF software version 6.1.4mc was used to generate the b-hadrons decays. The information for each event is written in an HEPG Bank, containing full information about them. For each decay mode, a file containing the HEPG Bank is then written and converted to `ROOT` n-tuples for further analysis.

Candidate Requirements

The data used in the analysis subject of this Thesis have been collected by the TTT, specialized to select multibody b-hadronic decay modes. To emulate the trigger, in this study we require that one of the tracks from the Λ_c^+ and one of the Λ_b^0 decay products each pass the requirements for an SVT track with a $p_T > 2$ GeV/c, $0.0120 < |d_0| < 0.1$ cm and a pseudo-rapidity $|\eta| < 1.0$. For the pair of tracks we don't have any requirement on charge combination, $2^\circ < \Delta\varphi_0 < 90^\circ$, $p_{T_1} + p_{T_2} > 5$ GeV/c and $L_{xy} > 0.02$ cm. The common requirements of skimming and analysis are summarized in Tab. C.3 and are the same for $\Lambda_b^0 \to \Lambda_c^+\pi^-$, $\Lambda_b^0 \to \Lambda_c^+\pi^-\pi^+\pi^-$ and their associated CS decay modes. Two further requirements

Appendix C. MC Estimate of the Cabibbo Suppressed decay modes contributions

are applied to select $\Lambda_b^0 \to \Lambda_c^+\pi^-\pi^+\pi^-$ and the associated CS decay: the three tracks from the Λ_b^0's decay vertex have to be in a cone fixed by $\Delta R = \sqrt{\Delta\eta^2 + \Delta\varphi^2}$ and the decay length of the Λ_b^0 candidate, projected in the transverse plane, has to be $L_{xy} > 0.02$ cm.

Summary of common requirements	
All tracks η	$\lvert\eta\rvert < 1$
All tracks d_0	$\lvert d_0\rvert < 0.2\ cm$
$p_{T_{\Lambda_b^0\ candidate}}$	$p_{T_{\Lambda_b^0}} > 8$ GeV/c
Λ_b^0 candidate L_{xy}	$L_{xy} > 0.02\ cm$
Triggering tracks	one track from Λ_b^0 and one from Λ_c^+ are SVT trigger tracks

Table C.3: *Common requirements for the selection* $\Lambda_b^0 \to \Lambda_c^+\pi^-$, $\Lambda_b^0 \to \Lambda_c^+\pi^-\pi^+\pi^-$ *and corresponding CS decay modes.*

With reference to Eq. C.2 the efficiency of each decay mode is calculated as:

$$\varepsilon_i = \frac{N^i_{reco}}{N^i_{gen}} \tag{C.9}$$

where N^i_{reco} is the number of events reconstructed, and N^i_{gen} is the number of events generated in the corresponding decay mode. We evaluated the efficiency after applying the trigger and the analysis requirements for both $\Lambda_c^+\pi^-$ and $\Lambda_c^+\pi^-\pi^+\pi^-$ selections, as reported in Tab. C.4.
To know how many events satisfy the overall selection, we use the information from the generated ntuples and analyze the histograms (see Fig. C.4, Fig. C.5, and Fig. C.6) to determine the number of these events (see Tab. C.5). The total efficiency of each decay mode is achieved by multiplying the efficiency values relative to each kind of selection (trigger and analysis).

Estimated Relative Branching Ratio

Once evaluated $\mathcal{B}(\Lambda_b^0 \to CS^i)/\mathcal{B}(\Lambda_b^0 \to CF^i)$ and $\varepsilon^i_{CS}/\varepsilon^i_{CF}$, after the overall selection (see Tab. C.5), we can estimate the amount of CS background we expect relative to the CF signal using Eq. C.2. The invariant mass spectrum, for each CS and CF decay mode is reported in Fig. C.4, Fig. C.5 and Fig. C.6. In Fig. C.4 and Fig. C.5 are shown the $\Lambda_c^+\pi^-\pi^+\pi^-$ invariant mass spectra for each CF (dashed blue line) and corresponding CS (continuous red line) decay mode after the trigger and the $\Lambda_c^+\pi^-\pi^+\pi^-$ selection. Note well, for the $\Lambda_b^0 \to \Lambda_c^+\pi^-\pi^+\pi^-$ in Fig. C.5(b), the generated CF events are 1/3 of the CS one. In Fig. C.6 is shown, for $\Lambda_c^+\pi^-$

decay mode	TTT effic.($\times 10^{-2}$)	$\Lambda_c^+\pi^-$ effic. ($\times 10^{-3}$)	$\Lambda_c^+\pi^-\pi^+\pi^-$ effic. ($\times 10^{-4}$)
$\Lambda_b^0 \to \Lambda_c(2593)^+\pi^-$	4.02±0.02	10.30±0.10	60.30±0.80
$\Lambda_b^0 \to \Lambda_c(2593)^+K^-$	3.97±0.02	10.50±0.10	62.80±0.80
$\Lambda_b^0 \to \Lambda_c(2625)^+\pi^-$	3.91±0.02	10.10±0.10	52.50±0.70
$\Lambda_b^0 \to \Lambda_c(2625)^+K^-$	3.87±0.02	10.30±0.10	54.60±0.70
$\Lambda_b^0 \to \Sigma_c(2455)^{++}\pi^-\pi^-$	2.50±0.02	3.09±0.06	31.50±0.60
$\Lambda_b^0 \to \Sigma_c(2455)^{++}\pi^-K^-$	2.37±0.02	2.28±0.05	32.40±0.60
$\Lambda_b^0 \to \Sigma_c(2455)^0\pi^-\pi^+$	2.67±0.02	1.64±0.04	6.10±0.20
$\Lambda_b^0 \to \Sigma_c(2455)^0K^-\pi^+$	2.69±0.02	1.66±0.04	6.50±0.30
$\Lambda_b^0 \to \Lambda_c^+\rho^0\pi^-$	2.15±0.01	1.11±0.03	10.80±0.30
$\Lambda_b^0 \to \Lambda_c^+\rho^0K^-$	2.07±0.01	0.73±0.03	11.00±0.30
$\Lambda_b^0 \to \Lambda_c^+\pi^-\pi^+\pi^-$	2.03±0.02	0.68±0.05	7.30±0.50
$\Lambda_b^0 \to \Lambda_c^+\pi^-\pi^+K^-$	1.86±0.01	0.44±0.02	8.40±0.30
$\Lambda_b^0 \to \Lambda_c^+\pi^-$	5.47±0.02	14.94±0.12	0
$\Lambda_b^0 \to \Lambda_c^+K^-$	5.45±0.02	14.97±0.12	0

Table C.4: *MC efficiency after trigger (TTT) and analysis cuts.*

(dashed blue line) and $\Lambda_c^+K^-$ (continuous red line), the invariant mass spectra in the mass hypothesis of $\Lambda_c^+\pi^-$ after the trigger and $\Lambda_c^+\pi^-$ selection. From the plots reported in these figures we count, for each decay mode, the number of CF and CS passing events. Finally in Fig. C.7, Fig. C.8 and Fig. C.9 we made, in logarithmic scale, the same plots of Fig. C.4, Fig. C.5 and Fig. C.6 normalizing each CS decay mode spectrum to the number of expected CS events (N^i_{CS}).

decay mode	(*#events CF*)	(*#events CS*)	(*#events CS exp.*)	N^i_{CS}/N^i_{CF}
$\Lambda_b^0 \to \Lambda_c^*(2595)^+$	6028	6281	526.60	0.087
$\Lambda_b^0 \to \Lambda_c^*(2625)^+$	5254	5456	300.74	0.057
$\Lambda_b^0 \to \Sigma_c(2455)^{++}$	3145	3241	281.92	0.089
$\Lambda_b^0 \to \Sigma_c(2455)^0$	614	654	36.80	0.060
$\Lambda_b^0 \to \Lambda_c^+\rho^0$	1075	1102	56.31	0.052
$\Lambda_b^0 \to \Lambda_c^+3\pi$	241	839	12.36	0.051
$\Lambda_b^0 \to \Lambda_c^+\pi$	14936	14965	805.16	0.054

Table C.5: *For each decay mode is reported the number of passing events for CF (#events CF = N^i_{CF}) and for CS (#events CS), the number of the expected CS events (#events CS exp. = N^i_{CS}) and the ratio N^i_{CS}/N^i_{CF} (scaling factor).*

The method described can be used to estimate the $\mathcal{B}(\Lambda_b^0 \to CS_i)/\mathcal{B}(\Lambda_b^0 \to CF_i)$ for the decay modes of Tab. C.1 using the corresponding B-mesons decays (see second column of Tab. C.6), and to estimate, for the same decay modes, the ratio of the MC efficiencies $\varepsilon^i_{CF}/\varepsilon^i_{CF}$. In the example illustrated here, we used a generator level MC and the resulting relative efficiencies are reported in the fourth column of Tab. C.6, while N^i_{CS}/N^i_{CF} is reported in the fifth column of the same Table. In the

Appendix C. MC Estimate of the Cabibbo Suppressed decay modes contributions

analysis this method was used to evaluate the systematic due to the CS yields in the Λ_b^0 mass window (see Sec. 7.1.1), using a fully simulated samples of 10^6 events for CS and CF decay mode of Tab. C.1. The CS events for each decay mode were normalized to the $10^6 \times \mathcal{B}(\Lambda_b^0 \to CS_i)/\mathcal{B}(\Lambda_b^0 \to CF_i)$. The fraction N^i_{CS}/N^i_{CF} after the trigger and the analysis cuts falling in the Λ_b^0 mass window of the ΔM^{--+} distribution was estimated counting the corresponding passing events, we call this fraction scaling factor. The systematic due to the CS background for each decay mode was then evaluated as the signal yield times this fraction.

Λ_b^0 decay mode	$R_i = \mathcal{B}_i/\mathcal{B}_0$	$\varepsilon_{analysis}$	$\varepsilon_i/\varepsilon_0$	$\Pi\ R_i(\varepsilon_i/\varepsilon_0)$
$\Lambda_b^0 \to \Lambda_c(2595)^+\pi^-$	1	$(2.42 \pm 0.09)\,10^{-4}$	1	1
$\Lambda_b^0 \to \Lambda_c(2595)^+K^-$	$(7.75 \pm 0.68)\,10^{-2}$	$(2.49 \pm 0.09)\,10^{-4}$	(1.03 ± 0.05)	$(7.98 \pm 1.09)\,10^{-2}$
$\Lambda_b^0 \to \Lambda_c(2625)^+\pi^-$	1	$(2.05 \pm 0.08)\,10^{-4}$	1	1
$\Lambda_b^0 \to \Lambda_c(2625)^+K^-$	$(5.55 \pm 0.28)\,10^{-2}$ [1]	$(2.11 \pm 0.08)\,10^{-4}$	(1.03 ± 0.05)	$(5.72 \pm 0.57)\,10^{-2}$
$\Lambda_b^0 \to \Sigma_c(2455)^{++}\pi^-\pi^-$	1	$(0.79 \pm 0.05)\,10^{-4}$	1	1
$\Lambda_b^0 \to \Sigma_c(2455)^{++}\pi^-K^-$	$(8.29 \pm 4.13)\,10^{-2}$	$(0.77 \pm 0.05)\,10^{-4}$	(0.97 ± 0.09)	$(8.04 \pm 4.75)\,10^{-2}$
$\Lambda_b^0 \to \Sigma_c(2455)^0\pi^+\pi^-$	1	$(0.16 \pm 0.05)\,10^{-4}$	1	1
$\Lambda_b^0 \to \Sigma_c(2455)^0\pi^+K^-$	$(5.40 \pm 3.26)\,10^{-2}$	$(0.17 \pm 0.05)\,10^{-4}$	(1.06 ± 0.46)	$(5.72 \pm 5.93)\,10^{-2}$
$\Lambda_b^0 \to \Lambda_c^+\rho^0\pi^-$	1	$(0.23 \pm 0.02)\,10^{-4}$	1	1
$\Lambda_b^0 \to \Lambda_c^+\rho^0K^-$	$(5.36 \pm 6.98)\,10^{-2}$	$(0.23 \pm 0.02)\,10^{-4}$	(1.00 ± 0.12)	$(5.36 \pm 7.62)\,10^{-2}$
$\Lambda_b^0 \to \Lambda_c^+\pi^-\pi^+\pi^-$	1	$(0.15 \pm 0.04)\,10^{-4}$	1	1
$\Lambda_b^0 \to \Lambda_c^+\pi^-\pi^+K^-$	$(5.42 \pm 2.11)\,10^{-2}$	$(0.16 \pm 0.02)\,10^{-4}$	(1.00 ± 0.02)	$(5.42 \pm 2.22)\,10^{-2}$
$\Lambda_b^0 \to \Lambda_c^+\pi^-$	1	$(8.17 \pm 0.13)\,10^{-4}$	1	1
$\Lambda_b^0 \to \Lambda_c^+K^-$	$(7.66 \pm 1.18)\,10^{-2}$	$(8.16 \pm 0.13)\,10^{-4}$	(0.99 ± 0.02)	$(7.58 \pm 1.32)\,10^{-2}$

Table C.6: *This summary reports, for each Λ_b^0 decay modes, the relative $\mathcal{B}$, the analysis efficiency, the relative efficiencies, and the product of $\Pi\ R_i(\varepsilon_i/\varepsilon_0)$, which for the i^{th} decay mode is the evaluated N^i_{CS}/N^i_{CF} (scaling factor for the i^{th} decay mode).*

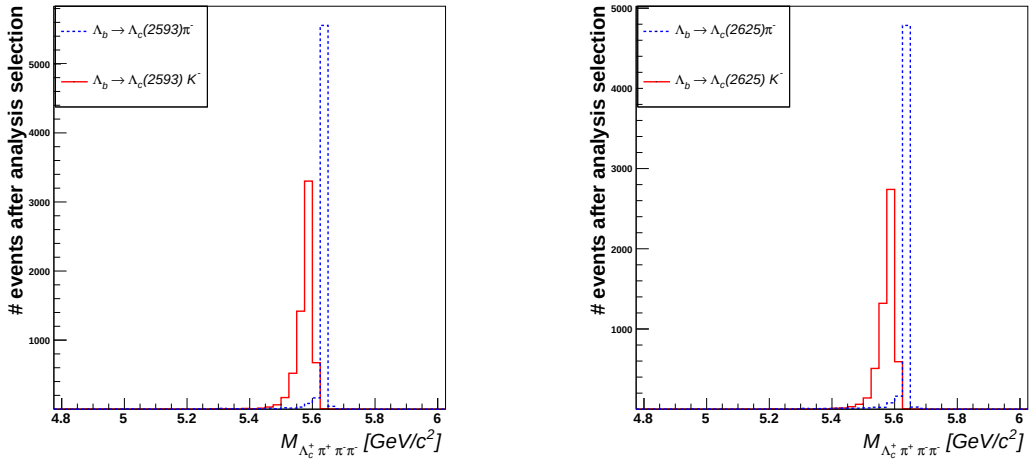

(a)

(b)

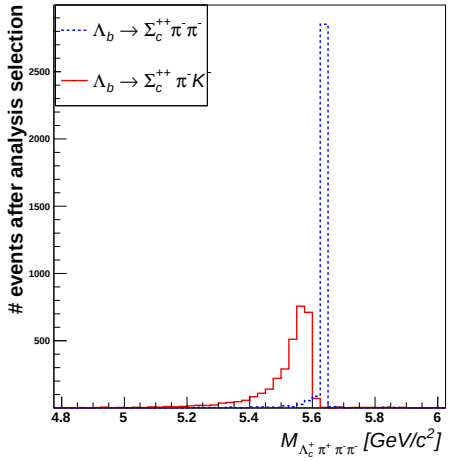

(c)

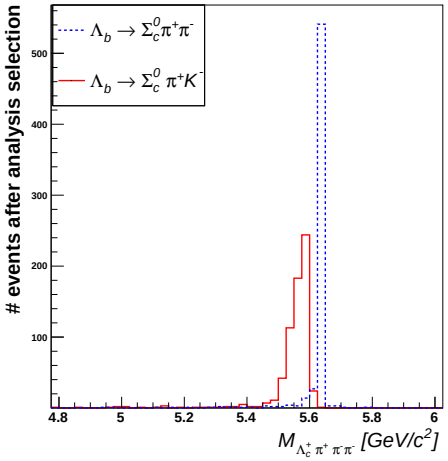

(d)

Figure C.4: *$\Lambda_c^+\pi^-\pi^+\pi^-$ invariant mass spectra for $\Lambda_b^0 \to \Lambda_c^+(2595)^+\pi^-$ and $\Lambda_b^0 \to \Lambda_c^+(2595)^+K^-$* **C.4(a)**, *$\Lambda_b^0 \to \Lambda_c^+(2625)^+\pi^-$ and $\Lambda_b^0 \to \Lambda_c^+(2625)^+K^-$* **C.4(b)**, *$\Lambda_b^0 \to \Sigma_c(2455)^{++}\pi^-\pi^-$ and $\Lambda_b^0 \to \Sigma_c(2455)^{++}\pi^-K^-$* **C.4(c)** *and $\Lambda_b^0 \to \Sigma_c(2455)^0\pi^+\pi^-$ and $\Lambda_b^0 \to \Sigma_c(2455)^0\pi^+K^-$* **C.4(d)** *resonant final states after the trigger and $\Lambda_c^+\pi^-\pi^+\pi^-$ selection.*

Appendix C. MC Estimate of the Cabibbo Suppressed decay modes contributions

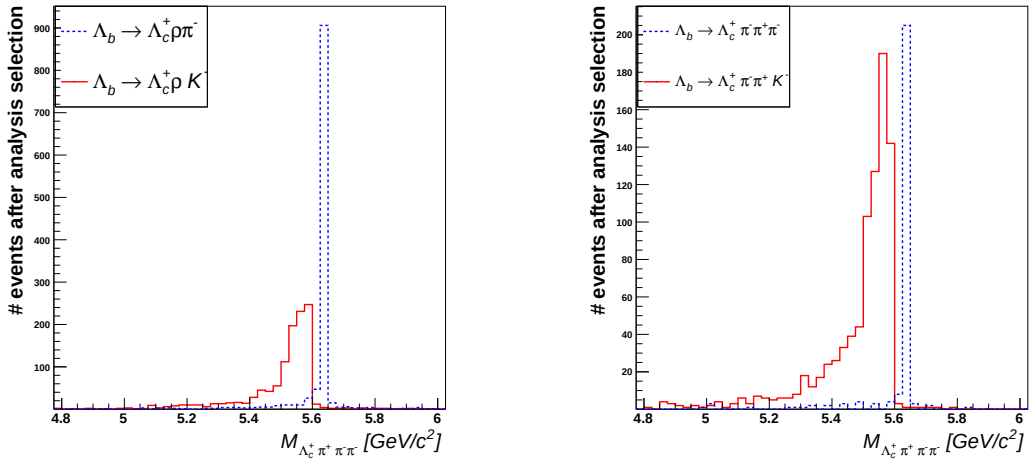

(a) (b)

Figure C.5: $\Lambda_c^+\pi^-\pi^+\pi^-$ *invariant mass spectra for* $\Lambda_b^0 \to \Lambda_c^+\rho^0\pi^-$ *and* $\Lambda_b^0 \to \Lambda_c^+\rho^0 K^-$ **C.5(a)** *and* $\Lambda_b^0 \to \Lambda_c^+\pi^-\pi^+\pi^-$ *and* $\Lambda_b^0 \to \Lambda_c^+\pi^-\pi^+ K^-$ **C.5(b)** *resonant final states after the trigger and* $\Lambda_c^+\pi^-\pi^+\pi^-$ *selection: the dashed line and the continuous one indicate the invariant mass distribution of the corresponding CF and CS decay modes reported in Tab. C.4.*

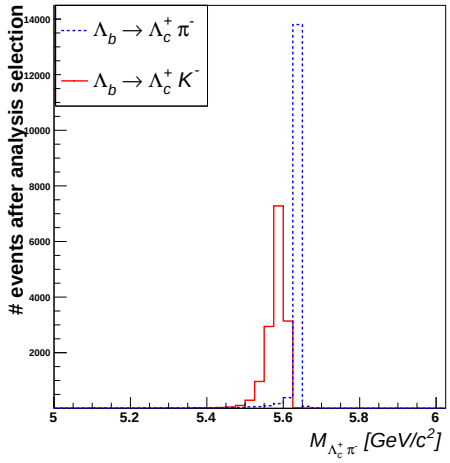

Figure C.6: $\Lambda_c^+\pi^-$ *invariant mass for the decay mode* $\Lambda_b^0 \to \Lambda_c^+\pi$ *(Tab. C.4) after the trigger and* $\Lambda_c^+\pi$ *requirements. The dashed line and the continuous one indicate the invariant mass distribution of the corresponding CF and CS decay modes.*

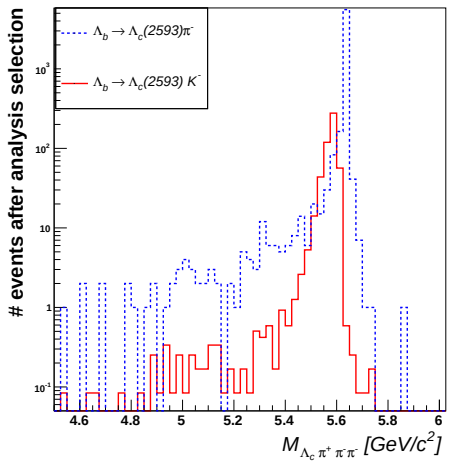

(a)

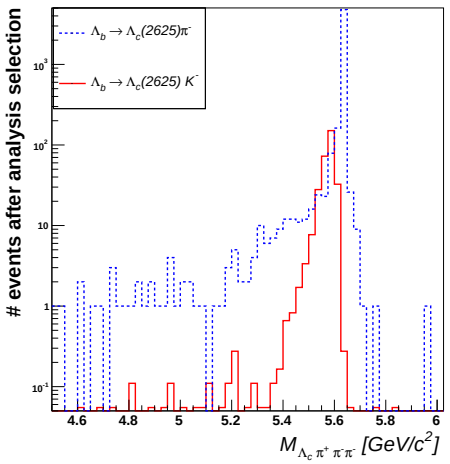

(b)

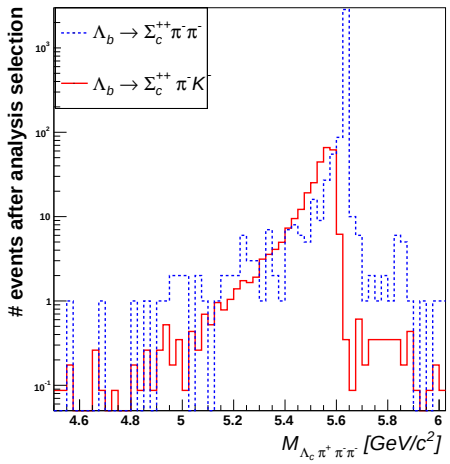

(c)

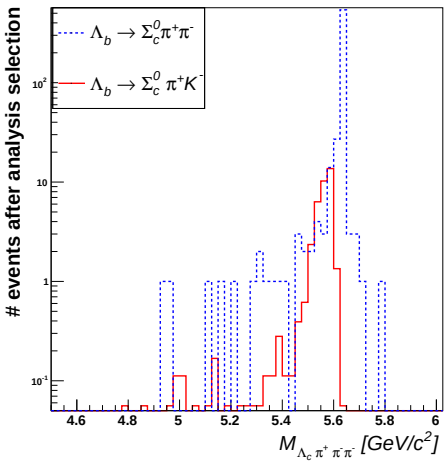

(d)

Figure C.7: $\Lambda_c^+\pi^-\pi^+\pi^-$ *invariant mass spectra for* $\Lambda_b^0 \to \Lambda_c^+(2595)^+\pi^-$ *and* $\Lambda_b^0 \to \Lambda_c^+(2595)^+K^-$ **C.7(a)**, $\Lambda_b^0 \to \Lambda_c^+(2625)^+\pi^-$ *and* $\Lambda_b^0 \to \Lambda_c^+(2625)^+K^-$ **C.7(b)**, $\Lambda_b^0 \to \Sigma_c(2455)^{++}\pi^-\pi^-$ *and* $\Lambda_b^0 \to \Sigma_c(2455)^{++}\pi^-K^-$ **C.7(c)** *and* $\Lambda_b^0 \to \Sigma_c(2455)^0\pi^+\pi^-$ *and* $\Lambda_b^0 \to \Sigma_c(2455)^0\pi^+K^-$ **C.7(d)** *resonant final states after trigger and* Λ_c^+ 3π *selection.*

Appendix C. MC Estimate of the Cabibbo Suppressed decay modes contributions

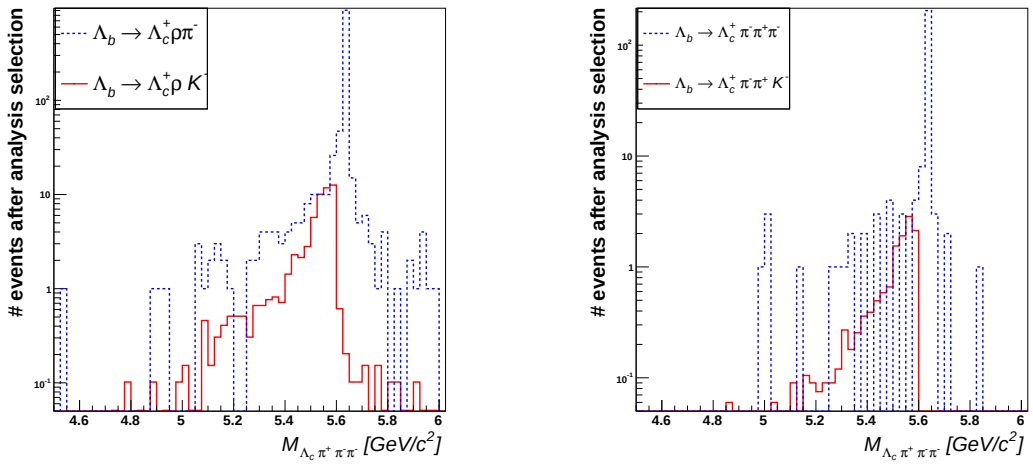

(a) (b)

Figure C.8: $\Lambda_c^+\pi^-\pi^+\pi^-$ *invariant mass spectra for* $\Lambda_b^0 \to \Lambda_c^+\rho^0\pi^-$ *and* $\Lambda_b^0 \to \Lambda_c^+\rho^0 K^-$ **C.8(a)** *and* $\Lambda_b^0 \to \Lambda_c^+\pi^-\pi^+\pi^-$ *and* $\Lambda_b^0 \to \Lambda_c^+\pi^-\pi^+ K^-$ **C.8(b)** *resonant final states after trigger and* Λ_c^+ 3π *selection: the dashed line and the continuous one indicate the invariant mass distribution of the corresponding CF and CS decay modes that are reported in Tab. C.4.*

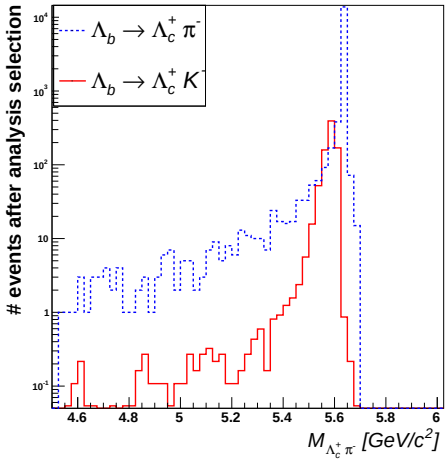

Figure C.9: $\Lambda_c^+\pi^-$ *invariant mass for the decay* $\Lambda_b^0 \to \Lambda_c^+\pi$ *in Tab. C.4 after the trigger and* $\Lambda_c^+\pi^-$ *selection. The dashed line indicate the invariant mass distribution of the corresponding CF decay.*

Appendix **D**

Study of $\Lambda_b^0 \to \Lambda_c^+\pi^-\pi^+\pi^-$ without Charmed Resonant Decay Modes

Here we investigate on the composition of the $\Lambda_b^0 \to \Lambda_c^+\pi^-\pi^+\pi^-$ signal, after the veto on the Λ_b^0 charmed resonant decay modes.This study was done after the the analysis presented in this Thesis was officially approved by the Collaboration.

D.1 Motivations

In Chap. 6 we assumed proportions (1/2, 1/2, 0) or (1/2, 0, 1/2) respectively of $\Lambda_b^0 \to \Lambda_c^+\rho^0\pi^- \to \Lambda_c^+\pi^-\pi^+\pi^-$, $\Lambda_b^0 \to \Lambda_c^+\pi^-\pi^+\pi^-(nr)$ and $\Lambda_b^0 \to \Lambda_c^+ a_1(1260)^- \to \Lambda_c^+\rho^0\pi^- \to \Lambda_c^+\pi^-\pi^+\pi^-$ contributing to the mixed E, since, we declared, we were not able to separate the contributions of these states, and to extract their yields. The proportions assumed are importants since determine how to evaluate the efficiency of the mixed E state. As example, when assumed proportions are (1/2, 1/2, 0), the efficiency of the mixed E state is the average of the efficiencies of $\Lambda_b^0 \to \Lambda_c^+\rho^0\pi^- \to \Lambda_c^+\pi^-\pi^+\pi^-$ (F state) and of $\Lambda_b^0 \to \Lambda_c^+\pi^-\pi^+\pi^-(nr)$ (G state), since we can write:

$$\frac{N(E)^{prod}}{2} = N(F)^{prod} = \frac{N(F)^{obs}}{\varepsilon_F} \tag{D.1}$$

$$\frac{N(E)^{prod}}{2} = N(G)^{prod} = \frac{N(G)^{obs}}{\varepsilon_G} \tag{D.2}$$

$$\frac{N(F)^{obs} + N(G)^{obs}}{N(E)^{prod}} = \frac{\varepsilon_F + \varepsilon_G}{2} \tag{D.3}$$

Where $N(E)$, $N(F)$ and $N(G)$ indicate the number of events of the three states, and ε_F and ε_G are the MC efficiencies of the states F and G.

Appendix D. Study of $\Lambda_b^0 \to \Lambda_c^+\pi^-\pi^+\pi^-$ without Charmed Resonant Decay Modes

It is evident that it is important to know the decay modes which really contribute to $\Lambda_b^0 \to \Lambda_c^+\pi^-\pi^+\pi^-(nr)$ after the veto on the Λ_b^0 charmed resonant decay modes, as well as to measure theirs yields, since one of the dominant systematic in the measurement of the relative branching fractions, reported in Tab. 6.4 and Tab. 6.5, arises from the assumption of the unknown proportions. In the following we decribe the studies done to investigate on the composition of the $\Lambda_b^0 \to \Lambda_c^+\pi^-\pi^+\pi^-$ signal, after the veto on the Λ_b^0 charmed resonant decay modes.

D.2 ρ^0 Signal Contribution to the $\Lambda_b^0 \to \Lambda_c^+\pi^-\pi^+\pi^-$ Decay after the Veto on Charmed Resonant Decay Modes.

In Fig. 5.10(b) we reported the ΔM^{--+} distribution obtained after the veto on the Λ_b^0 charmed resonant decay modes (see Chap. 5) with overlaid the best fit results when assuming in the modeling a Gaussian function for the signal, an exponential for the combinatorial background, and including the $\overline{B}{}^0_{(s)} \to D^{(*)+}_{(s)}\pi^-\pi^+\pi^-$, with inclusive $D^{(*)+}_{(s)}$ and $\overline{B}{}^0_{(s)}$ contributions, for the physics background.

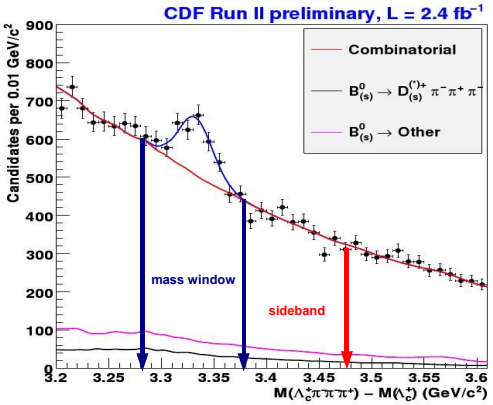

Figure D.1: *ΔM^{--+} distribution with indicated the mass window (MW) and the sideband (SB) used in the text.*

The resulting Gaussian mean and σ (`sig_gauss_M` in the legenda of Fig. 5.10(b)) from the best fit are used to define the $\Delta M^{--+} \pm 3\sigma$ mass window region (MW=$\Delta M^{--+}\pm 3\sigma = 3.332\pm 0.048$ GeV/c^2) and the sideband region (SB=$[\Delta M^{--+} + 3\sigma, \Delta M^{--+} + 6\sigma]$) as shown in Fig. D.1. Useful quantities, determined using the best fits and that will be used in the next section, are reported in Tab. D.1.

D.2. ρ^0 Signal Contribution to the $\Lambda_b^0 \to \Lambda_c^+\pi^-\pi^+\pi^-$ Decay after the Veto on Charmed Resonant Decay Modes.

total events in MW	5515
total events in SB	$\mathsf{SB}_{sb} = 3559$
signal events in MW	610 ± 88 (`sig_n` in the legenda of Fig. 5.10(b))
background events in MW	$\mathsf{MW}_{bkg} = 5515\text{-}610 = 4905$
sideband normalization	$\frac{\mathsf{MW}_{bkg}}{\mathsf{SB}_{sb}} = \frac{4905}{3559} = 1.38$

Table D.1: *Some useful quantities determined using the best fit parameters of the ΔM^{--+} distribution of Fig. 5.10(b).*

To demonstrate a ρ^0 signal in the Λ_b^0 mass window of Fig. D.1, we reconstruted, for each Λ_b^0 candidate in MW and in SB, the ρ^0 candidates using a pair of tracks of opposit sign, not from the Λ_c^+, assigning both the pion mass. For each Λ_b^0 candidate, the six tracks from the $\Lambda_b^0 \to \Lambda_c^+\pi^-\pi^+\pi^-$ decay mode are ordered in this way:

$$\overbrace{\underbrace{K^-}_{1}\ \underbrace{p}_{2}\ \underbrace{\pi^+}_{3}}^{\Lambda_c^+}\ \underbrace{\pi^-}_{4}\ \underbrace{\pi^-}_{5}\ \underbrace{\pi^+}_{6}$$

The same sign *pions* are ordered by momentum, and it means that $p_4 > p_5$.
The main difficulty is given by the fact that we are dealing with these two possible ρ^0 candidates: one with an high p_T (the ρ^0_{high} combination, using tracks 4 and 6) and the other one with a low p_T (the ρ^0_{low} combination, using tracks 5 and 6). Fig. D.2(a) shows the distribution of the invariant mass spectrum of the two pions forming the ρ^0_{high} candidates when the Λ_b^0 candidate is in the MW (red filled histogram) with overlaid the same distribution when the Λ_b^0 candidate is in the SB region (yellow filled histrogram, normalized to the background content of Fig. 5.10(b), see Tab. D.1, for the sideband normalization), while Fig. D.2(b) shows the same distributions but for the ρ^0_{low} candidates.
The two pion combinations have different invariant mass spectra ($M_{\rho^0_{high}}$ and $M_{\rho^0_{low}}$) both in MW and SB regions (see Fig. D.2(a) and Fig. D.2(b)), but in Fig. D.2(b) it is evident a clear signal of the ρ^0 resonance (ρ^0 Mass = (775.49 ± 0.34)MeV, Full width Γ=(149.1 ± 0.8)MeV [1]).

In the following we describe some of the techniques tested to extract the contributions from the $\Lambda_b^0 \to \Lambda_c^+\rho^0\pi^- \to \Lambda_c^+\pi^-\pi^+\pi^-$, $\Lambda_b^0 \to \Lambda_c^+ a_1(1260)^- \to \Lambda_c^+\rho^0\pi^- \to \Lambda_c^+\pi^-\pi^+\pi^-$ and the non-resonant $\Lambda_b^0 \to \Lambda_c^+\pi^-\pi^+\pi^-(nr)$ to the $\Lambda_b^0 \to \Lambda_c^+\pi^-\pi^+\pi^-$ without charmed resonances.

Appendix D. Study of $\Lambda_b^0 \to \Lambda_c^+\pi^-\pi^+\pi^-$ without Charmed Resonant Decay Modes

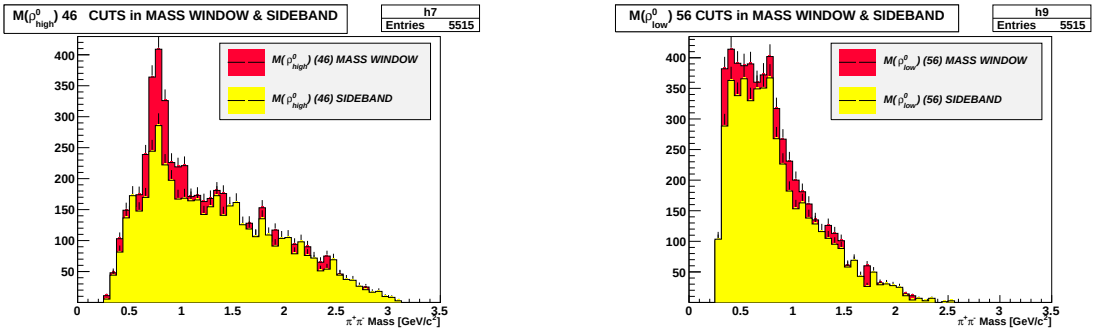

(a) (b)

Figure D.2: $M_{\rho^0_{high}}$ **D.2(a)** *and* $M_{\rho^0_{low}}$ **D.2(b)** $\pi^+\pi^-$ *invariant mass distribution in the mass window (red filled histogram) and in the sideband (yellow filled histogram) after vetoed the* Λ_b^0 *charmed resonant decay modes.*

D.2.1 Estimate of the yields for the decay modes with a ρ^0 and the $\Lambda_b^0 \to \Lambda_c^+\pi^-\pi^+\pi^-(nr)$

We want now extract the signal yields of the sum of the $\Lambda_b^0 \to \Lambda_c^+\rho^0\pi^- \to \Lambda_c^+\pi^-\pi^+\pi^-$ and of the $\Lambda_b^0 \to \Lambda_c^+ a_1(1260)^- \to \Lambda_c^+\rho^0\pi^- \to \Lambda_c^+\pi^-\pi^+\pi^-$, and of the $\Lambda_b^0 \to \Lambda_c^+\pi^-\pi^+\pi^-(nr)$.

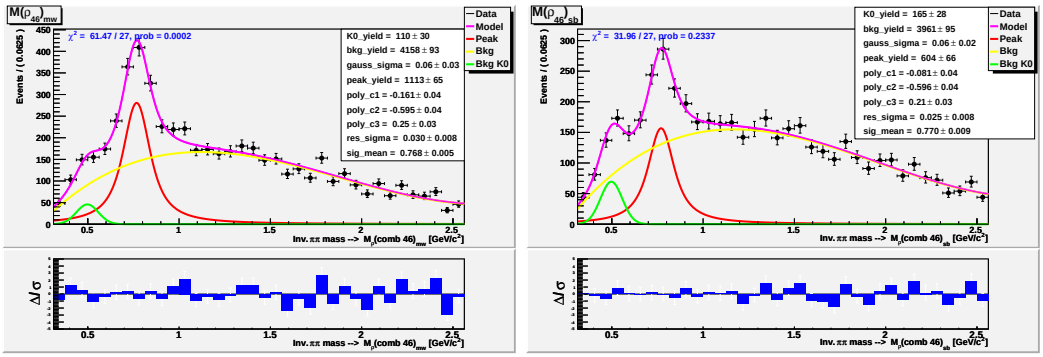

(a) (b)

Figure D.3: $M_{\rho^0_{high}}$ *mass distribution with overlaid the best fit curve (magenta curve) in the mass window* **D.3(a)** *and in the sideband* **D.3(b)** *in range* $[0.3 - 2.6]$ GeV/c^2.

In order to that, we made a fit of both $M_{\rho^0_{high}}$ and $M_{\rho^0_{low}}$ mass distribution in both

D.2. ρ^0 Signal Contribution to the $\Lambda_b^0 \to \Lambda_c^+\pi^-\pi^+\pi^-$ Decay after the Veto on Charmed Resonant Decay Modes.

MW and SB regions.
The fit is performed in the range $[0.3-2.6]$ GeV/c^2 using different PDFs to model the $M_{\rho^0_{high}}$ and $M_{\rho^0_{low}}$ in the MW and SB regions. The $M_{\rho^0_{high}}$ distribution is modeled, in MW and SB regions, with a PDF composed of: a Voigtian function for the ρ^0 signal, with a width fixed to the PDG value ($\Gamma_{\rho^0} = 0.149\,\text{GeV}$) and the mass resolution Gaussian with sigma and mean free to float in the fit, a Gaussian function with mean fixed to the central value of the K^0 mass ($M_{K^0} = 0.498\,\text{GeV}$ [1]) and the sigma free to float in the fit, and a third degree Chebyshev polynomial for the background.
The PDF function used to model the $M_{\rho^0_{low}}$ is parameterized like the $M_{\rho^0_{high}}$ one with the exception that we used a convolution between a Landau and an exponential function for the background.
In Fig. D.3 and Fig. D.4 we report the mass distribution fit in both MW and SB regions for the two possible combination ρ^0_{high} and ρ^0_{low}.
All have a signal of $\rho^0\pi^-\pi^+$, the ρ^0 mass returned by the best fits are in agreement with the measured ρ^0 mass (see variables `sig_mean` for the mass and the `res_sigma` for the uncertainty on it in the fit results legenda of these figures).
The parameters estimated from the fits in Fig. D.3(a) and Fig. D.3(b) are summarized on Tab. D.2, where the total ρ^0_{high} and ρ^0_{low} in the $\Lambda_b^0 \to \Lambda_c^+\pi^-\pi^+\pi^-$ signal is the difference between the ρ^0 signal yield fitted in the MW and the one fitted in the SB region, respectively for $M_{\rho^0_{high}}$ and $M_{\rho^0_{low}}$ combinations.

Yields of $\rho^0 \to \pi^-\pi^+$	
ρ^0_{high} in MW	1113 ± 65 (`peak_yield` in the legenda of Fig. D.3(a))
ρ^0_{high} in normalized SB	604 ± 66 (`peak_yield` in the legenda of Fig. D.3(b))
ρ^0_{high} in $\Lambda_b^0 \to \Lambda_c^+\pi^-\pi^+\pi^-$ signal	509 ± 93
ρ^0_{low} in MW	329 ± 64 (`peak_yield` in the legenda of Fig. D.4(a))
ρ^0_{low} in normalized SB	299 ± 71 (`peak_yield` in the legenda of Fig. D.4(b))
ρ^0_{low} in $\Lambda_b^0 \to \Lambda_c^+\pi^-\pi^+\pi^-$ signal	30 ± 96

Table D.2: *Yields of ρ^0_{high} and ρ^0_{low} in the MW and in the SB regions obtained from the best fit of $M_{\rho^0_{high}}$ and $M_{\rho^0_{low}}$ distributions reported in Fig. D.3(a) and Fig. D.3(b). The yield of the ρ^0_{high} (ρ^0_{low}) in the $\Lambda_b^0 \to \Lambda_c^+\pi^-\pi^+\pi^-$ is given by the difference between the yields ρ^0_{high} (ρ^0_{low}) in the MW and in the SB.*

In Tab. D.3 we report N_{TOT}, that is the resulting yield of the fit reported on Fig. 5.10(b), and the total yield of the ρ^0 (N_{ρ^0}), that in principle is due to the $\Lambda_b^0 \to \Lambda_c^+\rho^0\pi^- \to \pi^-\pi^+\pi^-$ and $\Lambda_b^0 \to \Lambda_c^+ a_1(1260)^- \to \Lambda_c^+\rho^0\pi^- \to \pi^-\pi^+\pi^-$ decays,

Appendix D. Study of $\Lambda_b^0 \to \Lambda_c^+\pi^-\pi^+\pi^-$ without Charmed Resonant Decay Modes

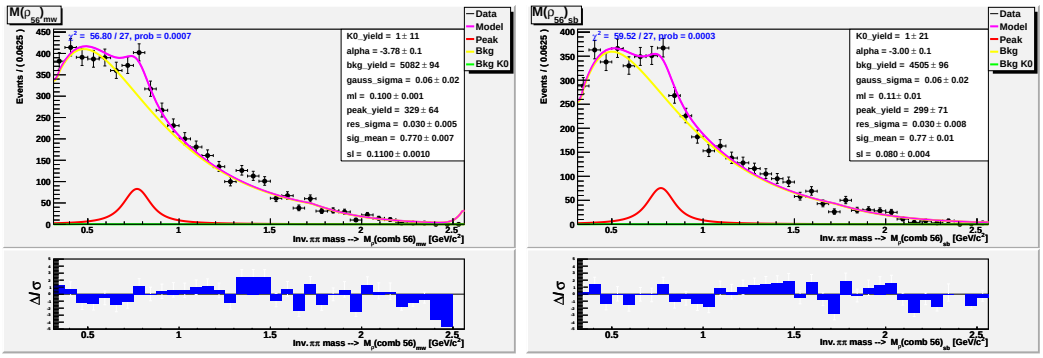

(a) (b)

Figure D.4: *$M_{\rho^0_{low}}$ mass distribution fit with overlaid the best fit curve (magenta curve) in the mass window* **D.4(a)** *and in the sideband* **D.4(b)** *in range* $[0.3 - 2.6]$ *GeV/c^2.*

calculated as the sum of ρ^0_{high} and ρ^0_{low} in $\Lambda_b^0 \to \Lambda_c^+\pi^-\pi^+\pi^-$ signal of Tab. D.2. In the same Table is reported the yield of the $\Lambda_b^0 \to \Lambda_c^+\pi^-\pi^+\pi^-(nr)$ (N_{nr}) calculated as the difference between the total number of Λ_b^0 signal yield, after the veto on the Λ_b^0 charmed resonant decay modes (N_{TOT}), and N_{ρ^0}. The quoted result for N_{nr} is consistent with the LHCb claim [17] which considers the proportion of $\Lambda_b^0 \to \Lambda_c^+\pi^-\pi^+\pi^-(nr)$ decay mode as null.

Λ_b^0 Decay Mode	Signal Yield
$N_{TOT} = N(\Lambda_b^0 \to \Lambda_c^+\rho^0\pi^- + N(\Lambda_b^0 \to \Lambda_c^+ a_1(1260)^-)_{obs}) + N(\Lambda_b^0 \to \Lambda_c^+\pi^-\pi^+\pi^-(nr))$	610 ± 88
$N_{\rho^0} = N(\Lambda_b^0 \to \Lambda_c^+\rho^0\pi^-)_{obs} + N(\Lambda_b^0 \to \Lambda_c^+ a_1(1260)^-)_{obs}$	539 ± 133
$N_{nr} = N(\Lambda_b^0 \to \Lambda_c^+\pi^-\pi^+\pi^-(nr))$	71 ± 159

Table D.3: *In this table we report the yield of the $\Lambda_b^0 \to \Lambda_c^+\pi^-\pi^+\pi^-$ after the veto on the charmed resonances (N_{TOT}), the yield of the ρ^0 (N_{ρ^0}) that in principle are due the $\Lambda_b^0 \to \Lambda_c^+\rho^0\pi^- \to \pi^-\pi^+\pi^-$ and $\Lambda_b^0 \to \Lambda_c^+ a_1(1260)^- \to \Lambda_c^+\rho^0\pi^- \to \pi^-\pi^+\pi^-$ decays, and the yield of the $\Lambda_b^0 \to \Lambda_c^+\pi^-\pi^+\pi^-(nr)$ (N_{nr}).*

D.3 $s\mathcal{P}lot$ to separate the contributions in $\Lambda_b^0 \to \Lambda_c^+\pi^-\pi^+\pi^-$

In these next Sections we want to use another technique to confirm, or improve, the results obtained in the previous one. The aim is to determine the composition of our $\Lambda_b^0 \to \Lambda_c^+\pi^-\pi^+\pi^-$ sample, after the veto on the charmed resonant decay modes, measuring the yields of the contributing decay modes: $\Lambda_b^0 \to \Lambda_c^+\rho^0\pi^-$, $\Lambda_b^0 \to \Lambda_c^+ a_1(1260)^-$ and $\Lambda_b^0 \to \Lambda_c^+\pi^-\pi^+\pi^-(nr)$, all in $\Lambda_b^0 \to \Lambda_c^+\pi^-\pi^+\pi^-$ final state. In order to do that, we decided to use a statistical tool dedicated to the exploration of data samples populated by several classes of events, called $s\mathcal{P}lot$ [100], [101].
With the $s\mathcal{P}lot$ we can explore a data sample, consisting of several classes of events merged into a single sample, assumed to be characterized by a set of variables which can be split into two components: the first one is a set of variables for which the distributions of all the classes of events are known (these variables are collectively referred to as a (unique) *discriminating variable*). The second component is a set of variables for which the distributions of some classes of events are either truly unknown or considered as such (these variables are collectively referred to as a (unique) *control variable*).
The $s\mathcal{P}lot$ technique allows us to reconstruct the distributions for the control variable, independently for each of the various classes of events, without making use of any a priori knowledge on this variable with the assumption that the control variable is uncorrelated with the discriminating variable. The general idea is to use the $s\mathcal{P}lot$, first of all, in the ΔM^{--+} mass distribution fit (see in Fig. 5.10(b)), where signal and background events can be separated by one-dimensional likelihood fit, in order to obtain the two respective yields. Then, this technique uses the results from the ΔM^{--+} fit to calculate a weight (termed SWeights) for each event, i.e. a sort of *signal-likeness/background-likeness* of a specific event, in order to obtain a *weighted dataset*. With the specific weights, the mass distribution of two pions can also be separated into the event classes, much better than an advanced sideband subtraction because this is an unbinned subtraction between signal and background, and the weighted dataset is being the result.
After having obtained the weighted dataset, we projected on it the variables that represent the mass distribution of two pions (ρ^0_{high} and ρ^0_{low}). We did the same with the invariant mass of three pions, $m3\pi$, not from Λ_c^+ (tracks 4, 5, 6 of Sec. D.2) to investigate on the $a_1(1260)^- \to \rho^0\pi^- \to \pi^-\pi^+\pi^-$ signal.
The projections for these three control variables ρ^0_{high}, ρ^0_{low} and $m3\pi$ on the weighted dataset are reported in Fig. D.5.

Appendix D. Study of $\Lambda_b^0 \to \Lambda_c^+\pi^-\pi^+\pi^-$ without Charmed Resonant Decay Modes

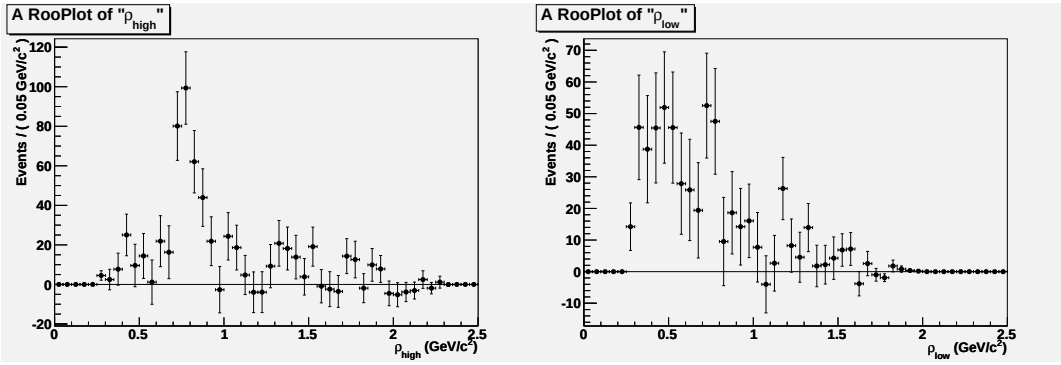

(a) (b)

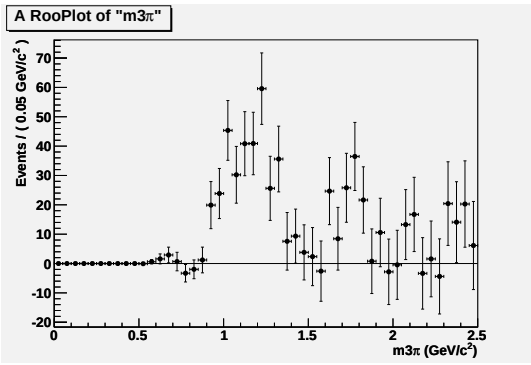

(c)

Figure D.5: ρ^0_{high} **D.5(a)**, ρ^0_{low} **D.5(b)** *and* $m3\pi$ **D.5(c)** *invariant mass projections on the weighted dataset.*

Fig. D.5(a) shows a clear ρ^0 peak and Fig. D.5(c) also shows peak due to the $a_1(1260)^-$ ($a_1(1260)^-$ Full width Γ from 250 to 600 MeV [1]), confirming the contribution of the $\Lambda_b^0 \to \Lambda_c^+ a_1(1260)^- \to \Lambda_c^+\rho^0\pi^- \to \Lambda_c^+\pi^-\pi^+\pi^-$ in the Λ_b^0 signal, after the veto on the charmed resonant decay modes.
At this point, once obtained the projections on the weighed dataset, the next step is to find a way to fit these distributions, in order to obtain the yields in the hypothesis that the decay modes contributing to the $\Lambda_b^0 \to \Lambda_c^+\pi^-\pi^+\pi^-$ signal after the veto on the charmed resonances are: $\Lambda_b^0 \to \Lambda_c^+\rho^0\pi^- \to \Lambda_c^+\pi^-\pi^+\pi^-$, $\Lambda_b^0 \to \Lambda_c^+\pi^-\pi^+\pi^-(nr)$ and $\Lambda_b^0 \to \Lambda_c^+ a_1(1260)^- \to \Lambda_c^+\rho^0\pi^- \to \Lambda_c^+\pi^-\pi^+\pi^-$.
First of all, as a cross check of the ρ^0 yield determined in Sec. D.2, we performed a fit of the projections of the two control variables ρ^0_{high} and ρ^0_{low} on the weighted dataset of Fig. D.5(a) and Fig. D.5(b) using MC templates of these distributions

for the three decay modes.
The fact that in principle there can be two different combinations of a pion pair, is a reason to make the fit of one of the two combinations (ρ^0_{high}, having the best mass resolution) and to use the achieved results in terms of composition as a cross-check on the other one. In the next Sections we illustrate the method to determine the templates of the three decay modes using MC samples and the fit procedure adopted to separate these contributions in the data.

D.3.1 Templates Extraction from MC

The main difficulty to separate the three decay modes concerns the separation of the $\Lambda_b^0 \to \Lambda_c^+\rho^0\pi^-$ from $\Lambda_b^0 \to \Lambda_c^+ a_1(1260)^-$ candidates, since $a_1(1260)^- \to \rho^0\pi^-$. In order to make the fit on the weighted dataset of the ρ^0_{high} and ρ^0_{low} distributions we construct MC templates (shapes) of these distributions from the three decay modes, that we describe in the following.
We generated MC samples of $\approx \times 10^6$ events for the $\Lambda_b^0 \to \Lambda_c^+ a_1(1260)^- \to \Lambda_c^+\rho^0\pi^- \to \Lambda_c^+\pi^-\pi^+\pi^-$, $\Lambda_b^0 \to \Lambda_c^+\rho^0\pi^- \to \Lambda_c^+\pi^-\pi^+\pi^-$, and $\Lambda_b^0 \to \Lambda_c^+\pi^-\pi^+\pi^-(nr)$ decay modes and reconstructed, like on data, ρ^0_{high} and ρ^0_{low} candidates in the Λ_b^0 mass window.
For each MC sample, corresponding to one of the three decay modes, we have two possible combinations, ρ^0_{high} and ρ^0_{low}, the first one using the tracks 4 and 6 (see Sec. D.2) and the second one using the tracks 5 and 6, and for each of them we fill two different kind of histograms that we call *good histogram* and *bad histogram*.
The *good histogram* is filled for the track pair 5 and 6 with the invariant mass of the reconstructed ρ^0_{low} candidate when the corresponding two pions are from the ρ^0 decay, while, when the pion pair is not from the ρ^0 decay, the *bad histogram* is filled with ρ^0_{low} candidate reconstructed mass. The same is done for the *good histogram* and *bad histogram* for the 4 and 6 tracks combination.
The ρ^0_{high} invariant mass spectrum for the weighted data sample is expected to have contributions from:

- $\Lambda_b^0 \to \Lambda_c^+\rho^0\pi^-$ decay mode, when the track pair is from the ρ^0 decay (Fig. D.6 top histogram reports the invariant mass distribution for the true track pair 4 and 6) and when the track pair is the wrong one (Fig. D.6 bottom histogram reports the invariant mass distribution for the wrong track pair 4 and 6).

- $\Lambda_b^0 \to \Lambda_c^+ a_1(1260)^- \to \Lambda_c^+\rho^0\pi^-$ decay mode, when the track pair is from the ρ^0 decay (Fig. D.8 top histogram reports the invariant mass distribution for the true track pair 4 and 6) and when the track pair is the wrong one (Fig. D.8, bottom histogram report the invariant mass distribution for the wrong track pair 4 and 6).

Appendix D. Study of $\Lambda_b^0 \to \Lambda_c^+\pi^-\pi^+\pi^-$ without Charmed Resonant Decay Modes

- $\Lambda_b^0 \to \Lambda_c^+\pi^-\pi^+\pi^-(nr)$, in this case the track pair is wrong in any case, (Fig. D.10, top histogram reports the invariant mass distribution for the track pair 4 and 6).

The corresponding distributions contributing to the ρ^0_{low} invariant mass spectrum are reported in Fig. D.7 (top histogram good combination, bottom histogram wrong combination for the $\Lambda_b^0 \to \Lambda_c^+\rho^0\pi^-$), Fig. D.9 (top histogram good combination, bottom histogram wrong combination for the $\Lambda_b^0 \to \Lambda_c^+ a_1(1260)^- \to \Lambda_c^+\rho^0\pi^-$) and in the bottom of Fig. D.10 (for the $\Lambda_b^0 \to \Lambda_c^+\pi^-\pi^+\pi^-(nr)$). For each decay mode, each pair of the invariant mass distibution of Fig. D.6, Fig. D.7, Fig. D.8, Fig. D.9, are fitted separately and then merged togheter to obtain the templates for the ρ^0_{high} and ρ^0_{low} mass distributions for the contribution mentioned above.
We could have used directly the distributions of ρ^0_{low} and ρ^0_{high} as reconstructed in the MC for each decay mode, but since the shapes of good and bad histograms are very different, this procedure guarantees a better description of them.
For the two pions contribution from $\Lambda_b^0 \to \Lambda_c^+\pi^-\pi^+\pi^-(nr)$, the templates for ρ^0_{high} and ρ^0_{low} are respectively obtained fitting the invariant mass distribution of Fig. D.10 top histogram and Fig. D.10 bottom histogram. Fig. D.11 shows the templates of the three decay modes normalized to the unit (PDFs) for the ρ^0_{high} (Fig. D.11(a)) and for the ρ^0_{low} (Fig. D.11(b)).

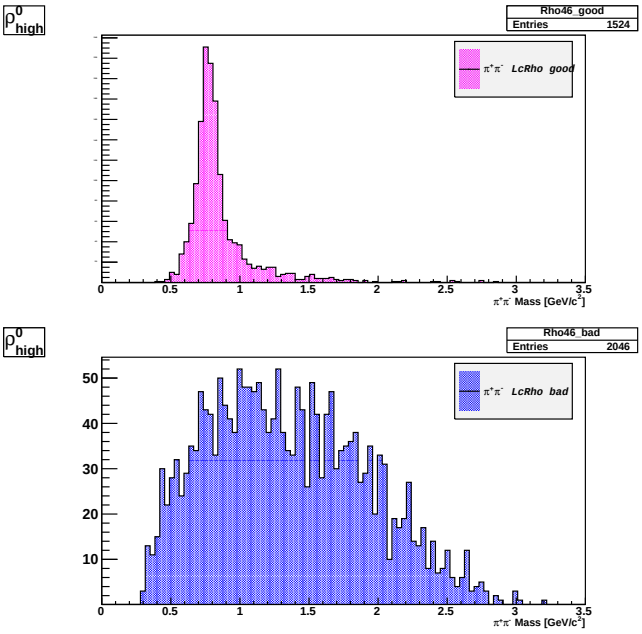

Figure D.6: *MC contributions to ρ^0_{high} from $\Lambda_b^0 \to \Lambda_c^+\rho^0\pi^-$ decay.*

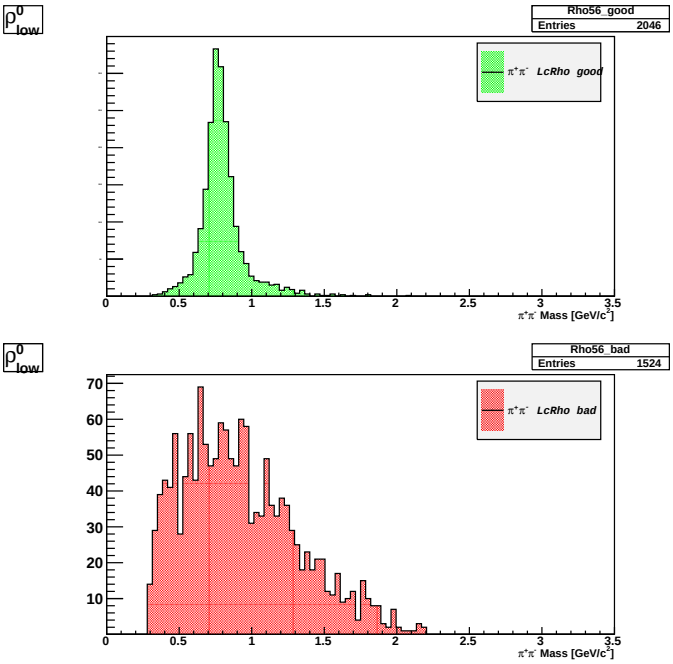

Figure D.7: *MC contributions to* ρ^0_{low} *from* $\Lambda_b^0 \to \Lambda_c^+\rho^0\pi^-$ *decay.*

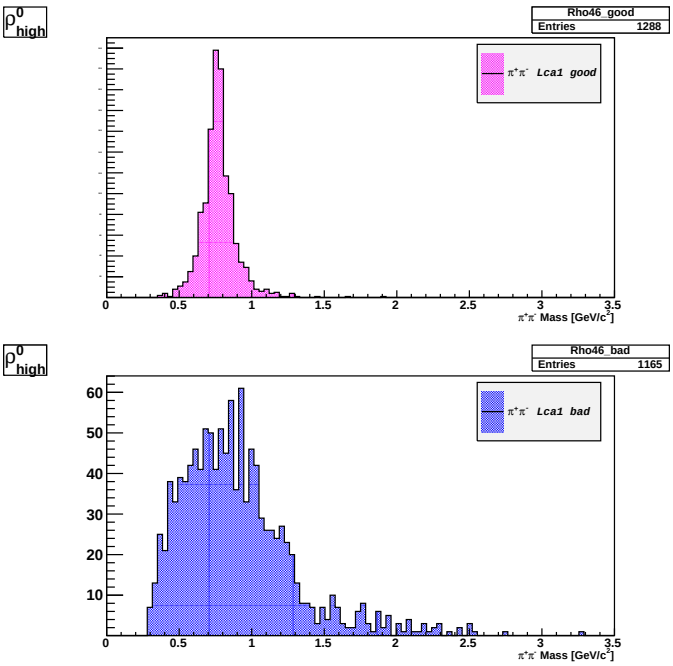

Figure D.8: *MC contributions to* ρ^0_{high} *from* $\Lambda_b^0 \to \Lambda_c^+a_1(1260)^-$ *decay.*

Appendix D. Study of $\Lambda_b^0 \to \Lambda_c^+\pi^-\pi^+\pi^-$ without Charmed Resonant Decay Modes

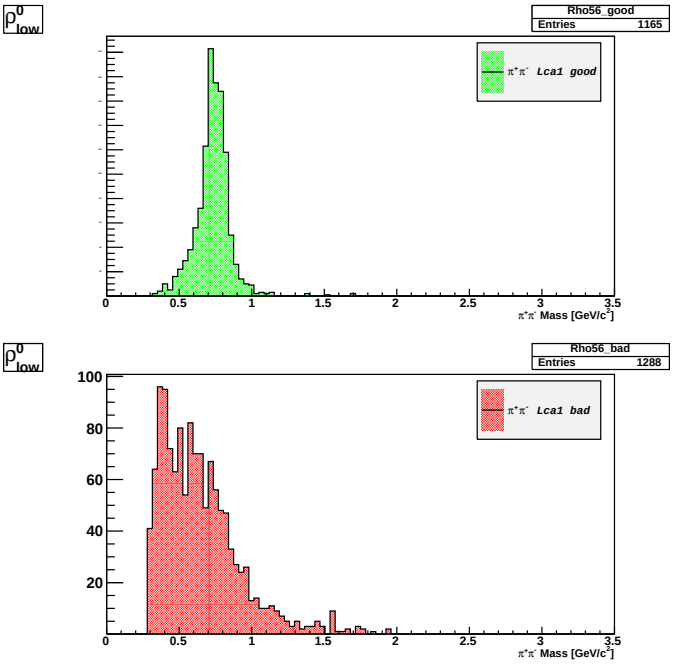

Figure D.9: *MC contributions to ρ^0_{low} from $\Lambda_b^0 \to \Lambda_c^+ a_1(1260)^-$ decay.*

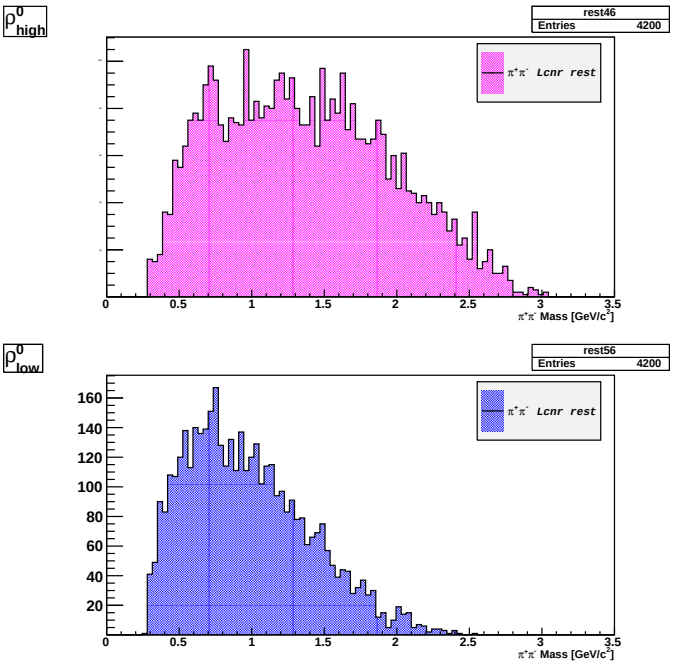

Figure D.10: *MC contributions to ρ^0_{high} (top) and to ρ^0_{low} (bottom) from $\Lambda_b^0 \to \Lambda_c^+\pi^-\pi^+\pi^-(nr)$ decay.*

D.3.2 Fit of Single Combinations

We made the fit on the weighted dataset of the ρ^0_{high} and ρ^0_{low} distributions of Fig. D.5(a) and Fig. D.5(b) modeling the contributions of the three decay modes with the corresponding PDFs of Fig. D.11, letting free to float in the fit their contribution. The fact that in principle there can be two different combinations of a pion pair, is a reason to make the fit of one of the two combinations (ρ^0_{high}, having the best mass resolution) and to use the achieved results, in terms of composition, as a cross-check on the other one, in order to verify that the fit of the $\pi^-\pi^+$ mass projection on the weighted dataset for ρ^0_{low} and ρ^0_{high} leads to the same results within the uncertainty.
The best fit result is reported respectively in Fig. D.12(a) for the ρ^0_{high} and in Fig. D.12(b) for the ρ^0_{low} combinations.
These fits show a clear and obvious difficulty in separating the ρ^0 contribution from the $\Lambda_b^0 \to \Lambda_c^+ a_1(1260)^-$ candidates, where $a_1(1260)^- \to \rho^0\pi^-$ and $\rho^0 \to \pi^-\pi^+$, and the ones from the $\Lambda_b^0 \to \Lambda_c^+\rho^0\pi^-$ candidates, where $\rho^0 \to \pi^-\pi^+$.
For the best fit of the ρ^0_{high} ditribution, the total yield of $\Lambda_b^0 \to \Lambda_c^+ a_1(1260)^-$ and $\Lambda_b^0 \to \Lambda_c^+\rho^0\pi^-$ and the yield of the $\Lambda_b^0 \to \Lambda_c^+\pi^-\pi^+\pi^-$ (see the fit results legenda) agrees with the same yields as determined in Sec. D.3. The same is not true for the ρ^0_{low} best fit where the yields are differents and only the $\Lambda_b^0 \to \Lambda_c^+\rho^0\pi^-$ is compatible with a null contribution.
We did several checks about the modeling of the templates without success.
The problem seems to be related to a wrong modeling of the ρ^0_{low} invariant mass distribution, the one with the lowest momentum.

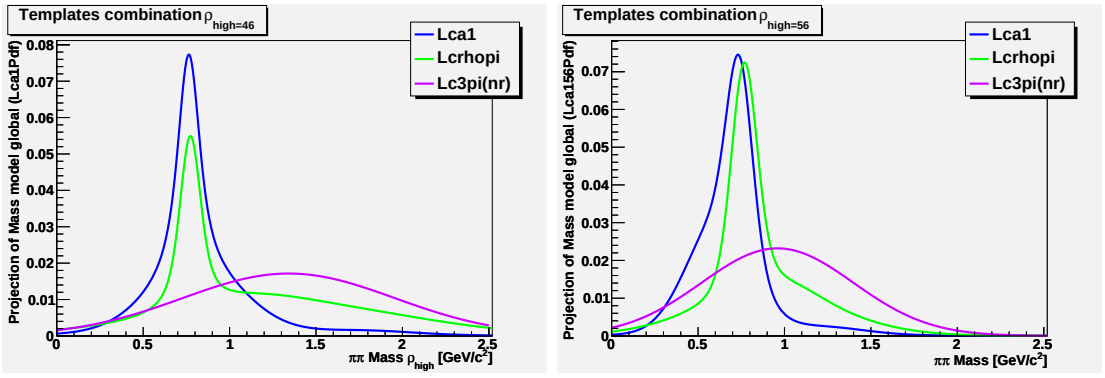

(a) (b)

Figure D.11: *MC templates used for the* ρ^0_{high} **D.11(a)** *and* ρ^0_{low} **D.11(b)** *contributions in the fit.*

Appendix D. Study of $\Lambda_b^0 \to \Lambda_c^+\pi^-\pi^+\pi^-$ without Charmed Resonant Decay Modes

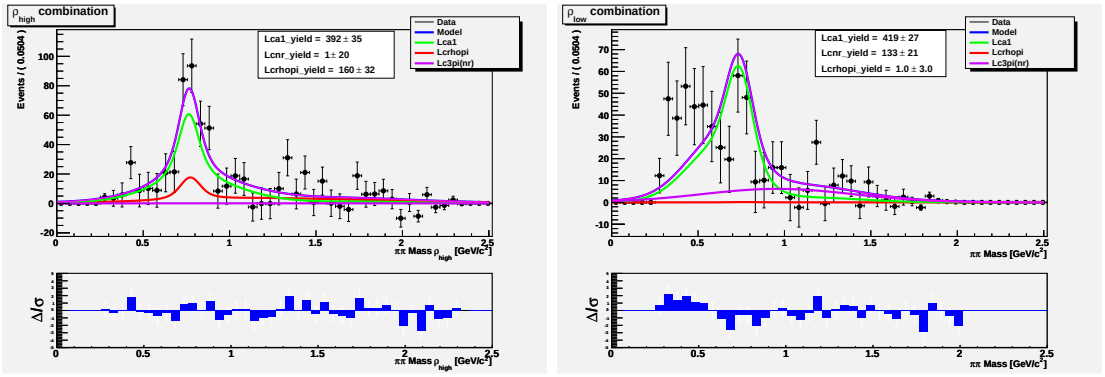

(a) (b)

Figure D.12: *Invariant mass distribution of* ρ^0_{high} **D.12(a)** *and* ρ^0_{low} **D.12(b)** *with overlaid the best fit curve (magenta curve).*

D.3.3 Final Considerations

The *sPlot* technique, since it is an unbinned method, definitely gave us the possibility to derive the maximum information, because of the low statistics we have. Unfortunately the idea that make the fit of one of the two combinations (ρ^0_{high}, having the best mass resolution) and to use the achieved results in terms of composition as a cross-check on the other one, did not work.
Comparing the two fits separately (see Fig. D.12(a) and Fig. D.12(b)), we realize that the combination ρ^0_{high}, characterized by the π^- with highest momentum, is one that gives less problems in the fit. Furthermore, for the best fit of the ρ^0_{high} ditribution, the total yield of $\Lambda_b^0 \to \Lambda_c^+ a_1(1260)^-$ and $\Lambda_b^0 \to \Lambda_c^+\rho^0\pi^-$ and the yield of the $\Lambda_b^0 \to \Lambda_c^+\pi^-\pi^+\pi^-(nr)$ (see the fit results legenda) agrees with the same yields as determined in Sec. D.3 where a different method is used to extract the contributions of the sum of the $\Lambda_b^0 \to \Lambda_c^+ a_1(1260)^-$ and $\Lambda_b^0 \to \Lambda_c^+\rho^0\pi^-$, and of the $\Lambda_b^0 \to \Lambda_c^+\pi^-\pi^+\pi^-(nr)$. Since, Fig. D.5(c) clearly shows a peak due to the $a_1(1260)^-$, this decay definitively contributes to the $\Lambda_b^0 \to \Lambda_c^+\pi^-\pi^+\pi^-$ signal.
Despite all the studies done, we cannot exclude the $\Lambda_b^0 \to \Lambda_c^+\pi^-\pi^+\pi^-(nr)$ and we decided to continue this analysis (the update) assuming equal proportion ($1/3$, $1/3$, $1/3$) of the three decay modes.

Acronyms

SM Standard Model

LHC Large Hadron Collider

LHCb Large Hadron Collider beauty

CDF Collider Detector at Fermilab

CDF II CDF in Run II

FNAL Fermi National Accelerator Laboratory

V_{CKM} Cabibbo-Kobayashi-Maskawa matrix

CKM Cabibbo-Kobayashi-Maskawa

QCD Quantum Chromo Dynamics

RF Radio-frequency cavities

PDG Particle Data Group

SLAC Stanford Linear Accelerator Center

SVXII Silicon VerteX

ISL Intermediate Silicon Layers

L00 Layer ØØ

COT Central Outer Tracker

Acronyms

TOF Time Of Flight detector

CEM Central Electro Magnetic calorimeter

CES Central Electromagnetic Strip multi-wire proportional chambers

CPR Central Pre-Radiator

CHA Central HAdronic calorimeter

WHA Wall HAdronic calorimeter

PEM Plug ElectroMagnetic calorimeter

PHA Plug HAdronic calorimeter

CMU Central MUon detector

CMP Central Muon uPgrade

CMX Central Muon eXtension

IMU Intermediate MUon system

BMU Barrel MUon chambers

BSU Barrel Scintillation counters

TSU Toroid Scintillation counters

CLC Cherenkov Luminosity Counters

BC bunch-crossing

HQET Heavy Quark Effective Theory

XFT eXtremely Fast Tracker

SVT Silicon Vertex Trigger

DAQ Data AcQuisition System

MC Monte Carlo

TTT Two Track Trigger

CSL Consumer Server/Data Logger

VME Vesa Module Eurocard

PMT PhotoMultiplier Tube

OPE Operator Product Expansion

LEP Large Electron Positron

CP CP transformation that combines charge conjugation C with parity P

CERN Conseil Europen pour la Recherche Nuclaire

ALEPH Apparatus for LEP Physics (LEP Experiment)

DELPHI Detector with Lepton, Photon and Hadron Identification (LEP Experiment)

FMPS Fermilab Multiparticle Spectrometer

WE Weak Exchange diagram

CPU Central Processing Unit

PDF Probability Density Function

SPS Super Proton Synchrotron (CERN)

HERA Hadron Electron Ring Accelerator (DESY)

NLO Next-to-Leading Order

SVX Silicon VerteX

VLSI Very Large-Scale Integration

AM Associative Memory

TDC Time to Digital Converter

PID Particle Identification

CWA Central Wall HAdronic calorimeters

BR Branching Ratio

CS Cabibbo suppressed

CF Cabibbo favored

Acronyms

CL Confidence Level

rms Root Mean Square

XTRP eXTRaPolator unit

WLS wavelength shifters

HEPG High Energy Physics Group

Bibliography

[1] **K. Nakamura** and ***others*** **(Particle Data Group)**, "Review of Particle Physics," *J. Phys.* **G 37** *(2010) 075021*.

[2] **A. V. Manohar** and **M. B. Wise**, "Heavy quark physics," *Camb. Monogr. Part. Phys. Nucl. Phys. Cosmol.* **10** *(2000) 1*.

[3] **N. Isgur**, **D. Scora**, **B. Grinstein**, and **M. B. Wise**, "Semileptonic B and D Decays in the Quark Model," *Phys. Rev.* **D 39** *(1989) 799*.

[4] **I. Dunietz**, "CP violation with beautiful baryons," *Z. Physik* **C 56** *(1992) 129*.

[5] **A. K. Leibovich**, **Z. Ligeti**, **I. W. Stewart**, and **M. B. Wise**, "Predictions for nonleptonic Λ_b and Θ_b decays," *Phys. Lett.* **B 586** *(2004) 337*.

[6] **H.-Y. Cheng**, "Nonleptonic weak decays of bottom baryons," *Phys. Rev.* **D 56** *(1997) 2799*.

[7] **T. Aaltonen** and ***others*** **(CDF Collaboration)**, "First Measurement of the Ratio of Branching Fractions $\mathcal{B}(\Lambda_b^0 \to \Lambda_c^+ \mu^- \overline{\nu}_\mu)$ / $\mathcal{B}(\Lambda_b^0 \to \Lambda_c^+ \pi^-)$," *Phys. Rev.* **D 79** *(2009) 032001*.

[8] **D. E. Acosta** and ***others*** **(CDF Collaboration)**, "Measurement of b hadron masses in exclusive J/ψ decays with the CDF detector," *Phys. Rev. Lett.* **96** *(2006) 202001*.

[9] **A. Abulencia** and ***others*** **(CDF Collaboration)**, "Measurement of the Λ_b^0 Lifetime in $\Lambda_b^0 \to J/\psi \Lambda^0$ in $p\bar{p}$ Collisions at $\sqrt{s} = 1.96\ TeV$," *Phys. Rev. Lett.* **98** *(2007) 122001*.

Bibliography

[10] **A. Abulencia** and ***others*** **(CDF Collaboration)**, "Measurement of $\sigma(\Lambda_b^0)/\sigma(\bar{B}^0) \times \mathcal{B}(\Lambda_b^0 \to \Lambda_c^+\pi^-)/\mathcal{B}(\overline{B^0} \to D^+\pi^-)$ in $p\bar{p}$ collisions at $\sqrt{s} = 1.96\,TeV$," *Phys. Rev. Lett.* **98** *(2007) 122002*.

[11] **T. Aaltonen** and ***others*** **(CDF Collaboration)**, "Measurement of Ratios of Fragmentation Fractions for Bottom Hadrons in $p\bar{p}$ Collisions at $\sqrt{s} = 1.96\,TeV$," *Phys. Rev.* **D 77** *(2008) 072003*.

[12] **T. Aaltonen**, **A. Abulencia**, and ***others*** **(CDF Collaboration)**, "Search for chargino-neutralino production in $p\bar{p}$ collisions at $\sqrt{s} = 1.96\,TeV$," *Phys. Rev. Lett.* **99** *(2007) 191806*.

[13] **T. Aaltonen**, **A. Abulencia**, **J. Adelman**, and ***others*** **(CDF Collaboration)**, "Observation and mass measurement of the baryon Ξ_b^-," *Phys. Rev. Lett.* **99** *(2007) 052002*.

[14] **T. Aaltonen** and ***others*** **(CDF Collaboration)**, "Observation of New Charmless Decays of Bottom Hadrons," *Phys. Rev. Lett.* **103** *(2009) 031801*.

[15] **P. Azzurri**, **P. Barria**, **M. A. Ciocci**, **S. Donati**, **P. Maestro**, and **E. Vataga**, "Measurement of $\mathcal{B}(\Lambda_b^0 \to \Lambda_c^+\pi^-\pi^+\pi^-)/\mathcal{B}(\Lambda_b^0 \to \Lambda_c^+\pi^-)$," *CDF Note 10563*.

[16] **P. Barria**, **P. Azzurri**, **M. A. Ciocci**, **S. Donati**, **P. Maestro**, and **E. Vataga**, "Measurement of $\mathcal{B}(\Lambda_b^0 \to \Lambda_c^+\pi^-\pi^+\pi^-)/\mathcal{B}(\Lambda_b^0 \to \Lambda_c^+\pi^-)$," *CDF Note 10564*.

[17] **R. Aaij** et al., "Measurements of the Branching fractions for $B_s \to D_s\pi\pi\pi$ and $\Lambda_b^0 \to \Lambda_c^+\pi\pi\pi$," *Phys. Rev.* **D 84** *(2011) 092001*.

[18] *CDF Web Page Analysis Blessed.* http://www-cdf.fnal.gov/physics/new/bottom/091029.blessed-Lb2Lc3pi-structure/LbLc3pi.html

[19] **P. Azzurri**, **P. Barria**, **M. A. Ciocci**, **S. Donati**, and **E. Vataga**, "First observation and measurement of the resonant structure of the $\Lambda_b^0 \to \Lambda_c^+\pi^-\pi^+\pi^-$ decay mode," *[arXiv:0912.4380]*.

[20] **F. Mandl** and **G. Shaw**, *Quantum Field Theory.* John Wiley & Son.

[21] **E. M. Peskin** and **D. V. Schroeder**, "An Introduction to quantum field theory," Addison-Wesley (1995) 842 p.

[22] **D. H. Perkins**, "Introduction to High-Energy Physics," Addison-Wesley (1982) 437p.

[23] **M. Kobayashi**, **H. Kondo**, and **T. Maskawa**, "Symmetry breaking of chiral u(3) x u(3) and x $\rightarrow \eta\ \pi\ \pi$ decay amplitude," *Prog. Theor. Phys.* **49** *(1973) 634, [doi:10.1143/PTP.49.634].*

[24] **N. Cabibbo**, "Unitary symmetry and leptonic decays," *Phys. Rev. Lett.* **10** *(1963) 531, [doi:10.1103/PhysRevLett.10.531].*

[25] **A. Sherstnev**, "Prospects for b-quark production cross section measurements in p p collisions at the LHC," *Nucl. Phys.* **167** *(Proc. Suppl.) (2007) 21,[arXiv:hep-ph/0609143].*

[26] **A. D. Martin**, **W. J. Stirling**, and **R. G. Roberts**, "New information on parton distributions," *Phys. Rev.* **D 47** *(1993) 867.*

[27] **T. Sjostrand**, "Status of Fragmentation Models," *Int. J. Mod. Phys.* **A 3** *(1988) 751.*

[28] **S. Yu**, **R. Tesarek**, **D. Litvintsev**, **J. Heinrich**, and **N. Lockyer**, "Correction of $\Lambda_b^0 \rightarrow B^0$ Production Cross-Section Ratio," *CDF Note 7558.*

[29] **S. Yu**, **D. Litvintsev**, **R. Tesarek**, **J. Heinrich**, and **N. Lockyer**, "Ratio of $\mathcal{B}(\Lambda_b^0 \rightarrow \Lambda_c^+ \mu\nu) \rightarrow \mathcal{B}(\Lambda_b^0 \rightarrow \Lambda_c^+ \pi)$ in the two track trigger," *CDF Note 7559.*

[30] **S. Yu**, "First measurement of the ratio of branching fractions $\mathcal{B}(\Lambda_b^0 \rightarrow \Lambda_c^+ \mu\nu) \rightarrow \mathcal{B}(\Lambda_b^0 \rightarrow \Lambda_c^+ \pi^-)$," *CDF Thesis 7604.*

[31] **A. A. Affolder** and ***others*** **(CDF Collaboration)**, "Measurement of b quark fragmentation fractions in $p\bar{p}$ collisions at $\sqrt{s} = 1.8\ TeV$," *Phys. Rev. Lett.* **84** *(2000) 1663.*

[32] **C. Albajar** and ***others*** **(UA1 Collaboration)**, "First observation of the beauty baryon Λ_b^0 in the decay channel $\Lambda_b^0 \rightarrow J/\psi\Lambda$ at the CERN proton - anti-proton collider," *Phys. Lett.* **B 273** *(1991) 540.*

[33] **F. Abe** and ***others*** **(CDF Collaboration)**, "Search for $\Lambda_b \rightarrow J/\psi\Lambda^0$ in $p\bar{p}$ collisions at $\sqrt{s} = 1.8\ TeV$," *Phys. Rev.* **D 47** *(1993) 2639.*

[34] **P. Abreu** and ***others*** **(DELPHI Collaboration)**, "Search for exclusive decays of the Λ_b baryon and measurement of its mass," *Phys. Lett.* **B 374** *(1996) 351.*

[35] **F. Abe** and ***others*** **(CDF Collaboration)**, "Observation of $\Lambda_b^0 \rightarrow J/\psi\Lambda$ at the Fermilab proton antiproton collider," *Phys. Rev.* **D 55** *(1997) 1142.*

Bibliography

[36] **M. W. Arenton** and ***others*** , "Observation of massive $\Lambda K^0(s)\pi^+\pi^+\pi^-\pi^-$ events above 5 GeV/c^2," *Nucl. Phys.* **B 274** *(1986) 707*.

[37] **R. Barate** and ***others*** **(ALEPH Collaboration)**, "Measurement of the B baryon lifetime and branching fractions in Z decays," *Eur. Phys. J.* **C 2** *(1998) 197*.

[38] **J. Abdallah** and ***others*** **(DELPHI Collaboration)**, "Measurement of the Λ_b^0 decay form factor," *Phys. Lett.* **B 585** *(2004) 63*.

[39] **D. E. Acosta** and ***others*** **(CDF Collaboration)**, "Search for $\Lambda_b \to p\pi$ and $\Lambda_b \to pK$ decays in $p\bar{p}$ collisions at $\sqrt{s} = 1.96\,TeV$," *Phys. Rev.* **D 72** *(2005) 051104*.

[40] **D. E. Acosta** and ***others*** **(CDF Collaboration)**, "Search for radiative b-hadron decays in $p\bar{p}$ collisions at $\sqrt{s} = 1.8\,TeV$," *Phys. Rev.* **D 66** *(2002) 112002*.

[41] **K. G. Wilson**, "Nonlagrangian models of current algebra," *Phys. Rev.* **179** *(1969) 1499, [doi:10.1103/PhysRev.179.1499]*.

[42] **T. Appelquist** and **H. D. Politzer**, "Heavy quarks and e^+e^- annihilation," *Phys. Rev. Lett.* **34** *(1975) 43*.

[43] **E. Eichten** and **B. Hill**, "An effective field theory for the calculation of matrix elements involving heavy quarks," *Phys. Lett.* **B 234** *(1990) 511*.

[44] **U. Aglietti**, "Prediction of beauty particle masses with the heavy quark effective theory," *Phys. Lett.* **B 281** *(1992) 341*.

[45] **S. Godfrey** and **N. Isgur**, "Mesons in a Relativized Quark Model with Chromodynamics," *Phys. Rev.* **D 32** *(1985) 189, [doi:10.1103/PhysRevD.32.189]*.

[46] **N. Isgur** and **M. B. Wise**, "Weak Transition Form-Factors between Heavy Mesons," *Phys. Lett.* **B 237** *(1990) 527, [doi:10.1016/0370-2693(90)91219-2]*.

[47] **H. Georgi**, **B. Grinstein**, and **M. B. Wise**, "Λ_b semileptonic decay form factors for $m_c \neq \infty$," *Phys. Lett.* **B 252** *(1990) 456, [doi:10.1016/0370-2693(90)90569-R]*.

[48] **G. Aubrecht** and ***others*** , *A Teachers Guide To The Nuclear Science Wall Chart*. Contemporary Physics Education Project.

[49] **M. Popovic**, **L. Allen**, and **C. W. Schmidt**, "Fermilab Linac Injector, revisited," prepared for 16th IEEE Particle Accelerator Conference (PAC 95) and International Conference on High-energy Accelerators (IUPAP), Dallas, Texas, 1-5 May 1995.

[50] **D. Mohl**, "Physics and technique of stochastic cooling," *Phys. Reports*," vol. 58, 1980.

[51] **S. Nagaitsev** and ***others*** , "Experimental demonstration of relativistic electron cooling," *Phys. Rev. Lett.* **96** *(2006) 044801*.

[52] **F. B. Division**, *RUN II Handbook*. http://www-bd.fnal.gov/lug/runII_handbook/RunII_index.html

[53] **D. Tonelli**, "First observation of the $B_s^0 \to K^+K^-$ decay mode, and measurement of the B^0 and B_s^0 mesons decay-rates into two-body, charmless final states at cdf," *CDF Thesis 8667*.

[54] **Collaboration CDF**, "The CDF IIb detector: Technical Design Report."

[55] **Collaboration CDF**, "The CDF II Detector Technical Design Report," October, 1996, summary of the CDF RunII Detector Parameters.

[56] **Collaboration CDF**, "Proposal for Ehnancement of the CDF II Detector: an Inner Silicon Layer and a Time of Flight Detector," October 23, 1998.

[57] **D. Acosta** and ***others*** , "The performance of the CDF luminosity monitor," *Nucl. Instrum. Meth.* **A494** *(2002) 57*.

[58] **F. Abe** and ***others*** **(CDF Collaboration)**, "The CDF detector: an overview," *Nucl. Instrum. Meth.* **A271** *(1988) 387*, FERMILAB-PUB-94/024-E (1994).

[59] **R. Blair** and ***others*** **(CDF Collaboration)**, "The CDF II detector: Technical Design Report," FERMILAB-PUB-96/390-E (1996).

[60] **T. K. Nelson**, "The CDF Layer ØØ detector," *Int. J. Mod. Phys.* **A 16S1C** *(2001) 1091*.

[61] **A. Sill**, "CDF Run II silicon tracking projects," *Nucl. Instrum. Meth.* **A447** *(2000) 1*.

[62] **A. A. Affolder** and ***others*** , "Status report of the intermediate silicon layers detector at CDFII," *Nucl. Instrum. Meth.* **A485** *(2002) 6*.

Bibliography

[63] **K. T. Pitts**, "The CDF Central Outer Tracker," *Nucl. Phys.* **61B** *(Proc. Suppl.) (1998) 230*.

[64] **C. S. Hill**, "Operational experience and performance of the CDFII silicon detector," *Nucl. Instrum. Meth.* **A530** *(2004) 1*.

[65] *Public Web Page*. http://penn01.fnal.gov

[66] **S. D'Auria**, **D. Lucchesi**, **S. Da Ronco**, **R. Carosi**, **M. Ciocci**, **S. Donati**, **P. Catastini**, **M. Morello**, **G. Punzi**, **P. Squillacioti**, **D. Tonelli**, **S. Torre**, **M. Rescigno**, **S. De Cecco**, **S. Giagu**, **M. Casarsa**, and **A. Cerri**, "Track-based calibration of the COT specific ionization," *CDF Note 6932*.

[67] **S. E. Yu**, "COT dE/dx measurement and corrections," *CDF Note 6361*.

[68] **P. Azzi**, **G. Busetto**, **P. Gatti**, and **A. Ribon**, "Histogram tracking in the COT," *CDF Note 5562*.

[69] **F. D. Snider**, "Tracking at CDF: Algorithms and experience from Run I and Run II," *Nucl. Instrum. Meth.* **A566** *(2006) 133*.

[70] **C. P. Hays** and ***others*** , "Inside-out tracking at CDF," *Nucl. Instrum. Meth.* **A538** *(2005) 249*.

[71] **J. Goldstein**, **C. Issever**, **T. Nelson**, **R. Snider**, and **D. Stuart**, "Silicon tracking for plug electrons," *CDF Note 5970*.

[72] **D. Acosta** and ***others*** **(CDF Collaboration)**, "A Time-Of-Flight detector in CDF-II," *Nucl. Instrum. Meth.* **A518** *(2004) 605*.

[73] **C. M. Ginsburg**, "CDF Run II Muon System," *Eur. Phys. J.* **C 33** *(2004) s1002*.

[74] **G. Ascoli** and ***others*** , "CDF central muon detector," *Nucl. Instrum. Meth.* **A268** *(1988) 33*.

[75] **S. Klimenko**, **J. Konigsberg**, and **T. M. Liss**, "Averaging of the inelastic cross sections measured by the CDF and the E811 experiments." http://lss.fnal.gov/archive/test-fn/0000/fermilab-fn-0741.pdf

[76] **G. Gomez-Ceballos** and ***others*** , "Event builder and Level 3 at the CDF experiment," *Nucl. Instrum. Meth.* **A518** *(2004) 522*.

[77] **T. Trigger** and **D. W. Group**, "Run II trigger table and datasets plan," *CDF Note 4718*.

[78] **E. J. Thomson** and ***others*** , "Online track processor for the CDF upgrade," *IEEE Trans. Nucl. Sci.* ***49****, 2002 (1063).*

[79] **A. Rahaman** and **R. Oldeman**, "Level-1 trigger rates of the two-track trigger at high-luminosities," *CDF Note 7370.*

[80] **S. R. Amendolia** and ***others*** , "The AMchip: a Full-custom CMOS VLSI Associative Memory for Pattern Recognition," *IEEE Trans. Nucl. Sci.* ***39****, 1992 (795).*

[81] **W. Ashmanskas** and ***others*** **(CDF Collaboration)**, "Performance of the CDF online silicon vertex tracker," *IEEE Trans. Nucl. Sci.* ***49****, 2002 (1177), [doi:10.1109/TNS.2002.1039633].*

[82] **R. Brun** and ***others*** , *GEANT: Simulation Program For Particle Physics Experiments. User Guide and Reference Manual.*

[83] **P. A. M. Fernandez**, "Performance of the CDF calorimeter simulation in Tevatron Run II," *AIP Conf. Proc.*," vol. 867, pp. 487–494, 2006.

[84] **R. Veenhof**, "Garfield, a drift chamber simulation program," prepared for International Conference on Programming and Mathematical Methods for Solving Physical Problems, Dubna, Russia, 14-19 Jun 1993.

[85] **R. Veenhof**, "GARFIELD, recent developments," *Nucl. Instrum. Meth.* **A419** *(1998) 726.*

[86] **W. Badgett**, "The CDF Run II Database and Online Java API," *CDF Note 5672.*

[87] **M. Ciocci**, **R. Tesarek**, and **E. Vataga**, "Datasets for fully reconstructed decays of $\Lambda_b^0 \to \Lambda_c^+\pi^-$ and $\Lambda_b^0 \to \Lambda_c^+\pi^-\pi^+\pi^-$," *CDF Note 9042.*

[88] **J. Marriner**, "Secondary vertex fit with mass and pointing constraints (CTVMFT)," *CDF Note 1996.*

[89] **K. Anikeev**, **P. Murat**, and **C. Paus**, "Description of Bgenerator II," *CDF Note 5092.*

[90] **D. Litvintsev** and ***others*** , "Measurement of the Λ_b^0 p_T spectrum in the Two Track Trigger data using fully reconstructed decay $\Lambda_b^0 \to \Lambda_c^+\pi^-$," *CDF Note 8156.*

[91] **W. Bell**, **J. P. Fernandez**, **L. Flores**, **F. Wuerthwein**, and **R. J. Tesarek**, *Users Guide to EvtGen at CDF.* http://www.slac.stanford.edu/lange/EvtGen

Bibliography

[92] **L. Aitala** and ***others*** , "Multidimendional Resonace Analysis of $\Lambda_c^+ \to pk^-\pi^+$," *Phys. Lett.* **B 471** *(2000) 449*.

[93] **W. Verkerke** and **D. Kirkby**, *RooFit Users Manual v2.07*. http://roofit.sourceforge.net/

[94] **A. E. Blechman**, **A. F. Falk**, **D. Pirjol**, and **J. M. Yelton**, "Threshold effects in excited charmed baryon decays," *Phys. Rev.* **D 67** *(2003) 074033*.

[95] **H. Albrecht** and ***others*** **(ARGUS Collaboration)**, "Search for Hadronic $b \to u$ decays," *Phys. Lett.* **B 241** *(1990) 278*.

[96] **B. Di Ruzza**, **L. Ortolan**, **G. Artoni**, **M. Dorigo**, **M. Rescigno**, and **A. Zanetti**, "Study of the $B_s^0 \to \phi\phi$ decay and measurement of its branching ratio," *CDF Note 9743*.

[97] **P. Azzurri**, **P. Barria**, **M. A. Ciocci**, **S. Donati**, **R. J. Tesarek**, and **E. Vataga**, "A Study of some Cabibbo suppressed Backgrounds to the Decay $\Lambda_b^0 \to \Lambda_c^+\pi^-\pi^+\pi^-$," *CDF Note 9845*.

[98] **W. Bell**, **J. P. Fernandez**, **L. Flores**, **F. Wuerthwein**, and **R. J. Tesarek**, "User Guide For EvtGen CDF," *CDF Note 5618*.

[99] **E. M. Aitala** and ***others*** **(E791 Collaboration)**, "Multidimensional resonance analysis of $\Lambda_c^+ \to pk^-\pi^+$," *Phys. Lett.* **B 471** *(2000) 449*.

[100] **M. Pivk** and **F. R. Le Diberder**, "*sPlot*: a statistical tool to unfold data distributions," *Nucl. Instrum. Meth.* **A555** *(2005) 356*.

[101] **M. Šimečková**, "Maximum Weighted Likelihood Estimator in Logistic Regression," *WDS'05 Proceedings of Contributed Papers, Part I*, p. 144148, 2005.

List of Figures

List of Figures

List of Figures

List of Figures

List of Figures

List of Figures

List of Figures

List of Figures

List of Tables

List of Tables

List of Tables

List of Tables

Acknowledgements

Am I dreaming or is it really over?

If I get here I think it is also the time to write "the end" to this adventure and to say thank you to all those who have been involved with me in this adventure. As it is well known to all, synthesis is not my best quality, but this time I'd surprise everyone.

I would like to start thanking my supervisor Agnese especially for this final multilanguage brain storming and for giving me the opportunity to know the CDF experiment but above all the CDF people.

A thank goes to my colleagues of the "Fellowship of the Lambda B" Elena Vataga, Paolo Azzurri, Rick Tesarek and Simone Donati. I really appreciate it, especially in difficult times.

This adventure would not be the same if I had not met Ciccio, Gerardo, Mr. Drive Foxes, Saba, Janu, Maria, Simpatia, Mr. Montecherlo, The Parmesan guy, The hungry guy, Betta, Svampi, Ricciotto, Marcolino, Pretty woman, Farunfi, Boss, Little Joint, and many other people who shared with me good and bad times.

Ciccio thanks for giving me unconsciously a challenge more or less every day.
Thanks Oscar for having done what someone else would have done.
Saba how can I do without you at home?

A special thanks goes to Paola, omnipresent in my life in these last days, taking care of me.

Acknowledgements

Bombolona, Manu, Bea, Stefy I have a message for you: "I'm still alive!".

A special thought goes to my 5 sigmas of happiness, Viviana, for sharing with me this PhD with all the complications. I couldn't have asked for a better "partner" to share travels and a lot of fun. I didn't tell you but all the "omissis" in this Thesis are dedicated to you. You have been really important for me and without you it would not be the same thing.
It will not be easy to get rid of me but you must not take it as a threat.
See you to the next challenge ... blindfolded archery .

Thanks also to my friends in Rome, Pisa and Fermilab.
Sorry guys if you don't see here your name but, as you know, I'm extremely inclusive and you are so many.

This thesis is dedicated to my family and in particular to my father, that always supported me and believed in me no matter the crazy choices I took and above all, despite the fact that these choices have let me go away.

Each of you gave me a lot of fun and since fun is important I will come to check you one by one no matter where you are. Since I'm The Ultimate Ace now it's time to close and write the word *The End* to this story. It will be difficult to forget each of you.

That's all folks!